Universitat Autònoma de Barcelona

Systematic Design Methodology for Acoustic Wave Filters Integrated in Multiplexers and Codesigned Modules

Patricia María Silveira Taboadela

Universitat Autònoma de Barcelona

Department of Telecommunications and Systems Engineering

Systematic Design Methodology for Acoustic Wave Filters Integrated in Multiplexers and Codesigned Modules

Theoretical and Practical Approaches

Ph.D. Dissertation in Electrical and Telecommunications Engineering by

Patricia María Silveira Taboadela
E-mail:patricia.silveira@uab.cat

Thesis Advisor: Prof. Pedro de Paco Sánchez
E-mail: pedro.depaco@uab.cat
Universitat Autònoma de Barcelona (UAB)
Escola d'Enginyeria

June, 2021

“The mind is not a vessel to be filled but a fire to be ignited.”

Plutarch

Abstract

The worldwide implementation of 5G technology and the extended use of wireless networks have boosted the fast-paced increase in the radio frequency bands number supported by smartphones and other mobile devices. Simultaneously, to increment the connection speed, the modulation scheme complexity, antenna number, and carrier aggregated are increasing. These specifications require advances in the RF filter technology to ensure the proper selection of each carrier and the full information acquisition. Additionally, smaller devices are needed for a shrinking space and also be able to handle higher powers in a highly integrated scenario.

In this challenging environment, resonators based on acoustic wave (AW) technology have demonstrated to be the solution for the market requirements. The AW filter design has been driven by optimization techniques that require a time-consuming process and computational efforts, being inefficient from the industry point of view. Nevertheless, simulation tools based on advanced synthesis techniques considering the technological accommodation have been developed in our research group in the last years. These tools provide precise and fast solutions as the first tier for a later optimization procedure.

The principal purpose of this thesis is to meet the current demands of integration of multiple filters in one RF module, namely multiplexers, and also including power amplifiers (PA) to reduce the device size inside the smartphones. For the multiplexers design, the Minimum Susceptance Networks (MSN) concept has been exploited, introducing the reflection coefficient phase control as a key element for this kind of network classification. Two probable scenarios were analyzed regarding the frequency plan: fixed and flexible. The latter is a complex case boosted by the advent of the Carrier Aggregation technology and the market requirements. The proposed methodology guarantees technological feasibility and mask specifications fulfillment for each channel.

As part of the AW filters module integration, this thesis addresses the synthesis considering complex source/load impedances. The proposal allows the co-design of filters with active or passive networks removing the common inter-stage matching network. It is illustrated the co-design process for power amplifiers and filters analyzing each part's features to ensure high efficiency and output power in the passband. Simultaneously, a Chebyshev filter response is obtained in the resulting device.

Moreover, the phase control with different purposes is also discussed in this document. The theoretical analysis has been supported by simulated examples and manufacturing prototypes that show the approach's pertinence. The achieving results have been summarized at each chapter's end.

Resumen

La implementación de la tecnología 5G a nivel mundial y el extendido uso de conexiones inalámbricas han impulsado el incremento acelerado del número de bandas de radio frecuencia (RF) que deben ser soportadas por los teléfonos inteligentes y los dispositivos móviles. Al mismo tiempo aumenta la complejidad de los esquemas de modulación, el número de antenas y la cantidad de portadoras con el objetivo de aumentar la velocidad de conexión. Estas demandas requieren avances en la tecnología de filtros de RF que garanticen la selección correcta de cada portadora y la adquisicion íntegra de la información deseada. Sumamos además la necesidad de tener dispositivos cada vez más pequeños en un espacio cada vez más reducido y capaces de manejar mayores potencias en un escenario de alta integración.

En este contexto tan desafiante, los filtros basados en resonadores de tecnología microacústica han demostrado ser la solución para cubrir las necesidades del mercado. El diseño de filtros en esta tecnología ha estado dominado por técnicas de optimización que requieren un gran tiempo de procesado y un esfuerzo computacional no eficientes desde el punto de vista industrial. Sin embargo, herramientas de simulación basadas en métodos de síntesis avanzados que consideran los requerimientos propios de la tecnología han sido desarrollados en los últimos años en nuestro grupo de investigación con el objetivo de proporcionar una solución precisa y rápida que sirva de semilla para una posterior optimización.

Esta tesis persigue como objetivo dar respuesta a la tendencia actual de integración de múltiples filtros en módulos de RF que incluyen amplificadores de potencia (PA) para disminuir la ocupación dentro de los smartphones. Durante el proceso de diseño de multiplexores he aplicado conceptos con fundamentos teóricos sólidos como las Redes de Mínima Susceptancia y he introducido el control de la fase en el proceso de síntesis como elemento clave en la clasificación de dichas redes de filtrado. Dos posibles escenarios fueron analizados según el plan de frecuencia: fijo y flexible. Este último escenario es especialmente complejo y constituye una demanda industrial reciente debido a la aparición de la tecnología de Carrier Aggregation. La metodología presentada garantiza la viabilidad tecnológica y el cumplimiento de las especificaciones para cada banda de frecuencia.

Como parte de la integración en módulos, esta tesis también incluye la síntesis de filtros acústicos con impedancia compleja a la entrada y/o salida. Esta propuesta permite el codiseño de filtros con elementos activos o pasivos para eliminar redes intermedias de adaptacion de impedancia. Se ilustra el proceso de codiseño de amplificadores de potencia y filtros en tecnología microacústica desde un punto de vista integrador para garantizar una alta eficiencia en la conversión de energía y potencias de salida estables en toda la banda de frecuencia. Simultáneamente, una respuesta de filtrado tipo Chebyshev es obtenida en el dispositivo final.

El control de la fase con diferentes objetivos es también abordado en este documento. Todos los análisis teóricos han sido acompañados de ejemplos simulados y prototipos fabricados que demuestran la ideoneidad de los planteamientos. Los resultados alcanzados han sido resumidos en cada capítulo.

Acknowledgements

The journey has ended and the dissertation is written, so is time to stop for acknowledging the valuable help that I have received in the course of this Ph.D. program. First of all, I want to express my deep gratitude to my advisor Prof. Pedro de Paco Sánchez for accepting me as his student and give me the opportunity of working on such interesting research. I want to thanks the trust, the patience, the perseverance, the advice, the reviews, the support, and the dedication at all times. Beyond his technical knowledge, I believe that his personal charisma and leadership gave me the inspiration and motivation in tough times. In these years he has earned my deepest respect and esteem.

Also, I would like to thank the members of Antennas and Microwave Systems Group, especially Dr. Jordi Verdú Tirado for his support, dedication, and suggestions made over the years. His contributions were critical for the development of this thesis. Additionally, I want to recognize the advice and feedback received from Prof. Josep Parrón and Prof. Gary Junkin. A special mention to Ernesto Díaz for his helpful technical assistance in the laboratory. As part of the Department of Telecommunications and Systems Engineering, I want to acknowledge the work performed by the administrative staff, especially Susana Ferrer. Additionally, thanks to Zoya Popović and José Estrada from the University of Colorado at Boulder for the collaboration.

I want to thanks my current and past office mates Iuliia, Ángel, Eloi, and LLuis for the support, brainstorming, and technical discussions, but also for the jokes and good moments. Also, I want to mention all my Ph.D. program colleagues Edith, Iván, Giulio, Guillem, Sergi, and Edwar. Special thanks go to my friend and colleague Daniel Rivas for his unconditional friendship, support, and advice.

Beyond the academic environment, I want to mention special people who supported me on this journey: Adrián and his loving family, my "crazy haploides" team led by Pep, my friends Karina, Patricia, Carol, Moré, Talía, Alejandro, and Lily.

Last but not least, I want to express my infinite gratitude and love to my family who always encourages me to follow my dreams. Thanks to my parents Marta and Eduardo, and my sister María Carla for the patience, the trust, the support, and the love despite the distance. I owe everything I am to his teachings.

Patricia Silveira Taboadela

Contents

List of Figures

List of Tables

Acronyms

ADS	Advanced Design System
AlN	Aluminium Nitride
AW	Acoustic Wave
BAW	Bulk Acoustic Wave
BVD	Butterworth-Van Dyke
BW	Bandwidth
CA	Carrier Aggregation
CMOS	Complementary Metal–Oxide–Semiconductor
CPRL	Common Port Return Loss
DTF	Doubly Terminated Filter
FBAR	Film Bulk Acoustic Resonator
FBW	Fractional Bandwidth
FIR	Frequency Invariant Reactance
FPA	Filtering Power Amplifier
HPUE	High Performance User Equipment
IDT	Interdigital Transducer
I.H.P.	Incredible High Performance
IL	Insertion Loss
k_{eff}^2	Effective piezoelectric coupling coefficient
$LiNbO_3$	Lithium Niobate
$LiTaO_3$	Lithium Tantalate
mBVD	modified Butterworth-Van Dyke
MEMS	Micro-electromechanical Systems
MIMO	Multiple-Input Multiple-Output
MRN	Minimum Reactance Network
MSN	Minimum Susceptance Network

NRN	Non-Resonant Node
OoB	Out of Band
PA	Power Amplifier
PAE	Power Added Efficiency
PAW	Plate Acoustic Wave
Q	Quality factor
RF	Radio Frequency
RFFE	Radio Frequency Front End
RL	Return Loss
RN	Resonant Node
Rx	Reception
SAW	Surface Acoustic Wave
ScAlN	Scandium-doping of aluminum nitride
SiO_2	Silicon dioxide
SMR	Solidly Mounted Resonator
STF	Singly Terminated Filter
TC	Temperature-Compensated
TCF	Temperature Coefficient of Frequency
Tx	Transmission
TZ	Transmission Zero
XBAR	laterally eXcited Bulk Acoustic Resonator
4G	Fourth Generation
5G	Fifth Generation

CHAPTER 1

Introduction

Wireless connectivity is exploding on a global basis. The extraordinary need for faster speeds and increased bandwidth, significantly lower latency, and more reliable and secure wireless connectivity has never been more pronounced. The newest technologies are dramatically altering the world, creating a market for diverse and transformative applications, and changing how individuals live, work, play and learn. At the same time, connectivity is expanding into an adjacent set of IoT markets. From smart homes to the smart grid and from industrial to wearables, the number of connected devices is rapidly proliferating.

The number of frequency bands used in mobile telecommunication has undergone a considerable increase from 4 bands in the 2000s to more than 50 bands today [1]. To manage this growth, also pushed by the upcoming 5G, radio frequency (RF) modules have been widely developed. Nowadays, filtering is one of the most substantial growing market among the numerous RF component families dedicated to mobile telecommunication applications, thanks to the traditional need of new antennas and development of multiple carrier aggregation (CA) [2].

The RF filters embedded into a smartphone reject and accept the appropriate signals that fall in certain radio spectrum areas with high selectivity. These filters are needed to prevent the interaction between the sensitive receive (Rx) path and the transmitted signals (Tx), and avoid the noise from various RF sources. Highly selective RF-filters between antennas and pre-amplifiers ensure that only signals from the correct Rx band will be amplified. The narrow transition range between Rx and Tx filter, which can be up to 10 MHz, should change from $>$ 50 dB attenuation at the upper edge of the related Tx band to $<$ 3 dB insertion loss at the lower edge of the Rx band. To achieve such steep filter skirts, the reactance elements in such a filter must have extremely low losses. Selective RF-filters are also needed in the Tx path of a mobile phone as regulations forbid it to emit RF-power outside the specified band. These Tx filters take care that the power amplifier will not amplify noise and tones at frequencies outside the Tx band [3].

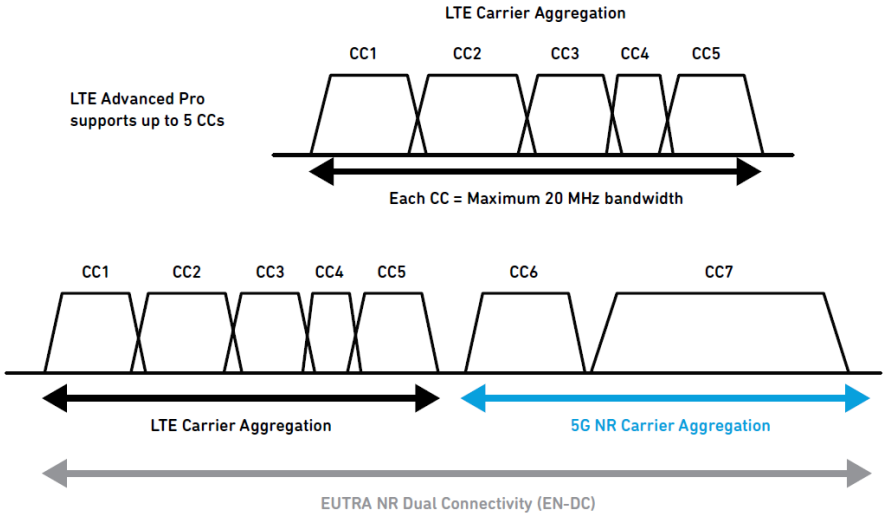

Figure 1.1: LTE and 5G NR carrier aggregation [5].

With the completion of 3GPP release 16 in July 2020, multiple new bands for Sub-6 and mmWave 5G were introduced [1]. As per 3GPP release 15, the frequency bands for 5G new radio (NR) have been designated, providing the list of bands in which 5G NR can operate. The specification defines the frequency bands as frequency range 1 (FR1) and frequency range 2 (FR2). FR1 covers the Sub-6 GHz band from 450 to 6000 MHz, while FR2 from 24250 to 52600 MHz. In addition to the narrow bands around 3.5 GHz and 4.9 GHz, many countries have released several mm-Wave bands for 5G NR communications like n77, n78, and n79 [4]. Consequently, the overwhelming development of wireless communications, the system architecture, transceiver channels, integrated circuits (ICs), passive and active components, and propagation channel modeling have become the leading cutting edges of research.

1.1 Carrier Aggregation and 5G: present and future

Many sources report that mobile data consumption is increasing exponentially and should exceed 160 EB/month by 2025. This estimation concurs with what has been seen in the past in terms of data consumption increase, but this load is not sustainable on a 4G network [6]. On the other hand, the maximum wireless data-rate is driven by the Shannon theory where the capacity channel C depend on the number of channels M, the bandwidth BW, and the signal to (Interference+Noise) ratio $SINR$.

$$C = M * BW * \log_2(1 + SINR) \tag{1.1}$$

To increase the data-rate, 5G deploys more instantaneous bandwidth (n77, n78, etc.) and the aggregation of the spectrum (CA), increases the transmit power in the High-Power User Equipment (HPUE) standard, inserts more antennas for the densification of the network (MIMO), and uses higher modulation schemes.

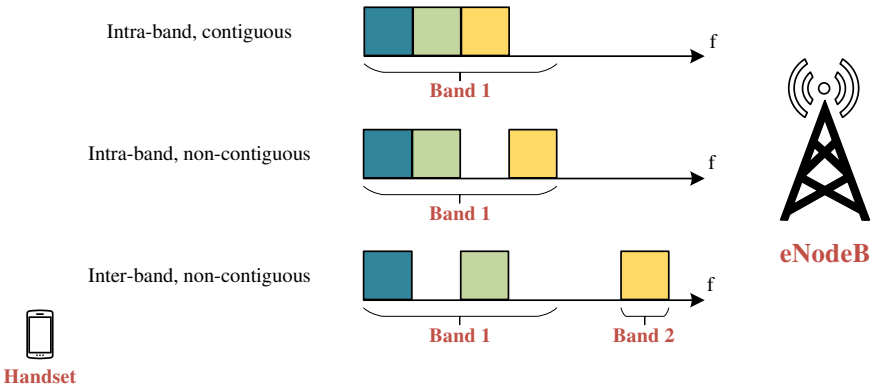

Figure 1.2: Carrier Aggregation scenarios: Intra-band and inter-band aggregation alternatives. The spacing between the centre frequencies of two contiguous CCs is Nx300 kHz, N=integer. For non-contiguous cases the CCs are separated by one, or more, frequency gap(s).

Carrier Aggregation is used in LTE-Advanced in order to increase the bandwidth, and thereby increase the bitrate through the combination of two or more LTE carriers into single data channel. CA in 5G NR will provide multi-connectivity with asymmetric upload and download, providing even more bandwidth to a single user; up to 700 MHz is available in millimeter-wave frequencies. In the sub-7 GHz band, up to 400 MHz of instantaneous bandwidth can be achieved using four 100 MHz channels. 4G LTE-Advanced Pro supports up to 5 component carriers (CC), each with a bandwidth of up to 20 MHz, resulting in a total transmission bandwidth of up to 100 MHz as shown in Fig. 1.1. 5G new radio CA now supports up to 16 contiguous and non-contiguous CCs and can aggregate new 5G bands up to approximately 1 GHz of spectrum. Additionally, dual connectivity allows user equipment to simultaneously transmit and receive data on multiple CCs from two cell groups.

The easiest way to arrange aggregation is using contiguous component carriers within the same operating frequency band (as defined for LTE), called intra-band contiguous. This might not always be possible due to operator frequency allocation scenarios. For non-contiguous allocation, it could either be intra-band, i.e., the component carriers belong to the same operating frequency band, but have a gap, or gaps, in between, or it could be inter-band, in which case the component carriers belong to different operating frequency bands [1]. Fig. 1.2 illustrates the CA scenarios described before.

The onset of 5G is materializing much faster than predicted. To fulfill the CA demands, end-user terminals need multiband/multistandard RF solutions with smaller footprint, higher power handling, while providing higher overall performance. These requirements impose the use of multiplexers and co-designed structures. The classical mobile device architecture in which the bands are selected using a switch connected to duplexers has to be updated with a solution with more filters and co-designed power amplifiers (PA) for the up-link bands.

Currently, RFFE leader manufacturers are developing modules integrating multiplexers and PA to enable more simultaneous connections, use the available bands more efficiently, and reduce power con-

sumption. The recent 3GPP TS 38.101-1 and 3GPP TS 38.101-2 [7, 8] specify the maximum transmit power over NR channel bandwidth, namely, the power class (PC), for FR1 and FR2 respectively according to the user equipment (UE) type. The maximum output power +26 dBm used as a reference for handset UE concerning FR1 demands +30 dBm at the input of the filter approximately, while a filter placed in a fixed wireless access (FWA) UE should handle around +39 dBm in an FR2 scenario according to the established output power of +35 dBm.

1.2 Motivation and Purpose of the Thesis

Advanced wireless communication standards are already an integral part of our lives, and its role will only continue to grow. 4G/LTE and the upcoming 5G include the implementation of advanced digital modulation schemes with higher spectral efficiency; multiple-input, multiple-output (MIMO)-based radio interfaces; and carrier aggregation. The allocation of new frequencies ranges for mobile communication and the overcrowded bands, require RF modules and bandpass filters with steeper skirts and larger bandwidths (BWs). Additionally, the market requests RF solutions with high level of integration, looking for more capability in an smaller space.

Thanks to the expansion of telecommunications, filters based on acoustic resonators have become the mainstay of mobile terminals for filtering functionality. This upsurge is based on the need for smaller form factor devices that comply with all the specifications demanded by the new technologies. The suitability of acoustic filters in end-user-equipments has been demonstrated thanks to the features and functionalities that will be discussed in the next chapter.

The characterization of the resonators through the knowledge of their physical properties, configuration of the layers, quality of the manufacturing process, electromagnetic behavior, and the influence of factors such as temperature or the package are essential for an accurate and efficient design process. However, this process must be preceded by, as is also done in other technologies, the use of synthesis procedures capable of methodologically link a mathematical prototype with a real and feasible device. For acoustic resonators, the Butterworth Van Dyke model provides an excellent electrical approach to this aim. In this sense, several recent thesis dissertations of our research group have delved into different topics [9–11], creating mathematical tools that combine in a robust methodology the synthesis, topology, and technology according to the objective pursued. In [9], the design of filters based on acoustic resonators from a methodological perspective by using synthesis techniques was addressed. In contrast, [10] proposed a direct bandpass synthesis methodology to overcome the limitations of the classical approach. Finally, [11] focused on advanced synthesis techniques for parallel-connected and cross-coupled filters. These methodologies allow obtaining fast results with minimal computational effort. The discussion in these dissertations was run from an stand-alone filter perspective; however this thesis tackles filter synthesis from a modular point of view to achieve a higher integration level.

The main purpose of this thesis is to develop a theoretical and practical approach for designing AW

modules where the integration of filters into a multiplexer or the co-design with active elements were addressed relying on the technological limitations. This proposal aims to provide a systematical methodology that prevents the common practice of modifying a previous design and optimize the variables to fulfill the new requirements. Optimization solution, pushed by the lead times, is usually carried out with a seed that does not assure a good outcome with finite iterations. Additionally, this optimization procedure can be very time-consuming with a large computational effort. Therefore and thanks to the native-oriented methodology to accommodate the AW technology, the outcomes proposed in this thesis provide an initial solution closer to a real one and ready for a following faster optimization process.

With the increase of the bands and the arrival of CA, multiplexers and modules are becoming more compact and complex. This new leap implies new challenges for the multiplexer designer, who must now take into account the influence that each filter has on the rest in addition to the individual performance in each band. The complexity rises if it is considered the flexibility of the frequency plan that allows to connect or disconnect channels depending on the demand. Taking into account the above, part of the effort in this thesis has focused on the design of a systematic methodology that allows a quick and accurate evaluation of the main figure of merit associated with star-junction multiplexers performance based on AW resonators, that is, insertion loss (IL), common port return loss (CPRL) and the fundamental cross isolations and out of band (OoB) rejection typical in multiplexers. The multiplexer design was based on minimum susceptance network (MSN) theory and a deep analysis was carried out to provide solutions according to the characteristics of the frequency plan, channel distribution and technological requirements within the specified parameters range.

Additionally, designers have recently focused on integrating active and passive devices on the same chip. This trend is closely linked to filters, as they are fundamental elements in RF systems, particularly the integration of power amplifier and Tx filter [12–14]. Even though the authors propose a valuable approach to the design of compact and high-performance multi-physical RF modules, matching networks are still included in the proposed architecture. With this in mind, this dissertation proposes the synthesis of acoustic filters considering complex impedance and evaluating, at the same time, technological constraints. An illustrative example is presented based on coaxial resonator technology to validate the complex filter termination theory and exploit the in-line fully canonical topology. A co-designed power amplifier bandpass filter module where the PA's output impedance influence is considered on the filter performance to obtain both a well-shaped filter and high effective PA efficiency. A two-pole filter has been designed, providing a complex input-impedance to obtain the best efficiency but simultaneously taking care of filter transmission response that will appear affected by a non-complex conjugate transistor output impedance.

1.3 Thesis Outline

In this introductory chapter, the strong challenges that 5G and new technologies like CA bring to the acoustic wave technology industry were reviewed.

At the beginning of Chapter 2, the acoustic resonators, either based on surface or bulk acoustic waves were examined. Propagation modes, systems materials, and configurations are tackled to provide a technological background. Well-known and upcoming resonator's technologies are presented for the state-of-the-art analysis. The main technological requirements were also reviewed. On the other hand, the electrical model based on the Butterworth Van Dyke was employed to derived an equivalent electrical and nodal network in the lowpass domain. Closed-form expressions are established for the inline ladder configuration.

Chapter 3 is dedicated to the synthesis of acoustic wave ladder-type filters. The characteristics polynomials of generalized Chebyshev filtering function are computed through a recursive technique. For the low pass elements extraction, an iterative procedure based on the [ABCD] transfer matrix polynomials is described. These polynomials are translated into an electrical circuit prototype from which an AW filter may be implemented. A matrix coupling representation is also presented in this chapter for modeling the circuit in matrix form including some of the real-world properties of the elements of the filter. Moreover, the reflection coefficient input phase has arisen as a fundamental parameter to be aware of. The introduction of the additional phase into the characteristic polynomial $F(s)$ is useful not only to avoid external input elements in stand-alone filters and loading effect in duplexers/multiplexers for 50 Ω systems. The proper phase management provides the designer a freedom degree for technological accommodation and size minimization.

Chapter 4 addressed the synthesis of multiplexers for fixed and flexible frequency plans. At first, a multiplexer topology review with an end-user segment perspective is conducted. The behavior of doubly and singly terminated networks as minimum susceptance networks (MSN) is analyzed in the chapter. During the analysis, the input reflection coefficient phase is evaluated as the key parameter for such classification. The comparison between both networks and the mechanisms to improve the multiplexer performance are also discussed. Under the MSN interpretation, a novel strategy to design star-junction multiplexers combining MSNs and non-MSNs is shown for contiguous and non-contiguous bands multiplexers according to the frequency plan scenario, with customized suggestions. Additionally, taking into account that the loading effect due to the interaction between filters establishes the multiplexer system response, a numerical solution to evaluate the main multiplexer figures of merit like transmission, reflection, and multiport cross-isolation responses in early design stages is presented base on a circuital analysis.

Due to the disposition for integration, Chapter 5 included general synthesis methodology of acoustic ladder filters with complex source and/or load terminations based on electrical parameter extraction

procedure of an inline topology using non-resonating nodes. Considerations about the influence of the complex terminations on the filter element values are presented. Moreover, was addressed the tuneability of the first input elements to match the filter to different complex source impedances.

Additionally, using a commercial GaN transistor, a co-designed PA-filter module was manufactured. The expected Chebyshev filter behavior was achieved, while keeping excellent PA performance in the passband. In the co-design approach was introduced an input reflection coefficient phase control to accurately set the second harmonic reflect for waveform shaping purposes, achieving a less complex, efficient, and compact design.Also in this chapter, a dual-band dual-output PA-filter was designed exploiting together multiplexer theory and co-design techniques. This turns out in an effective co-design strategy allowing lower complexity and size.

Finally, Chapter 6 summarizes the conclusions of this dissertation and presented some future works recommendations.

A few only-simulation examples and experimental validations are shown in this dissertation to demonstrate the proposed theoretical approaches. All of them were summarized in tables with the numerical results.

1.4 Research Contributions

This dissertation encompasses technical papers published and submitted in the course of the Ph.D. program. A complete list of the scientific contributions is presented hereunder:

- P. Silveira, J. Verdú and P. de Paco, "Dual-Band Dual-Output codesigned Power Amplifier in Acoustic Wave Technology", 2021 IEEE International Ultrasonics Symposium (IUS), Virtual Symposium, 2021. (Accepted)

- E. Guerrero, P. Silveira, J. Verdú, Y. Yang, S. Gong and P. de Paco, "A Synthesis Approach to Acoustic Wave Ladder Filters and Duplexers Starting With Shunt Resonator," in IEEE Transactions on Microwave Theory and Techniques, vol. 69, no. 1, pp. 629-638, Jan. 2021, doi: 10.1109/TMTT.2020.3033554.

- J. Verdú, P. Silveira, E. Guerrero, L. Acosta and P. de Paco "Capabilities of LiNbO3 Based Acoustic Wave Resonators for Wideband Applications", 2021 IEEE MTT-S Latin America Microwave Conference (LATAM 2021), Cali, Colombia, 2021.

- LL. Acosta, E. Guerrero, P. Silveira, J. Verdú and P. de Paco, "Synthesis methodology of AW filters for RF applications based on Matrix Rotations to overcome round-off errors", 2021 IEEE International Ultrasonics Symposium (IUS), Virtual Symposium, 2021. (Accepted)

- P. Silveira, J. Verdú and P. de Paco, "Scattering matrix solution for an ideal star-junction multiplexer based on ladder-type filters", International Journal of Microwave and Wireless Technologies, 12(10), 954-959, 2020, doi:10.1017/S1759078720000422.

- J. Verdú, I. Baro, E. Guerrero, P. Silveira, A. Triano, G. Junkin, P. de Paco, "Sensitivity considerations for inline fully canonical filters at ku-band", Progress In Electromagnetics Research M, Vol. 95, 125-133, 2020.

- P. Silveira, J. Verdú and P. de Paco, "Flexible Frequency Plan Acoustic Star-Junction Multiplexer Based on Minimum Susceptance Networks," 2020 IEEE International Ultrasonics Symposium (IUS), Las Vegas, NV, USA, 2020, pp. 1-3, doi: 10.1109/IUS46767.2020.9251761.

- E. Guerrero, P. Silveira, A. Triano, J. Verdú and P. de Paco, "Synthesis Considerations for Shunt-Starting Acoustic Wave Ladder Filters and Duplexers," 2020 IEEE/MTT-S International Microwave Symposium (IMS), Los Angeles, CA, USA, 2020, pp. 920-923, doi: 10.1109/IMS30576.2020.9224085.

- E. Guerrero, P. Silveira, J. Verdú and P. de Paco, "Design Guidelines for Acoustic Wave Ladder Filters Starting in Shunt Resonator," 2020 IEEE International Ultrasonics Symposium (IUS), Las Vegas, NV, USA, 2020, pp. 1-4, doi: 10.1109/IUS46767.2020.9251832.

- P. Silveira, J. Verdú, P. de Paco, "The Role of the Reflection Coefficient Phase in the Design of Acoustic Wave Filters," 2019 United States National Committee of URSI National Radio Science Meeting (USNC-URSI NRSM), Boulder, CO, January, 2019.

- P. Silveira, J. Verdú and P. de Paco, "Scattering Matrix Solution for an Ideal Star-Junction Multiplexer Based on Ladder-Type Filters," 2019 European Microwave Conference in Central Europe (EuMCE), Prague, Czech Republic, 2019, pp. 601-604.

- P. Silveira, J. Verdú and P. de Paco, "Star-Junction Multiplexer Design Under Minimum Susceptance Networks Approach," 2019 IEEE MTT-S International Microwave Symposium (IMS), Boston, MA, USA, 2019, pp. 1194-1197, doi: 10.1109/MWSYM.2019.8700827.

- Á. Triano, P. Silveira, J. Verdú and P. de Paco, "Phase Correction of Asymmetrical Chebyshev Polynomials for Extracted-Pole Fully Canonical Filters," 2019 IEEE MTT-S International Microwave Symposium (IMS), Boston, MA, USA, 2019, pp. 838-841, doi: 10.1109/MWSYM.2019.8700911.

- P. Silveira, A. Triano, J. Verdú, P. de Paco, " Metodología de Síntesis para el Diseño de Filtros en Escalera, Duplexores y Multiplexores en Tecnología Acústica," International Union of Radio Science (URSI), Sevilla, Spain, September, 2019.

- P. Silveira, Á. Triano, J. Verdú and P. d. Paco, "Complex Terminating Impedance for AW Filters: the Key for Power Amplifier Co-design," 2019 IEEE International Ultrasonics Symposium (IUS), Glasgow, UK, 2019, pp. 2580-2583, doi: 10.1109/ULTSYM.2019.8926248.

- Á. Triano, P. Silveira, J. Verdú and P. de Paco, "Synthesis Methodology for Mixed-topology Acoustic Wave Filters," 2019 IEEE International Ultrasonics Symposium (IUS), Glasgow, UK, 2019, pp. 2568-2571, doi: 10.1109/ULTSYM.2019.8925584.

- J. Verdu, A. Gimenez, A. Triano, I. Evdokimova, P. Silveira and P. de Paco, " Distortion of the Bandpass Filter Response under Heterogeneous Temperature Distribution", in Microwave Technology and Techniques Workshop, European Space Agency, Noordwijk, Netherlands, April 2017.

CHAPTER 2

Acoustic Wave Resonator: Physical Foundations and Circuital Approach

RF acoustic wave (AW) filters have emerged as the best solution to achieve filter operations under the current dynamic context. Indeed, acoustic wave filters offer low manufacturing costs and a high level of integration and performance. Up to now, no other technological solution offers a better trade-off [15–17]. Acoustic wave filtering is attractive because typical acoustic wavelengths are about five orders of magnitude smaller than electromagnetic wavelengths at the same frequency. This fact makes possible submillimeter-sized resonators and even complete filters suitable for mobile handsets [18].

This chapter tackles the foundations of resonators based on AW, from its physical structure, propagation modes and characterization, to its electrical equivalent network in the lowpass and bandpass domain. A description of the basic operation principles of SAW and BAW resonators is presented in this chapter. To approximate the acoustic wave resonator (AWR) electrical behaviour, its widely accepted Butterworth Van Dyke model is used for both cases as a useful tool as initial step in the design flow.

2.1 Critical Acoustic Resonators Properties

2.1.1 Quality Factor and Coupling: Compromising the FOM

A piezoelectric-based resonator can be described by two key parameters: the piezoelectric coupling factor (K^2) and Q. The first parameter is a unitless quantity, which represents the efficiency in converting an applied microwave signal into mechanical energy associated with the acoustic-wave type and determines, by a given relative bandwidth, the insertion loss of the device. K^2 depends on the material properties: the piezoelectric constant, the stiffness, and the dielectric constant [19]. In terms of coupling, piezoelectric substrates like PZT and $LiNbO_3$ are clearly the leaders, followed by ZnO and AlN [20].

To measure the efficiency of an AW resonator to convert electrical to mechanical energy and vice versa is computed the effective coupling coefficient k^2_{eff}. In particular, in CA multiplexers, the increasing coupling is necessary to meet the additional rejection requirements while maintaining passband return loss. It is worth noticing that K^2 and k^2_{eff} do not describe the same mechanism; the latter depends on the resonator implementation such as the electrode configuration, acoustic reflector, and parasitics [21]. An effective electromechanical coupling factor is customary to be defined as a function of the distance between series and parallel resonance f_s and f_p respectively to quantify this conversion efficiency. For this thesis, the definition recommended by [22] will be implemented for computing k^2_{eff}

$$k^2_{eff} = \frac{\pi}{2}\frac{f_s}{f_p}\cot\left(\frac{\pi}{2}\frac{f_s}{f_p}\right) \tag{2.1}$$

Several formulations can be found in the literature performing approximations that fit better with specific configurations. In [23] the authors made a summary of these equations and also showed a comparative table for the results. Series and parallel resonance frequencies can be derived simply by finding the impedance extreme and/or the points where the impedance phase becomes zero, as will be explained later.

Another figure that is frequently used as a measure of SAW resonators performance is the capacitance ratio r, which is given by [24]

$$r = \frac{C_0}{C_a} = \frac{1}{(f_p/f_s)^2 - 1} \tag{2.2}$$

where C_0 and C_a are the static and motional capacitance of the Butterworth Van Dyke resonator model.

On the other hand, Q determines the filter insertion loss, roll-off sharpness and out of band rejection/isolation. The rounded corners produced because of low Q can be problematic for narrow-band modulations. This factor can be simply defined as the ratio of the stored energy divided by the power dissipated in the resonator. Q is a frequency dependent figure, so can be extracted from the slope of the phase response. Then, according to Lakin [25] at series and parallel resonances, Q can be expressed as a function of the phase of the measured impedance (φ):

$$Q_s = \frac{f}{2}\left|\frac{\partial\varphi}{\partial f}\right|_{f=f_s} \approx \frac{2\pi f_s L_a}{R_a + R_s} \tag{2.3a}$$

$$Q_p = \frac{f}{2}\left|\frac{\partial\varphi}{\partial f}\right|_{f=f_p} \approx \frac{2\pi f_p L_a}{R_a + R_0} \tag{2.3b}$$

where R_s, R_a and R_0 models the electrode electrical losses, acoustical losses, and the losses associated with the dielectric material respectively in the modified Butterworth Van Dyke model (mBVD) [26]. This more accurate representation of the BVD model is depicted in Fig. 2.1.

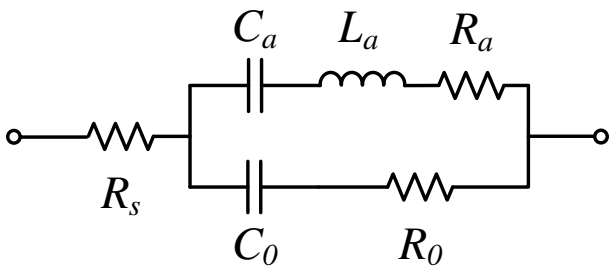

Figure 2.1: Modified Butterworth Van Dyke model for AW resonator.

Even though the Lakin proposal has been used accurately to evaluate Q at resonance frequencies, it was proved its misstatement at frequencies above, below, and in between f_s and f_p [27]. A new formulation was then introduced by [28], where even the midpoint between resonance frequencies f_{90} is appropriately evaluated:

$$Q(\omega) = \omega\tau_{gd}\frac{|\Gamma|}{1-|\Gamma|^2} \tag{2.4}$$

In (2.4), τ_{gd} is the group delay = -$\partial\phi/\partial\omega$, and ϕ is the phase of the reflection coefficient Γ.

Not all bands need high k^2_{eff} and Q simultaneously, but an optimized combination of them. The figure of merit (FOM) to evaluate the performance of an acoustic resonator is expressed as [19]

$$FOM(f) = \frac{k^2_{eff}Q(f)}{1-k^2_{eff}} \tag{2.5}$$

For small values of k^2_{eff}, the formulation is reduced to $FOM = k^2_{eff}Q(f)$. FOM values vary from 50 to 200 for BAW and SAW resonators [28]. The FOM is optimized for a particular material system, and once it has been maximized, a balance between k^2_{eff} and Q is performed. In many cases, a small sacrifice in k^2_{eff}, will give a large boost in Q, leading to steeper skirts and fewer frequency variations due to manufacturing process.

The coupling factor determines the sustainable filter bandwidth, but the improvement of k^2_{eff} goes hand-in-hand with a decrease in the Q-factor. A common measure is that the achievable fractional bandwidth is around half the effective coupling coefficient [29]. In the case of BAW filters with high coupling piezolayers, a value of k^2_{eff} as high as 9.2% can be expected and Q on the order of 4000 [30]. In SAW resonators, the degradation of the Q-factor is mainly caused by a SAW energy leakage, a material viscous loss, and an electrode ohmic loss. A large number of studies for the Q improvement have been reported as shown in references [31, 32], and the Q values reported are 500 to 1500 around 2 GHz.

Additionally, it is desired even k^2_{eff} or r-factor in all filter's resonators regarding manufacturing feasibility. This aim could be complicated to achieve, so external reactive elements with reduced Q are

placed in the laminate in series or parallel position to the resonators. As a usual practice, series inductors are placed in parallel resonators to shift the series resonance frequency to lower frequencies, achieving a higher r-factor, while putting parallel capacitors to the resonators achieve lower r-factor due to the displacement of f_p to higher frequencies. The amount of these additional elements should be reduced to avoid the overall FOM degradation due to the low Q value of this inductances and capacitances [33]. In the case of BAW resonators, only 3 different resonances are allowed, because it is possible to implement up to three different material thicknesses in the same wafer. An additional resonance can be achieved via trimming of the thickness of the top metal electrode and thus is only a variation of one of the overall three.

2.1.2 Piezoelectric and electrode materials

The choice of the piezoelectric material is crucial for designing high-performance RF acoustic resonators because the effective electromechanical coupling set the limit for the filter bandwidth. Piezoelectric materials for filtering applications should have high electromechanical coupling coefficients, low electromechanical losses, good thermal stability, and CMOS compatibility.

The resonant frequency of a piezoelectric slab is primarily dependent on the slab thickness and material properties as described in (2.6)

$$f_n = \frac{v}{\lambda} = \frac{n}{\lambda}\sqrt{\frac{c_{ij}}{\rho_{ij}}} \tag{2.6}$$

where n=nth harmonic,and c and ρ are the elastic stiffness coefficient and density respectively. Note that due to mass loading effects, the device's actual resonant frequency is reduced by the electrode metal. In general, metal with large stiffness and low density (hard and light) is preferred to reduce the mass loading.

The most popular and widely exploited piezoelectric materials in use are aluminum nitride (AlN), zinc oxide (ZnO), and lead zirconium titanate (PZT). Among these materials, AlN synthesis appears to present the best compromise between performance and manufacturability because of its high thermal and chemical stability, high stiffness, and high piezoelectric constant [34]. Additionally, in recent years, scandium (Sc) doping in AlN films has paid much attention due to its drastic enhancement of the electromechanical coupling [35]. With the improvement of manufacturing processes, mono-crystalline substrate like lithium tantalate ($LiTaO_3$) or lithium niobate ($LiNbO_3$) has also gained significant interest as a promising materials platform to deliver high electromechanical coupling and quality factor.

For electrode's material in BAW resonators, Molybdenum (Mo), tungsten (W), chromium (Cr), and ruthenium (Ru) are often used because their large acoustic impedance offers an increase in the electromechanical coupling factor, and they act as a good seed layer for the AlN growth [36]. Additionally, hexagonal structures such as titanium (Ti) or cubic structures like platinum (Pt), gold (Au), aluminum

(Al) or titanium nitride (TiN) are successfully employed and studied for SAW and BAW [37, 38].

2.1.3 Power Handling

The uplink (Tx) filters should handle high power levels from the power amplifier in the previous step. A part of the applied power will dissipate and cause a temperature increase within the filter, affecting the filter performance. The narrow band gap from the transmission to rejection may not be fulfilled, or the IL could be degraded. Additionally, the devices' expected lifetime, typically >5000 hours at maximum power and normal operating temperature, will be reduced due to the self-heating effect [39]. These effects should be considered as well with the co-designed filtering PA because of the filter impedance shift.

The typical maximum power in transmitting operation for a WCDMA and LTE system can be up to 30 dBm at the input of the filters, but this figure is increasing. For that reason, many works address the design and characterization of acoustic filters under high power stimuli [3, 40, 41]. Comparing SAW and BAW filters shows that the higher thermal conductivity of BAW enables high power handling up to $\sim$ 36 dBm even above 2 GHz versus up to $\sim$ 31 dBm in SAW filters. Furthermore, to address power durability, the power density must be preserved under a maximum permissible level over the passband. This level depends on the selected technology, where BAW is less sensitive than SAW [33].

It is a common practice to cascade resonators for better power handling. However, cascading a resonator is equivalent to double the static capacitance value and therefore increase the device total area. A circuital approach for computing the AW resonators power density as function of frequency was presented in [9]. Lossy networks were considered using the mBVD model.

2.1.4 Temperature Coefficient of Frequency (TCF)

The temperature coefficient of frequency (TCF) is the parameter that describes the frequency shift caused on the resonator by temperature variations [24]. This parameter is related to the temperature inducing a change of the electric constants, modifying the acoustic velocity wave propagation. Thus, combining materials with different thermal expansion coefficients, a zero-TCF device can be fabricated. The temperature drift of a filter is determined by the ppm/°C characteristic of the process and the temperature excursion of the end application's filter experiences.

This parameter is computed as:

$$TCF = \frac{1}{f_n}\frac{\partial f_n}{\partial T} = \frac{-1}{t}\frac{\partial t}{\partial T} - \frac{1}{2\rho}\frac{\partial \rho}{\partial T} + \frac{1}{2c_{ij}}\frac{\partial c_{ij}}{\partial T} \tag{2.7}$$

As it is observed in (2.7), the TCF is dependent on the substrate thickness t, the density, and the elastic stiffness change over temperature T.

Amorphous SiO_2 possesses a unique feature in acoustics, namely, SiO_2 becomes stiff with temperature T. In contrast, most of all materials including AlN, Mo, and Ru become soft with T. Thus the TCF can be improved by the inclusion of SiO_2 in the resonator structure. It should be noted that SiO_2 is non-piezoelectric and relatively lossy. Thus the TCF compensation by SiO_2 is only possible at the expense of the k^2_{eff} and Q reduction. The SiO_2 deposition technique and conditions must be carefully executed to guarantee the compensation purpose. In general, BAW-SMRs offer better TCF but worse Q than BAW-FBARs because SiO_2 is used in the Bragg reflector [42].

2.2 Implemented Acoustic Wave Technologies for Filtering Devices

At present, the most ruling implementation of RF filters is dominated by surface acoustic wave (SAW) and bulk acoustic wave (BAW) filters. Until now, SAW and BAW filters have been well suited for distinct frequency bands. SAW filters are best suited for lower frequencies from 0.4 to 2.5 GHz, while BAW filters for higher frequencies up to 6 GHz. In the middle range (from 1.2 to 2.5 GHz), both SAW and BAW filters have tied market quotas, existing a trade-off between performance and production cost. However, recent technologies like plate acoustic wave (PAW) resonators have attracted wide attention because of the ultra-large coupling factor, which is strongly needed for the current and emerging RF front-ends. A review of the leading acoustic filter technologies is presented in this section, analyzing their principal configurations, advantages, and market segment.

2.2.1 SAW Resonators

SAW filter technology started to become attractive with the invention of the interdigital transducer (IDT) by White and Voltmer in 1965 [43]. The relatively simple manufacturing process facilitated Rf filters' massive production on this technology, becoming the most popular on the market.

An electrical input signal is converted to an acoustic wave in a SAW resonator by introducing IDTs on a piezoelectric substrate. The acoustic wave propagates on the surface of the substrate along the direction perpendicular to the fingers (Rayleigh waves) as it is shown in Fig. 2.2. The acoustic wave wavelength is defined by the pitch p (the width of the metal finger plus gap) of the IDT, where two adjacent strips pitch with opposite polarity (a finger pair) is $p = \lambda/2$. Its slow velocity makes it possible to fit many wavelengths across the IDTs in a tiny device. Some IDT's properties should be taken into account in the design, such as the aperture (distance between the finger ends with opposite sign), the finger width, or the metallization ratio (ratio between the finger width and free space within the pitch) [24]. Additionally, the wave amplitude quickly decays in the vertical direction so that ideally, no energy is emitted in the vertical direction.

Grating structures between the interdigital transducers can be placed to transmit or reject waves at certain frequencies. Grating type reflectors at both ends of the SAW device take care that acoustic energy

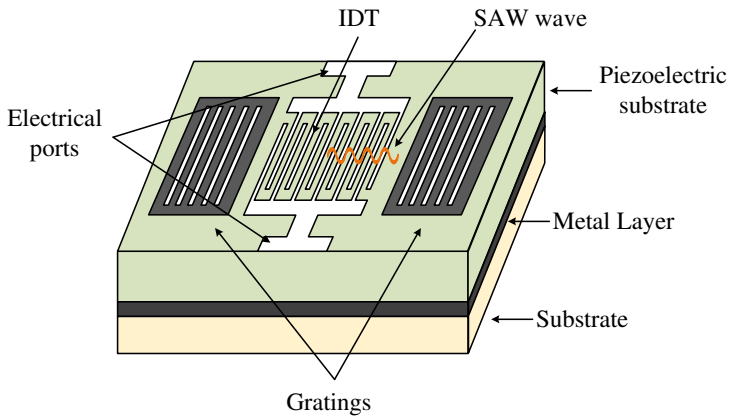

Figure 2.2: Surface Acoustic Wave resonator structure.

stays in the device until finally it will be converted back into the electrical domain. The filter function is defined by the metal lines' structure in the interdigital transducers and the gratings. [3].

As the resonance of a SAW resonator is dependent on the lateral dimensions $f = v/2p$, i.e., the electrode width and separation, it is limited by the resolution of photolithography. The resolution is restricted to 0.25 μm, so the operational frequency is limited to 2 GHz for a good performance. Thus, SAW filters at fundamental mode for frequencies above 2.5 GHz are practically not available today. A second big issue is the power handling capability of SAW filters at high frequencies. To transmit 1 W of RF power, the narrow comb fingers have to carry huge current densities, which causes problems like electromigration and overheating. This issue leads to a filter frequency shift that could not be afford by a multiplexer with a narrow gap between the channels.

TC-SAW Resonator

SAW resonators are very sensitive to temperature variations due to the stiffness of the substrate material decreasing at higher temperatures, and acoustic velocity diminishes [44]. A SAW filter's response may shift downward by as much as 4 MHz as temperature increases. This limitation has become more significant as guard bands become narrower in the 4G/5G scenario, and consumer devices are specified to operate across a wide temperature range, typically, –30°C to +85°C.

To overcome the filter performance impact, the temperature coefficient of frequency (TCF) has been reduced through temperature-compensated approaches. Lower TCF means filter passband drifts less over temperature. In recent years, temperature-compensated SAW (TC-SAW) filters have become available. Fig. 2.3 shows the two widely used TC-SAW configurations: $LiTaO_3/Si$ (or $LiTaO_3$/Sapphire) and $SiO_2/LiNbO_3$. The first configuration (see Fig. 2.3a) improves the thermal expansion coefficient (TEC) by bonding the piezoelectric substrate to a low TEC base-substrate thicker such as sapphire or silicon. On the other hand, the configuration displayed in Fig. 2.3b includes overcoating of the IDT structures

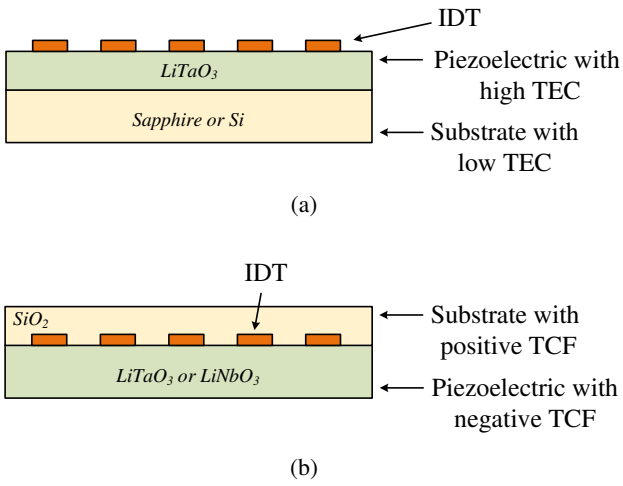

Figure 2.3: TC-SAW configurations.

with opposite TCF layers like SiO_2 that increase stiffness at higher temperatures [45]. As the SiO_2 overcoat thickness increases, the coupling of the TC-SAW resonators will decrease. Therefore, there exists a trade-off between the TCF and the coupling coefficient.

Although an uncompensated SAW device typically has a TCF about –45 parts per million per degree Celsius (ppm/°C), TC techniques can reduce the TCF to –15 to –25 ppm/°C up to 0 ppm/°C for the most stringent applications. However, because the process doubles the number of required mask layers, TC-SAW filters are more complex and more expensive to manufacture — but still less expensive than BAW filters.

IHP SAW Resonator

The new frequency bands demand high quality factor (Q) and low TCF in SAW resonators to realize high-performance filtering devices. In order to confine the acoustic energy at the surface, Takai et al. from Murata have focused on the suppression of the leaked SAW energy as a bulk wave emission, and energy confinement in the depth direction [46,47]. A new multilayered structure substrate was proposed, realizing incredible high performances and rising Q up to 4000 and decreasing TCF up to 8 ppm/°C. These results are a significant improvement compared with conventional SAW structures. To suppress the leakage, the authors have studied the acoustic Bragg reflector stack using low acoustic impedance materials combined with high impedance materials: low impedance layers of SiO_2 and high impedance layers of AlN are attached alternately [48].

2.2.2 BAW Resonators

RF BAW filters dominated the middle and high band operation frequencies thanks to the low insertion loss and better selectivity. Its thermal conductivity enables high power handling [17, 29, 49].

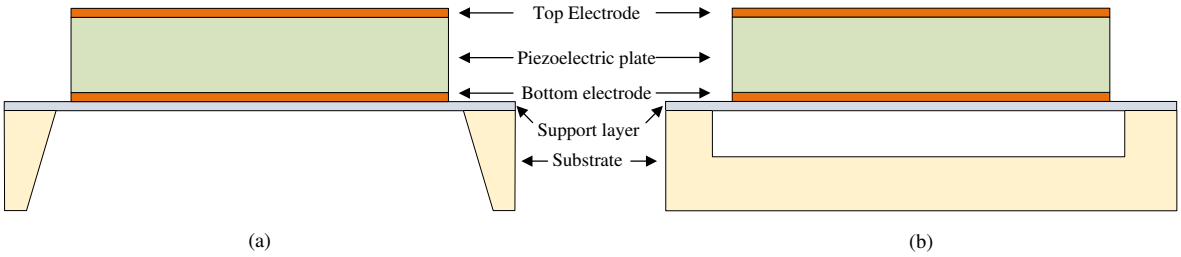

Figure 2.4: Membrane FBAR resonator formed from (a) etching the back and (b) air-gap resonator.

The most basic configuration of a BAW resonator consists of a piezoelectric stack structure sandwiched between two metallic electrodes. The electric field is generated in the direction of the thickness, thereby exciting the acoustic wave [24, 50]. When air or vacuum is the interface, the waves generated by the transduction process stay confined to the material volume. The air behaves like a short-circuit, forcing the acoustic wave to reflect between the top and bottom surfaces and generating the resonant mode. Regardless of the electrodes, the resonant frequency depends on the acoustic velocity v and the thickness of the piezoelectric film h:

$$f = \frac{v}{2h} \tag{2.8}$$

Also, the thickness of the electrode can affect the resonant frequency due to mass loading. The typical thickness of the piezolayer is in the range of a few μm or below.

Two technologies have been implemented over the years: film bulk acoustic resonators (FBAR) and solidly mounted resonators (SMR) to confine the acoustic waves. Additionally, emerging technologies like XBAW are pushing into the new era looking for higher coupling factors and bandwidth with enhanced performance. A brief discussion of these approaches is included in this section.

BAW-Film Bulk Acoustic Resonator

The basic configuration of FBAR is a suspended membrane structure consisted of a piezoelectric thin film sandwiched between two electrodes [51, 52]. The membrane can be formed either by etching the Si substrate from the back by chemical etching or deep reaction ion etching as displayed in Fig. 2.4a or from the front surface by etching a pre-buried sacrificial layer with another material such as phosphosilicate glass as showed in Fig. 2.4b. Creating etch holes through the back of the supporting Si structure weakens the substrate, making it especially susceptible to breakage. In both cases, the acoustic wave is reflected at the air interface, thus confined the wave in the piezoelectric thin film, resulting in high Q factors up to 4000 [28].

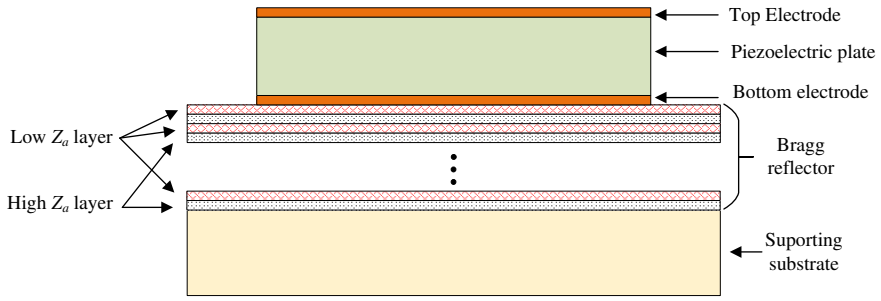

Figure 2.5: Solidly Mounted Resonator structure.

BAW-Solidly Mounted Resonator

Solidly Mounted resonators (SMR) present a more robust structure than FBAR by including a Bragg reflector on the bottom side of the piezoelectric and maintaining the top electrode exposed to air [50]. The acoustic Bragg reflector is a structure formed from multiple λ/4 layers of alternating materials with the varying refractive index which implies different acoustic impedances Z_a as shown in Fig. 2.5. Generally, SiO_2 is used for low acoustic impedance (Z_a) layers while AlN or W are chosen for high Z_a layers. The interference resulting from incident and reflected waves in the stacked layers simulates a mirror, reflecting the acoustic energy back into the resonator. In this manner, the energy is confined mainly in the piezoelectric layer. The Bragg reflector must be made up of at least 3 to 4 pairs of acoustically dissimilar materials.

Due to misalignments in the manufacturing process, an amount of acoustic energy penetrates into the Bragg reflector decreasing the Q, being smaller than FBAR's with a figure near 2000. As a direct result, the filter roll-off and the passband insertion loss can be reduced correspondingly. The capacity to handle power is one of SMR advantages because of the heat extraction through the reflector. SMR is also superior to FBAR in terms of mechanical robustness.

2.2.3 PAW Resonators

The emergence of plate acoustic wave resonators (PAW), which can be considered hybrid SAW-BAW technology, has attracted attention in the last decades [53, 54]. These devices are composed of a metallic interdigital transducer IDTs that are alternatively connected to ground and signal, on top of a mechanically suspended cavity or solidly mounted resonator with an alternately laminated acoustic impedance $\lambda/4$ multilayer and a glass substrate. Fig. 2.6 illustrates a perspective and cross-sectional views of a cavity PAW resonator. When the piezoelectric is thin, the IDT excites plate (thickness) modes efficiently, including shear horizontal (SH), and Lamb wave longitudinal symmetrical S and asymmetrical modes A [55].

Regarding the piezoelectric substrate employed in this kind of resonator, AlN was the first material

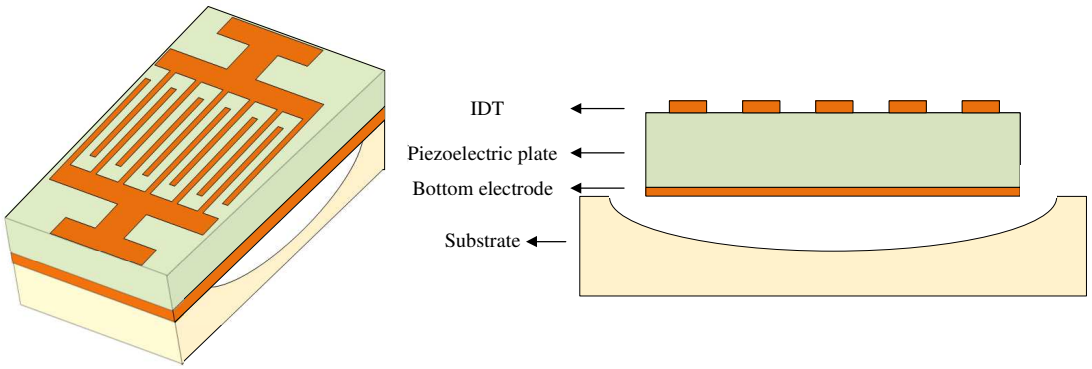

Figure 2.6: Cavity Plate Wave Resonator structure.

investigated due to its advantage in BAW resonators: the multi-frequency and CMOS-compatible ability [34, 56], but SH plate modes cannot be excited due to the characteristic of this material. To increase the FOM, $LiNbO_3$ was gaining traction due to SAW resonators' potentially higher coupling factor $\sim 30\%$. Furthermore, bulk modes in $LiNbO_3$ provide better acoustic confinement, without the acoustic energy leakage identified in SAW devices [57, 58].

2.2.4 Actual solutions for the future: XBAR and XBAW

For the past few decades, SAW and BAW based filters have dominated the RF filter market due to their unquestionable superiority and its large-scale manufacturing process for a low cost. The accelerated pace to 5G compels to find new solutions that cover the necessity of compact filters with larger bandwidth, higher power handling, and remarkable performance at frequencies higher than traditional sub 2.7 GHz. The newer 3.3-5 GHz range has attracted a lot of interest, namely the emerging 5G bands n77, n78, and n79 that require 900, 600, and 500 MHz of bandwidth, respectively, with a relatively large fractional bandwidth (FBW), up to 10%. To overcome the challenging scenario, two promising players have come up in the last years: Akoustis with its XBAW technology and Resonant with its XBAR.

XBAW® from Akoustis

In 2016, Akoustis Technologies Inc. presented that single-crystal AlN-based devices had more than double that of polycrystalline devices owing to the better piezoelectric coupling inherent in single-crystal AlN. While the quality factor Q is slightly lower in single-crystal devices, the FOM is typically 30 % higher due to the increase in mechanical coupling efficiency [59]. The main product of the company, XBAW filters, are FBAR-type structures with a piezoelectric growth step using metal organic chemical vapor deposition technology. According to its publications, XBAW is a patented MEMS-based technology optimized to address the most stringent frequency selectivity requirements with superior resonator characteristics ideally suited for frequencies in the range from 1 to 7 GHz. Nowadays, Akoustis commercializes seven XBAW filters oriented to infrastructure, Wi-Fi and defense, covering the 5G NR

bands [60].

XBAR® from Resonant

To address the aforementioned 5G requirements, a laterally eXcited bulk acoustic wave resonator (XBAR) was proposed by [61]. In contrast to XBAW resonators, XBARs are formed with a relatively simple structure involving an IDT system, but with a small metallization ratio, [62] The resonator with IDTs on a suspended $LiNbO_3$ plate creates horizontal electric fields that generate standing bulk acoustic shear wave resonance (A_1) by applying a lateral electrical field parallel to the crystalline y-axis. The maximum acoustic amplitude is located in the free membrane area between the electrodes. Contrary to piezo-MEMs, the device does not need anchors and can exploit many hundreds of electrodes. It is pretty evident that XBAR is the commercial brand from Resonant for the emerging PAW resonators described before.

Resonant's XBAR RF filter technology is optimized for wide bandwidths, high frequencies, low loss, and high rejection required for the industry to realize its capacity and speeds fully. The claimed percentage bandwidth is more than 10% compared to 3 % to 5 % for 4G devices thanks to its strong piezoelectric coupling $\sim 25\%$. Likewise, it can handle the high-power RF signal needed to accommodate signal attenuation at these frequencies, around 31 dBm. Although the resonators have moderate Q-factors, estimated to be around 500, a minimal insertion loss of 1 dB near 5 GHz is predicted in combination with extremely high coupling. XBAR filters can facilitate more extended battery life [62].

2.3 Acoustic Wave and its Propagation Modes

Elastic waves or acoustic waves in solids are composed of mechanical deformations, strain (s) of a material, and the associated internal forces, stresses (T). Deformations in a solid are displacements of its constituent particles from their steady-state position [63]. Depending on the particle displacement, acoustic waves can be classified in longitudinal, also named pressure waves, and shear waves also called transversal waves. In a longitudinal wave, the particle displacement is parallel to the propagation direction, whereas, in a shear wave, such displacement is normal to the propagation direction. The phase velocity of the acoustic wave (V_{ij}) is determined by the stiffness (c_{ij}) and density of the media (ρ_{ij}) in which the wave propagates as expressed in (2.9) [24].

$$V_{ij} = \sqrt{\frac{c_{ij}}{\rho_{ij}}} \tag{2.9}$$

Acoustic attenuation increases with frequency, and therefore materials with higher velocity are preferable to reduce the propagation loss. Observing (2.9) it is noticed that large acoustic velocities are achievable only in materials that present high stiffness and low densities, such as diamond [24]. The AW velocity is in the range of 1–7 km/s for commonly used single-crystal materials but can reach 12

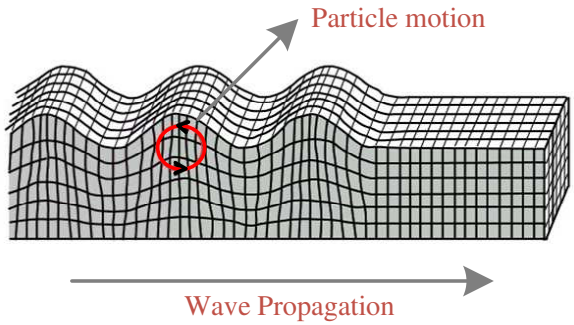

Figure 2.7: Rayleigh wave propagation.

km/s for layered systems [64].

The acoustic waves propagate through a solid medium combining the two primary plane waves, longitudinal and shear. The boundary conditions of the medium define the character of the waves, i.e., in a homogeneous material with a plane surface, the wave is guided along the surface resulting in a surface acoustic wave (SAW), with its amplitude decaying exponentially with depth. The surface wave is strongly confined, with typically 90 % of the energy propagating within one wavelength of the surface [65]. Depending on the boundary conditions, and the characteristics and properties of the piezoelectric materials, many other types of waves can be generated. In systems confined by plates or with stacking configurations, complex propagation modes can appear. When the piezoelectric layer is larger than the wavelength, the waves behave as if there is no surface boundary, resulting in bulk acoustic waves (BAW).

The main types of guided waves used for today's microwave applications include various BAWs, SAWs, and pseudo-SAW waves such as classical Rayleigh waves, leaky SAWs, Bleustein–Gulyaev waves, Lamb waves, Shear Horizontal waves (Love waves), SSBWs, STWs, etc. Rayleigh, Lamb, and Horizontal Shear waves will be briefly defined below due to their relevance in the implementation of acoustic filters.

2.3.1 Rayleigh waves

In the case of Rayleigh, the wave travels along the free surface of a piezoelectric half-space, and its energy is concentrated up to about a depth of one wavelength. The wave is nondispersive and involves longitudinal and shear components at the same time. The surface particles move in ellipses in planes normal to the surface and parallel to the direction of propagation as it is depicted in Fig. 2.7.

In a Rayleigh surface wave, particles at the surface trace out a counter-clockwise ellipse, while particles at a depth of more than 1/5th of a wavelength trace out clockwise ellipses. This motion is often referred to as being "retrograde" since at the surface, the horizontal component of the particle motion is in the opposite direction as the wave propagation direction. The motion amplitude decays, and the ellipses' eccentricity changes as the depth into the material increases. Its higher mode, Sezawa, is also

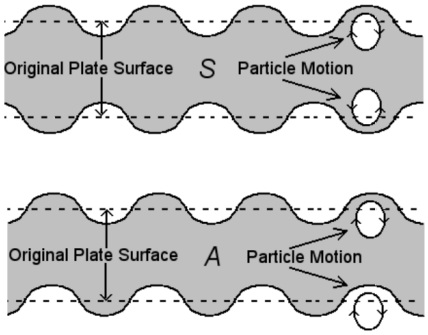

Figure 2.8: Symmetric and Asymmetric Lamb wave modes [56] .

exploited in acoustic devices, principally in the sensors field.

2.3.2 Lamb waves

Lamb waves were first analyzed and described by the English mathematician Horace Lamb [66]. These elastic waves made up of a superposition of longitudinal and shear modes propagate in plates of finite thickness, and their propagation characteristics vary with entry angle, excitation, and structural geometry [67]. Generally, the plate supports a number of these waves depending on the plate thickness to wavelength ratio.

Lamb waves are divided into symmetric (S_0, S_1, etc.) and asymmetric (A_0, A_1, etc.) modes to indicate the symmetry of the particle displacements associated with the waves relative to the median plane of the plate, as it is shown in Fig. 2.8. For sufficiently thin plates, only two waves occur, A_0 and S_0. Thinner membranes exhibit lower phase velocities for the A_0 mode, in which the plate undergoes flexure as the wave propagates, while phase velocity reaches its maximum value for the S_0 mode [68]. As in Rayleigh waves, which propagate along single free surfaces, the particle motion in Lamb waves is elliptical with its x and z components depending on the plate's depth.

2.3.3 Shear Horizontal waves

In addition to Lamb modes, a transverse (shear) motion, different from normal shear waves (vertical shear mode), was detected between layers of the laminate by Love in 1911 [70]. Love waves are purely shear waves with a particle displacement normal to the propagation direction, i.e., perpendicular to the wave travel plane (see Fig. 2.9). Such a mode was accordingly named shear horizontal (SH) mode (Love wave). Moving deeper into the material, motion can decrease to a "node" and then alternately increase and decrease as one examines deeper layers of particles. The amplitude, or maximum particle motion, often decreases rapidly with depth.

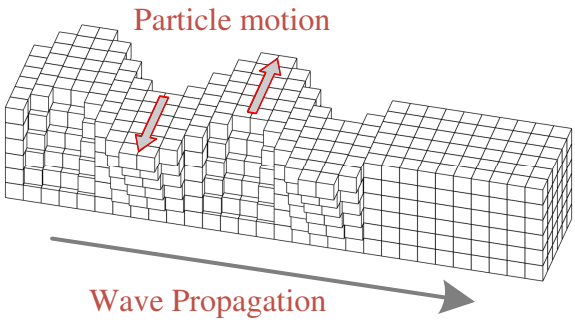

Figure 2.9: Shear Horizontal SH wave (Love wave) performance.

2.4 AW Resonator Electrical Modeling

Once the main physical characteristics and fundamental properties have been described, a resonator model is necessary for modeling, analyzing and estimating the behavior of the filtering network. In particular, SMR BAW resonators can be characterized using Mason models [71, 72] or equivalent one-dimensional transfer matrix models. Mason models as well as transfer matrix methods describe effects introduced by the acoustic mirror and also predict other parasitic spikes in the filter response. To model the electro-acoustic properties of one or several IDTs combined with the gratings in a SAW resonator, a precise prediction can be obtained employing the coupling-of-modes or P-matrix approach [73].

A simpler approach that can be implemented in any linear circuit simulator is achieved with the lossless Butterworth Van Dyke model (BVD) [26]. The classical definition is composed of reactive lumped elements: LC series resonator in parallel to a capacitor as it is depicted in Fig. 2.10. The motional arm conformed by L_a and C_a is related to the technological system that influences the confinement of the acoustic wave, while C_0 represents the static capacitance. The latter capacitance is due to the parallel electrodes in BAW or the fingers in SAW. This model only responds to the fundamental frequency, therefore higher-order modes are neglected in the analysis. To include higher-order modes, additional motional arms should be placed in a shunt configuration.

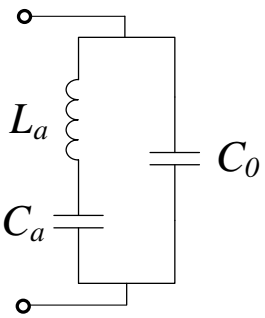

Figure 2.10: BVD equivalent circuital network.

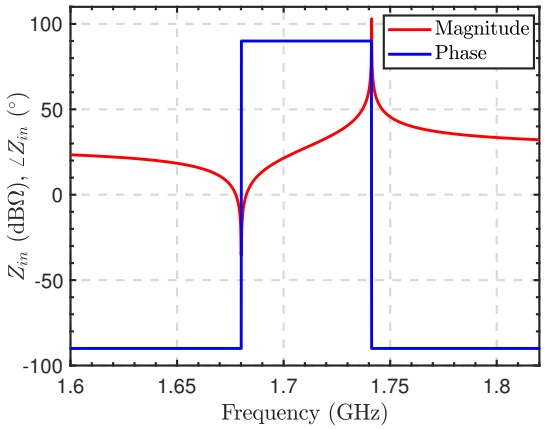

Figure 2.11: Input impedance magnitude and phase of a simulated lossless AW resonator.

This simple model makes it suitable for the extraction of the parameters synthesized that might be included in an optimization routine in any topology and also maybe introduced into the Mason model to improve the accuracy. The input impedance of the implemented BVD circuit from Fig. 2.10 is computed as:

$$Z_{in}(\omega) = \frac{j(\omega L_a - \frac{1}{\omega C_a})}{1 - \omega^2 C_0 L_a + \frac{C_0}{C_a}} \tag{2.10}$$

where ω is the bandpass frequency variable. The input impedance presents two recognizable resonances: series and parallel as depicted in Fig. 2.11. At series resonance, the magnitude of the input impedance is minimum, producing a short circuit in an ideal case; while at anti-resonance or parallel frequency, the magnitude tends to its maximum value, behaving as an open circuit in an ideal case. Between both frequencies, the resonator shows an inductive behavior as it is illustrated in the figure with a phase value of $90°$, but outside these frequencies, the phase about $-90°$ indicates a shift to capacitive behavior. This dual circuital performance is the fundamental property for designing ladder-type AW filters as will be explained further in this section.

Having the characteristics of the resonator, the resonances can be easily defined as

$$f_s = \frac{1}{2\pi\sqrt{L_a C_a}} \tag{2.11a}$$

$$f_p = \frac{1}{2\pi}\sqrt{\frac{C_a + C_0}{L_a C_a C_0}} = f_s\sqrt{1 + \frac{C_a}{C_0}} \tag{2.11b}$$

The always positive capacitance ratio in (2.11b), ensures that $f_p > f_s$ under normal conditions. The distance between both resonance is also related to the resonator conversion capacity to transform electrical to mechanical energy described by the coupling coefficient k^2_{eff} (see (2.1))

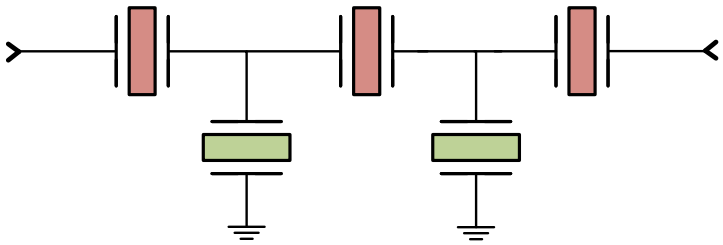

Figure 2.12: AW ladder-type fifth-order filter schematic.

Regarding the coupling mechanism, AWRs can be classified into two main groups: electrical connected or acoustically coupled. Ladder-type and lattice-type filters are included in the first group, while Dual Mode Saw (DMS) for SAW resonators and Stacked Crystal Filters (SCF) and Coupled Resonator Filter (CRF) belong the second approach. One of the most important topologies for current filter applications is ladder-type. A ladder-type filter can be realized in BAW and SAW and can operate in single-ended to single-ended mode or balanced to balanced mode. The ladder structure offers high selectivity and higher power durability, so it is preferred in Tx filters, but low OoB rejection, which is controlled by the resonator's number. This thesis covers the synthesis of ladder-type filters, therefore, the proposed methodology in Chapter 3 is based on the configuration shown in Fig. 2.12. Supplementary information about the other topologies can be found in [24, 29].

To realize a filter in a ladder-type circuit, two basic configurations are required: series and shunt resonators that alternate in several stages. As the resonator stages increase, the OoB rejection improves. Both resonators have the same layer structure, but an additional layer is included in the parallel one [74]. As a result of the mass loading of the additional layer, the admittance of parallel resonator shifts toward slightly lower frequencies compared to the series resonator.

In ladder-type filters, the resonators alternation in series and shunt positions make possible the introduction of transmission zeros (TZ) at one of the characteristic resonance frequencies series or parallel. At the parallel resonance frequency of a series resonator, namely f_p^{SE}, the impedance is ideally $Z_{in} = \infty$ Ω causing an open-circuit in the signal path and hence producing a TZ at this frequency. In the same manner, at the series resonance frequency of the shunt resonator f_s^{SH}, the short circuit produced by $Z_{in} = 0\,\Omega$, impose a finite TZ at this frequency. Overall, series resonators implement TZs above filter's passband and shunt resonators place them below. At f_p^{SH} and f_s^{SE} the signal flows through the path thanks to the high and low resistance respectively. The resonances are clearly identified in Fig. 2.13a. By connecting series and parallel resonators in a ladder-type circuit, as shown in Fig. 2.13a, a filter is implemented.

Far from the resonances, the acoustic resonator has a capacitive behavior, controlled by the capacitive voltage divider made of the static capacitances C_0 of all resonators as it is shown in Fig. 2.13b. Increasing the ladder sections will improve de OoB rejection, but also will increase the in-band insertion loss. To overcome the ladder weaknesses, several configurations including cross-coupled resonators are extended

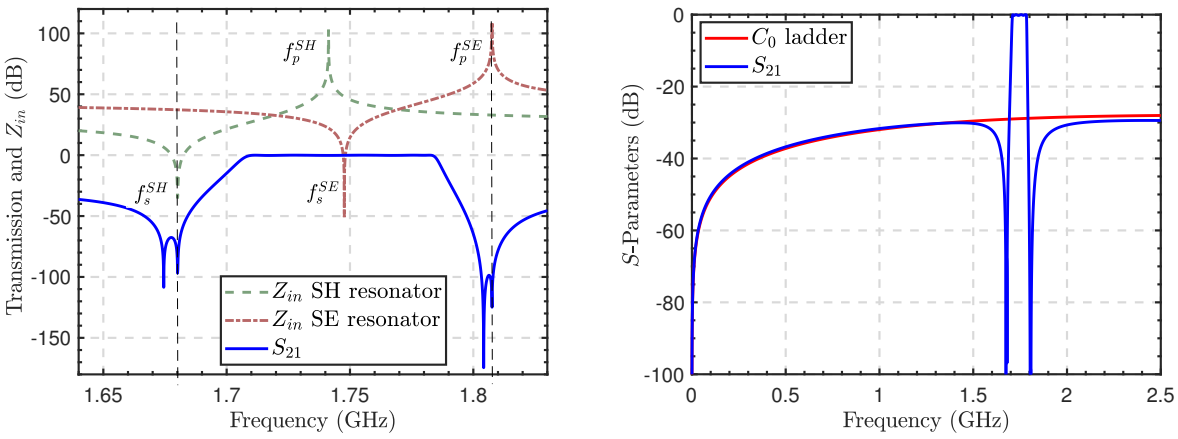

Figure 2.13: Input impedance magnitude and phase of a simulated lossless AW resonator.

in [9, 11].

2.5 Lowpass Equivalent Network for an AWR

In the main resonance vicinity, the resonator is modeled by the BVD equivalent network which is defined in the bandpass domain where $\omega = 2\pi f$. On the basis that the ladder filter will be synthesized from a lowpass function in the next chapter, an equivalent circuit in the low pass domain for the BVD is needed. To overcome the restrictions of classical networks synthesis assessing symmetrical responses, a mathematical tool was introduced by [75]: the Frequency Invariant Reactance (FIR). Its reactive nature is transformed as a single element to the bandpass domain regarding its sign and also applying an impedance scaling.

For notation purposes, the FIR is referred to as a reactance X or susceptance B. The main drawback of assuming frequency independence is its accuracy as a narrow band approximation. Since material systems and topologies limit the bandwidth of AW filters to narrow-band implementations, the FIRs are suitable for the lowpass model representation. The inaccurate transformation impact on the OoB region has a minor negative impingement in the final result due to the more stringent specifications are concentrated around the filter's central frequency. To carry out the FIR transformation ω_0 is considered.

To obtain the BVD model in the lowpass domain, the LC series motional branch is transformed to an inductor L_m, as natural conversion due to the classical transformation, in series with the FIR X_m to tune the series resonance f_s. The static capacitance C_0 is converted into X_0 since no resonance is produced by this branch single-handedly. Altogether, the lowpass equivalent circuit is depicted in Fig. 2.14.

The lowpass prototype input impedance is calculated as

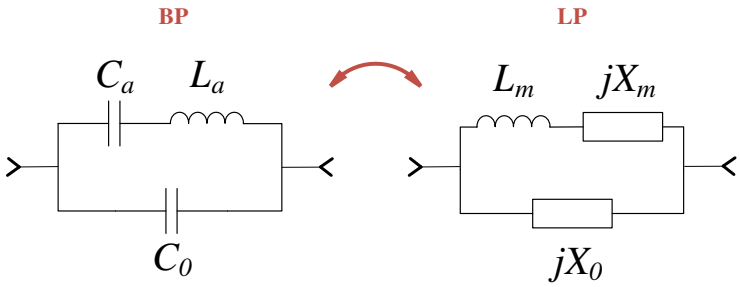

Figure 2.14: Equivalence between bandpass and lowpass BVD model .

$$Z_{in}(\Omega) = \frac{jX_0(\Omega L_m + X_m)}{X_0 + \Omega L_m + X_m} \tag{2.12}$$

where Ω is the normalized lowpass frequency. The transformation is performed applying the well-known narrow-band bilateral equation

$$\Omega = \alpha \left(\frac{\omega}{\omega_0} - \frac{\omega_0}{\omega} \right). \tag{2.13}$$

Previous equation relates the central frequency ω_0 with the inverse of the relative bandwidth α. The former is computed as the geometric mean of the passband edges ω_1 and ω_2, it is to say $\omega_0 = \sqrt{\omega_1 \omega_2}$, while α is defined as $\alpha = \omega_0/(\omega_2 - \omega_1)$. By simple inspection of (2.13), the passband in the low-passs domain is enclosed in $\Omega = \mp 1$ rad/seg range for lower and upper edge frequency respectively whereas the central frequency ω_0 is placed at $\Omega_0 = 0$ rad/seg.

To find the bond between the bandpass and lowpass elements is necessary to set the parallel branches displayed in Fig. 2.14 equal to each other, and hence the input impedances in (2.10) and (2.12). Equating the composed series branches and given the domain transformation, mathematical equality is obtained:

$$j\alpha \left(\frac{\omega}{\omega_0} - \frac{\omega_0}{\omega} \right) L_m + jX_m = j\omega L_a + \frac{1}{j\omega C_a} \tag{2.14}$$

A second equation must be introduced to isolate L_a and C_a, which is obtained determining the first derivative with respect to Ω:

$$j\alpha \left(\frac{1}{\omega_0} - \frac{\omega_0}{\omega^2} \right) L_m = jL_a + \frac{1}{j\omega^2 C_a} \tag{2.15}$$

Having the equation system and applying the denormalization of the unity source and load to any characteristic impedance value Z_0, the last step of impedance scaling provides the final relationship that allows mapping BVD prototype in both domains. Lastly, the value of the series branch is defined as

$$L_a = \frac{Z_0}{2}\left(\frac{2\alpha L_m + X_m}{\omega_0}\right) \tag{2.16a}$$

$$C_a = \frac{2}{Z_0}\frac{1}{\omega_0\left(2\alpha L_m - X_m\right)} \tag{2.16b}$$

The single-element branches containing X_0 and C_0 are equaled and scaled to attain the relationship down below:

$$C_0 = -\frac{1}{Z_0 X_0 \omega_0} \tag{2.17}$$

It is worth noticing that all evaluations are made at the central frequency ω_0. This approximation results in an exact performance at the vicinity of this frequency. Nonetheless, as the frequency Ω moves away in a positive or negative direction, the transformation losses accuracy. For that reason, duplexers with a large gap between the channels, i.e. Band 4, need to be adjusted in the bandpass domain when the open-circuit condition is calculated in the lowpass domain as will be demonstrated in Chapter 3.

2.5.1 Dangling Resonator Structure

The AWR is the fundamental cell of a ladder-type filter. The synthesis of such filter through the well-known extracted pole technique that allows independent extraction and control of the attenuation poles can be applied [76]. For this purpose, a nodal representation is introduced hereafter with the model description and mathematical relation between lowpass BVD and dangling resonator. This representation is a very useful tool to further creation of the coupling matrix as described in Chapter 3.

An AW resonator performs a finite transmission zero below or above the passband regarding the position in shunt or series configuration in a ladder-type filter as shown in Fig. 2.13a. This finite TZ can be realized with a dangling resonating structure as displayed in Fig. 2.15a and firstly introduced by [77]. The structure is formed by a resonant node (RN) hanging from a FIR B. The resonant node, displayed as a solid black circle in the figure, can be represented in the lowpass domain by a unitary capacitor ($Y_c = 1S$) in parallel to a FIR with value b_i which performs the frequency tuning to the desired TZ. The admittance inverter J_r connects the resonant and non-resonant (NRN) nodes as displayed in Fig. 2.15b. The concept of NRNs, and therefore, the application of FIRs to the nodal representation, was introduced by [78]. The nodal representation is addressed from the admittance point of view, explaining why shunt capacitors are used as resonant elements and the NRNs are labeled as susceptances.

The input admittance of the NRN-RN basic cell is calculated as

$$Y_{in} = jB + \frac{J_r^2}{s + jb} \tag{2.18}$$

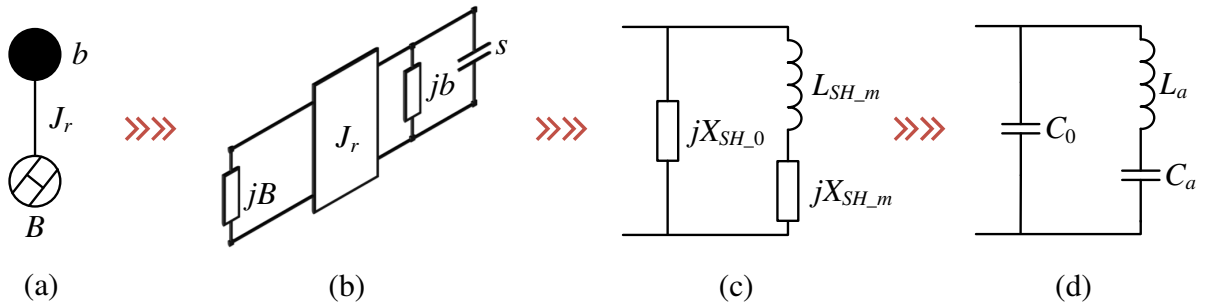

Figure 2.15: Equivalence between nodal representation and lowpass BVD model for a shunt resonator.

The admittance becomes infinite if $s = -jb$, placing a short circuit and therefore a TZ at the normalized frequency $\Omega_{TZ} = -b$. b can either be positive or negative. If the dangling resonator is in a series resonator position, this TZ is implemented by the parallel frequency, while in the shunt resonator case, is accounted as the series frequency. In the same way, the admittance in (2.18) can be nullified, enabling the signal passing.

Closed-form expressions were established in [9] that relates the nodal elements B, J_r and b to the lowpass BVD circuit X_{SH_0}, L_{SH_m} and X_{SH_m}, where the subscripts 0 and m corresponds to the static and motional branch respectively. For the elemental block depicted in Fig. 2.15c, corresponding to shunt acoustic resonator, the equations were calculated as

$$X_{SH\_0} = -\frac{1}{B} \tag{2.19a}$$

$$L_{SH\_m} = \frac{1}{J_r^2} \tag{2.19b}$$

$$X_{SH\_m} = \frac{b}{J_r^2} \tag{2.19c}$$

To complete the ladder configuration, a nodal interpretation for series resonators is needed too. Two admittance inverters J_{ml} with opposite sign are attached to each side of the NRN for this case as observed in Fig. 2.16 to serialize the shunt resonator and obtain the series one. The sign alternation is needed to maintain the phase characteristics of the dangling resonator. Since these inverters are used only for serialization purposes, no physical implementation is accomplished. The subscript ml refers to the main-line path in the inline arrangement. The calculated elements of the BVD series resonator are defined as

$$X_{SE\_0} = \frac{B}{J_{ml}^2} \tag{2.20a}$$

$$L_{SE\_m} = \frac{B^2}{J_r^2 J_{ml}^2} \tag{2.20b}$$

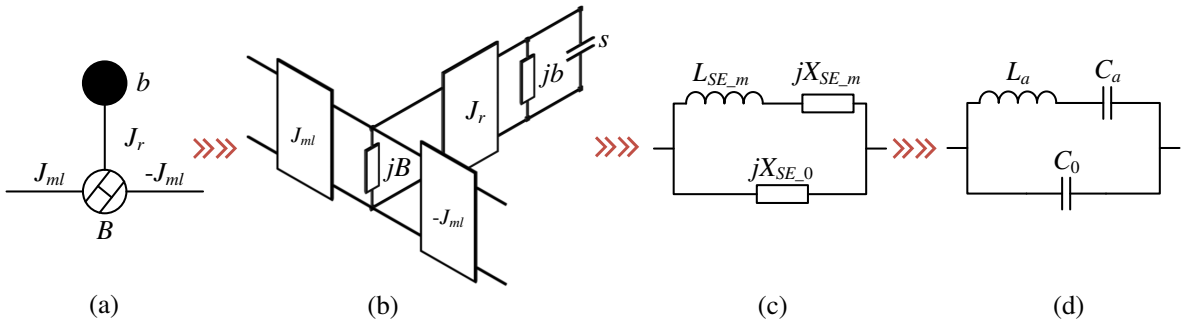

Figure 2.16: Equivalence between nodal representation and lowpass BVD model for a series resonator.

$$X_{SE\_m} = \frac{B}{J_{ml}^2}\left(b\frac{B}{J_r^2} - 1\right) \tag{2.20c}$$

The nodal representation of an entire fifth-order inline filter starting in series position is presented in Fig. 2.17. The set of formulae (2.19) and (2.20) provides the element values to perform the next step: the synthesis based on the extracted-pole technique. Each dangling resonator contributes with a finite TZ independently, hence, a fully canonical filter requires filter's order equals to the dangling resonator's number, namely $N = n_{TZs}$. As stated before, the series resonator (red-underlined), is sandwiched between the admittance inverters in the mainline.

It is important to notice that the new figure presents at source and load ports new reactive elements compared with Fig. 2.12. B_S and B_L are FIRs that transform in capacitors or inductors on the dependence of the susceptance sign. These elements are required in the synthesis process and can not be neglected to have a matched filter. In Chapter 3, the importance and role of these elements are discussed in detail. Despite this thesis is focused on the implementation of series-starting filters, the shunt-starting ones have been studied also to accommodate properly the reactive input/output elements. An extended discussion is addressed in [79], but some aspect will be mentioned in the next chapter.

Having defined the equivalent nodal representation for the further matrix implementation, some aspects should be highlighted related to the constraints imposed by micro-acoustic technology. When the series resonator is considered, b has to be negative to achieve the TZ above the passband and b has to be positive to achieve the TZ below the passband in the shunt resonator case. On the other hand, the sign of the NRN B has to be negative for series resonators and positive for shunt one since it is directly related with static capacitance according to (2.19a) and (2.20a). Finally, with the mandatory alternation of the main-line inverters, all the elements are adequately defined and characterized for the synthesis procedure. This nodal representation presents some advantages: modularity since each dangling resonator section contributes with a finite TZ independently; and the possibility of having a fully canonical filter response without the traditional direct source to load coupling. In this case, this coupling is achieved by the reactive path through NRNs.

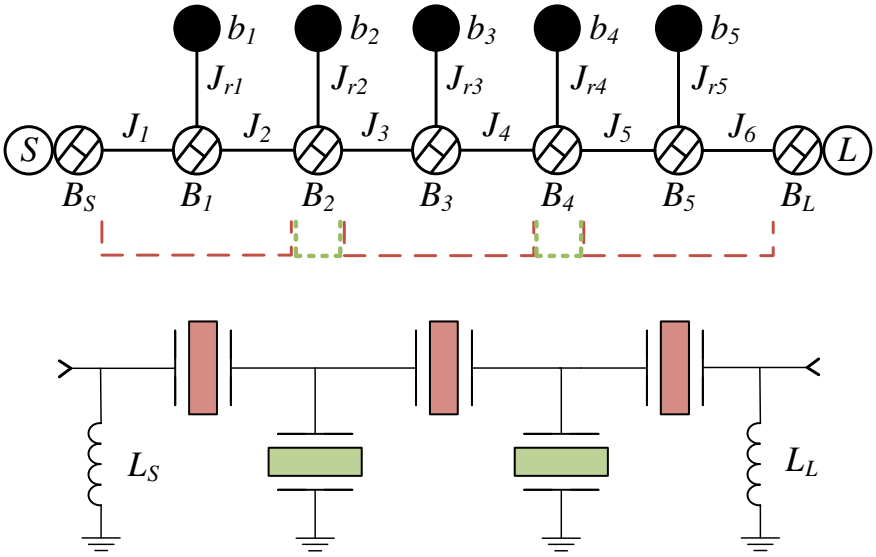

Figure 2.17: Equivalence between a fifth-order filter and the lowpass inline network made of dangling resonators.

2.6 Chapter Summary

This chapter tackles the working principles of acoustic wave resonators as the fundamental block to engineering an AW filter. Physical foundations of such resonators have been explained along this chapter to establish a technological frame. Two consolidated technologies SAW and BAW that provides good performance for the current frequency spectrum are addressed, including propagation modes, piezoelectric material characterization, and definition of the main parameters for the design. Moreover, less mature technologies are also mentioned as a solution for the emerging frequency bands and the drawbacks presented by SAW and BAW like overheating, power durability, and narrow bandwidth.

To deal with the AWR electrical behavior, the widely accepted Butterworth Van Dyke model was presented as a useful tool for the initial steps into the design flow. It is accepted that the BVD model offers a faithful representation of the electrical performance for piezoelectric resonators in the main resonance vicinity with the system losses included. This equivalent circuital model was also interpreted in the lowpass domain as a previous requirement for the synthesis of the filter. Nodal representation of this model was also introduced with the dangling resonator definition that allows the implementation of the extracted-pole technique.

The objective ladder-type filter was modeled as an inline topology composed of dangling resonators sandwiched between admittance inverters. This approach presents some advantages like modularity and the lack of a direct source-load path to ensure the fully canonical behavior. As was stated in this chapter, this configuration provides a fully canonical network since the filter's order is equal to the TZ numbers.

CHAPTER 3

Synthesis of Acoustic Wave Ladder-Type Filters

The frequency characteristics of a ladder-type filter understood as an in-line topology composed of extracted pole sections should be defined by a mathematical function to perform the synthesis of its circuital components. Until the early 1970s, the microwave filter synthesis was based on the extraction of lumped lowpass elements or transmission lines from the polynomials that fulfill the filter's electrical performance in mathematical terms. Many contributions were made to create advanced filter transfer functions and polynomial generation [75, 80, 81]. The crowded available spectrum pushes to specifications on channel filters more demanding in terms of group delay, insertion loss and OoB rejection, and then, advanced filtering synthesis procedures.

This chapter covers the lowpass synthesis procedure for the design of acoustic wave filters. At first, the definition of the filtering function is provided followed by the extraction process to obtain the circuital elements and their disposition in the lowpass and bandpass domain later. The network is evaluated to verify the fulfillment of mask specifications and technological requirements. A coupling matrix network is also defined for this ladder topology, including RN and NRN nodes as well as the main-line coupling J_i and the inverters corresponding to the dangling resonators J_{ri}. It is worth mentioning that limitations presented by the synthesis in the lowpass domain like a narrow-band approximation of NRNs, are overcome in [82, 83] using the direct bandpass methodology. However, the method is restricted to a certain number of topologies as was discussed in [10].

3.1 General Synthesis Procedure for a Chebyshev Filter Function

An AW ladder-type filter where the number of resonators N is equal to the prescribed transmission zeros n_{fz}, leading to a fully canonical filter, can be realized with a generalized Chebyshev filtering function. The characteristic polynomials generated through an efficient recursive technique, obtaining $E(s)$, $F(s)$

and $P(s)$ polynomials and the normalization constants ϵ and ϵ_r are turned into an electrical circuit prototype using a synthesis approach based on the [ABCD] transfer matrix [84]. Despite several filtering functions are described in the literature, the general kind of Chebyshev function is the most suitable to describe the behavior of AW filters. This function cover odd and even filter's degree, symmetric and asymmetric definition, and results in an equiripple passband characteristic. Additionally, arbitrary distribution of TZs can be imposed. On the other hand, the generalized Chebyshev characteristics polynomials allows the design of doubly terminated networks.

3.1.1 Generation of Transfer and Reflection Polynomials

The filter design process begins with the generation of the rational polynomials embodying the transfer and reflection characteristics S_{21} and S_{11}, which satisfy the rejection and in-band input parameters specifications. For a two-port linear network, the scattering parameters relate the power waves propagating away from ports 1 and 2, b_1 and b_2 respectively, and the incident waves at ports 1 and 2, a_1 and a_2 respectively. The matrix is defined as:

$$\begin{bmatrix} b_1 \\ b_2 \end{bmatrix} = \begin{bmatrix} S_{11} & S_{12} \\ S_{21} & S_{22} \end{bmatrix} \begin{bmatrix} a_1 \\ a_2 \end{bmatrix} \tag{3.1}$$

The scattering matrix can be expressed as the ratio of three finite-degree polynomials $P(s)$, $F(s)$ and $E(s)$ and its normalized constant ϵ and ϵ_r

$$\begin{bmatrix} S_{11}(s) & S_{12}(s) \\ S_{21}(s) & S_{22}(s) \end{bmatrix} = \frac{1}{E(s)} \begin{bmatrix} F(s)/\epsilon_r & P(s)/\epsilon \\ P(s)/\epsilon & (-1)^N F(s)^*/\epsilon_r \end{bmatrix} \tag{3.2}$$

where the scattering parameters are to be a function of s ($= j\Omega$), the frequency variable, and N is the degree of the filter network under consideration. Since the input impedance of a terminated network is a positive real function, the three polynomials $P(s)$, $F(s)$ and $E(s)$, referred to as characteristics polynomials that define a lowpass prototype filter network, should fulfill the following properties:

- $\diamond$ $P(s)$**:** is an Nth-degree polynomial with complex coefficients that alternates between purely real and purely imaginary. Its roots lie on the imaginary axis in conjugate pairs. Such roots represent frequencies at which all power is reflected, and the filter loss is infinite. These frequencies are often referred to as *transmission zeros* or attenuation poles. Its roots can also occur as conjugate pairs on the real axis or as a complex quad in the s-plane. The highest coefficient of $P(s)$ is unity. In all-pole networks with TZs at infinity ($n_{fz} = 0$), $P(s)$ is a constant.

- $\diamond$ $F(s)$**:** is an Nth-degree polynomial with complex coefficients that alternates between real and imaginary. Its roots lie along the imaginary axis. $F(s)$ can have multiple roots only at the origin. The roots represent frequencies at which no power is reflected ($b_i = 0$), often termed *reflection zeros*. At these frequencies, the filter transmission is perfect.

- $\diamond$ $E(s)$**:** is an Nth-degree and strictly Hurwitz polynomial, with all its roots lying inside the left half of the s-plane. These roots need not be symmetric about the real axis.

On the other hand, ϵ_r allows the normalization of the highest-degree coefficients of $F(s)$ and $E(s)$ to unity (i.e., e_N and f_N = 1).

Considering that the filter is a passive, lossless, and reciprocal network, two conservation of energy equations can be derived as

$$S_{11}(s)S_{11}(s)^* + S_{21}(s)S_{21}(s)^* = 1 \tag{3.3a}$$

$$S_{22}(s)S_{22}(s)^* + S_{12}(s)S_{12}(s)^* = 1 \tag{3.3b}$$

and one unique orthogonality equation

$$S_{11}(s)S_{12}(s)^* + S_{21}(s)S_{22}(s)^* = 0 \tag{3.4}$$

If two of the three characteristics polynomials are known, the third is derived from the above conservation of energy equation as follows:

$$E(s)E(s)^* = \frac{F(s)F(s)^*}{\epsilon_r^2} + \frac{P(s)P(s)^*}{\epsilon^2} \tag{3.5}$$

It is important to establish that operator * refers to the paraconjugation operation in complex-variable polynomials so as $A(s)^* = A^*(-s)$. Rewriting (3.3) into a simple representation in polar coordinates, it is straightforward to note that $|S_{21}|^2 = 1 - |S_{11}|^2$ recognizing that $|S_{11}| = |S_{22}|$. The orthogonality equation in the polar form is attained by

$$|S_{11}|\,|S_{21}|\,(e^{j(\theta_{11}-\theta_{21})} + e^{j(\theta_{21}-\theta_{22})}) = 0 \longrightarrow e^{j(\theta_{11}-\theta_{21})} = -e^{j(\theta_{21}-\theta_{22})}. \tag{3.6}$$

Considering that the negative factor in the right-hand side of (3.6) can be replaced by term $e^{j\pi(2k\pm1)}$ with k being an integer, the phases θ_{ij} yield the following relation to accomplish the orthogonality condition:

$$-\theta_{21} + \frac{\theta_{11}+\theta_{22}}{2} = \frac{\pi}{2}(2k \pm 1) \tag{3.7}$$

Having defined the relationship between the characteristics polynomials and the S-parameters in (3.2), a direct mapping is done: θ_{21}, θ_{11} and θ_{22} correspond to the angles of the numerator polynomials S_{21}, S_{11} and S_{22} respectively. Become aware of at any value of frequency variable s, the difference

between the angle of the $S_{21(s)}$ numerator vector and the average of phases of the $S_{11(s)}$ and $S_{22(s)}$ numerator vectors must be an odd multiple of $\pi/2$ radians, that is, orthogonal.

Formal definition implies that input and output reflection coefficient numerators are $F_{11}(s)$ and $F_{22}(s)$ respectively. Both terms and their angles are linked with the following expressions:

$$F_{22}(s) = (-1)^N F_{11}(s)^* \tag{3.8}$$

$$\theta_{22}(s) = -\theta_{11}(s) + N\pi \tag{3.9}$$

Given the above equation, a substitution is made in (3.7). Because of the symmetry of the TZs in the transfer function about the imaginary axis and irrespective of n_{fz} and s values, $\theta_{21}(s)$ is an integral number of $\pi/2$ radians. Therefore, a new relation concerning orthogonality is found:

$$(N - n_{fz})\frac{\pi}{2} - \kappa'\pi = \frac{\pi}{2}(2k \pm 1) \tag{3.10}$$

where κ' is an integer. To satisfy the equality, the integer quantity $(N - n_{fz})$ must be odd. In cases where $(N - n_{fz})$ are even, an extra $\pi/2$ radians must be added to the left-hand side of the equation to maintain the orthogonality condition, which is equivalent to adding $\pi/2$ to $\theta_{21}(s)$ or multiplying polynomial $P(s)$ by j. All in all, the transmission polynomial $S_{21}(s)$ expression depends on the value of the filter's order and TZs number

$$S_{21}(s) = \frac{P(s)/\epsilon}{E(s)} \quad \longrightarrow \quad (N - n_{fz})\ odd$$

$$S_{21}(s) = \frac{jP(s)/\epsilon}{E(s)} \quad \longrightarrow \quad (N - n_{fz})\ even$$

3.1.2 Relationship between ϵ and ϵ_r

The monic condition aforementioned for polynomials $P(s)$ and $F(s)$ results from the normalization constant ϵ and ϵ_r respectively, such that $|S_{21}(s)|$ and $|S_{11}(s)|$ are ≤ 1 at any value of s. The latter conditions are mandatory in passive networks like AW filters.

The real constant ϵ is determined by evaluating $P(s)/E(s)$ at a frequency s where the value of $S_{11}(s)$ is known. In the case of Chebyshev filters, the equirriple return loss (RL) level is prescribed at the border of the passband, i.e. $\Omega = \pm 1$, therefore $S_{21(s)}$ can be deduced, and ϵ computed as

$$\epsilon = \frac{1}{\sqrt{1 - 10^{-RL/10}}} \left| \frac{P(\Omega)}{E(\Omega)} \right|_{\Omega \pm 1}. \tag{3.11}$$

Analyzing S-parameters, a relation between the normalization constants can be derived:

$$\frac{\epsilon}{\epsilon_r} = \frac{1}{\sqrt{10^{RL/10}-1}} \left| \frac{P(\Omega)}{F(\Omega)} \right|_{\Omega \pm 1} \tag{3.12}$$

The value of ϵ_r is determined taking into account the number of TZs n_{fz}. In case of non-fully canonical networks, that is to say $n_{fz} < N$, the reflection parameter tends to 1 when $s = \pm j\infty$, therefore $\epsilon_r = 1$. However, in fully canonical case when $n_{fz} = N$, the attenuation at $s = \pm j\infty$ is finite. Evaluating the conservation of energy equation (3.3) at infinity, and later substituting the S-parameters for the monic characteristics polynomials, ϵ_r for fully canonical networks is defined as

$$\epsilon_r = \frac{\epsilon}{\sqrt{\epsilon^2 - 1}} \tag{3.13}$$

Considering that ϵ is always greater than 1, ϵ_r will be slightly greater than 1 in (3.13). Additionally, with the normalization constants, the reflected and transmitted parameters at infinity can be forecast as

$$S_{21}(\pm j\infty) = \frac{1}{\epsilon} = 20 * \log_{10} \epsilon [dB] \tag{3.14a}$$

$$S_{11}(\pm j\infty) = \frac{1}{\epsilon_r} = 20 * \log_{10} \epsilon_r [dB] \tag{3.14b}$$

Both equations are applied to doubly and singly filtering functions in fully canonical networks, where acoustic wave filters belong. The recalculation of ϵ and ϵ_r in singly cases implemented in Chapter 4 allows a comparative analysis based on (3.14).

Polynomial Synthesis of Chebyshev Function: Recursive Method

Once the transfer and reflection parameters have been related to the characteristics polynomials, it is necessary to calculate them. The method deployed in [84] includes the design of the transfer functions and the synthesis of the prototype filter networks with characteristics belonging to the general class of Chebyshev filter function. For the recursive technique, prescribed return loss RL and TZs are required.

For the general Chebyshev characteristic, the filtering function $C_N(\Omega) = F(\Omega)/P(\Omega)$ has the form

$$C_N(\Omega) = \cosh \left[\sum_{n=1}^{N} \cosh^{-1}(x_n(\Omega)) \right] \tag{3.15}$$

where

$$x_n(\Omega) = \frac{1 - \Omega\Omega_n}{\Omega - \Omega_n} \tag{3.16}$$

Figure 3.1: Workflow for obtaining the characteristics Chebyshev polynomials.

and Ω_n are the positions of the n_{fz}.

For the polynomial synthesis method, TZs prescribed in the complex s-plane define the polynomial $P(\Omega)$. The coefficients of $F(\Omega)$ are computed through a recursive method [85]. Having obtained this polynomial, $E(\Omega)$ is constructed by using the alternating singularity principle that follows the conservation of energy equation (3.5) resulting in $P(\Omega)/\epsilon - jF(\Omega)/\epsilon_r$. Since the real part of all its roots must be in the left-hand side of the complex s-plane to fulfill the aforementioned Hurwitz condition, the $E(\Omega)$roots are conjugating and rotating to obtain the final polynomial. The complete process is described in [84].

Up to this point, the characteristic polynomials $P(s)$, $F(s)$, and $E(s)$ are completely determined based on the Chebyshev filtering function. This function permits to synthesize symmetric and asymmetric filters of even or odd degrees for doubly terminated networks with any set of prescribed finite TZs and RL. Fig. 3.1 displays a summarized workflow for obtaining the characteristics polynomials. The control of the filtering function is achieved by knowing the TZs, filter's order, and RL.

3.2 General Circuit Synthesis Procedure

The next step in the design is to translate the characteristic polynomials into a prototype electrical circuit from which an AW filter may be implemented. Remembering that AW ladder-type filters are represented as inline dangling resonators with RN-NRN pairs in the lowpass domain, the approach proposed by [86] is applied in the circuit synthesis in this thesis. This approach introduces a general synthesis technique for filter configurations using both RNs and NRNs arbitrarily coupled to each other not only for pure inline but also for cross-coupled topologies. A drawback of this synthesis procedure is that cross-coupling cannot cross each other.

This section covers the theory required for the extraction of every filtering network parameter of extracted pole sections, considering only inline topologies. Other network topologies have been addressed in [11] with the focus on mixed-topology filters combining inline with transversal networks. Moreover, this general method allows exploring the leakage effects due to electromagnetic couplings through the packaging of acoustic wave filters [87, 88].

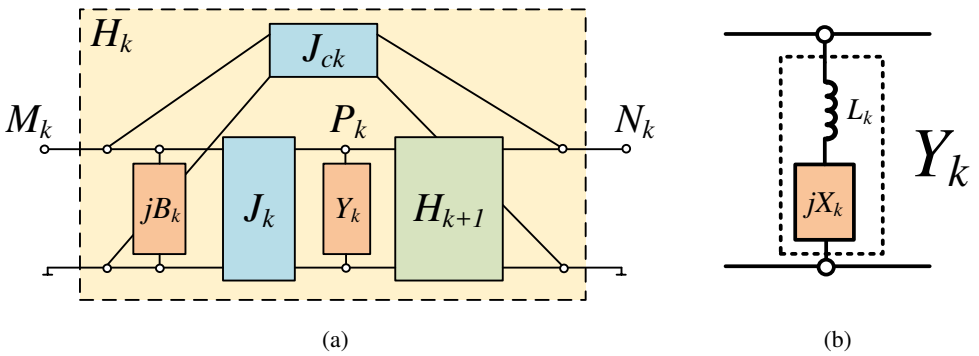

(a) (b)

Figure 3.2: (a) Sub-network k to be synthesized and (b) Y_k network for finite frequency.

3.2.1 Synthesis Method: Complete Procedure

The procedure proposed by [86] is based on a recursive extraction of N basic sub-network, being N the number of poles of the filter. Although the extraction can be performed from both directions to improve the numerical stability at higher filter's order, i.e. source to load or load to source according to the implemented topology, the subsequent steps performed along the network are executed from source to load in this thesis.

The basic sub-network is composed of three cascaded elements and a cross inverter between input and output sub-network ports as depicted in Fig. 3.2a. Three nodes are defined as M_k, P_k and N_k to identify the node for each step where k represents the step number. Since the natural model of extraction, from the left to the right is carried out in this thesis, M_k and N_k are the input and output nodes respectively, and P_k is defined as $P_k = M_k + 1$, indicating where the admittance Y_k is extracted. At each step, the sub-circuit H_k is considered and H_{k+1} is the remaining network for the next step. The subnetwork H_k is composed of a frequency invariant susceptance B_k, an admittance inverter J_k, an admittance Y_k, and a cross admittance inverter J_{ck}.

Analyzing Fig. 3.2a and 2.17, the elements of network H_k can be equalized to the dangling configuration in the inline topology for AW filters. The susceptance B_k is the B_i FIR, J_k is the unity admittance inverter is the mainline J_{ml}. Y_k is defined as capacitance or inductance in series with a FIR depending on the extraction frequency: $c \rightarrow$ RN for $f = \infty$ or L_k; $X_k \rightarrow$ pair RN-NRN for finite frequency as displayed in Fig. 3.2b. Regarding the AW configuration, Y_k portraits the dangling resonator composed by J_r, c and b. The following equations relates both set of variables:

$$L_k = \frac{1}{J_r^2} \tag{3.17a}$$

$$X_k = \frac{b}{J_r^2} \tag{3.17b}$$

Fig. 3.3 illustrates the equivalence between the extracted network proposed by [86] and the nodal

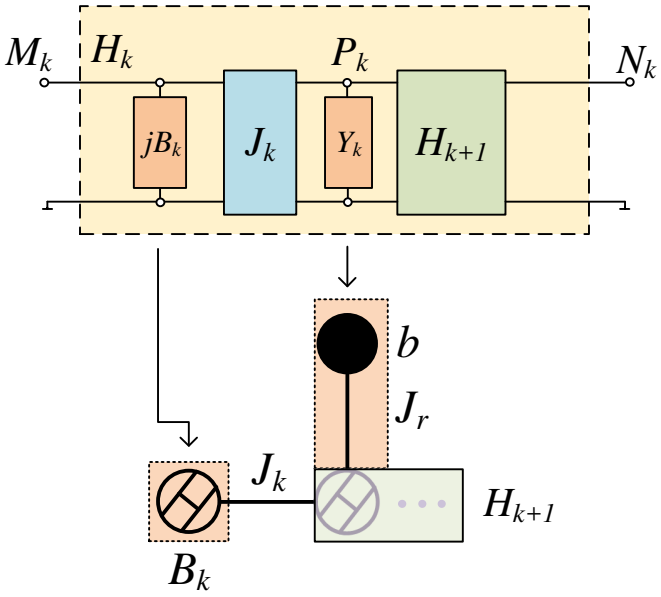

Figure 3.3: Equivalence between the extracted network and the nodal representation for the AW filter, the light purple parts in the nodal schemes are non-extracted elements yet.

representation of AW filter with dangling resonators. It is worth noting that each extraction comprises the FIR that precedes the dangling resonator. As the NRN is calculated to accommodate the next dangling section phase, the extraction of this elements is computed at the same step.

Transfer Matrix Polynomials [ABCD]

To start the extraction procedure, the network is expressed as an [ABCD] transfer matrix using the classic two-port matrix transformation relations with normalized characteristic impedance. In this section, the source and load are going to be considered unitary, but a general definition will be exploited in Chapter 5. Leveraging the relation between S-parameters and the characteristics polynomials, the transfer matrix numerators can be reformulated as:

$$A_n(s) = \frac{1}{2}[(E(s) + F(s)/\varepsilon_r) - (-1)^N (E(s) + F(s)/\varepsilon_r)^*] \tag{3.18a}$$

$$B_n(s) = \frac{1}{2}[(E(s) + F(s)/\varepsilon_r) + (-1)^N (E(s) + F(s)/\varepsilon_r)^*] \tag{3.18b}$$

$$C_n(s) = \frac{1}{2}[(E(s) - F(s)/\varepsilon_r) + (-1)^N (E(s) - F(s)/\varepsilon_r)^*] \tag{3.18c}$$

$$D_n(s) = \frac{1}{2}[(E(s) - F(s)/\varepsilon_r) - (-1)^N (E(s) - F(s)/\varepsilon_r)^*] \tag{3.18d}$$

while the common denominator is $P(s)/\epsilon$. In case of $(N - n_{fz})$ even, $P(s) \rightarrow jP(s)$. The total transfer matrix is defined as

$$[ABCD] = \begin{bmatrix} A(s) & B(s) \\ C(s) & D_(s) \end{bmatrix} = \frac{1}{P(s)/\varepsilon} \begin{bmatrix} A_n(s) & B_n(s) \\ C_n(s) & D_n(s) \end{bmatrix} \tag{3.19}$$

Independently of whether N is even or odd, $B(s)$ has the highest degree N, $A(s)$ and $D(s)$ are of degree $N-1$, and $C(s)$ has the lowest degree $N-2$.

Recursive Synthesis Process for H_k Sub-Network

With the defined [ABCD] polynomials, the synthesis procedure is carried out by means of successive extractions associated with the recursive network H_k. Even though in this chapter the admittance Y_k is considered as an RN-NRN extracted at TZs frequency, the general method comprises the extraction at an infinite frequency ($Y_k \rightarrow$ RN) and finite frequency different from TZs. Moreover, the cross-coupling J_{ck} is null for each H_k sub-network.

Despite no cross-coupling is considered, the first step is the extraction of the cross inverter J_{ck} through the evaluation at the corresponding root of $P(s)$ as follows:

$$J_{ck} = -\frac{jP_k(j\Omega_k)}{B_{nk}(j\Omega_k)}. \tag{3.20}$$

It is clear that as long as Ω_k is a TZ, namely a root of $P(s)$, $J_{ck} = 0$. The sub-network after this operation is denoted as H'_k and the remained matrix polynomials $[ABCD]'_k$. Since $J_{ck} = 0$, $[ABCD]'_k$=$[ABCD]_k$. The above equation denominator refers to the polynomial $B_n(s)$ which is frequency-dependent. The following step is the extraction of the FIR B_k for preparing the removal of the TZ at $j\Omega_k$. The NRN is computed as

$$B_k = \frac{D'_{nk}(j\Omega_k)}{B'_{nk}(j\Omega_k)}. \tag{3.21}$$

Once B_k has been obtained, it must be removed from the transfer matrix to calculate the updated matrix $[ABCD]''_k$. The remaining polynomials are defined as

$$A''_{nk}(s) = A'_{nk}(s) \tag{3.22a}$$
$$B''_{nk}(s) = B'_{nk}(s) \tag{3.22b}$$
$$C''_{nk}(s) = C'_{nk}(s) - B_k A'_{nk}(s) \tag{3.22c}$$
$$D''_{nk}(s) = D'_{nk}(s) - B_k B'_{nk}(s) \tag{3.22d}$$
$$P''_k(s) = P'_k(s) \tag{3.22e}$$

Now, the unitary inverter J_k must be extracted, and an updated $[ABCD]'''_k$ transfer matrix is computed as

$$A'''_{nk}(s) = -jC''_{nk}(s) \tag{3.23a}$$
$$B'''_{nk}(s) = -jD''_{nk}(s) \tag{3.23b}$$
$$C'''_{nk}(s) = -jA''_{nk}(s) \tag{3.23c}$$
$$D'''_{nk}(s) = -jB''_{nk}(s) \tag{3.23d}$$
$$P'''_{k}(s) = P''_{k}(s) \tag{3.23e}$$

The last step corresponds to the extraction of Y_k which introduces a zero at $j\Omega_k$. Whereas inductance L_k in series with the FIR jX_k must be extracted, the admittance evaluated at Ω_k is computed as

$$Y_k = \frac{D'''_{nk}(j\Omega_k)}{B'''_{nk}(j\Omega_k)} = \left.\frac{J^2_{rk}}{s - j\Omega_k}\right|_{s=j\Omega_k} \tag{3.24}$$

As stated before in (3.17), the residue of the above division J^2_{rk} is related to L_k and X_k. To obtain its value the next operation is carried out:

$$J^2_{rk} = \left.\frac{D'''_{nk}(s)(s - j\Omega_k)}{B'''_{nk}(s)}\right|_{s=j\Omega_k} = \frac{D'''_{nk}(s)}{\widetilde{B}_{nk}(s)} \tag{3.25}$$

All the elements of H_k have been extracted, so the remaining polynomials must be updated for the next sub-network H_{k+1} extraction. At this point, all polynomials have been reduced one degree. The transfer matrix is now:

$$A_{n(k+1)}(s) = \frac{A'''_{nk}(s)}{s - j\Omega_k} \tag{3.26a}$$
$$B_{n(k+1)}(s) = \frac{B'''_{nk}(s)}{s - j\Omega_k} \tag{3.26b}$$
$$C_{n(k+1)}(s) = \frac{C'''_{nk}(s) - J^2_{rk}A_{n(k+1)}(s)}{s - j\Omega_k} \tag{3.26c}$$
$$D_{n(k+1)}(s) = \frac{D'''_{nk}(s) - J^2_{rk}B_{n(k+1)}(s)}{s - j\Omega_k} \tag{3.26d}$$
$$P_{(k+1)}(s) = \frac{P'''_{k}(s)}{s - j\Omega_k} \tag{3.26e}$$

Finalization of the Synthesis Process

When all the extractions at finite frequencies TZs are carried out, exist a residual network H_k, ($k = N + 1$), constituted by the last mainline inverter J_{N+1} between the FIRs B_N and B_L as it is represented in Fig. 3.4.

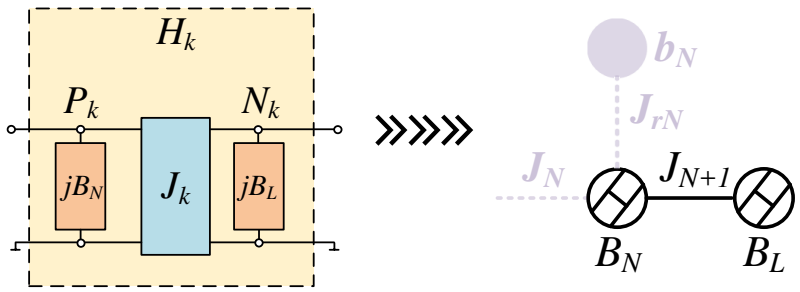

Figure 3.4: Engaged elements in the last synthesis iteration $k = N + 1$.

The [ABCD] matrix of this three elements sub-network is given by the cascaded of them:

$$[ABCD] = \frac{1}{J_{N+1}} \begin{bmatrix} -B_N & j \\ j(J_{N+1}^2 - B_N B_L) & -B_L \end{bmatrix} \tag{3.27}$$

Knowing that the residual [ABCD] at the last step is computed from (3.26) and considering that all polynomials have at this moment degree 0, the elements can be calculated dividing the constant values as

$$J_{N+1} = -\frac{P_{N+1}}{B_{n(N+1)}} \tag{3.28}$$

$$B_N = jJ_{N+1}\frac{A_{n(N+1)}}{P_{N+1}} \tag{3.29}$$

$$B_L = jJ_{N+1}\frac{D_{n(N+1)}}{P_{N+1}} \tag{3.30}$$

After performing this extraction, the final [ABCD] matrix is empty and therefore the whole network has been fully synthesized.

Mainline Inverters: Towards the Evenly Distribution

As depicted in (3.28) , the last inverter depends on the residual values of $P(s)$ and $B(s)$. In order to convert into ladder-filter topologies, the main-line inverters are desired to be equal with opposite phases; usually set to ± 1 for serialization of the dangling resonators purpose. However, J_{N+1} might be not unitary according to the arrangement of the TZs and the source and load values. Symmetric filters, namely transmission zeros distributed like $\Omega_{TZ1} = \Omega_{TZN}$, $\Omega_{TZ2} = \Omega_{TZ(N-1)}$, etc., entail an even value of the main-line admittance inverters J_i. Even values are needed to serialize the dangling structures corresponding to series resonators in the ladder-type configuration. When the prescribed TZs are distributed asymmetrically, the equalization of the last inverter is performed through an admittance redistribution in the last step.

The uneven inverter can be placed in any position, but as long as the extraction procedure is performed from source to load, the last inverter will be the uneven one. Although a simultaneous extraction

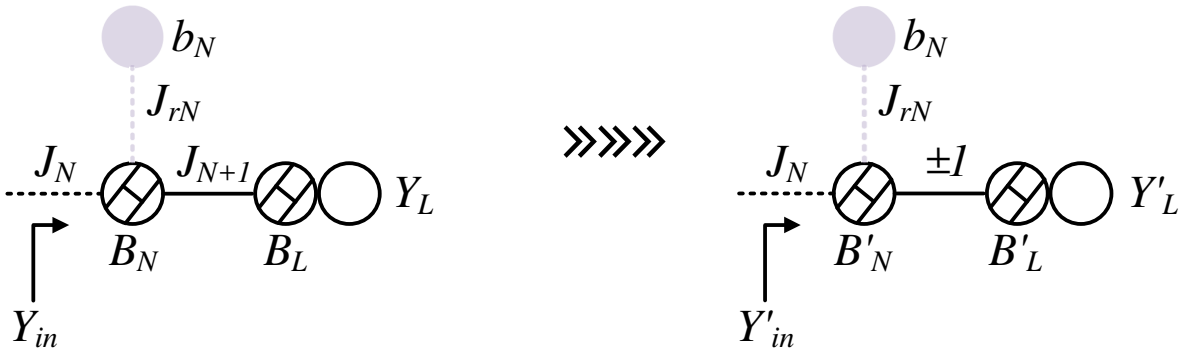

Figure 3.5: Last extraction step and the equivalent rearranged network with recalculated NRN's values to obtain a unitary last inverter.

from source and load is desirable to minimize the effect of round-off errors, the extraction in one direction is accurate enough in lower order filters. The uneven inverter is then forced to J_{N+1} position.

In the NRN's extraction procedure step in [77], a relation between the inverters J_{rk} and J_k is noticed, leading to the impossibility of determining both values at the same time. This ratio allows multiple solutions for a given synthesis problem. Fig. 3.5 depicts the initial scenario for the last extraction step and the redistributed one to obtain $|J_{N+1}| = 1$.

The input admittance before the B_N extraction relates B_N, the output element B_L, the non-unity inverter between them J_{N+1}, and the loaded unitary termination Y_L as it is expressed in (3.31a). The circuital transformation performed in the right side of Fig. 3.5 assumes a unitary last inverter that guarantees the initial calculated Y_{in}, so, the real and imaginary part of Y_{in} in both cases would be equal.

$$Y_{in} = jB_N + \frac{J_{N+1}^2}{jB_L + Y_L} \tag{3.31a}$$

$$\Re(Y_{in}) = \frac{Y_L J_{N+1}^2}{Y_L^2 + B_L^2} \tag{3.31b}$$

$$\Im(Y_{in}) = B_N - \frac{B_L J_{N+1}^2}{Y_L^2 + B_L^2} \tag{3.31c}$$

Imposing $|J_{N+1}| = 1$ in (3.31b) and considering $\Re(Y_{in}) = \Re(Y'_{in})$, the rearranged output element B'_L results in:

$$B'_L = \pm\sqrt{\frac{Y_L}{\Re(Y_{in})} - Y_L^2}. \tag{3.32}$$

Imposing $|J_{N+1}| = 1$ in (3.31c) and considering $\Im(Y_{in}) = \Im(Y'_{in})$, the rearranged last FIR B'_N results in:

$$B'_N = \Im(Y_{in}) + \frac{B'_L}{Y_L^2 + B_L'^2} = \Im(Y_{in}) + \frac{\Re(Y_{in})B'_L}{Y_L} \tag{3.33}$$

Equation (3.32) offers two solutions for B'_L value, and therefore, two possible solutions for B'_N. Even though both are realizable solutions, we have to select the proper one according to the topology, i.e., negative B'_N are required to transform dangling resonators into series. In contrast, positive B'_N corresponds to shunt resonators. It should also be emphasized that there could be cases where the reachable values do not fit with the nature of the Nth resonator, so the filter can not be transformed into the acoustic domain.

In principle, the load Y_L and Y'_L must be equals. To guarantee the feasibility of B'_L susceptance, according to (3.32), $Y'_L \leq 1/\Re(Y_{in})$. When this inequality is not fulfilled, Y'_L would be force to its maximum possible value $Y'_L = 1/\Re(Y_{in})$ getting $B'_L = 0$. In this scenario, $Y'_L \neq Y_L$, and consequently, a mismatch will be produced in the output port. In Chapter 5, a generalized theory is presented considering source/load port as a generic complex number. Moreover, some examples illustrating the mismatch effect are accomplished.

The above admittance redistribution is the most common solution to equalize the inverters. Even though the simplicity and usefulness of the admittance redistribution approach, may not be appropriated for every case. For instance, in cross-coupled topologies case where source-load coupling embraces the whole network or part of it, the redistribution method must be dismissed. To overcome this limitation, a general methodology based on the phase correction of the characteristic polynomials of the filtering function $F_{11}(s)$, $F_{22}(s)$ and $E(s)$ is presented in [11] and [89]. Therefore, the use of asymmetric polynomials allows to equalize the uneven admittance inverter employing characteristic polynomials phase modification, yielding uniform absolute values to the set of admittance inverters in the main-line for any TZs distribution.

3.2.2 Annotations about Shunt -Starting/-Ending Filters

Regarding the position of the first/last resonator, the ladder network can be classified in series or shunt -starting/-ending network. All the theory described before applies to both configuration, but the input/output FIRs B_S and B_L. In the case of the first/last resonator is in shunt position, the preceding/succeeding admittance inverter in Fig. 2.17 that has not been absorbed by the dangling resonator, is neglected after the circuital transformation. The absence of the inverter does not affect the filter response magnitude but introduces a 90° shift when the source/load are normalized to 1 in a 50-Ω system. This situation avoids the proper synthesis of duplexers and multiplexers that require specific phase matching. In the case of complex source/load impedance, neither stand-alone nor duplexers/multiplexers can ignore the inverter.

To complete the ladder topology, a series input/output element should be extracted, which involves the addition of an extra inverter, now J_1 to serialize the FIR. A modified nodal representation for a shunt-

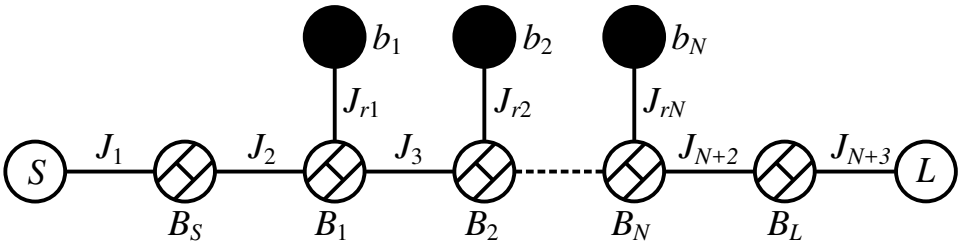

Figure 3.6: Lowpass nodal representation of an odd-order shunt-starting acoustic wave ladder network.

starting acoustic wave ladder network is shown in Fig. 3.6. The synthesis procedure described before should be slightly modified: the unitary inverter J_1 is computed with (3.23) while B_S is calculated with (3.21) moving on with the same steps as described before.

When the last resonator is shunt and we are facing FIR B_N, the first step is the extraction of J_{N+3} with (3.23) turning the direction from load to source. This change is equivalent to interchange $A(s)$ and $D(s)$ polynomials. Once the inverter has been extracted, the network is turned again to the original reference point B_N. Applying (3.28), (3.29) and (3.30) the remaining elements J_{N+2}, B_N and B_L can be extracted successfully.

The above solution contemplates a single input/output element that does not cover all situations. In [79], the authors demonstrate that the filter is feasible with a single element in duplexer's case only if the first resonator's resonance frequency f_s is below the center of the counter band. To overcome this limitation, two reactive elements are placed and a simple rule is provided to decide the right topology. In terms of the low-pass filter function, the first f_s is controlled with the position of the first TZ.

3.2.3 Coupling Matrix Representation and Analysis

A coupling matrix is a mathematical tool that describes, in the low-pass domain, the arrangement of filter elements. The coupling matrix (CM) approach is ideally suited to design filters with completely arbitrary couplings, allowing the realization of any possible transfer function. By leveraging the matrix representation of the network, a variety of filter topologies providing the same desired response can be derived through matrix operations like inversion, similarity transformation, and partitioning [85,90]. Due to the CM relies on circuit theory approximation with frequency-independent couplings (J_i and J_{ri}), it is suited for the design of narrow-band bandpass filters.

The entries of the conventional N x N matrix presented by [91], and its expanded version N+2 x N+2 including source and load nodes, can be directly related to the physical elements of the filter structure. The nodal diagram representation of the inline acoustic filter with dangling resonators in Fig. 2.17 requires a CM extension to include the NRNs and the couplings between them and the resonators (J_{ri}). A resized $2N$+2 symmetric square matrix is obtained. The entries on the main diagonal are the susceptances corresponding to resonating and non-resonating nodes, while the admittance inverters are

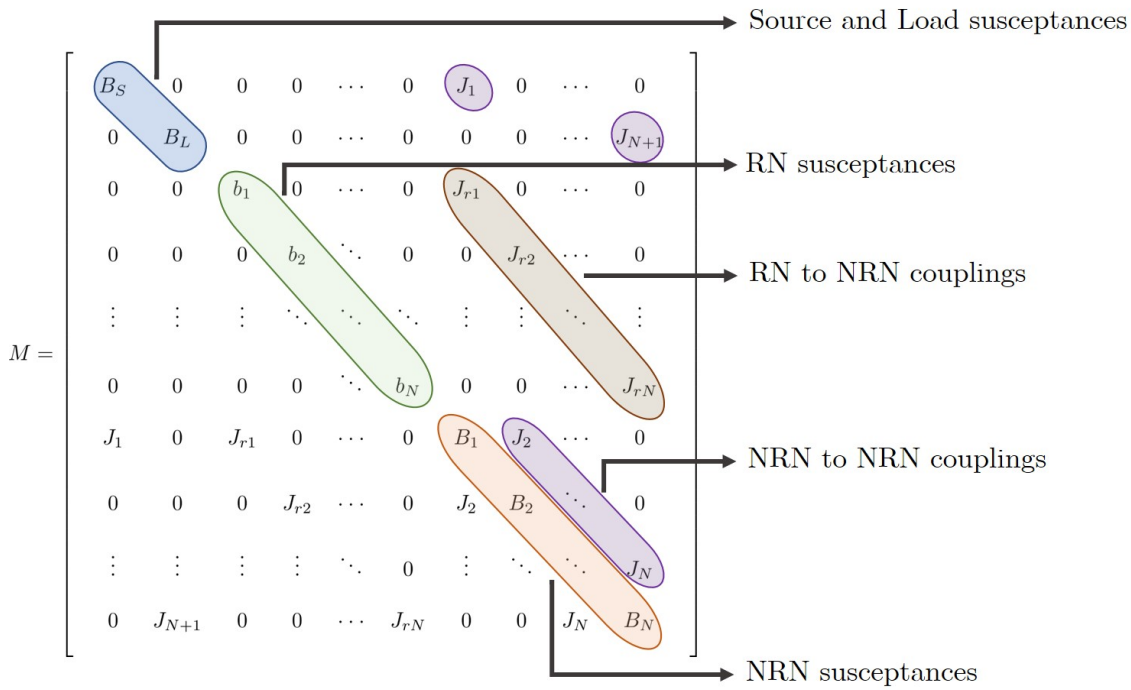

Figure 3.7: Coupling matrix for the inline dangling resonator structure.

distributed along with the matrix as it is observed in Fig. 3.7.

The matrix elements are grouped according to their function sequentially:

- ◇ **Source and Load Nodes:** The susceptances B_S and B_L located in the two first positions of the main diagonal (M_{11} and M_{22}) represent the input/output matching elements of the network. The values can be either positive or negative, depending on the network input parameters.
- ◇ **Resonant Nodes:** The susceptances b_i distributed in the main diagonal from M_{33} to $M_{(N+2)(N+2)}$ indicate the self-coupled resonator, assumed as a frequency invariant reactance element in parallel to a unity capacitor.
- ◇ **Non-Resonant Nodes:** The susceptances B_i are the N last elements in the main diagonal. These frequency invariant reactances correspond to each dangling resonator. The values can be either positive or negative depending on the TZs arrangement.
- ◇ **Main Line Admittance Inverters:** The N+1 admittance inverters J_i are situated coupling the NRNs in the mainline. The alternate sign guarantees the suited phase in the serialization procedure.
- ◇ **Dangling Admittance Inverters:** The N admittance inverters J_{ri} couples the RN to the NRN. Its values are always positive.

Having defined the CM, exists two other elements to consider: W and Y. Assuming that a two-port

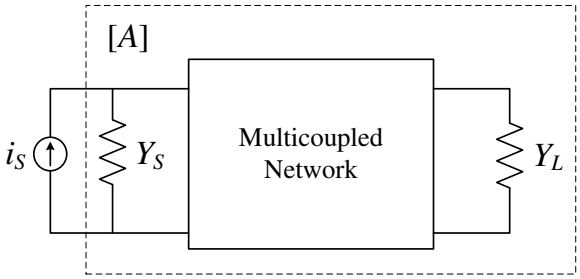

Figure 3.8: Multicoupled network connected to a current source of admittance Y_S and loaded with Y_L.

network operates between a current source i_s generating amperes and an internal admittance Y_S and a load impedance Y_L, and admittance matrix $[A]$ represents the network behaviour as displayed in Fig. 3.8. The admittance matrix may be expanded as follows [84]:

$$[A]\,[v] = j\,[i] = [M + \Omega W - jY]\,[v] \tag{3.34}$$

where M is the main CM, W is a diagonal matrix that contains the frequency-dependent components (the unitary capacitors corresponding to the resonant nodes), and Y contains the source and load admittance. All matrices are $2N$+2 square sized. W entries are filled with zeros except for the diagonal positions where the node is resonant.

Having into account that voltage in source and load defines the network performance, the S-parameters can be calculated as:

$$S_{21} = S_{12} = -2j\sqrt{G_S G_L}\left[A^{-1}\right]_{21} \tag{3.35a}$$

$$S_{11} = 1 + 2jG_S\left[A^{-1}\right]_{11} \tag{3.35b}$$

$$S_{22} = 1 + 2jG_L\left[A^{-1}\right]_{22} \tag{3.35c}$$

where G_S and G_L are the real part of Y_S and Y_L respectively.

3.3 Numerical Example

A numerical example is provided to illustrate the methodology described in this chapter. A symmetric filter was designed for B7-Rx with a passband from 2.62 to 2.69 GHz. Taking into account the filter specifications (spectrum mask) for this band, and in order to fit with an effective electromechanical coupling constant k^2_{eff} = 6.83% (r-factor=17) in all resonators, and also fulfill the technological bounds of the static capacitance of the filter ($C_0 < 4$ pF) in each resonator, the synthesis procedure through an automatic search engine was performed. The following configuration was encountered as the filter specifications:

Table 3.1: Chebyshev characteristics polynomials.

Degree	$P(s)$	$F(s)$	$E(s)$
7	j	1	1
6	2.25	$-0.2520j$	$1.7957 - 0.2520j$
5	$12.08j$	1.8427	$3.4550 - 0.4588j$
4	25.89	$-0.4053j$	$3.6413 - 0.8230j$
3	$48.49j$	0.9941	$3.2621 - 0.8264j$
2	103.36	$-0.1702j$	$1.9358 - 0.6579j$
1	$64.66j$	0.1408	$0.8079 - 0.3280j$
0	137.02	$-0.0120j$	$0.1729 - 0.0949j$
ϵ		695.87	
ϵ_r		1	

◇ TZs Ω_z (rad/s): {2.2017 , -2.0596, 1.879, -1.8874, 1.879, -2.0596, 2.2017 }

◇ RL (dB): 17.9

The transfer and reflection polynomials for Chebyshev filtering characteristics, and the normalizing real constant ϵ and ϵ_r are summarized in Table 3.1.

To carry out the lowpass elements extraction following the steps described in 3.2.1, the [ABCD] matrix was calculated with (3.18). The resulting values are listed in Table 3.2. The extracted elements in the lowpass domain are shown in Table 3.3. It is worth to notice that as this is a symmetric filter case, all inverters fulfill the unitary condition for the main-line admittances inverters J_i.

The calculated lowpass elements are transformed in frequency with impedance denormalization to obtain the BVD equivalent circuit. Table 3.4 resumes the BVD element values extracted from the network. The first and last resonators are series in the selected topology so that the external elements would be in shunt position. S-parameters response in lowpass domain is shown in Fig. 3.9a considering a series and parallel quality factor Q=1500. Finally, the filter's simulation using the values of the BVD model in the bandpass domain is depicted in Fig. 3.9b.

The technological constraints imposed at the beginning of the synthesis were fulfilled properly. All resonators show equal k^2_{eff} with static capacitance lower than 4 pF. An equirriple response is obtained according to the Chebyshev definition. Input and output external inductors L_S and L_L respectively behave as high reactance elements at the operation frequency, therefore, to reduce the filter size, these elements can be neglected in the final implementation.

Table 3.2: Transfer matrix polynomials.

Degree	$A(s)$	$B(s)$	$C(s)$	$D(s)$
7	–	2.0000	–	–
6	1.7957	$-0.5040j$	–	1.7957
5	$-0.4588j$	5.2978	1.6123	$-0.4588j$
4	3.6413	$-1.2282j$	$-0.4177j$	3.6413
3	$-0.8264j$	4.2562	2.2680	$-0.8264j$
2	1.9358	$-0.8281j$	$-0.4876j$	1.9358
1	$-0.3280j$	0.9487	0.6671	$-0.3280j$
0	0.1729	$-0.1069j$	$-0.0830j$	0.1729

Table 3.3: Extracted nodal elements in the lowpass domain.

$Res.$	B_k	b_k	J_r
1	-1.8215	-2.20	1.8623
2	3.0369	2.06	2.3949
3	-2.6734	-2.88	2.2379
4	3.0652	2.88	2.3960
5	-2.6734	-2.88	2.2379
6	3.0369	2.06	2.3949
7	-1.8215	-2.20	1.8623
B_S/B_L	-0.4722		

Table 3.4: Bandpass elements of the filter obtained from the BVD model.

f_s [GHz]	k^2_{eff} [%]	C_0 [pF]	C_a [pF]	L_a [nH]
2.6697	6.83	0.6639	0.0390	90.9581
2.5754	6.83	3.4172	0.2010	18.998
2.6575	6.83	0.4481	0.0263	135.99
2.5818	6.83	3.4663	0.2038	18.642
2.6575	6.83	0.4481	0.0263	135.99
2.5754	6.83	3.4172	0.2010	18.998
2.6697	6.83	0.6639	0.0390	90.9581
L_S/L_L	6.34 nH			

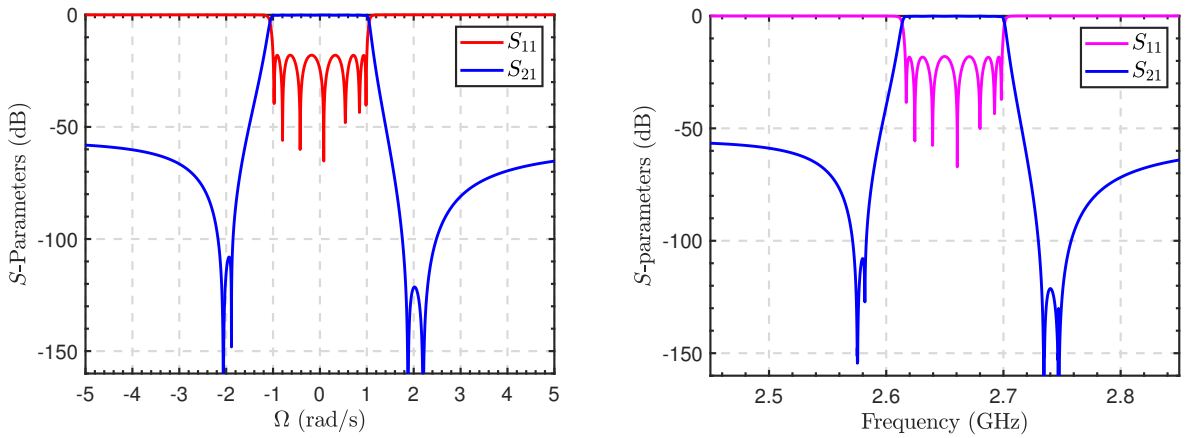

(a) (b)

Figure 3.9: S-parameters of a seventh-order filter response in (a) the lowpass domain and (b) bandpass domain using the BVD model of the resonators.

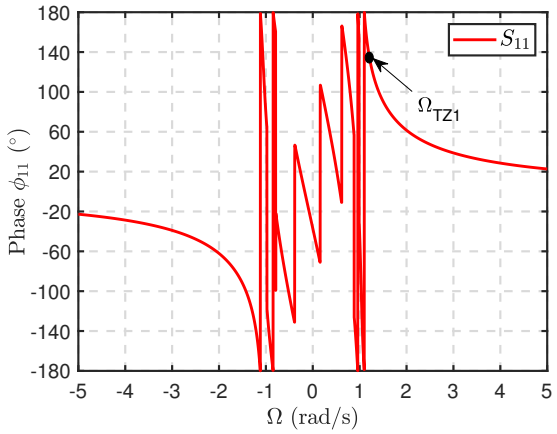

Figure 3.10: Fully canonical seventh-order filter reflection coefficient phase.

3.4 Phase Role in Ladder-Type Acoustic Wave Filters

A suitable handling of the reflection coefficient phase ϕ_{11} is essential for the network elements extraction. Therefore, the introduction of an additional phase term ϕ_{add_11} shifting $\angle S_{11}$ has been exploited in diverse scenarios depending on the future implementations as duplexer, multiplexer or stand-alone filter without external input/output elements [9, 92, 93]. Since the phase term ϕ_{add_11} is a real quantity, the magnitude $|S_{11}|$ remains unaltered. This section tackles the role-playing by ϕ_{add_11} in diverse practical cases and the paramount importance of an appropriate interpretation. The discussion is focused on networks starting in series resonator. Considerations regarding filters and duplexers starting with shunt resonators can be found in [79]. It is worth stressing that this section considers the symmetric polynomial definition with $F_{11}(s) = F_{22}^{*}(s) = F(s)$ where modification of $F(s)$ phase changes the input and output phase alike.

The major role that the phase of S_{11} plays in the success of the synthesis was highlighted in [77] where two different cases were considered depending on whether the first node is resonating or not. If the first node is a resonator, a transmission zero at infinity is expected due to the transformation of this node to a pure LC tank in the bandpass domain. Evaluating S_{11} at infinity (see (3.2)) results in $S_{11}(\infty)$= 1 since $E(s)$ and $F(s)$ are monic and ϵ_r=1; thereby, $|S_{11}|$=1 and ϕ_{11} = 0º.

For the second case, in presence of a dangling resonator that places a transmission zero at a finite frequency Ω_z, evaluating $S_{11}(\Omega_z)$, a complex number is obtained. The modulus remains unitary, but the phase is not zero anymore $\phi_{11} \neq 0°$. For illustration purpose, a seventh-order fully canonical filter was synthesized with the corresponding $\Omega_{TZ} = \{1.2, -3, 1.6, -1.8, 2.5, -1.5, 2.1\}$ and RL=20 dB. $\angle S_{11}$ is displayed in Fig. 3.10 where $\phi_{11}(\Omega_{TZ1}) = 137.8°$. The former example will run the coming discussion to facilitate the numerical comparison in all cases.

Reflection and transmission parameters can be expressed as the ratio of two finite-degree polynomials

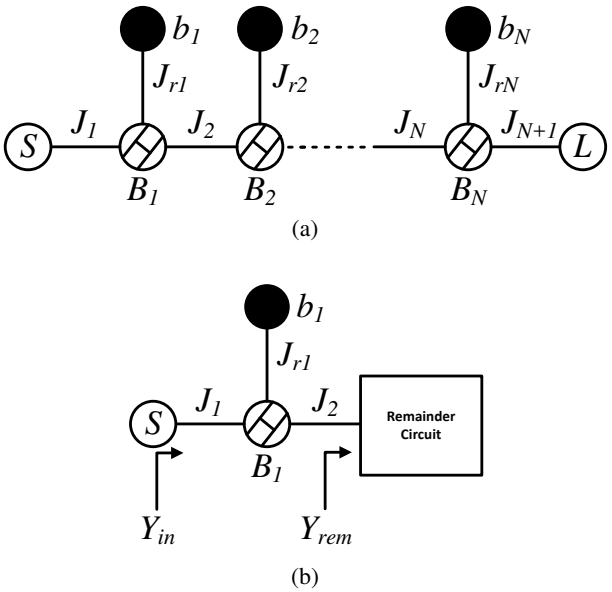

Figure 3.11: Fully canonical Nth-order inline filter with dangling resonators.

and normalization constant, where $E(s)$ and $F(s)$ are the characteristics polynomials of a generalized Chebyshev filtering function, associated to the scattering parameter S_{11} as

$$S_{11}(s) = e^{j\phi_{add\_11}} \frac{F(s)/\epsilon_r}{E(s)}. \tag{3.36}$$

The selected evaluation frequency s determines the existence of input/output reactive elements in a stand-alone filter case whereas defines the loading effect produced in duplexer and multiplexers examples. Two cases will be cover to demonstrate the paramount role-playing by the reflection coefficient.

3.4.1 External Input/Output Elements, Duplexers and Multiplexers

Fully canonical filters concatenate dangling resonators through admittance inverters as depicted in Fig. 3.11a. Looking from source to load there is a resonator at resonance $s = j\Omega_{TZ1}$ with $\phi_{11} = 0°$, but from the filter function, there is a remaining phase. For the above seventh-order example, to extract the elements of the first dangling resonator, keeping $\phi_{11}(\Omega_{TZ1}) = 137.8°$, it is necessary a phase shifter implementing the remaining phase of the Chebyshev function. This new element at the network's input, namely a frequency invariant reactance (FIR) B_S allows the complete extraction of the network acting as a phase-matching element. $B_S = -2.53$ was obtained as a result of the synthesis procedure. In this case, no phase term ϕ_{add_11} has been added. The same approach is applied when the network is faced from load to source, forcing to place an external output element B_L.

To avoid external input/output elements B_S/B_L, Amari and Macchiarella proposed in [77] the evaluation of the input admittance at the resonance frequency. Looking at Fig. 3.11b, the network input

admittance can be expressed as

$$Y_{in}(s) = \frac{J_1^2}{jB_1 + \frac{J_{r1}^2}{s+jb_1} + \frac{J_2^2}{Y_{rem}(s)}} \tag{3.37}$$

The equation shows that when $s = j\Omega_{TZ1}$, considering that $\Omega_{TZ1} = -b_1$, the input admittance becomes zero, producing a transmission zero at Ω_{TZ1}. Hence, evaluating (3.36) at $s = j\Omega_{TZ1}$, an additional phase is obtained to implement the filtering function without external elements

$$\phi_{add\_11} = -\angle \left(\frac{F(s)/\epsilon_r}{E(s)} \bigg|_{s=j\Omega_{TZ1}} \right). \tag{3.38}$$

This term is introduced in the filter function recomputing the $F(s)$ polynomial; $F(s) \longleftarrow F(s)e^{j\phi_{add\_11}}$. As expected, the FIR element B_S is nullified, and an acoustic wave stand-alone ladder-type filter that does not need an input reactive element is attained.

On the other hand, the mange of ϕ_{add_11} is very important in duplexer and multiplexer cases. One of the most significant characteristics of duplexers is Tx to Rx isolation in the Tx band which determines the leakage power from the transmitter to receiver because Tx leakage makes the largest interference for the receiver. To dismiss or nullify the interference, the loading effect produced by the combination of the filters (multiplexers case) or the counter band (duplexers case) in a common node near the antenna should be minimized. The interference provokes by adjacent filters in duplexers and multiplexers, can be controlled under some conditions, allowing constructive interference instead of destructive.

To achieve loading minimization, in a star-junction configuration, an open circuit is desired at the frequency of the counterpart in duplexer cases, namely f_{CB}. Rx filters should behave as an open circuit at the central frequency of Tx and vice-versa. This condition is achieved imposing a reflection coefficient phase ϕ_{11}=0º at f_{CB}. The additional phase that ensures this condition is computed evaluating (3.38) at Ω_{CB} as follows,

$$\phi_{add\_11} = -\angle \left(\frac{F(s)/\epsilon_r}{E(s)} \bigg|_{s=j\Omega_{CB}} \right) \tag{3.39}$$

where Ω_{CB} is either referred to Rx or Tx center frequency depending on the analyzed filter. As the counter band frequency moves away from the first transmission zero, the value of the external input element B_S will be more significant, and a reactive element would be placed at the network input.

The obtained value has the same absolute value but opposite sign than the phase of the Chebyshev filtering function at the center frequency of the counter band. Like in stand-alone case, polynomial $F(s)$ of each filter is updated with the inclusion of the new phase term. The open-circuit condition is evaluated at a single frequency, so it would be only a "good" open circuit at the vicinity of f_{CB}. Also, it is important to notice that due to the narrowband characteristic of the bandpass frequency transformation equation (see

(2.13)), the greater the gap between the center frequencies in the duplexer, the less precise will be (3.39). Thus, a manual adjustment would be necessary in these cases to procure an open circuit condition in the bandpass domain.

Despite this limitation, and thanks to the narrow-band characteristic of the analyzed filters, this approximation can be considered quite suitable for the design of duplexers. The introduced distortion is acceptable and the improvement in terms of device complexity and area are tangible because of the avoided use of any additional phase shifter or transmission lines.

A duplexer for uplink and downlink band 7 was synthesized to show the results of the accurate calculation of the additional phase. Tx and Rx filters start in series resonator configuration, covering 2500-2570 MHz and 2620-2690 MHz respectively. Technological constraints like uniform coupling coefficient k^2_{eff} and performance specifications like high cross-isolation were taken into account. The input parameters for the synthesis process are listed below:

B7 Transmitter

- Ω_{Tx} (rad/s): {1.8967, -2.1340, 1.8842, -1.9107, 1.8842, -2.1340, 1.8967 }
- RL (dB): 22
- $\phi_{add\_11}(^\circ)$: -42.8728

B7 Receiver

- Ω_{Rx} (rad/s): {2.5423, -2.0931, 1.8897, -1.8930, 1.8897, -2.0931, 2.5423 }
- RL (dB): 21
- $\phi_{add\_11}(^\circ)$: 34.2295

Phase ϕ_{add_11} was computed by (3.39) to fix the duplexer condition in each case. The expected open circuit condition is shown in Fig. 3.12 where the normalized input admittance of B7-Tx at the central frequency of the counter band, B7-Rx, has a null imaginary part, namely $\Im(Y_{inTx}(f_{cRx})) = 0$. B7-Rx reports the same performance regarding its counter band. As discussed before, this open circuit condition allows to minimize the loading effects in the adjacent filter, but marginal changes can be appreciated in the final duplexer response because this condition is not exactly met along the whole passband. In the case of multiplexers, the phasing among different channels is extended to all filters, following the approach proposed in Chapter 4.

BVD bandpass elements corresponding to each filter are summarized in Table 3.5 and Table 3.6. Finally, Fig. 3.13a illustrates the simulated duplexer's performance and Fig. 3.13b, the high cross-isolation better than -60 dB attained for this design. For this simulation, the assumed Q-factor for the acoustic resonators and external inductive elements were $Q_{AW} = 1500$ and $Q_L = 50$ respectively.

Table 3.5: Bandpass elements of B7-Tx filter obtained from the BVD model.

f_s [GHz]	k^2_{eff} [%]	C_0 [pF]	C_a [pF]	L_a [nH]
2.5357	6.76	1.0465	0.0615	63.997
2.4550	6.76	3.0679	0.1804	23.287
2.5353	6.76	0.4276	0.0251	156.67
2.4628	6.76	3.1962	0.1880	22.212
2.5353	6.76	0.4276	0.0251	156.67
2.4550	6.76	3.0679	0.1804	23.287
2.5357	6.76	1.0465	0.0615	63.997
L_S,L_L	12.30 nH			

Table 3.6: Bandpass elements of B7-Rx filter obtained from the BVD model.

f_s [GHz]	k^2_{eff} [%]	C_0 [pF]	C_a [pF]	L_a [nH]
2.6424	6.76	0.7913	0.0456	75.677
2.5428	6.76	4.9314	0.2908	13.179
2.6224	6.76	0.6618	0.0389	92.154
2.5481	6.76	4.9432	0.2907	13.073
2.6224	6.76	0.6618	0.0389	92.154
2.5428	6.76	4.9314	0.2908	13.179
2.6470	6.76	0.7913	0.0456	75.677
L_S,L_L	3.403 nH			

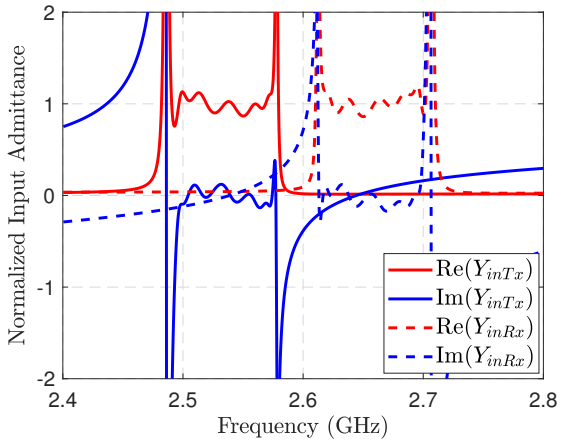

Figure 3.12: Input admittance of each duplexer's filter independently calculated.

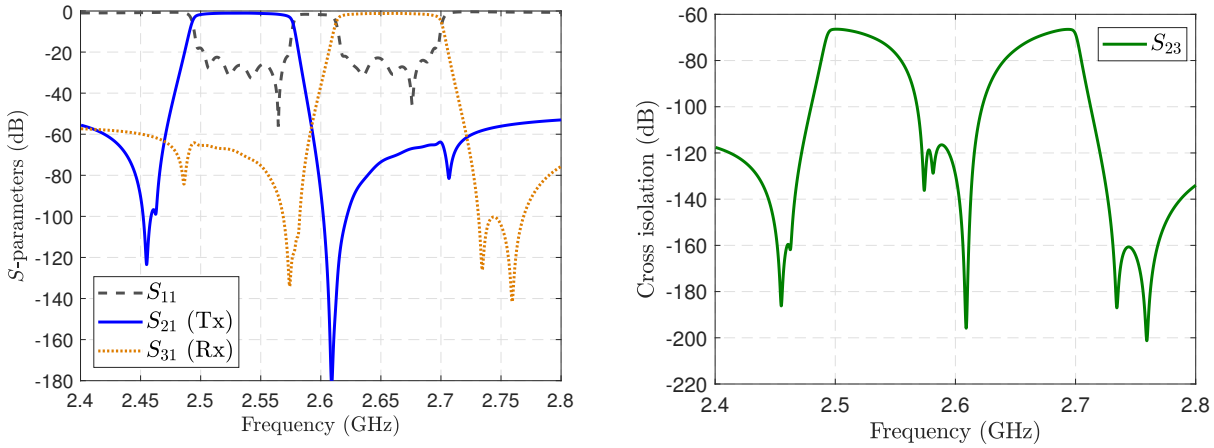

(a) (b)

Figure 3.13: Simulated bandpass duplexer response (a) Transmission and return loss and (b) Cross-isolation.

3.5 Phase Influence on Technological Parameters of AW Filters Starting with Series Resonator

As illustrated previously, in stand-alone filters, the management of the reflection coefficient phase through ϕ_{add_11} is used to prevent the presence of external reactive elements at the input/output stage. In duplexers and multiplexers, the input phase is used to avoid the loading effect in the common port. However, it has been observed that the phase can also be used to improve the performance of the designed filter significantly reducing the total area without affecting the amplitude response of the filter. For instance, BAW resonators area is linked to the static capacitance, permittivity ϵ^s and thickness t as computed in (3.40). Analyzing the total static capacitance behavior by sweeping the additional phase values offers a degree of freedom to the designer.

$$A = \frac{C_0 t}{\epsilon^s} \tag{3.40}$$

Equations 3.38 or 3.39 results in a unique solution, instead of the multiple existing possibilities for another defined additional phase. The possible solutions are achievable in stand-alone filters where the addition of an extra element is feasible in return for an area reduction. If the phase is not properly considered, the magnitude of the reflection coefficient is still unitary, nevertheless, it remains a phase part that must be implemented with a frequency invariant reactance (FIR) element at the input/output node to have the proper phase-matching condition. The extracted value of the first element in the network and its reactive nature (capacitive or inductive) in the bandpass domain depends on the value given to ϕ_{add_11}.

It is straightforward to prove that the phase value will affect the static capacitance of all resonators of the filter C_0, but also the capacitance ratio r-factor of the first and last resonator, defined as the ratio between the static and acoustic capacitance C_a (see (2.2)). Therefore, the designer may take advantage of this situation to obtain filtering networks that better accommodate the technology, reducing the area of the filter expressed as the total static capacitance of the filter C_{0tot}, but also in terms of uniform r-factor among all resonator to reduce the number of reactive elements.

The synthesis methodology is very useful also to analyze the effect of different ϕ_{add_11} in terms of total static capacitance C_{0tot} and r-factor. To visualize the phase effect into the network parameters, the synthesis by sweeping all possible values of ϕ_{add_11} in (3.36) has been carried out in a series-starting AW ladder filter. The synthesis case of filters and duplexers starting with shunt resonator is fully covered in [79], where the feasibility is analyzed keeping in mind the TZs position and the additional phase. Furthermore, is given a rule on the position of the resonance frequency of the first resonator to ensure the feasibility of a shunt-starting duplexer with a single input element, and the expression to synthesize the additional element if two elements are allowed.

To analyze the impact of ϕ_{add_11}, a fully canonical asymmetrical stand-alone seventh-order filter was considered for band B7-Rx. This band was chosen for continuity and comparison purposes with the

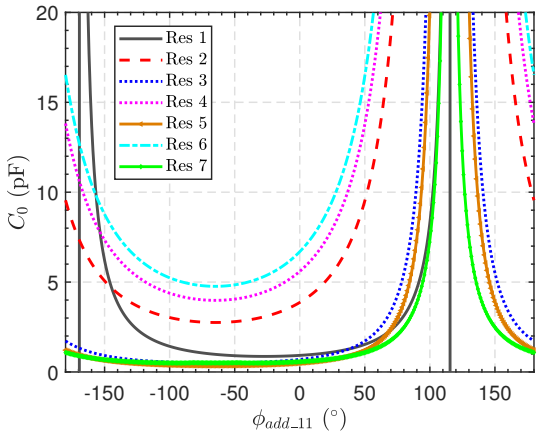

Figure 3.14: Static capacitance of each resonator sweeping ϕ_{add_11} from -180 to 180 degrees.

example presented in section 3.4.1. The low-pass TZs were placed in Ω_{B7Rx} (rad/s): {1.8, -2.1 , 1.49 , -2.57 , 1.9 , -3.37 , 2.53 } and return loss level of 18 dB. The objective capacitance ratio is r-factor=17. The sweep covers from $-180°$ to $180°$ with $1°$ resolution .

3.5.1 Analysis of the Influence of the Input Phase in the Filter Size

Each resonator C_0's value as function of the additional phase is shown in Fig. 3.14. ϕ_{add_11} affects the static capacitance of all resonators of the filter, therefore, the total area represented by C_{0tot}. The corresponding phases to C_0 minimum values of each resonator might coincide for some resonators depending on the input design parameters. A brief description of the behavior of the outer resonators is discussed further in this section.

Observing Fig. 3.14 we can notice a phase region where C_0 reaches non-feasible values, greater than the AW technology can support. Furthermore, the first series resonator stars getting negative value when $\phi_{add\_11} < -170°$ and $\phi_{add\_11} > 115°$. FIR element B_1, related to C_{01}, should be negative for obtaining positive C_0 values according to the relationship between the low-pass and band-pass equivalent circuit parameters, where

$$C_{0\_SE} = -\frac{1}{\omega_0 B_k Z_0} \tag{3.41a}$$

$$C_{0\_SH} = \frac{B_k}{\omega_0 Z_0}. \tag{3.41b}$$

It is clear the paramount importance of the sign of the FIR element B_k to carry out the transformation of the acoustic resonator to the BVD model. According to (3.41), series resonators demand $B_k < 0$ and conversely, shunt resonators $B_k > 0$, implying an alternation of B_k elements sign in a ladder filter topology. If this order is not fulfilled, the negative capacitance observed in Fig. 3.14 would be interpreted

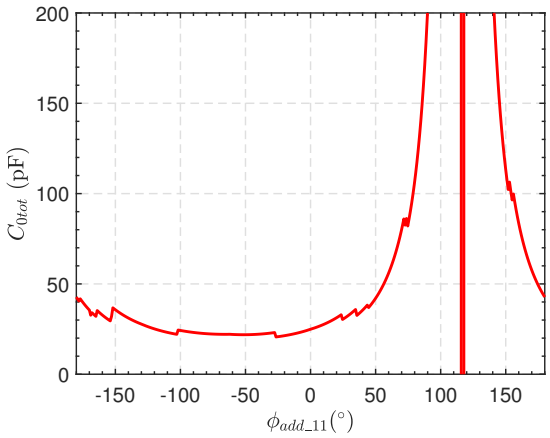

Figure 3.15: Total static capacitance sweeping ϕ_{add_11} from -180 to 180 degrees.

as an inductive element leading to a synthesized filter not feasible in the acoustic domain. Even though the minimum C_0 values are not obtained at the original Chebyshev filter function, namely $\phi_{add\_11} = 0°$, the sweep demonstrates that any phase correction is needed to accommodate series-starting AW filters since no negative capacitances appear.

On the other hand, the total capacitance is defined by the sum of C_0 of each resonator considering the resonator cascading for better power handling when it was necessary. If the normalized power density of each resonator is higher than the maximum reactive power density that each resonator can support, then the resonator must be split. An unrealistic value for reactive power threshold is used in this example The phase dependence of the total static capacitance, C_{0tot}, is shown in Fig. 3.15. The swept highlights an additional phase where a minimum filter area is reached demonstrating that a feasible filter design with a smaller size can be obtained with the election of the proper phase. The C_{0tot} minimum value for this example is 20.64 pF with $\phi_{add\_11} = -26.57°$, and in consequence with 3.40, the filter area is minimum too. As expected, the total static capacitance rises fast for certain added phase values as a consequence of the aggregation of all static capacitances.

Moreover, the applied term phase into $F(s)$ polynomial affects, as was explained before, the input and output due to the symmetric polynomial definition. Therefore, sweeping ϕ_{add_11}, the input/output external elements performances and natures can be evaluated. In series-starting filtering networks, FIRs B_S and B_L are transformed as inductive/capacitive parallel elements in the band-pass domain. Fig. 3.16a and 3.16b display B_S and B_L for this example respectively. The current network is an odd order, therefore, the first and last resonators are series, and B_S and B_L are transformed both to parallel reactive elements. The calculation for the bandpass domain is arranged according to the FIR sign as stated below:

$$B_{S/L} > 0 \longrightarrow C_{S/L} = \frac{B_{S/L}}{\omega_0 Z_0}$$

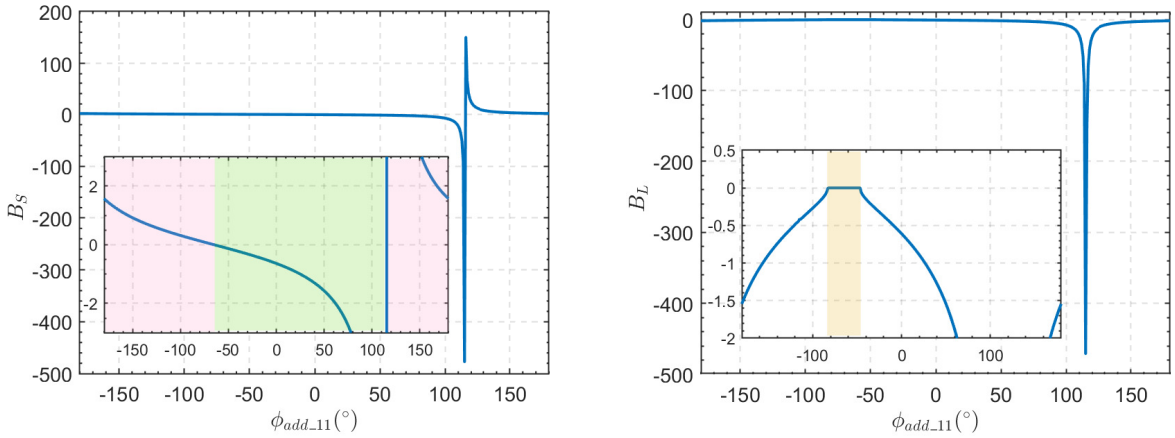

(a) (b)

Figure 3.16: Evaluation of the external (a) input and (b) output FIRs sweeping ϕ_{add_11} from -180 to 180 degrees.

$$B_{S/L} < 0 \longrightarrow L_{S/L} = -\frac{Z_0}{\omega_0 B_{S/L}}$$

Observing the inset in Fig. 3.16a is straightforward to notice that B_S take positive or negative value for different phase regions. Pink regions, where $\phi_{add\_11} < -65°$ and $\phi_{add\_11} > 115.5°$ embrace positive B_S values, while green region delimited by the pink one, encloses negative values. That means that the external input elements could be a capacitor (pink zone) or an inductor (green zone) relaying on ϕ_{add_11} figure.

Additionally, small B_S values in both regions provide input external reactance values (C_S or L_S) that can be neglected. For instance, taking into account that a parallel inductance greater than 15 nH or a conductance smaller than 0.4 pF at the filter central frequency can be treated as very large impedances, there is a phase range where no input extra elements are needed in the filtering network, as it is desired in stand-alone filters. When these elements are neglected, no substantial change in the filter performance can be appreciated. In accordance with the B_S graph, filter synthesized with $-100° < \phi_{add\_11} < -45°$ could neglect the input reactive element, minimizing the space occupied by the filter.

Conversely, the nature of the output element B_L displayed in Fig. 3.16b does not change with the phase sweep, being always inductive for this example. It is worth noticing that there is a phase range $-82° < \phi_{add\_11} < -46°$, highlighted in yellow, where B_L value have been forced to 0 in the synthesis process. The compulsion was required to designate the last inverter with a unitary value to serialize the last dangling resonator, as was explained for the redistribution procedure. As consequence, the filter is slightly mismatched, but still fulfilling the mask specifications. A large L_L value is reached with $-95° < \phi_{add\_11} < -35°$ as is shown in 3.16b thanks to the tiny B_L, then the output external element can be dismissed applying this phase zone.

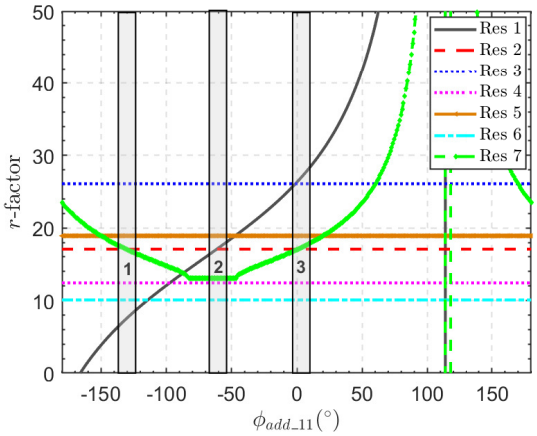

Figure 3.17: r-factor of each resonator sweeping ϕ_{add_11} from -180 to 180 degrees.

All in all, the superposition of both graphics indicates that to avoid input and output external components at the same time, and also maintain a small device size, the designer can select ϕ_{add_11} within a wide range. A good compromise is attained when $\phi_{add\_11} = -50°$, obtaining a total area $C_{0tot} = 21.5$ pF, $L_S = 23$ nH and $L_L = \inf$ H.

3.5.2 Analysis of the Influence of the Input Phase in Capacitance Ratio

As it has been headlined at the section's beginning, a variation on the additional phase affects the r-factor of the first and last resonator. Fig. 3.17 shows the resulting r-factor for an ϕ_{add_11} swept from -180 to 180 degrees. r-factor remains constant for inner resonators while it varies for outer resonators.

The objective r-factor = 17 is fulfilled by resonator 2 hence external elements are needed for the other resonators. Resonators 3 and 5 present a higher r-factor than the objective, requiring an external parallel capacitor to accommodate the technology while resonators 4 and 6 present lower r-factor than the objective, requiring an external series inductor to accommodate the technology. The external tailored elements for resonators 1 and 7 switch between capacitor and inductor depending on the phase region. Surprisingly, there is a direct relation with the defined regions in the former section for resonator 1. That is to say, the pink interval includes r_1-factor$<$17 while in the green zone, r_1-factor$>$17. (see Fig. 3.16a)

It is also observed in Fig. 3.17 that there are three intersection points where two resonators have the same value 17. In position 1 and 3, where $\phi_{add\_11} = -130°$ and $\phi_{add\_11} = 0°$ respectively , resonator 7 has the aimed r-factor and in position 2 with $\phi_{add\_11} = -62°$, resonator 1 holds the same value. A reduction in the number of external elements connected to the resonators is accomplished in these positions. As it can be seen, the synthesis tool can provide the nature and allocation of the external elements if they are required to accommodate the technology.

In the case of the last resonator, r_7-factor behaviour follows a more difficult pattern to explain. Fig.

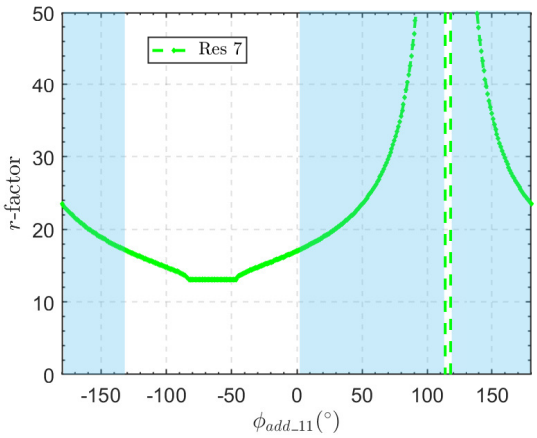

Figure 3.18: r-factor of resonator 7 sweeping ϕ_{add_11} from -180 to 180 degrees.

3.18 illustrates r_7-factor in detail. If $\phi_{add\_11} < -130^\circ \vee 0^\circ < \phi_{add\_11} < 113.5^\circ \vee \phi_{add\_11} > 117.8^\circ$, the capacitance ratio is larger than 17, thereby, a parallel capacitor should be placed for technological accommodation. With the phase values out of the former regions, r-factor < 17 are achieved, therefore series inductance would be required. Additionally, the yellow zone delimited in Fig. 3.16b coincides with equal capacitance ratio = 13.8.

As it was seen in the above example, the designer could select the phase shift applied to the filter to minimize its size ($\phi_{add\_11} = -26.57^\circ$), despite the non-uniform r-factor if the miniaturization is the aim. Instead, the designer could select another phase to reduce the number of external elements in each resonator to accommodate the technology if an r-factor homogenization is demanded.

There is a range of phases where r-factor and C_0 get extreme positive values for resonators 1 and 7. This behavior involves a filter size increase and larger external capacitances to achieve technological feasibility. By contrast, there is a range of phases where r-factor and C_0 get negative values, resulting in an interpretation of C_0 as an inductor. The network construction in both cases is not feasible in acoustic filters.

A uniform r-factor in all resonators would be desired to avoid external elements connected to the resonators, which depends directly on the fabrication technology. This condition is more frequently achieve in symmetrical filters since there is a phase value where all the resonators have uniformity. The symmetrical seventh-order filter synthesized for B7-Rx in section 3.4.1 is going to run the analysis hereafter. In Fig. 3.19 is shown the phase dependence of the total static capacitance and capacitance ratio. The filter reaches minimum area $C_{0tot} = 18.45$ pF with an additional phase $\phi_{add\_11} = -48.6^\circ$ as is depicted in Fig. 3.19a. In contrast, uniform r-factor is achieved when $\phi_{add\_11} = 35^\circ$ as shown in Fig. 3.19b. These points of interest are closer than in the previous example.

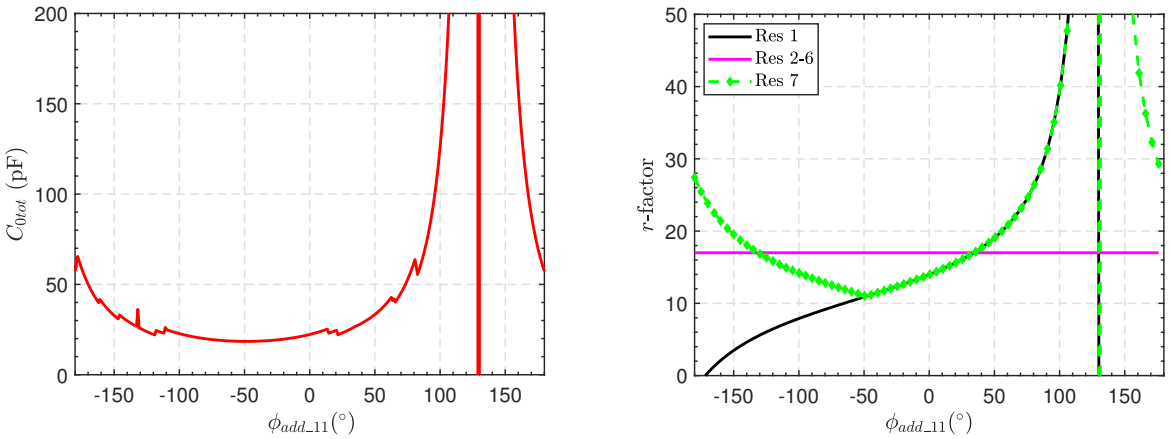

Figure 3.19: Sweep phase for evaluation of (a) total capacitance and (b) capacitance ratio in a symmetrical filter.

3.6 Chapter Summary

In this chapter, the design of the filter is considered from a methodological point of view. First, the definition of a general kind of Chebyshev filtering function to meet the system requirements. The generalized Chebyshev filter function has been chosen to obtain the lowpass prototype response of an AW ladder filter. The computation of the function is made via a recursive algorithm. The main features are equiripple in the bandpass, transmission zeros decoupled from the reflection zeros at finite frequencies; suitable for fully canonical networks, even/odd orders, and symmetric/asymmetric response characteristics.

With the initial input specifications, TZ and RL, the characteristics polynomials $P(s)$, $F(s)$, and $E(s)$ are obtained. The lowpass network elements are computed hereafter using an iterative extraction method from the [ABCD] matrix. Even though in this dissertation the topologies that include cross-coupling are not tackled, the methodology provides flexibility to implement mixed topologies or model parasitic effects for instance. During the final step, an admittance redistribution is carried out to achieve uniformity in the main-line admittance inverters.

The introduction of the additional phase into the characteristic polynomial $F(s)$ is useful not only to avoid external input elements in stand-alone filters and loading effect in duplexers/multiplexers for 50 Ω systems. The proper management provides the designer a freedom degree for technological accommodation and size minimization also. The value of the elements of the synthesized filter with defined transmission zeros, return loss and order, varies in dependence on the input phase. The analysis carried out shows how the input phase affects the static capacitance of all the resonators of the filter, therefore, the total area, in a fully canonical asymmetrical and symmetrical stand-alone seventh-order filters. Also, a variation on the input phase affects r-factor. r-factor remains constant for inner resonators while it

varies for outer resonators. There is a range of phases where r-factor and C_0 get positive/negative extreme values. This behavior involves a filter size increase. The network construction in both cases is not feasible for AW technology.

To summarize, the phase plays an important role to find the best solution for the specific goals as can be seen in this chapter, providing the filter designer with more flexibility and a new guideline for the design.

CHAPTER 4

Minimum Susceptance Networks Applied to the Design of Star-Junction Multiplexers

The telecommunications industry grows at a fast pace set by data consumption. For 5G networks, mobile network operators and component handset manufacturers are applying a combination of techniques to increase the network performance and support the demands in the near term. Three approaches are the key to achieving this goal: advanced carrier aggregation (CA), higher-order modulation, and multiple-input multiple-output (MIMO) techniques. Each of these approaches adds RF complexity to RF Front-End Modules (FEM), and smartphones will need to support all three to provide high data rates.

Not only the number of bands in advanced 4G LTE smartphones has placed significant demands on the manufacturers of SAW and BAW bandpass filters. With the introduction of Carrier Aggregation (CA), which is the primary method that operators are using to drive higher data rates, and due to spectrum roaming, there has been an extraordinary increase in the number of different band combinations that handsets must support. Consequently, the modules have moved from stand-alone or duplexed filters to complex multiplexers architectures commonly from three to seven channels with contiguous or non-contiguous configurations where the opportunity to connect or disconnect filters on-demand to the common port has become an important feature.

Addressing the design of flexible frequency bands multiplexers for end-user applications is a challenging task. In this chapter, a multiplexer topology review with an end-user segment perspective and synthesis approaches are revised, highlighting the role and importance of minimum susceptance networks (MSN). It is shown that doubly-terminated networks can be understood as MSN under specific input phase condition of the reflection coefficient, as well as, singly terminated networks can be understood as non-MSN. The comparison between both networks and the mechanisms to improve the multiplexer performance are also discussed. According to the frequency plan scenario, the design of star-junction multiplexers is faced along the chapter with customized suggestions. A triplexer presenting a spectrum

frequency band plan on demand was designed, fabricated, and characterized to validate the developed theory experimentally. Without loss of generality, commercial acoustic-wave filters have been used to that aim.

On the other hand, simulation tools are ubiquitous in electronic design. The rapidly increasing complexity of RFFE architectures requires an unparalleled level of accuracy in simulation and modeling. Therefore, acoustic multiplexers design requires a scalable model that precisely predicts performance over a wide frequency range. To obtain shorter development production time, it is fundamental to have accurate simulation tools to evaluate the multiplexer performance from the first step. To take stock of the star-junction multiplexer behavior, a direct scattering matrix solution-based on the circuit theory is presented in this chapter by leveraging the suitable environment provided by a numerical computing tool like MATLAB.

4.1 Multiplexer Topologies and Synthesis

The most commonly used multiplexer configurations are classified into two main families: first, directional configurations that include hybrid-coupled multiplexers, Fig. 4.1a, circulator-coupled multiplexers and directional multiplexers, and secondly, manifold-coupled multiplexers including comb and herringbone configuration shown in Fig. 4.1b and Fig. 4.1c respectively. Star topology can be understood as a particular case of herringbone. In a hybrid-coupled multiplexer configuration, each channel includes two paired filters and two identical quadrature couplers. The modularity is the best advantage for this approach. The directional coupler minimizes the interaction among the channel filters. From the performance point of view, it is also advantageous that only half of the input power goes through each filter; however, its large size is a weakness, mainly for the user segment, since two filters and two hybrid couplers per channel are necessary.

Regarding realizable miniaturization and absolute insertion loss, the manifold-coupled topology is considered the optimum choice. Designing a multiplexer with a manifold-coupled configuration requires all the channel filters at the same time so that the effect of channel interactions can be corrected during the design process. Consequently, a manifold-coupled multiplexer is not pleasant for a flexible frequency plan; any modification in the allocation band or the number of bands considered requires a new multiplexer design. Moreover, this approach becomes more challenging to implement as the number of channels increase.

Several common manifold multiplexer configurations can be found in the literature. A manifold multiplexer is given by channel filters connected to a common output port; the most relevant are comb configuration where the filters are connected to one side of the manifold, herringbone to both sides, as shown in Fig. 4.1c, or a common junction. These three types are quite similar in concept and design procedure. Manifold configurations are used for a large number of channels [84,94] at the cost of increasing the size. In contrast, the star configuration is usually used for a reduced number of filters leading to a

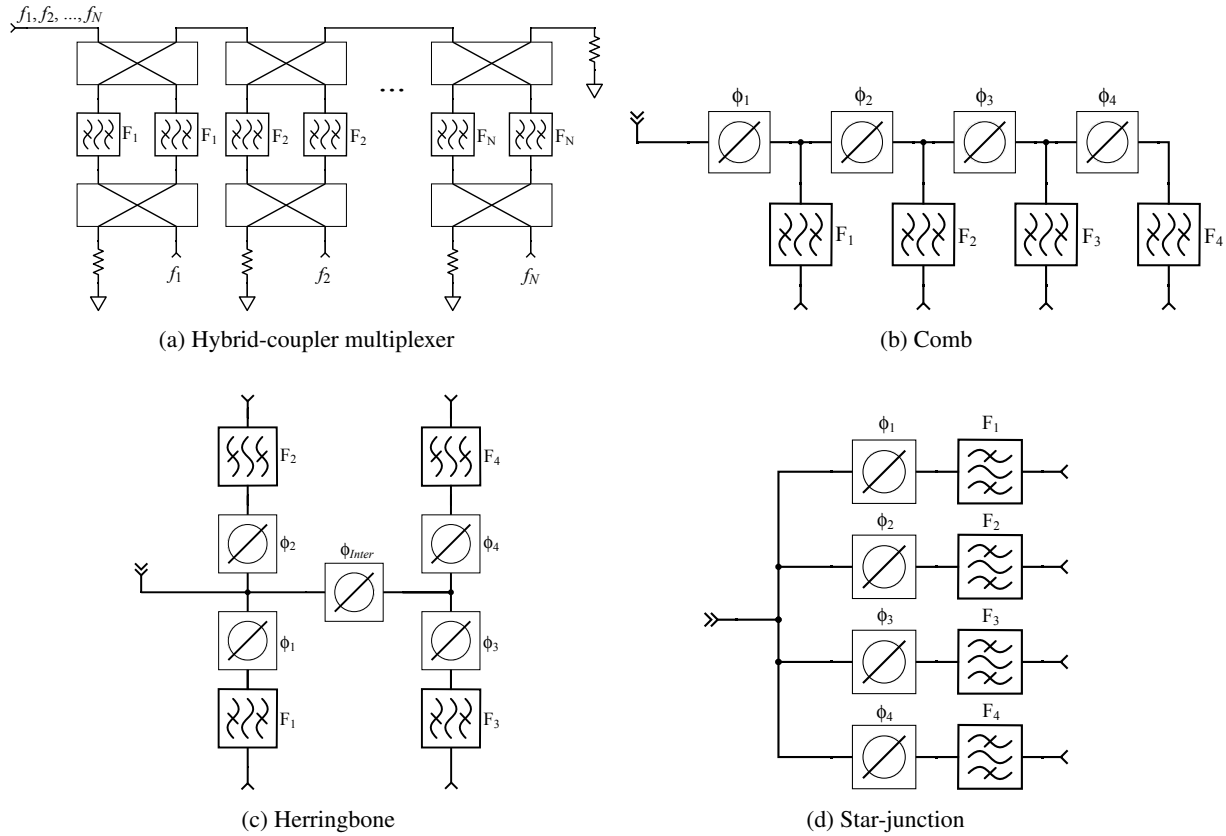

(a) Hybrid-coupler multiplexer

(b) Comb

(c) Herringbone

(d) Star-junction

Figure 4.1: Schematic of hybrid-coupler multiplexer and manifold-coupled multiplexers with comb, herringbone and star-junction configuration

more compact design and size reduction, which is very appropriate for end-user devices. The general scheme of a star-junction multiplexer is shown in Fig. 4.1d, where four filters are directly connected to the common port.

The synthesis of multiplexers is, in general, a complex and time-consuming process. Optimization tools have been addressed since the early 80s. The main drawback is the direct dependency of the starting point to achieve a good result. Singly terminated filters have been considered for many years the best seed for designing multiplexers that operate in a contiguous channel configuration because of the natural mutually cancellation of the imaginary part of the input admittance, providing a conjugate match for each other [81, 84, 95]. An optimization process or the addition of dummy channels are needed in this case to achieve an equiripple common port return loss (CPRL).

To reduce the computational effort, synthesis techniques have been developed during the last years. In [96], a method based on the definition of a coupling matrix with non-resonant nodes at the input/output ports allowing the generation of only one transmission zero for each filter in multiport networks is proposed. In [97, 98], the authors have presented a novel method for the polynomial synthesis of microwave star-junction multiplexers with a resonating junction. The channel filters can be arbitrarily specified, including the assignment of transmission zeros. The main drawback of the proposed synthesis technique is

the round-off errors arising in fixed-length numerical computations, whose effect becomes more relevant with the growth of channel filters and each filter's order. The approach in [99] is also an attractive solution where the filters are synthesized considering a complex frequency-invariant load, closer to the real scenario. Although it is proven for a duplexer, as the number of channels is increased, the process becomes very challenging. Beside the drawbacks mentioned for each reference, these works do not contemplate fully canonical networks. Therefore, for AW multiplexers, a different approach should be considered.

In [93], the general synthesis procedure for star-junction multiplexer combining singly and doubly-terminated filters was first introduced. As discussed in [93], the doubly-terminated networks may present an input admittance in which the imaginary part tends to be null in the out-of-band region as happens with singly-terminated networks under specific conditions related to the phase of the input reflection coefficient. That is why it is more convenient to focus the discussion on the MSN concept. It is proven that the proper combination of such networks highly reduces the loading effects of one filter on the others. In this section, a general analysis of MSN networks is carried out, which allows facing the design of fixed frequency plan multiplexers and flexible frequency plan multiplexers where the different channels can be connected or disconnected on demand.

4.2 Minimum Susceptance Network Definition

A general filter network is characterized by its system transfer function, expressed as the ratio of the response or output variable to the excitation or input variable. A special type of transfer function in which the input and output variables are voltages or currents measured between the same pair of terminals in an electrical network is known as a driving-point function [80]. Therefore, an input admittance/impedance function is a driving-point function that can be expressed as a quotient of two polynomials:

$$Y_{in}(s) = \frac{a_0 + a_1 s + a_2 s^2 + ... + a_n s^n}{b_0 + b_1 s + b_2 s^2 + ... + b_m s^m} \tag{4.1}$$

where $m - n = \pm 1$ or 0. The s variable represents the complex frequency and it is equal to $\sigma + j\Omega$. Eq. (4.1) can also be written in terms of their poles and zeros as

$$Y_{in}(s) = \frac{a_n}{b_m} \frac{\prod_{i=1}^{n} (s - z_i)}{\prod_{i=1}^{m} (s - p_i)} \tag{4.2}$$

An admittance function is defined as minimum susceptance network (MSN) if none of the poles p_i are pure imaginary and for which $n \leq m$ [81]. Accordingly, the input admittance of an MSN is finite for all real frequencies Ω, including infinity. A filter having minimum susceptance input admittance acquire an attractive attribute where the real part of its input admittance has the same frequency dependence as its transmission attenuation response [81].

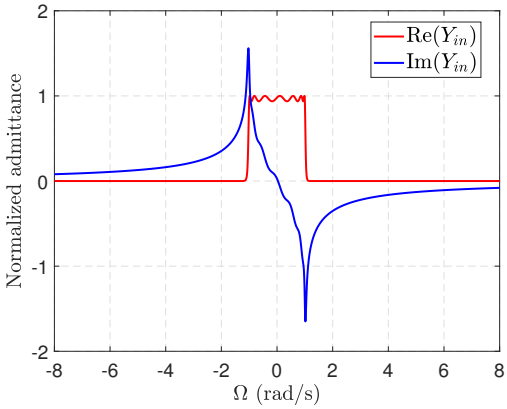

Figure 4.2: Real and imaginary part of a singly filter input admittance.

In [80], real and imaginary part of minimum susceptance networks have been related as follows:

$$\int_0^\infty [G(\Omega) - G(\infty)]^2 d\Omega = \int_0^\infty [B(\Omega)]^2 d\Omega \tag{4.3}$$

where $G(\Omega)$ and $B(\Omega)$ are the real and imaginary part of the input admittance of a minimum susceptance network.

If $G(\Omega)$ is constant for all frequencies, then LHS's integral is identically zero. Since the RHS of (4.3) is the integral of a quantity squared, it can be concluded that $B(\Omega)$ would also be zero. In the case of MSNs, $G(\Omega)$ is constant over a band of frequencies (referred to as the passband) and zero in the out-of-band region. The imaginary part $B(\Omega)$ is characterized by a positive slope in the out-of-band region and negative slope in the passband as depicted in Fig. 4.2.

It is important to point out that if two or more MSNs are connected in parallel, the resulting network is also an MSN. Similarly, if two or more minimum reactance networks (MRN) are connected in series, the resulting network is also minimum reactance. This characteristic is widely discussed and implemented in [81] and recently exploited in [100] applying the partially complementary condition design in multiplexers.

The literature only has accounted for singly filters as MSN, and no consideration about the input phase of the reflection coefficient has been discussed. However, as it will be developed through this chapter, in case the input phase of the reflection coefficient is ϕ_{add_11}= 0°, the condition to be classified as an MSN is accomplished in both singly and doubly terminated filter networks. Moreover, in doubly networks, generalized Chebyshev filtering functions can still be accommodated while still fulfilling the MSN criteria [93].

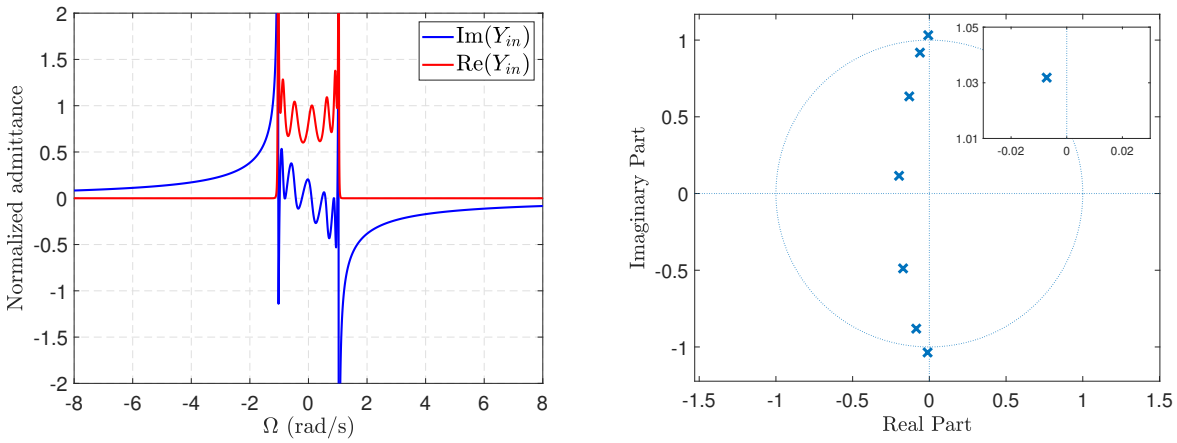

(a) (b)

Figure 4.3: (a) Real and imaginary part of a doubly terminated filter input admittance. (b) Location of input admittance poles.

4.2.1 Doubly Terminated Filter as MSN

For stand-alone doubly terminated filters (DTF), the reflection coefficient is defined through the characteristic polynomials as follows:

$$S_{11}(s) = e^{j\phi_{add\_11}} \frac{F(s)/\epsilon_r}{E(s)} \tag{4.4}$$

where ϕ_{add_11} is a real quantity and can be understood as a phase offset. In order to drive the discussion, a fully canonical seventh-order DTF with $RL = 12$ dB and normalized transmission zeros Ω_{TZ} = {1.77 -1.70 1.65 -1.60 1.76 -1.75 1.70} with $\phi_{add\_11} = 0°$ is considered. Fig. 4.3a and 4.3b illustrate the shape of the real and imaginary part of the input admittance and the locus of its poles, respectively. $G(\Omega)$ is close to the normalized admittance 1 S over the filter passband, dropping to zero in the out-of-band region. $B(\Omega)$ crosses to 0 in the center frequency of the passband, dropping to near zero in the out-of-band region.

Despite the rippled shape of the real and imaginary part characteristic of the Chebyshev filtering function, the DTF with $\phi_{add\_11} = 0°$ fulfills the mathematical definition of MSN. However, the observed input admittance behaviour of a network synthesized with $\phi_{add\_11} \neq 0°$ is different. For sake of clarity, three different cases are analyzed with $\phi_{add\_11} = -100°, 0°$ and $75°$. The real and imaginary parts of the input admittance for each case are found in Fig. 4.4a.

As stated in the MSN definition, the input admittance must be finite for all real frequencies Ω. When $\phi_{add\_11} \neq 0°$, an asymptotic behavior is observed for the real part, then the MSN condition is not fulfilled. On the other hand, as the phase moves away from 0°, there will be a crossing through 0 S at closer frequencies to the passband. For positive values of ϕ_{add_11}, the imaginary part of the admittance crosses

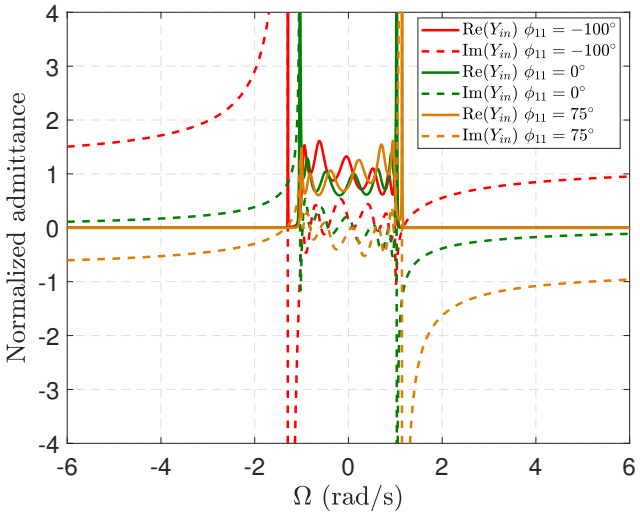

(a)

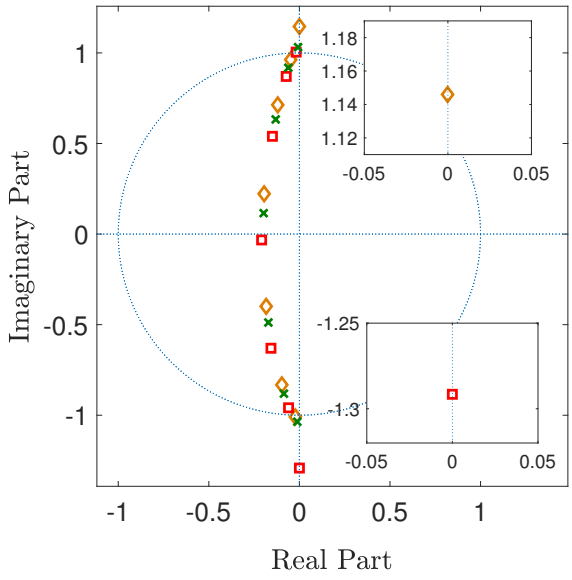

(b)

Figure 4.4: (a) Real and imaginary part of double terminated filter input admittance.(b) Position in the s-plane of the poles of DTF's input admittance considering ϕ_{add_11}=-100°, 0° and 75° (red-square, green-cross and yellow-diamond respectively)

through 0 S at $\Omega < -1$, while, for negative values, this happens at $\Omega > 1$. In both cases, the imaginary part does not tend to 0 S as the frequency goes to infinity, which is one of the MSN conditions.

In relation with the poles allocation, Fig. 4.4b shows them in the s-plane for ϕ_{add_11} = -100°, 0° and 75°. Table 4.1 includes the real part value of closer poles to the imaginary axis (p_1) for evaluation purposes. The more the absolute value of ϕ_{add_11} moves away from 0°, the lower the real part of the pole p_1, approaching to a pure imaginary value. In this case, as seen in (4.2), the magnitude of the admittance

Table 4.1: Real part of pole closer to imaginary axis (p_1) for doubly terminated filter.

ϕ_{add_11}	Real (p_1)
0°	-0.0072
75°	-1.66*10^{-4}
-100°	-1.72*10^{-5}

will grow to infinity. Although this behaviour does not satisfy the MSN definition, this kind of response is still interesting to cancel out the imaginary part of Y_{in} on the design of multiplexers with a fixed frequency plan, as it will be seen later in Section 4.6.

4.2.2 Singly Terminated Filters as non-MSN

Singly terminated filters (STF) have been traditionally considered as MSN; however, it can be proved that the definition is fulfilled only for a distinct phase value, $\phi_{add\_11} = 0°$, as it is the case of DTF. Nevertheless, how to change the input phase for an STF when the conventional return loss definition (4.4) is meaningless since source impedance is 0 Ω or infinity. To tackle this limitation, it is proposed an exact method to describe the transmission and reflection response considering the network, such as doubly terminated filter following the hereafter procedure.

The construction of the transfer matrix polynomials $[ABCD]_S$ for an STF is only based on the characteristic polynomials $E(s)$ and $P(s)$, obtained from the classical synthesis of generalized Chebyshev filtering function. Therefore, unlike DTF, the direct phase control employing the polynomial $F(s)$ is not possible.

To overcome this situation, a novel procedure with closed formulae has been developed in [93] to calculate the transfer matrix polynomials for a singly terminated network but being considered like a doubly terminated network, which allows having control on the input phase again. This new $[ABCD]$ matrix will be $[ABCD]_{SD}$. With the combination of the synthesis of the singly polynomials $[ABCD]_S$, and the transfer matrix polynomials definition for a two-port network operating between unity source and load $[ABCD]_D$, a new set of characteristics polynomials $P_s(s)$, $F_s(s)$ and $E_s(s)$ describing singly behaviour response in the low-pass domain is obtained. These polynomials are used to calculate $[ABCD]_{SD}$.

The proposed method begins, as usual, with a set of normalized transmission zeros, return loss level RL and filter degree N. The detailed step-by-step procedure is given as follows:

1. Calculate $P(s)$, $E(s)$, $F(s)$ polynomials and the normalization constant ϵ and ϵ_r using the efficient well-known recursive technique.

2. Calculate $[ABCD]_S$ polynomials. $A(s)$ and $B(s)$ are easily found from the coefficients of the known $E(s)$. $C(s)$ and $D(s)$ polynomials are found by means of the property of network reciprocity [95].

3. With $[ABCD]_S$ known, and assuming a two-port network, the new characteristic singly polynomials are obtained as follows:

$$P_s(s) = P(s) \tag{4.5}$$

$$F_s(s) = \epsilon_r(A(s) + B(s) - C(s) - D(s))/2 \tag{4.6}$$

$$E_s(s) = (A(s) + B(s) + C(s) + D(s))/2 \tag{4.7}$$

4. The normalization constant ϵ_s and ϵ_{rs} must be calculated according to

$$\epsilon_s = \frac{1}{\sqrt{1 - 10^{\frac{-RL_s}{10}}}} \left| \frac{P_s(\omega)}{E_s(\omega)} \right|_{\omega=\pm 1} \tag{4.8}$$

$$RL_s = 10 \log \frac{1 - \left(\left| \frac{P_s(\omega)}{F_s(\omega)} \right|_{\omega=\pm 1} \right)^2}{1 - \left(\left| \frac{P_s(\omega)}{E_s(\omega)} \right|_{\omega=\pm 1} \right)^2} \tag{4.9}$$

$$\epsilon_{rs} = \frac{\epsilon_s}{\sqrt{\epsilon_s^2 - 1}} \tag{4.10}$$

where $P_s(\omega)$, $F_s(\omega)$ and $E_s(\omega)$ are figured out from $P_s(s)$, $F_s(s)$, and $E_s(s)$ respectively.

5. According to the calculated normalization constants, the characteristics polynomials $P_s(s)$ and $F_s(s)$ must be reassessed as

$$P_s(s) = P_s(s)\epsilon_s/\epsilon \tag{4.11a}$$

$$F_s(s) = F_s(s)\epsilon_{rs}/\epsilon_r. \tag{4.11b}$$

6. With the characteristic polynomials and normalization constants, the new $[ABCD]_{SD}$ polynomials and the input admittance function are obtained using the conventional procedure for DTF.

   Finally, the input admittance function is defined as

$$Y_{in}(s) = \frac{C_{SD}(s) + D_{SD}(s)}{A_{SD}(s) + B_{SD}(s)}. \tag{4.12}$$

To validate the proposed methodology, the $[ABCD]_S$ matrix of a STF has been obtained using the classical definition, and, $[ABCD]_{SD}$ using the proposed methodology. For a seventh-order filter with RL = 15 dB, and normalized transmission zeros Ω_{TZ}={1.70 -1.66 1.54 -1.54 1.54 -1.66 1.70}, the obtained admittance coefficients calculated with (4.12) are found in Table 4.2. As it is expected, these values perfectly agrees with those obtained from $[ABCD]_{SD}$ when $\phi_{add\_11} = 0°$ as it can be seen in the filter response comparison shown in Fig. 4.5.

With this indirect approach, the input phase's role concerning the MSN behavior for STF can be analyzed as done for DTF case. Fig. 4.6a shows the real and imaginary parts of Y_{in} considering ϕ_{add_11}= -100°, 0° and 75°. Following the same analysis previously made for DTFs, we conclude that the MSN

Table 4.2: Original and proposed input admittance coefficients.

Degree	Denominator Coefficients	Numerator Coefficients
7	0.0001 + j0.000	1.000 + j0.000
6	0.652 - j0.001	1.562 - j0.350
5	1.019 - j0.233	3.120 - j0.552
4	1.796 - j0.368	3.061 - j1.024
3	1.626 - j0.592	2.790 - j0.961
2	1.233 - j0.508	1.605 - j0.783
1	0.564 - j0.318	0.684 - j0.383
0	0.149 - j0.119	0.149 - j0.122

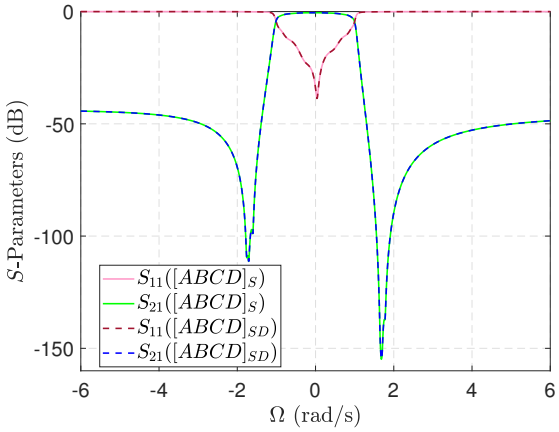

Figure 4.5: S-parameters response comparison between $[ABCD]_{SD}$ and $[ABCD]_S$ when ϕ_{add_11}= 0°.

behaviour is not satisfied with singly filters when $\phi_{add\_11} \neq 0°$ because the input admittance is not finite for all real frequencies. Table 4.3 shows the real part of closer pole to the imaginary axis p_1 of Y_{in} for the different phase values. On the other hand, the non-flat slope of the real part of the admittance as the phase moves away from 0° is evident. This is due to the fact that STF is more sensitive to phase modifications than DTF [101, 102].

Table 4.3: Real part of pole closer to imaginary axis for singly terminated filter

ϕ_{add_11}	Real (p_1)
0º	-0.03697
75º	-0.0069
-100º	-0.00087

4.2.3 Singly and Doubly Terminated Filters Comparison

The control of the input phase for STF allows the definition of a common framework in which both STF and DTF networks can be compared when the generalized Chebyshev function used to synthesize the

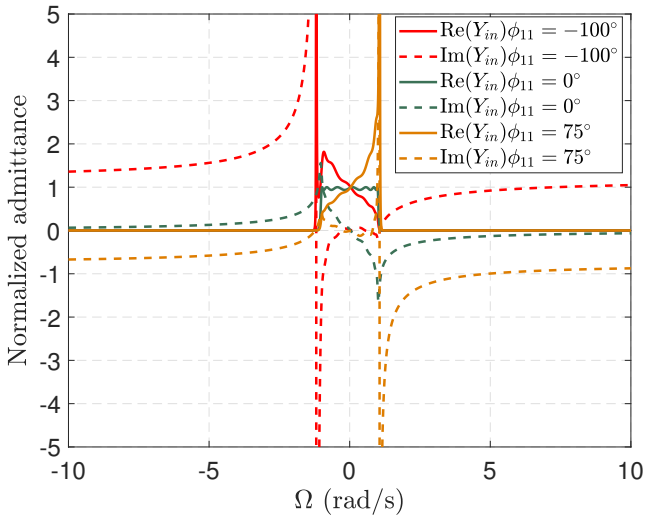

(a)

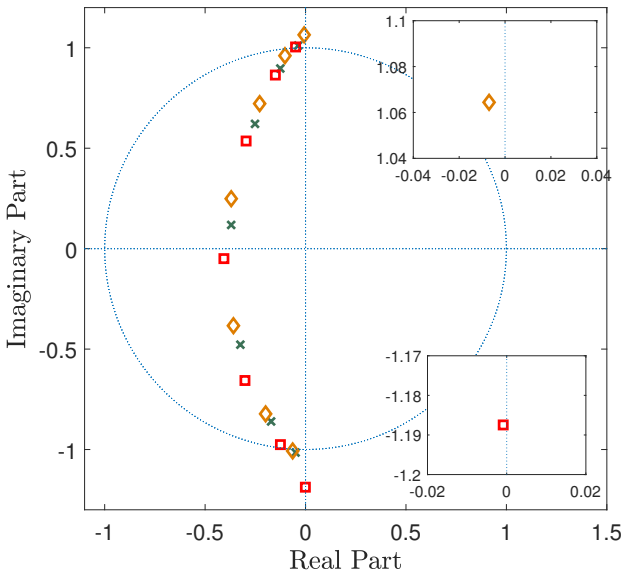

(b)

Figure 4.6: (a) Real and imaginary part of a singly filter input admittance. (b) Position in the s-plane of the poles of a singly filter input admittance considering -100°, 0° and 75°.

network is the same. Some conclusions are obtained from this comparison:

1. The absolute value of the pole's real part closer to the imaginary axis p_1 for STF is greater than for DTF. If the distance measured to the imaginary axis is a metric for the level of MSN fulfillment, an STF fulfills MSN conditions better than DTF.

2. As a consequence of the poles distribution in the complex plane, the in-band slope of the imaginary part of Y_{in} of STF exhibits a monotonically decreasing slope in contrast to DTF that shows a

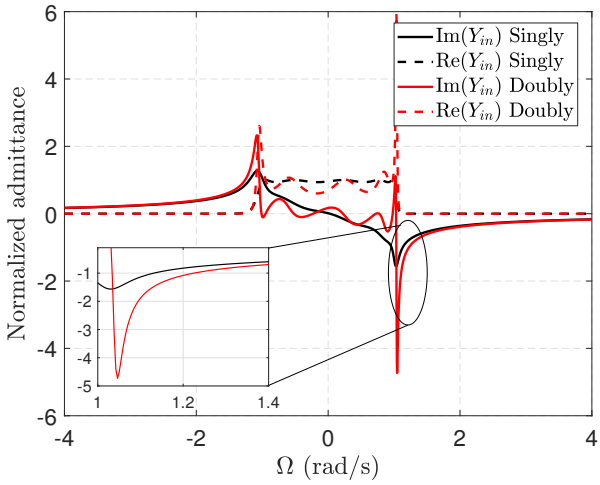

Figure 4.7: Comparison between the real and imaginary parts of doubly and singly filters input admittance synthesized with the same input characteristics.

rippled variation.

3. The slope change of the imaginary part of the admittance in the transition from the in-band to the out-of-band region is smoother in the STF but the 0 S value approach is faster, as seen in Fig. 4.7 due to the smaller $B(\Omega)$ value at the transition frequency .

4. The in-band ripple in DTF is higher than in STF, and the roll-off near the cut-off frequencies is slower than STF. In DTF, the reflection zeros are distributed in the in-band region, while, for STF, the reflection zeros are allocated close to the band's center.

5. For fully canonical filters, the out-of-band rejection in STF is worse than DTF due to evaluating the asymptotic behaviour at infinity. The constant ϵ_s value calculated in (4.8) is lower than the original ϵ; therefore, isolation at infinity will be lower. A direct relationship between transmission parameter at $s = \pm j\infty$ and ϵ for the fully canonical case demonstrates this claim

$$S_{21}(\pm j\infty)[dB] = 20 * \log_{10} \epsilon \tag{4.13}$$

4.3 Characterization and Enhancement of an MSN

The location of the poles and zeros of a transfer function provides qualitative insights into the response characteristics of a system [103]. It is possible to determine the frequency characteristics of a two-terminal network knowing the pole-zero location on a complex s-plane. By a pole-zero expansion of (4.2), the numerator and denominator are factorized as

$$Y_{in}(s) = K\frac{(s-z_1)(s-z_2)...(s-z_n)}{(s-p_1)(s-p_2)...(s-p_m)} \tag{4.14}$$

where $K = a_n/b_m$ is a constant (scale factor). Each of the poles/zeros may be written in terms of the real and imaginary part, i.e. $p_i = \sigma_i + j\Omega_i$, being $s = j\Omega$.

MSN definition is driven by the position of the poles in the complex plane and the behaviour of the imaginary part of the input admittance, more specifically, the pole closest to the imaginary axis, namely p_1. The slope value and the slope-sign change variation are very significant to minimize loading effects between filters in a contiguous multiplexer scheme. Therefore, the control of the allocation of the poles of Y_{in} is crucial to obtain the expected MSN or non-MSN performance. The analysis is carried out considering how the real and imaginary parts of p_1 affect the admittance behavior. More specifically, the objective is to set the conditions leading the $B(\Omega)$ to approach faster to 0 S.

4.3.1 Out-of-Band Admittance Evanescence Enhancement: The Real Part of the Pole

To evaluate the role of the real part of p_1, let's consider two filters A and B with same input admittance poles and zeros except the real part of p_1, being p_1 the closest to the imaginary axis. Defining the pole as $p_1 = \sigma_1 + j\Omega_1$ and evaluating (4.14) at the frequency Ω_1 ($|\Omega_1| > 1$), the value of Y_{in} is reduced to

$$Y_{in}(j\Omega_1) = \frac{\sigma_p + j\Omega_p}{-\sigma_1} \tag{4.15}$$

where $\sigma_p + j\Omega_p$ is a complex number resulting from the evaluation. Considering Ω_1 the real frequency and $|\sigma_{1A}| < |\sigma_{1B}|$.

$$\Im\{Y_{inA}(j\Omega_1)\} = \frac{\Omega_p}{-\sigma_{1A}} \tag{4.16a}$$

$$\Im\{Y_{inB}(j\Omega_1)\} = \frac{\Omega_p}{-\sigma_{1B}} \tag{4.16b}$$

$$\Im\{Y_{inA}(j\Omega_1)\} \begin{cases} < \Im\{Y_{inB}(j\Omega_1)\} & \text{if } \Omega_1 > \quad 1 (\Omega_p < 0), \\ > \Im\{Y_{inB}(j\Omega_1)\} & \text{if } \Omega_1 < -1 (\Omega_p > 0) \end{cases} \tag{4.16c}$$

Since $\Im\{Y_{in}(j\Omega_1)\}$ depends inversely of the value of the real part, and the poles of the input admittance function filters have always a negative real value, the increase of σ_1 magnitude produces a decrease in the imaginary input admittance absolute value. Fig. 4.8a shows the evolution of the imaginary part of the input admittance in the stop-band when $\Omega_1 > 1$ ($\Omega_p < 0$) in agreement with (4.16c).

Indeed, in a contiguous channel design, filter B will produce a lower loading effect than filter A. It is worth noting that the slope value is driven by the real part of the input admittance closest pole (σ_1), but when $\Omega_1 >> 1$, the susceptance is equal for both filters A and B regardless of σ_1 value.

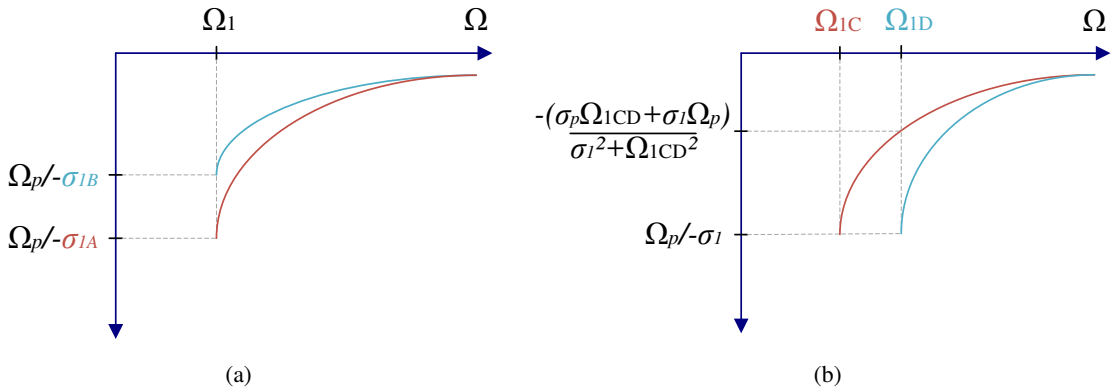

Figure 4.8: (a) Imaginary part of the input admittance evaluated at Ω_1 with $\sigma_{1A} \neq \sigma_{1B}$. ; (b) Imaginary part of the input admittance evaluated at Ω_{1C} and Ω_{1D} with equal σ_1.

4.3.2 Out-of-Band Admittance Evanescence Enhancement: The Imaginary Part of the Pole

In relation with the role of the imaginary part of the pole p_1, as done before, let's consider two different filters C and D with same admittance poles and zeros except the imaginary part of p_1. Both filters are evaluated at the respective real frequency where the transition is given: Ω_{1C} and Ω_{1D} respectively. $|\Omega_{1C}| < |\Omega_{1D}|$ ($|\Omega_{1C}|$ and $|\Omega_{1D}| >1$).

The outcome is analyzed in (4.17), where Ω_{1CD} is the result of multiplying Ω_{1C} by Ω_{1D}.

$$Y_{inC}(j\Omega_{1D}) = \frac{\sigma_p + j\Omega_p}{-\sigma_1 + j\Omega_{1CD}} \tag{4.17a}$$

$$Y_{inC}(j\Omega_{1C}) = Y_{inD}(j\Omega_{1D}) = \frac{\sigma_p + j\Omega_p}{-\sigma_1} \tag{4.17b}$$

$$\Im\{Y_{inC}(j\Omega_{1D})\} = \frac{-(\sigma_p\Omega_{1CD} + \sigma_1\Omega_p)}{{\sigma_1}^2 + {\Omega_{1CD}}^2} \tag{4.17c}$$

$$\Im\{Y_{inC}(j\Omega_{1C})\} = \Im\{Y_{inD}(j\Omega_{1D})\} = \frac{\Omega_p}{-\sigma_1} \tag{4.17d}$$

$$\Im\{Y_{inD}(j\Omega_{1D})\} \begin{cases} < \Im\{Y_{inC}(j\Omega_{1D})\} & \text{if } \Omega_{1D} > \Omega_{1C} \\ & (\Omega_{1C}, \Omega_{1D} > 1), \\ > \Im\{Y_{inC}(j\Omega_{1D})\} & \text{if } \Omega_{1D} < \Omega_{1C} \\ & (\Omega_{1C}, \Omega_{1D} < -1) \end{cases} \tag{4.17e}$$

The imaginary part of pole p_1 defines the frequency in which the slope of $B(\Omega)$ changes the sign, that is, the transition between passband and out-of-band region. Fig. 4.8b illustrates the above example when Ω_{1C}, Ω_{1D} >1 ($\Omega_p < 0$). It is shown that a lower absolute value of $|\Omega_1|$ leads to a lower absolute value of $\Im\{Y_{in}\}$ around $\Omega = 1$, decreasing its impact on adjacent channels.

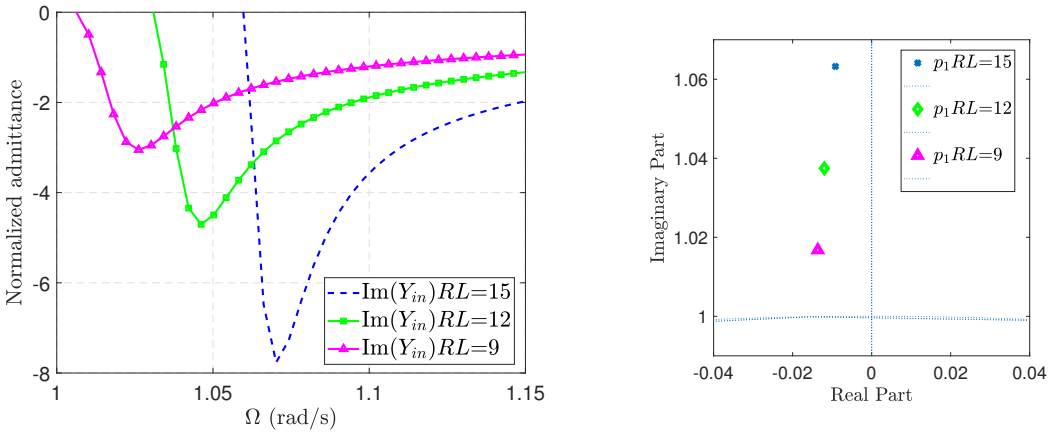

(a) (b)

Figure 4.9: (a) Imaginary part of the out of band input admittance calculated for different RL values. (b) Locus of p_1 poles for different RL values.

Table 4.4: Poles closer to the imaginary axis.

RL(dB)	p_1
15	$-0.0092 + j1.063$
12	$-0.0110 + j1.037$
9	$-0.0151 + j1.012$

In order to obtain an MSN with reduced influence of its $\Im\{Y_{in}\}$ in contiguous filters, the closest pole to the imaginary axis should have the absolute value of the real part as larger as possible and the imaginary part tending to 1.

4.3.3 Relation Between RL and the Imaginary Part of the Input Admittance

The return loss plays an important role in reducing the slope of $B(\Omega)$. Because RL is an input specification in the polynomial synthesis, the input admittance is involved, that is, its zeros and poles. To illustrate the influence of RL, Fig. 4.9a and Fig. 4.9b show the out-of-band slope of $B(\Omega)$ and the position of p_1 poles for different RL values: 9, 12 and 15 dB respectively. For all three cases, a DTF with equal transmission zeros and filter order is considered. The value of p_1 is given in Table 4.4 for each case.

As the RL decreases to lower values, p_1 get closer to the ideal position discussed before, that is being pure imaginary, leading to $B(\Omega)$ approach faster to 0 S. In this case, there is a trade-off since this is a desirable situation to minimize loading effects, but at the cost of degrading the RL. When $\Omega_1 >> 1$, the influence of RL is very similar regardless of its value.

4.4 Design of Star-Junction Multiplexer Combining MSN and non-MSN

The multiplexer design entails minimizing loading effects on multiple filters caused by the out-of-band admittance of all other filters to ensure proper matching conditions at the antenna port and well-shaped transmission response. Nevertheless, it also entails the optimization of a multitude of cross-isolation requirements. As a consequence, starting from an appropriate seed makes it more affordable such a complicated task.

The star-junction multiplexer simplest case is a duplexer, where only two filters are involved. To avoid loading effects, the phase of the input reflection coefficient is controlled by synthesis, achieving excellent results [104]. However, designing multiplexers will simultaneously require the proper combination of the imaginary part of the input admittance of all active filters at the center frequency of each f_{c_m}. This requirement for an N filters multiplexer implies that

$$\sum_{i=1}^{N} \mathrm{Im}(Y_{in_i}(f_{c_m})) = 0, \quad m = 1:N; m \neq i \tag{4.18a}$$

or

$$Im(Y_{in_i}(f_{c_m})) = 0, \quad m = 1:N; m \neq i \tag{4.18b}$$

The first approach to minimize loading effects is to consider that each band's aggregated input admittance is canceled at f_{c_m} (4.18a). This requires the presence of all the channel filters connected at the same time so that the effect of channel interactions can be accounted for during the design process. Although the complexity of this approach grows with the number of channels, becoming a cumbersome process, the main drawback is that this solution is not suitable for a flexible frequency plan, neither for reusing partially previous designs. Therefore, (4.18a), it is only suitable for a fixed spectrum band plan scenario.

The second approach (4.18b) considers that all filters must present $B(\Omega)$ being 0 S not only at one f_{c_m} but in the wider out-of-band region. A similar behavior is observed in MSNs as shown in Fig. 4.2. Although $B(\Omega)$ is not strictly 0 S, especially at frequencies close to f_0, it must be close enough to minimize loading effects properly. Unlike the previous approach, using this one, a flexible frequency plan multiplexer where the operative bands can be selected on demand is viable, as it will be seen in Section 4.6.2.

4.4.1 General Synthesis Method

A general synthesis method for designing star-junction multiplexers valid for both contiguous and non-contiguous bands is addressed in this section. Numerical examples illustrating different scenarios will be provided in next sections. The admittance behavior analysis depending on the input phase ϕ_{add_11} allows

to define a general strategy combining MSN and non-MSN networks (DTF or STF) depending on the number of channels and the gap between them.

When the multiplexer frequency plan is fixed a priori, and the channel spacing is close enough to consider them contiguous, the suggested approach consists of combining MSN and non-MSN filters to comply with (4.18a). The proposed star-junction multiplexer will be configured with N filters: inner filters (2:(N-1)) will be designed as MSN and outer filters (1 and N) as non-MSN. The input phase of the first and last filters (outer) will be calculated to operate as an open-circuit for the contiguous bands 2 and N-1, respectively. At the same time, the inner channels will present a natural admittance cancellation. In non-contiguous channels, both the previous approach or considering all MSN filters can be adopted as a convenience.

It must be noticed that, outer non-MSN filters (either DTF or STF) will require $\phi_{add\_11} \neq 0°$. Although the phase accommodation will not depend on the filter class, DTF's intrinsic behavior encourages its choice. The reason behind this is that the DTF reflection response describes an equiripple shape in the passband with a sharp roll-off near the cut-off frequency while STF holds a funnel-shape in the passband as it is observed in Fig. 4.5. Considering the comparison performed in section 4.2.3, it is straightforward to notice that using STF non-MSN in outer positions will cause a non-equiripple CPRL in the multiplexer because of the monotonically decreasing slope of the susceptance. Then, STF is more difficult to compensate in that position with only a phase variation.

Furthermore, it has been observed that STF return loss is more responsive to variations of the input phase than DTF [101]. This behaviour is especially exploited in contiguous bands multiplexers when all filters are designed as MSN class singly, and an optimization process is carried out. The optimization process corrects then the response of the outers channels achieving an equiripple CPRL as shown in [105].

When the multiplexer frequency plan is flexible, the suggested approach consists of combining MSNs in all positions, fulfilling (4.18b). Nevertheless, this first vision is also dependent on the space between channels and their bandwidths. Shifting input phase would be necessary according to the frequency plan. Section 4.6.2 displays two examples, including an experimental validation.

4.5 Scattering Matrix Solution for Multiplexer Representation

Multiplexer design is a challenging task due to the high number of variables involved, raising the difficulty as the number of filters increase. Fortunately, numerical computing tools provide a suitable environment to evaluate topologies and technologies before starting the long journey to the device. In this section, a scattering matrix formulation for a star-junction depending on the number of junction ports P, which allows evaluating multiport response in a numerical environment like MATLAB, is presented. The outcome is integrated with the S-parameter matrix of the filters attained through the general synthesis

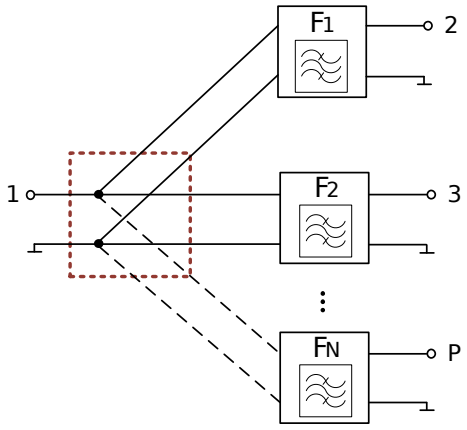

Figure 4.10: General topology of an ideal star-junction P ports multiplexer.

methodology presented in Chapter 3 to obtain the final matrix response of the multiplexer. This approach allows the acquisition of main multiplexer parameters like transmission, reflection, and cross-isolation response in a compact way, achieving a good starting point for further full-wave optimization. A triplexer under the previous section's approach is presented and evaluated using lumped elements. This section is based on the work presented in [106].

A general star-junction multiplexer is composed of N bandpass filters connected to a common node, usually an antenna through an N+1 port junction. It results in a P (P=N+1) ports network, as it is shown in Fig. 4.10. First in this section, a numerical nodal junction approach is developed, addressing the ideal junction matrix. The achieved results allow the acquisition of input/output multiport responses and the evaluation of technological constraints without needing external verification tools. Later, an evaluation and discussion of an implemented lumped elements triplexer are shown. The excellent agreement between the simulated matrix approach and transmission, reflection, and cross-isolation triplexer responses is illustrated.

4.5.1 Multiplexer Scattering Matrix Definition

The multiplexer S-parameters are calculated considering the scattering matrices of the individually designed filters (S^{F_n}) and the junction (S^M) represented in Fig. 4.11. The scattering matrix of the overall multiplexer [S^P] can be written as follows

$$S^P = S^{PP} + S^{PC}[L - S^{CC}]^{-1}S^{CP} \tag{4.19}$$

where the matrices S^{PP}, S^{PC}, S^{CC}, and S^{CP} represent the relation between external and internal network ports P and C respectively, and L is the connection matrix that relates the internal ports C. All these matrices are appropriately defined in [84] and linked to S^{F_n} and S^M. The external ports P define the scattering matrix of the multiplexer network.

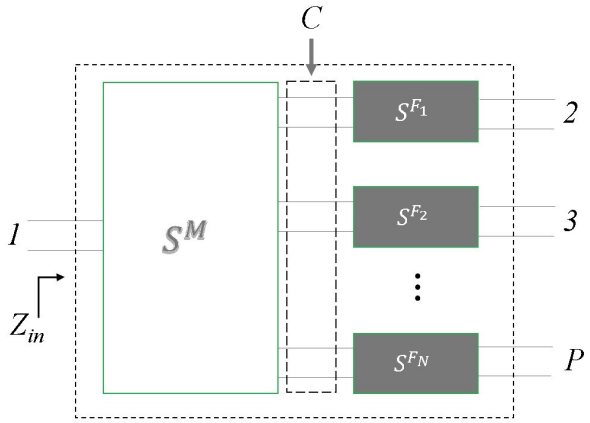

Figure 4.11: N channel multiplexer.

Ideal Star-Junction Matrix Implementation

According to the selected topology, Fig. 4.10 illustrates in dashed line, an ideal star-junction. This nodal idealization is useful for representing the node where incident power in port 1 is distributed to all filters. This network is reciprocal and ideally lossless, taking into account its geometry. Considering a star-junction of P ports, the circuit theory provides a direct scattering matrix solution. This solution is the first basic model to evaluate the ideal junction behavior of multiplexers with zero electrical length from the filters to the junction. It would be straightforward to introduce the electrical delay in the filter side or through a reference plane shift over the junction matrix elements.

To analyze the junction behaviour, port 1 and internal ports C from Fig.4.11 are loading with a reference impedance Z_{0i}, considering $Z_{01} = Z_{02} = ...Z_P = Z_0$. The input impedance can be calculated as

$$Z_{in} = Z_{01}||Z_{02}||...||Z_P = \frac{Z_0}{P-1} \tag{4.20}$$

resulting in a network that is not matched at any port since $Z_{in} \neq Z_0$. The reflection coefficient at each port S_{ii} is calculated substituting (4.20) in (4.21). S_{ii} is obtained as

$$S_{ii} = \frac{Z_{in} - Z_0}{Z_{in} + Z_0} = \frac{2-P}{P}. \tag{4.21}$$

For a lossless and passive device, its scattering matrix is unitary and

$$\sum_{m=1}^{P} |S_{m1}|^2 = |S_{11}|^2 + |S_{21}|^2 + \ldots + |S_{P1}|^2 = 1. \tag{4.22}$$

Considering the network symmetry, $S_{ij} = S_{ji}; i \neq j$ so,

Table 4.5: Triplexer design specifications

	F1	F2	F3
f_0 (MHz)	203	278	347
BW (MHz)	40		
RL (dB)	12		
Ω_z (rad/s)	{3, -2.5, 1.7, -2.56, 2}		
ϕ_{add_11}(º)	2.05	0	13.08

$$|S_{ii}|^2 + (P-1)\,|S_{ij}|^2 = 1 \tag{4.23}$$

Substituting (4.21) in (4.23), S_{ij} can be expressed as

$$|S_{ij}| = \frac{2}{P} \tag{4.24}$$

Finally, since no electrical delay is considered due to the ideal nodal approach, no phase contribution is comprised. Then, the representing matrix of the P ports star-junction is defined as follows:

$$S^M_{[\mathrm{PxP}]} = \begin{bmatrix} \frac{2-P}{P} & \frac{2}{P} & \cdots & \frac{2}{P} \\ \frac{2}{P} & \frac{2-P}{P} & \cdots & \frac{2}{P} \\ \vdots & \vdots & \ddots & \vdots \\ \frac{2}{P} & \frac{2}{P} & \cdots & \frac{2-P}{P} \end{bmatrix} \tag{4.25}$$

Once the junction matrix is obtained, each filter's scattering matrix S^{F_n} is computed. For a defined set of TZs, RL and filter degree, the scattering matrices of the filters individually designed S^{F_n} are obtained following the previous chapter synthesis methodology.

4.5.2 Triplexer Example

For a non-contiguous bands example, a triplexer compound of fully canonical 5th-order filters was designed. The inner filter was designed as an MSN doubly terminated filter as proposed in 4.4.1 for a non-contiguos fixed scenario. The outer filters were calculated as non-MSN doubly terminated, with the proper input phase adjustment following (4.26). The synthesis input parameters are shown in Table 4.5.

$$\begin{aligned} e^{j\phi_{add\_11,1}} &= \varepsilon_{r1} E_1(s)/\ F_1(s)|_{s=j\Omega_{C2}} \\ e^{j\phi_{add\_11,3}} &= \varepsilon_{r3} E_3(s)/\ F_3(s)|_{s=j\Omega_{C2}} \end{aligned} \tag{4.26}$$

Applying the theory developed before, S^M is obtained with (4.25), and S^{F_n} with the synthesis methodology from Chapter 3. Finally, the scattering matrix of the multiplexer S^P is calculated applying (4.19). In the triplexer case, $P = 4$ and $C = N = 3$. The dimensions of each matrix are related to the quoted parameters above. The involved matrices in the matrix system for this example are expressed as:

$$S^{M}_{[\mathrm{PxP}]} = \begin{bmatrix} -0.5 & 0.5 & 0.5 & 0.5 \\ 0.5 & -0.5 & 0.5 & 0.5 \\ 0.5 & 0.5 & -0.5 & 0.5 \\ 0.5 & 0.5 & 0.5 & -0.5 \end{bmatrix}$$

$$S^{PP}_{[\mathrm{PxP}]} = \begin{bmatrix} S^{M}_{11} & 0 & & 0 \\ & S^{F_1}_{22} & 0 & \\ 0 & & S^{F_2}_{22} & 0 \\ & 0 & & S^{F_3}_{22} \end{bmatrix}$$

$$S^{CP}_{[2\mathrm{CxP}]} = \begin{bmatrix} S^{M}_{21} & 0 & & 0 \\ S^{M}_{31} & & 0 & \\ S^{M}_{41} & 0 & & 0 \\ 0 & S^{F_1}_{12} & 0 & \\ & & S^{F_2}_{12} & \\ 0 & 0 & & S^{F_3}_{12} \end{bmatrix}$$

$$S^{PC}_{[P\times 2C]} = \begin{bmatrix} S^{M}_{12} & S^{M}_{13} & S^{M}_{14} & 0 & & 0 \\ 0 & & 0 & S^{F_1}_{21} & 0 & \\ & 0 & & 0 & S^{F_2}_{21} & 0 \\ 0 & & 0 & 0 & & S^{F_3}_{21} \end{bmatrix}$$

$$S^{CC}_{[2C\times 2C]} \begin{bmatrix} S^{M}_{22} & S^{M}_{23} & S^{M}_{24} & 0 & & 0 \\ S^{M}_{32} & S^{M}_{33} & S^{M}_{34} & & 0 & \\ S^{M}_{42} & S^{M}_{43} & S^{M}_{44} & 0 & & 0 \\ & 0 & & S^{F_1}_{11} & 0 & \\ 0 & & 0 & & S^{F_2}_{11} & 0 \\ & 0 & & 0 & 0 & S^{F_3}_{11} \end{bmatrix}$$

$$L_{[2C\times 2C]} \begin{bmatrix} 0 & & 0 & 1 & & 0 \\ & 0 & & 0 & 1 & \\ 0 & & 0 & & 0 & 1 \\ 1 & 0 & & 0 & & 0 \\ & 1 & 0 & & 0 & \\ 0 & & 1 & 0 & & 0 \end{bmatrix}$$

The proposed filter design methodology and the numerical analysis that has been elaborated are technologically independent. Therefore, the experimental validation has been addressed using equivalent lumped reactance elements and microstrip technology for manufacturing simplicity. Fig. 4.12 shows the equivalent electrical circuit of each channel based on the BVD model. The input and output filter's access lines were designed as 50-Ω lines. Its lengths were a priori fixed following a geometrical criterion and later integrated into the filter synthesis process due to its behavior as a phase shifter.

Table 4.6 displays the synthesized values of the elements for each triplexer filter. Considering the available commercial values, most of the elements were split into two series inductors or parallel capacitors. The external parallel inductors (L_S, L_L) of filter F1 and F2 were dismissed because of their behavior as an open circuit at the triplexer frequency. The prototype manufactured in a single 1.52-mm-thick FR4 substrate is shown in Fig. 4.13. The triplexer has been integrated using wirewound high-Q chip inductors and multi-layer high-Q capacitors from Johanson Technology. The inductors and capacitors' Q-factor depends on each element's value and the selected frequency, ranging from 35 to 45 for Q_L (Q-factor of inductors) and 500 to 3000 for Q_C (Q-factor of capacitors) for our design specifications.

Table 4.6: Bandpass elements of the Butterworth Van-Dyke Model for the triplexer's filters

Circuital elements	F1	F2	F3
$La1\ [nH]$	149.2009	149.5388	128.9948
$La2\ [nH]$	49.0579	38.0131	28.4881
$La3\ [nH]$	218.0706	220.1207	179.7163
$La4\ [nH]$	48.1377	37.2738	27.9238
$La5\ [nH]$	134.7453	130.4068	130.746
$Ca1\ [pH]$	3.4328	1.849	1.2792
$Ca2\ [pF]$	19.7809	11.9503	9.2645
$Ca3\ [pF]$	2.3604	1.2568	0.9351
$Ca4\ [pF]$	20.4338	12.3168	9.5431
$Ca5\ [pF]$	3.8478	2.1549	1.2506
$C01\ [pF]$	4.0074	2.8537	2.3447
$C02\ [pF]$	25.2649	20.7342	18.0132
$C03\ [pF]$	4.9668	3.5424	2.9416
$C04\ [pF]$	24.7391	20.3531	17.6965
$C05\ [pF]$	6.6267	4.7914	3.7449
$Ls\ [nH]$	141	111.3980	57.0229
$Ll\ [nH]$	707	1809279707.01	81.7814

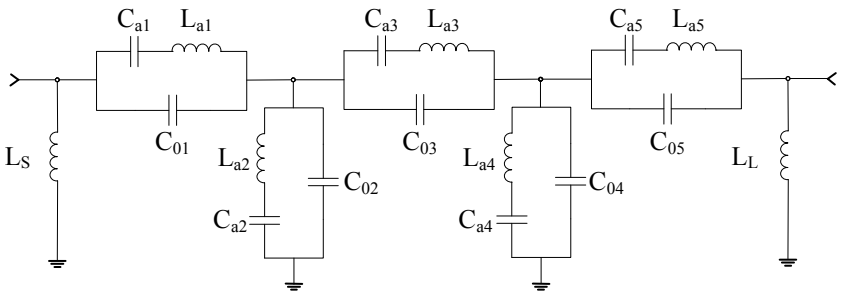

Figure 4.12: Circuital elements of 5th-order bandpass ladder-type filter based on the BVD model.

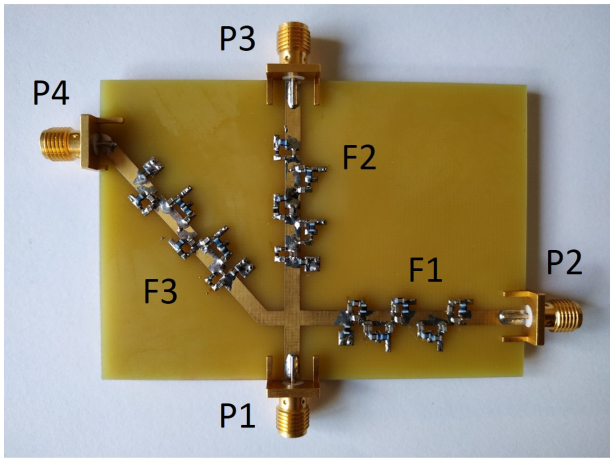

Figure 4.13: Fabricated triplexer with lumped elements.

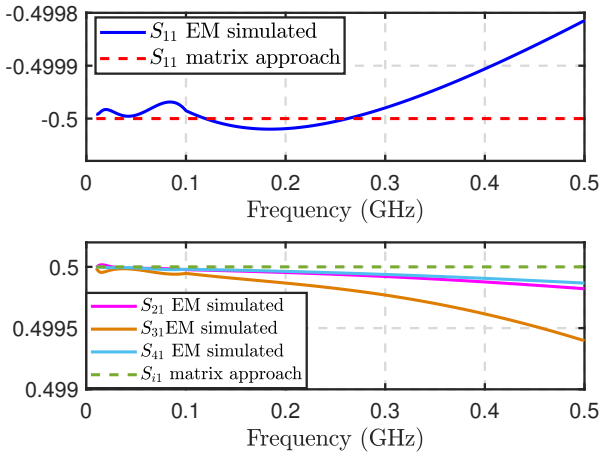

Figure 4.14: S-parameters comparison between the star-junction electromagnetic simulation and the matrix approach.

Electromagnetic simulation of the star-junction was carried out to evaluate the accuracy of (4.25). Fig. 4.14 shows the excellent agreement between the solution obtained using the matrix approach and the simulation results. As expected, the higher the frequency, the higher the deviation from the theoretical value, but keeping very acceptable values to give an accurate result in the multiplexer response evaluation.

The simulated and measured transmission, reflection, and cross-isolation responses are shown in Fig. 4.15a, 4.15b and 4.16 respectively. As a consequence of the low Q-factor, especially Q_L, the F1, F2, and F3 insertion loss are kind of high: -2.89, -4.05, and -4.19 dB, respectively. The triplexer performance is not good but still demonstrates the theory presented in this section. The technology and frequency range were chosen to help with a fast and easily manufactured proof of concept. However, the developed theory can be applied at higher frequencies and other technologies where other effects should be considered.

To demonstrate the minimization of the loading effect in the filter passband with the proposed methodology, filter F1 was measured detached from the triplexer. Fig. 4.17 shows the excellent agree-

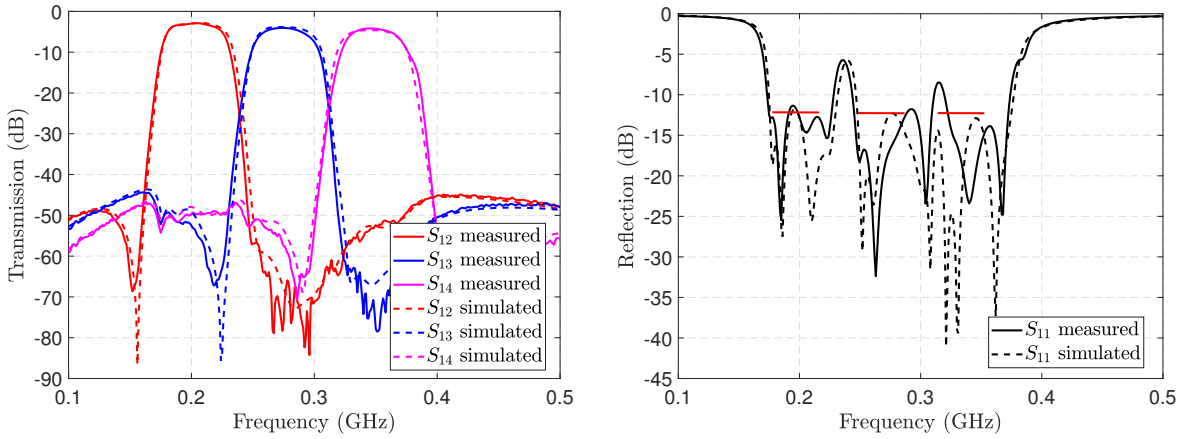

(a) (b)

Figure 4.15: (a) Simulated and measured transmission triplexer response. (b) Simulated and measured cross-isolation response.

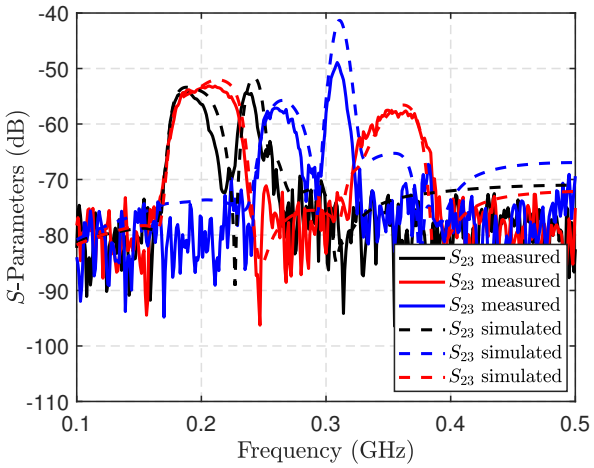

Figure 4.16: Simulated and measured cross-isolation response.

ment between the measurements when the filter is part of the triplexer and when it is considered as stand-alone. Despite the technology effects on the outcome, the experimental validation evidences the methodology accuracy to minimize the loading effect through the proper choice of ϕ_{add_11}.

4.6 Validation Examples

Three validation examples covering different situations are presented to verify the proposed methodology in 4.4. Initially, considering a fixed frequency plan multiplexer, a first example is differentiated with a contiguous bands quadplexer. The second and third examples cover the assessment of a flexible frequency plan pentaplexer and triplexer, respectively, based on the same theory. The non-contiguous triplexer has been experimentally validated.

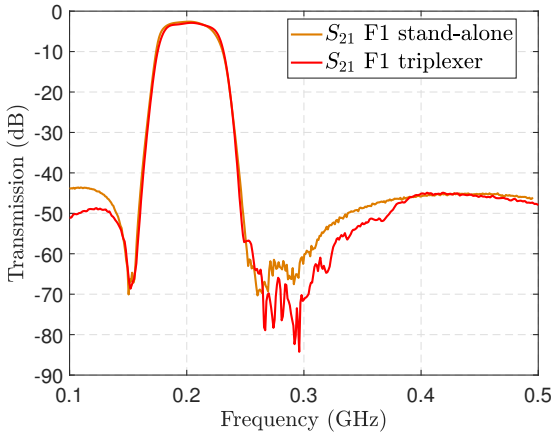

Figure 4.17: Comparison between filter F1 transmission response when it is measured as stand-alone and connected as part of the triplexer.

All examples are acoustic-wave technology-driven, but the theory discussed in this chapter is independent of the technology under consideration. All multiplexer filters shown in this section rely on a fully canonical ladder configuration based on AW resonators with r-factor=17.2. Characteristic polynomials that describe the generalized Chebyshev filtering function were calculated for each channel. The general method proposed in Section 4.4.1 focuses on the relevance of MSN distinction in different cases. In all of them, inner channels are considered MSN, no matters the filtering type doubly or singly. The examples selected in this section encompass both cases to stand out its performance as MSN.

4.6.1 Fixed Frequency Plan Multiplexer

Contiguous Bands Quadplexer Example

For contiguous bands example, inner filters are synthesized as minimum susceptance network, STF class. The outer filters are calculated as non-MSN ($\phi_{add\_11} \neq 0°$) and belonging to the DTF class. Considering the contiguous band's definition [84], four fully canonical seventh-order filters have been designed with the specifications listed below. All filters fulfill the technological constraints under consideration with a selected quality factor Q_{AW}=1500.

- ◇ Band (MHz): 782-812; 816-846; 850-880 and 884-914.
- ◇ RL (dB): 15; 5; 5 and 15.

It is worth noticing that the inner STFs have been synthesized with a low RL level. This low value is justified with the analysis performed in section 4.3.3 in order to obtain the minimum influence of the imaginary part in adjacent channels. Analyzing (4.18a), we realize that the partially complementary

condition explained in [100, 105] is fulfilled because the combination of the other channels will naturally construct the complementary admittance of this channel (1-Y_{in}). As expected, when the filters are connected, the outcoming return loss will be higher than the original due to the complementary condition.

In regards to ϕ_{add_11}, calculation for outer filters was performed following:

$$\begin{aligned} e^{j\phi_{add\_11,1}} &= \varepsilon_{r_1} E_1(s)/\ F_1(s)|_{s=j\Omega_{C2}} \\ e^{j\phi_{add\_11,4}} &= \varepsilon_{r_4} E_4(s)/\ F_4(s)|_{s=j\Omega_{C3}} \end{aligned} \tag{4.27}$$

The synthesis methodology gives out the needed phase values applying (4.27) and TZ positions to obtain an equiripple CPRL. The step-by-step description depicted in 4.2.2 has been followed for filters 2 and 3 design. The attained additional phase term and transmission zeros parameters are:

- ◇ $\phi_{add\_11}(^\circ)$: -46.75, 0, 0 and 47.84.
- ◇ Normalized Transmission zeros Ω_z (rad/s):

  {1.497 , -1.512 , 1.426 , -1.329 , 1.426 , -1.518 , 1.471};

  {1.694 , -1.275 , 1.393 , -1.213 , 1.421 , -1.382 , 1.699};

  {1.899 , -1.467 , 1.525 , -1.425 , 1.559 , -1.717 , 1.391};

  {2.300 , -1.351 , 1.369 , -1.189 , 1.361 , -1.360 , 2.004}.

The extraction procedure can be followed by using the methodology described in Section 3.2. The synthesized BVD quadplexer elements are shown and summarized in Table 4.7. Despite technology feasibility was not the main concern in this example, the static capacitance ratio is good enough. All filters start/end with series resonators, so the input and output inductors L_S and L_L are configured in parallel. This allows to join all input inductors on the antenna node, but in this case only Filter 4 input element should be considered due to L_S for Filters 1, 2 and 3 behave as an open circuit at the corresponding frequency channel. On the other side, again only Filter 4 requires the output element to match the multiplexer, while the others can be neglected because of its high values.

Moreover, external reactive elements C_{ext} and L_{ext} have been placed to adjust the homogeneous required r-factor value. In this quadplexer, as explained before in 2.1.1, capacitors are placed in parallel to series and parallel resonators to decrease the capacitance ratio, and inductors in series with the first series resonators to increase r-factor. Technological constraints can be very stringent, therefore, minimize the external elements is a paramount task to reduce the filter size and loss effects. Quality factors equal to 100 and 50 were taken into account for external capacitances and inductors.

Fig. 4.18 shows each individually designed filter's input admittance where the open circuit condition for channels 2 and 3 imposed by ϕ_{add_11} is observed. Fig. 4.19 illustrates the response of each filter individually designed. The expected funnel-shape return loss for inner filters was modified because of

Table 4.7: Quadplexer example's BVD elements.

Resonator	L_a (nH)	C_a (pF)	C_0 (pF)	$r-factor$	C_{ext} (pf)	L_{ext} (nH)
Filter 1						
1	173.34	0.23	3.93	17.2		
2	140.46	0.30	5.18	17.2	0.93	
3	354.83	0.11	1.93	17.2	0.02	
4	151.81	0.28	4.76	17.2	0.85	
5	355.60	0.11	1.93	17.2	0.02	
6	139.58	0.30	5.21	17.2	0.89	
7	165.40	0.24	4.13	17.2		
L_S(nH)				43.92		
L_L(nH)				47.65		
Filter 2						
1	370.14	0.09	1.70	17.2		0.29
2	173.63	0.22	3.81	17.2	1.74	
3	305.24	0.12	2.08	17.2		
4	194.73	0.20	3.39	17.2	1.54	
5	313.56	0.12	2.03	17.2		
6	166.67	0.23	3.99	17.2	1.81	
7	222.07	0.16	2.82	17.2		
L_S(nH)				26.43		
L_L(nH)				21.93		
Filter 3						
1	474.20	0.08	1.21	17.2		2.64
2	110.28	0.32	5.56	17.2	1.10	
3	372.71	0.09	1.57	17.2		
4	112.76	0.31	5.43	17.2	0.90	
5	383.41	0.08	1.52	17.2		
6	93.14	0.38	6.62	17.2	0.22	
7	127.94	0.26	4.58	17.2	0.05	
L_S(nH)				29.43		
L_L(nH)				-		
Filter 4						
1	261.17	0.12	1.99	17.2		2.60
2	102.17	0.32	5.53	17.2	2.66	
3	168.47	0.19	3.20	17.2	0.05	
4	128.99	0.25	4.35	17.2	1.98	
5	169.50	0.18	3.17	17.2	0.09	
6	101.82	0.32	5.55	17.2	2.52	
7	191.99	0.16	2.74	17.2		
L_S(nH)				8.91		
L_L(nH)				9.17		

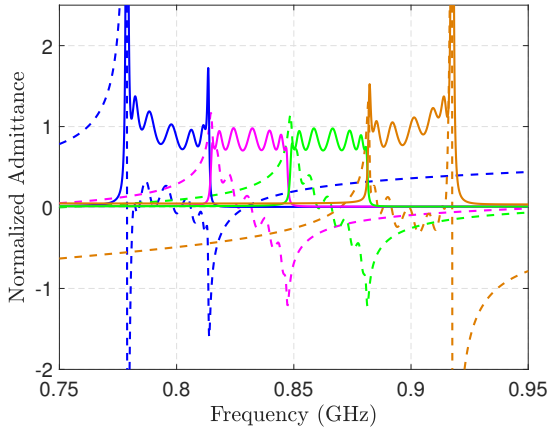

Figure 4.18: Real (solid) and imaginary (dashed) parts of input admittance of each filter of the quadplexer.

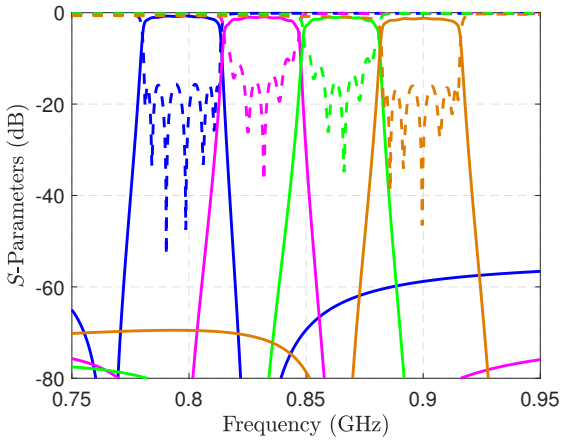

Figure 4.19: Transmission and reflection response of each individually designed filter.

the low RL while the characteristic equirriple Chebyshev responses can be appreciated in outer filters. Finally, Fig. 4.20 displays the transmission and reflection response of the whole quadplexer. The expected compensation effects for the inner filters are produced when the filters are connected, resulting in a CPRL better than 13 dB in the passband multiplexer. CPRL can be improved with fine-tuning of the input phases during a post-optimization process using the method developed in section 4.2.2. For example, by tuning the third filter (STF), a CPRL better than 15 dB is achieved. Fig. 4.21 shows the obtained reflection response.

Fine-tuning phase compensation produces modifications lower than 1 % of the initial value in the first and last resonator technological parameters: r-factor, static capacitance C_0 and input/output external elements of the filters L_S and L_L, proving that the selected initial values for the BVD model provide a good seed for later optimization processes. Finally, cross-isolation response better than 55 dB was obtained for the whole multiplexer band as shown in Fig. 4.22.

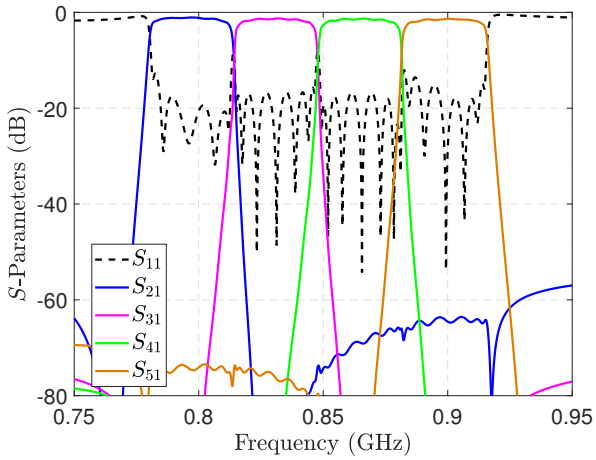

Figure 4.20: Transmission and reflection response of the whole quadplexer.

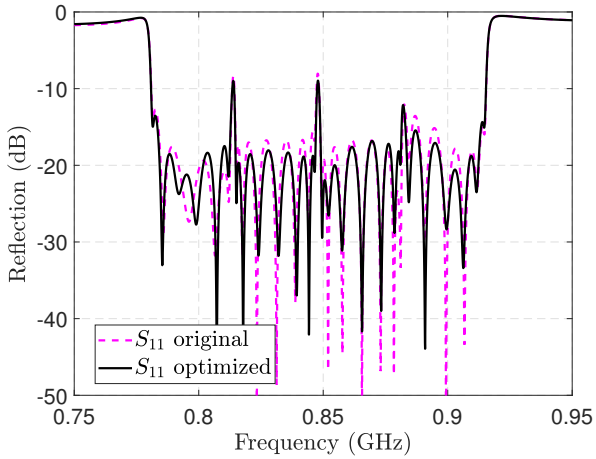

Figure 4.21: Comparison between original and optimized quadplexer reflection response.

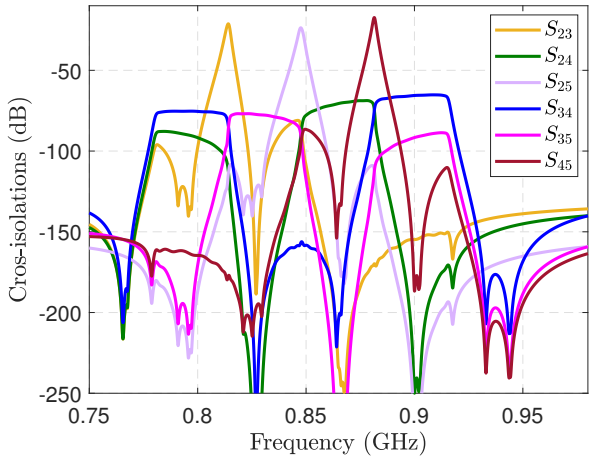

Figure 4.22: Cross-isolation responses of the whole quadplexer.

4.6.2 Flexible Frequency Plan Multiplexer

With a flexible frequency plan multiplexer, an architecture able to connect and disconnect filters on demand while keeping the same performance is considered. Consequently, the response of each filter has to be independent of the other filters. This design performance fits with MSN behavior, as was discussed previously. The multiplexer should then comply with (4.18b). Under this consideration, all filters (1:N) would be designed like MSN ($\phi_{add\_11} = 0°$). As a proof of concept, two examples obtained with this approach are shown.

Non-Contiguous Bands Pentaplexer Example

A star-junction pentaplexer for Band-24, Band-3Tx, and Band-1 was considered. Fully canonical stand-alone seventh-order filters starting in series resonator were designed with RL=12 dB, but different transmission zeros. All filters have been designed as DTF-MSN ($\phi_{add\_11} = 0°$). The filters were implemented considering acoustic wave technology constraints, the material system, channel specifications, input design parameters and obtained synthesized parameters are not shown in this example.

Depending on the space between channels, the number of filters, and each filter's bandwidth, a small phase tuning could be required to improve the design and counteract the lowpass's narrowband approximation to bandpass transformation. For instance, shifting input phases of B24Rx, B1Tx and B1Rx to 11.45°, -5.72° and -5.72° respectively provide a better compliance with (4.18b).

The pentaplexer generates 32 states according to its ability of connect and disconnect filters, namely, for CA operation, selected multiple bands can be turned ON simultaneously. In the case where all filters are switched ON, the loss signal transmission is less than 2 dB over the frequency range of 1.5–2.16 GHz. The pentaplexer response with all filters connected is shown in Fig. 4.23a whereas the input admittance is depicted in Fig. 4.24. The achieved input admittance compensation at each channel central frequency is observed in this figure, with susceptance near to zero.

Additionally, Fig. 4.23 displays multiplexer response when some filters have been switched OFF from the multiplexer. Only three states have been chosen due to the lack of space, but the same good performance was obtained in all of them. The selected states combine 4, 3 and 2 filters with different bandwidth and gap between channels to prove the soundness of this theory, highlighting the possible combinations. The small degradation suffer by each filter demonstrates a satisfactory agreement between theory and implementation. Due to the expected loading effect, the original equirriple RLs for the synthesized stand-alone filters were transformed in a non-equirriple CPRL. In all cases, the pentaplexer's filters have a return loss better than 12 dB. Transmission response values in all states were very similar to the obtained when all filters were connected. The most critical differences are found on the passband edges with variations around $\pm$ 0.2 dB.

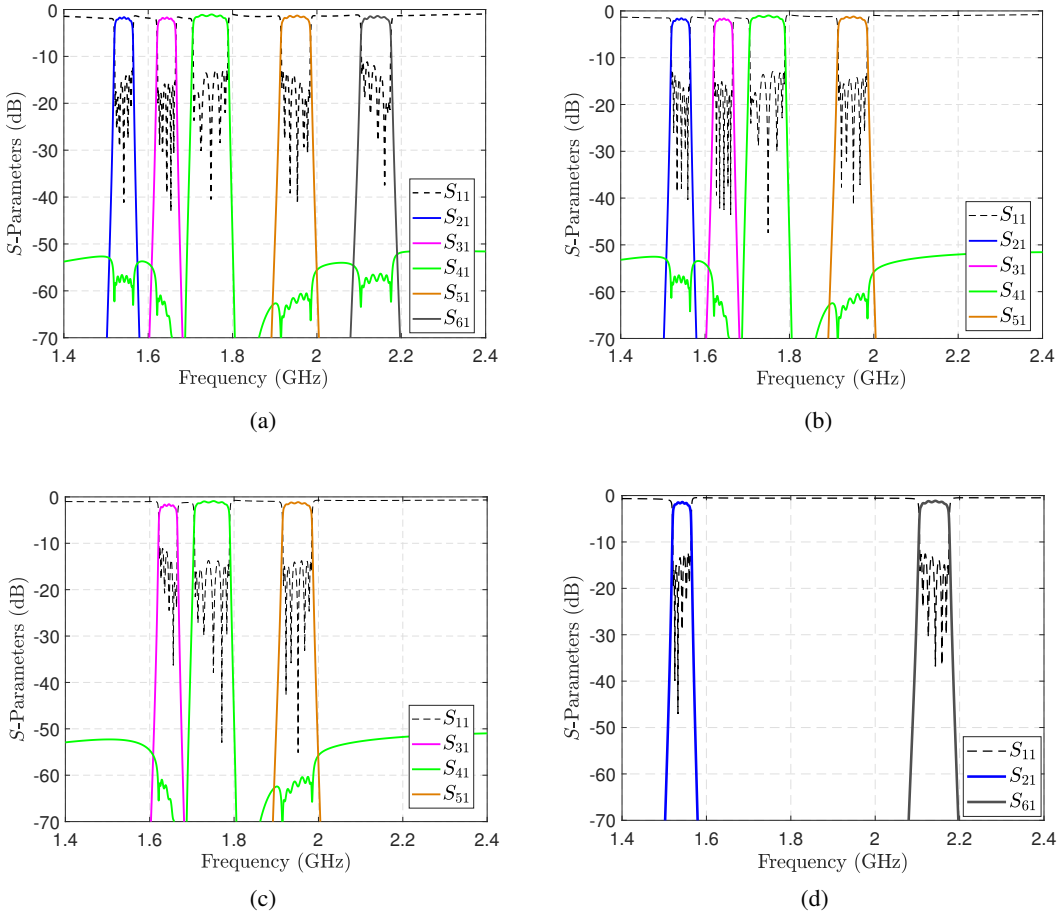

Figure 4.23: (a) Transmission and reflection response of the whole penta-plexer, (b) Multiplexer whitout B1Rx, (c) Multiplexer whitout B1Rx and B24Rx, and (d) Multiplexer whitout B1Tx, B3Tx and B24Tx.

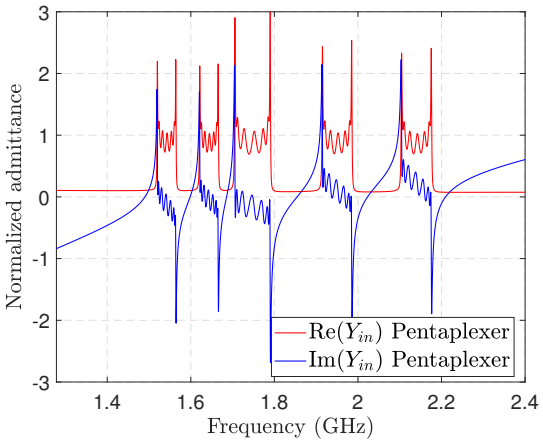

Figure 4.24: Real and imaginary part of the input admittance of the whole pentaplexer in the bandpass domain.

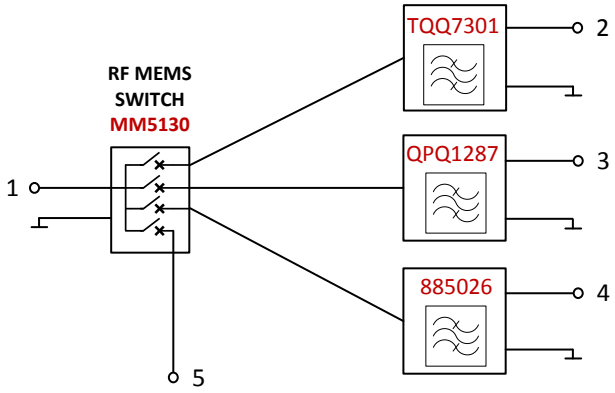

(a)

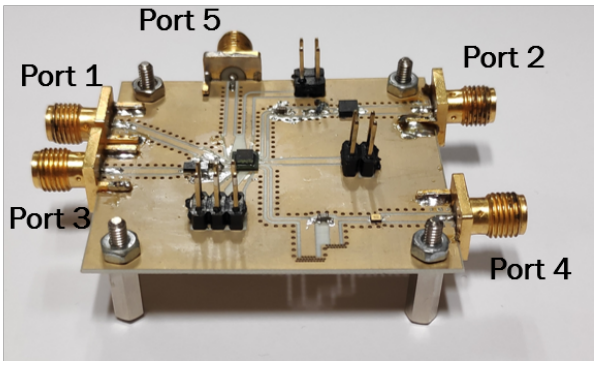

(b)

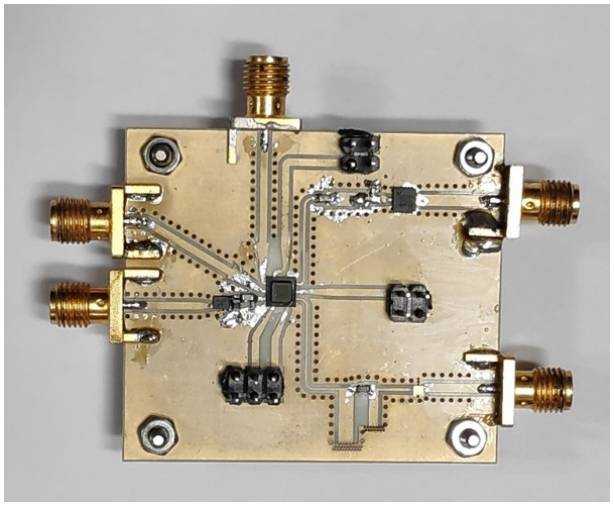

(c)

Figure 4.25: (a) Schematic and (b) Manufactured switched triplexer combining bandpass filters and RF MEMS switch. Ports distribution: Port 1: common port, Port 2, 3 and 4 correspond to TQQ7301, QPQ1287 and 885026 respectively and Port 5: direct path to evaluate the switch's IL.

Non-Contiguous Bands Manufactured Triplexer Example

To validate the MSN approach in a flexible frequency plan scenario, three BAW filters were selected and acquired from Qorvo for Band 1 (TQQ7301), Band 40 (QPQ1287), and Band 38 (885026) to assemble a triplexer. Since each filter was designed and packaged independently as stand-alone, the imaginary part of the input admittance in the out-of-band region was not necessarily accommodated to the MSN definition, resulting in a poor initial response due to phase loading effects. To overcome this degradation, each filter's input phase has been modified through a phase shifter to fulfill the MSN condition, i.e., an open circuit was imposed at the counter-band frequencies. Notice that having used the MSN concept in the synthesis stage of these commercial devices might have avoided utilizing external networks to implement this flexible frequency plan triplexer. The board's current size (45 x 50 mm) might shrink considerably, at least 50% without the phase shifters. Fig. 4.25 shows the manufactured switched multiplexer combin-

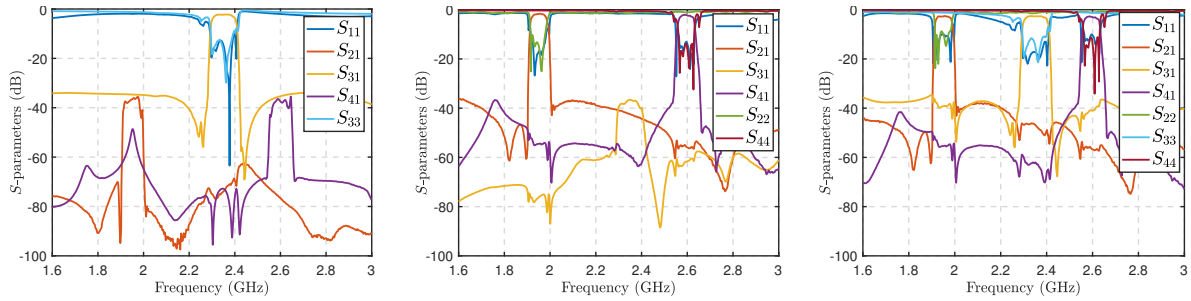

(a) (b) (c)

Figure 4.26: Transmission and reflection triplexer response simulation (a) State 2, (b) State 5 and (c) State 7.

Table 4.8: Triplexer's States

State/Filter	TQQ7301	QPQ1287	885026	Port 5
1	**ON**	OFF	OFF	OFF
2	OFF	**ON**	OFF	OFF
3	OFF	OFF	**ON**	OFF
4	**ON**	**ON**	OFF	OFF
5	**ON**	OFF	**ON**	OFF
6	OFF	**ON**	**ON**	OFF
7	**ON**	**ON**	**ON**	OFF
8	OFF	OFF	OFF	**ON**

ing bandpass filters and an RF MEMS switch. This configuration should meet the challenging system requirements for in-band isolation and cross-isolation, together with low insertion loss.

The recently launched MM5130 switch from Menlo Micro was employed to connect and disconnect the channels. The MM5130 device is a high power SP4T MEMS switch with low insertion loss and high linearity from 18 GHz down to DC. The four channels are individually controllable by applying 89 V to the corresponding RF GATE pin.

The simulation of the entire circuit was performed using HFSS simulator and vendors' models to evaluate the insertion loss, return loss, and cross-isolation for each of the 8 states generated in the implemented circuit shown in Table 4.8. According to the manufacturer datasheet, the three stand-alone devices present transmission and return losses under 2 dB and higher 10 dB respectively. Fig. 4.26 shows the simulated triplexer response for states 2, 5, and 7. For all states, the IL is better than -3 dB with $RL > 10$ dB. Comparing this result with the independent filters performances, a low loading effect is observed thanks to the followed compensation strategy. Fig. 4.26 demonstrates how each filter response degradation has been reduced. Each filter's contribution was independently designed to minimize the input admittance's imaginary part in the out-of-band region, fulfilling the MSN condition as mentioned earlier. Moreover, the switch introduces isolation around -30 dB.

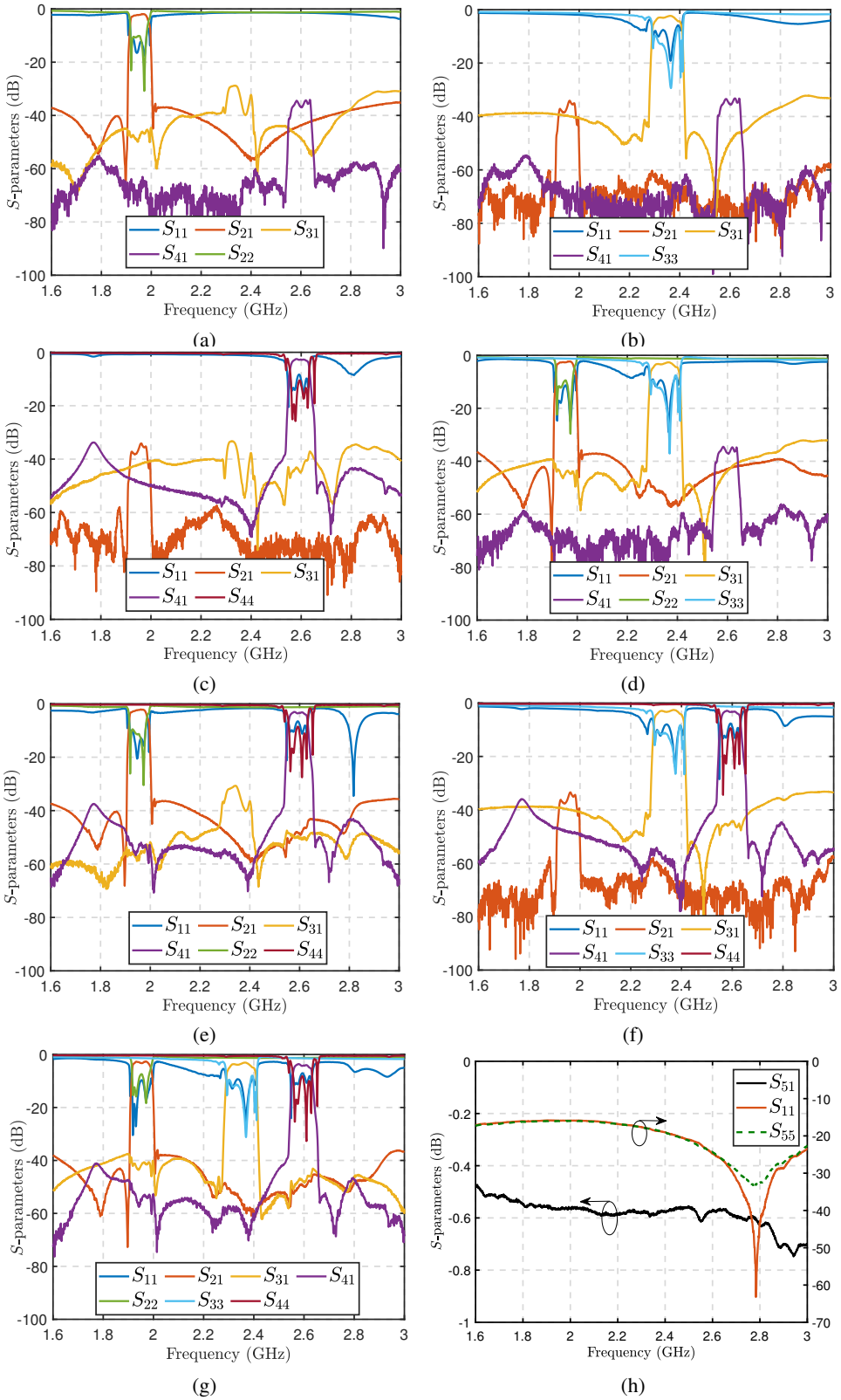

Figure 4.27: Transmission and reflection triplexer response measurement. First row: (a) State 1, (b) State 2, (c) State 3 and (d) State 4. Second row: (e) State 5, (f) State 6, (g) State 7 and (h) State 8: IL and RL when all filters are off .

The measures of the manufactured prototype are shown in Fig. 4.27. For all states, the IL is lower than 4 dB with $RL > 8$ dB. Comparing simulation and measurement, degradation can be appreciated due to the fabrication process, but a good agreement with the theory and the expected results. Moreover, the fourth channel has allowed the evaluation of the contribution to the switch's insertion loss.

To evaluate the loss inserted by the switch, access lines and SMA connectors, all filters were switched OFF and the transmission between Port 1 and 5 was measured (state 8) Fig. 4.27h displays the IL and reflected response in the multiplexer range frequency. Although microstrip access lines were designed for 50 Ω match and SMA connectors performance were de-embedding from the results, the measurement shows a degradation of IL from the manufactured claimed 0.25 dB to almost 0.6 dB. The return loss associated to these ports, is better than 10 dB in the whole range.

4.7 Chapter Summary

This chapter presents an exhaustive theoretical characterization of minimum susceptance networks and non-minimum susceptance networks regardless of the filtering function: doubly or singly for multiplexer implementation. The input phase value has been outlined as the crucial parameter for the network classification according to its input admittance, concluding that MSN definition corresponds to input phase value $\phi_{add\_11} = 0°$. Singly terminated filters have been considered minimum susceptance networks in the literature; however, in this research was introduced a new methodology allowing phase adjustment. Now, STF can be characterized as non-MSN. Conversely, doubly terminated filters have never been discussed as MSN; therefore, a robust theory has been introduced about this issue.

A numerical solution for implementing microwave star-junction multiplexers based on a matrix approach has been also presented. Taking into account the reciprocal and lossless properties and considering the symmetry and unitary conditions, a closed scattering matrix formula was found for an ideal star-junction multiplexer dependent on the port number of the junction P. This solution is a first approximation to evaluate the behavior of multiplexers in a numeric simulation environment. A non-contiguous bands triplexer was manufactured. The minimization of the interaction between filters was observed, endorsing the proposed multiplexer approach. Even though the introduced result only considers the ideal star-junction connection, it states a simple starting point through the circuit theory to characterize more complex junctions in any technology.

Three examples have been reported for illustrating the design process based on the proposed approach, yielding an excellent seed for further optimization process. A fine-tuning could be necessary if an equiripple return loss response is required. Moreover, filter frequencies, space between channels, and the number of channels in the multiplexer can be stated without restrictions. Although examples presented are driven by AW technology, this approach is suitable for any technology. Interaction between filters has been minimized mixing MSN and non-MSN in a fixed frequency plan case. An experimental validation using commercial devices has been shown for a flexible frequency scenario. The loading effect

of each filter on the others has been reduced with the MSN approach minimizing the imaginary part of each channel's input admittance in the out-of-band region.

CHAPTER 5

Synthesis of Acoustic Wave Filters Terminating in Complex Impedances

5G communication systems require bandpass filters embedded to eliminate interference due to the out-of-band signals. Many circuits in RFFE like antennas, power dividers, switches, couplers, and power amplifiers (PA) are cascading with bandpass filters. They are co-designed to reduce the whole system's loss and size. Passive multifunctional filtering circuits like filtennas, filtering power dividers, filtering baluns, and filtering couplers have been extensively reported on using microstrip resonators, low-temperature co-fired ceramic, and substrate integrated waveguides (SIWs) [107]. The conventional approach is to cascade a device and a bandpass filter, each matched to a typical purely real input impedance. However, this would result in a large device footprint and a degraded impedance matching over a wide bandwidth.

Front-end modules, including filters manufactured with acoustic wave technologies, are usually designed considering that the input and output ports' impedance are 50 Ω and describing the prescribed frequency response when their input and output ports are connected to a 50 Ω system impedance. Nevertheless, when a preceding/succeeding circuit presents a non-50 Ω output/input impedance, it will require an inter-stage matching network. To avoid the addition of lossy elements and the complexity and size increase, the filter should be synthesized, bearing in mind complex value port terminations.

A two-port network is usually represented by its scattering matrix parameters terminated by real-valued reference impedances at the two ends. However, this depiction should be generalized to any complex value termination at the input and/or output as in Fig. 5.1. This chapter addresses the synthesis of AW filters considering complex source and/or load terminations. Once the [ABCD] transfer matrix is obtained, the electrical parameters extraction procedure runs like in the case of normalized impedance $Z_S = Z_L = 1\ \Omega$. The filter performance with complex source/load termination impedance is exactly that obtained when a 50 Ω termination system is assumed as displayed in Fig. 5.2.

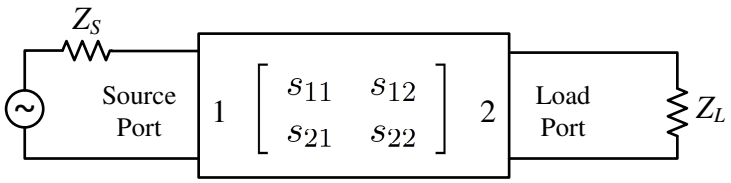

Figure 5.1: Multicoupled network terminated with arbitrary source and load impedances Z_S and Z_L respectively.

Figure 5.2: Reflection coefficient representation of filters with $Z_{in} = 50\ \Omega$ (blue) and $Z_{in} \neq 50\ \Omega$ when (a) $Z_S = 50\ \Omega$ and (b) $Z_S = Z_{in}^*\ \Omega$.

It is straightforward to observe with simple circuit transformations that a 50-Ω all-pole network definition with complex input/output impedance requires only the source/load and self-coupling matrix entries to be modified as highlighted in [108], [109]. However, it could be different for transmission response with finite transmission zeros, where some cross-couplings arise. While the cross-coupling does not affect the first resonator (equivalently the last resonator for output complex impedance), the circuit approach is valid. Nevertheless, this situation never occurs with fully canonical networks where all the couplings and self-couplings will be modified [84]. It is worth to notice that no cross-coupling are needed in AW ladder-type filters, but a similar effect will arise in this kind of network.

The synthesis process generalization accounting complex impedances does not violate the acoustic wave technology stringent constraints to consider: material system, power management capability, self-heating effects, number of different resonant frequencies, size and nature, and allocation of the external elements. Also, the compliance of the spectrum mask specifications is fulfilled as well. Moreover, the extracted BVD-model elements' values are adequately assimilated by the AW technology under consideration, which makes its manufacture feasible in general. A detailed synthesis and circuital extraction procedure are presented in this chapter. Technological considerations and limitations are also analyzed like the influence of the complex terminations on the filter element values.

As a proof of concept, this chapter presents a co-designed power amplifier-bandpass filter module, but using other technology without loss of generality. The PA's output impedance influence is considered

on the filter performance to obtain both a well-shaped filter and high effective PA efficiency. A two-pole filter was designed, providing a complex input-impedance to obtain the best efficiency but simultaneously taking care of filter transmission response that will appear affected by a non complex-conjugate transistor output impedance. PA output impedance has been calculated under large-signal operation using X-parameters. The PA output impedance frequency-dependent behavior was also considered during the simulation process to obtain the desired filter response. The systematic approach enables to assess the impact on the filter of filter source impedance variation.

A general methodology based on the exact synthesis technique is proposed to control the complex input impedance at the fundamental frequency, and simultaneously, the reflective termination at the second harmonic of a PA filtering matching network. Using a commercial GaN transistor, a co-designed PA-coaxial resonator filter module is implemented, providing the expected Chebyshev filter behaviour with high selectivity response. It presents a high maximum power-added efficiency of 50.4 % at 37.5 dBm output power.

5.1 [ABCD] Transfer Matrix Polynomials for Complex Terminated Networks

Summarizing, an AW ladder-type filter where the number of resonators (N) is equal to the prescribed transmission zeros (n_{fz}), leading to a fully canonical filter, can be realized with a generalized Chebyshev filtering function. The characteristic polynomials generated through an efficient recursive technique, obtaining $E(s)$, $F(s)$ and $P(s)$ polynomials and the normalization constants ϵ and ϵ_r are turned into an electrical circuit prototype using a synthesis approach based on the [ABCD] transfer matrix. The $F(s)$ polynomial is affected by a phase term in (5.1) that has not effect on the return and insertion losses of the filter since the argument ϕ_{add_11} is a real quantity.

$$F(s) = e^{j\phi_{add\_11}} F(s) \tag{5.1}$$

For a two-port network the [ABCD] matrix is built as follows:

$$[ABCD] = \begin{bmatrix} A(s) & B(s) \\ C(s) & D_(s) \end{bmatrix} = \frac{1}{P(s)/\varepsilon} \begin{bmatrix} A_n(s) & B_n(s) \\ C_n(s) & D_n(s) \end{bmatrix} \tag{5.2}$$

where $A_n(s)$, $B_n(s)$, $C_n(s)$ and $D_n(s)$ are the numerators of the [ABCD] polynomials and $P(s) \rightarrow jP(s)$ for $(N - n_{fz})$ even to satisfy the orthogonality condition.

If the network is operating between normalized complex source and load impedances Z_S and Z_L, then the [ABCD] matrix polynomials are related to the values of those terminations and the characteristic polynomials as [84]:

$$A_n(s) = \frac{1}{2}[(Z_S^* E(s) + Z_S F(s)/\varepsilon_R) - (-1)^N (Z_S^* E(s) + Z_S F(s)/\varepsilon_R)^*] \tag{5.3a}$$

$$B_n(s) = \frac{1}{2}[Z_L^* (Z_S^* E(s) + Z_S F(s)/\varepsilon_R) + (-1)^N Z_L (Z_S^* E(s) + Z_S F(s)/\varepsilon_R)^*] \tag{5.3b}$$

$$C_n(s) = \frac{1}{2}[(E(s) - F(s)/\varepsilon_R) + (-1)^N (E(s) - F(s)/\varepsilon_R)^*] \tag{5.3c}$$

$$D_n(s) = \frac{1}{2}[Z_L^* (E(s) - F(s)/\varepsilon_R) - (-1)^N Z_L (E(s) - F(s)/\varepsilon_R)^*] \tag{5.3d}$$

$$P(s) = P(s)\sqrt{(R_S R_L)} \tag{5.3e}$$

where R_S and R_L represent the real part of the source and load impedances respectively. The circuital extraction procedure is the same as the stand-alone filter when Z_S=Z_L=1 Ω since the [ABCD] matrix has been re-normalized with respect to another reference impedance different from 50 Ω.

Observing (5.3e), polynomial $P(s)$ depends on the real part of Z_S and Z_L. If one of them is null, the polynomial will be nullified. Consequently, the equation of energy conservation for a lossless reciprocal network will not be fulfilled (see (3.5)), and a filter realization can not be possible. The generalized synthesis procedure for any source or load has a constraint: Z_S and Z_L can not be purely imaginary.

Substituting (5.3) in (5.2) the general [ABCD] matrix for a two-port network with arbitrary impedances at load and source is obtained. Finally, the two-port S-parameter matrix is reformulated in terms of the known termination impedances and the[ABCD] polynomials as follows [110]:

$$S_{11}(s) = \frac{A(s)Z_L + B(s) - C(s)Z_S^* Z_L - D(s)Z_S^*}{A(s)Z_L + B(s) + C(s)Z_S Z_L + D(s)Z_S} \tag{5.4a}$$

$$S_{12}(s) = \frac{2(A(s)D(s) - B(s)C(s))\sqrt{(R_S R_L)}}{A(s)Z_L + B(s) + C(s)Z_S Z_L + D(s)Z_S} \tag{5.4b}$$

$$S_{21}(s) = \frac{2\sqrt{(R_S R_L)}}{A(s)Z_L + B(s) + C(s)Z_S Z_L + D(s)Z_S} \tag{5.4c}$$

$$S_{22}(s) = \frac{-A(s)Z_L^* + B(s) - C(s)Z_S Z_L^* + D(s)Z_S}{A(s)Z_L + B(s) + C(s)Z_S Z_L + D(s)Z_S} \tag{5.4d}$$

Having the S-parameters formulation for a two-port network loaded with arbitrary impedance values, the impedances looking into the network may also be derived. The input and output impedance are formulated as follows:

$$Z_{in}(s) = \frac{{Z_S}^* + S_{11}(s)Z_S}{1 - S_{11}(s)} \tag{5.5a}$$

$$Z_{out}(s) = \frac{{Z_L}^* + S_{22}(s)Z_L}{1 - S_{22}(s)} \tag{5.5b}$$

Table 5.1: Coupling matrix elements with different normalized terminations for a 5th-order filter with $\Omega_{TZ} = \{2.1, -2, 1.6, -2, 2.1\}$ rad/seg and RL= 18 dB. Main line inverters $J_{1:5}$ are unitary in all cases.

Z_S	1	$1 + j0.7$	$1 + j0.7$
Z_L	1	$1 - j0.4$	$2 * (1 - j0.4)$
B_1	-1.6166	-1.0996	-1.0996
B_2	2.8102	6.9434	6.9434
B_3	-1.9699	-0.7973	-0.7973
B_4	2.8102	6.9434	6.9434
B_5	-1.6166	-0.5203	-0.5203
J_{r1}	1.6917	1.0763	1.0763
J_{r2}	2.2670	3.5635	3.5635
J_{r3}	1.7196	1.0940	1.0940
J_{r4}	2.2670	3.5635	3.5635
J_{r5}	1.6917	1.0763	1.0763
J_6	1.0000	0.5267	0.3724
B_S	-0.5197	-0.8169	-0.8169
B_L	-0.5197	-0.4303	-0.2151

5.1.1 Coupling Matrix Comparison

The general synthesis procedure described in Section 3.1 is also valid for complex terminations yielding the coupling matrix that corresponds with the resulting network (see Fig. (3.7)) where [ABCD] transfer matrix is substituted by 5.3.

Analyzing the classical M matrix, in case of non-fully canonical networks, it may be seen that only the tuning state of the first and last resonators and the input and output couplings to them have been affected by the change in termination impedances [99, 111, 112]. On the other hand, in fully canonical networks, in comparison with the matrix with unit terminations, all the coupling values change [84]. The effect of complex terminations to the coupling matrix defined in Section 3.2.3 is revealed in Table 5.1. This table listed the filter's elements obtained from the synthesis procedure for three fully canonical fifth-order filters with equal input parameters TZs and RL, but different reference impedances. The susceptances related to the resonator $b_k = \{-2.1, 2, -1.6, 2, -2.1\}$ have the same value for all examples in the table since the TZs do not vary.

Two properties could be concluded by comparing the first column with the second one and the third column with the second one. First, all matrix values change if the terminations switch to complex impedances. Second, the reference impedance scaling is equivalent to the scaling of the output element B_L while other elements remain unchanged, except the last inverter J_6. Like in a non-fully canonical case, if the transmission zeros are far enough in fully canonical networks, only vary the elements and couplings related to the first/last resonator that have been affected by the changed impedance termina-

Table 5.2: Coupling matrix elements with different normalized terminations for a 2nd-order filter with $\Omega_{TZ} = \{-30.1 - 18\}$ rad/seg and RL= 18 dB. Main line inverters $J_{1,2}$ are unitary in all cases

Z_S	1	1
Z_L	1	$1.3 - j0.8$
B_1	22.8446	22.8446
B_2	10.6800	11.1841
J_{r1}	26.1805	26.1805
J_{r2}	13.8087	13.8087
J_3	-0.8844	-0.8124
B_S	0.0440	0.0440
B_L	0.0735	0.0592

tions. The rest of the elements have an unnoticeable change. The extracted elements of a second-order filter with $\Omega_{TZ} = \{-30.1 - 18\}$ is shown in Table 5.2. The NRN associated with the last dangling resonator B_2, the last inverter J_3, and the output FIR B_L are modified with the switch of Z_L from 1 Ω to $1.3 - j0.8$ Ω.

5.2 Synthesis Procedure: Last Inverter Extraction

As the main-line admittance inverters can be changed through scaling rules and even values are desired, a convenient solution would be arbitrarily set them to unity. Also, a sign alternation is needed for the resonator's serialization purpose in the case of ladder topologies. Even though the normalized case $Z_L = Z_S = 1\Omega$ is the most common in practical applications, only represents a fraction of all possible combination for Z_S and Z_L. In Chapter 3 and previous works, [11, 104], the load has been considered unity, but an approach considering complex terminating networks is more suitable for generalization purposes. With that in mind, a general procedure for the admittance redistribution is presented in this section due to the symmetry comprises not only the TZs distribution but the source and load ports.

Real and imaginary parts of the load impedance are identified as η and κ respectively for mathematical representation where $\eta > 0$. Fig. 5.3 depicts the initial scenario for the last extraction step and the redistributed one to obtain $|J_{N+1}| = 1$.

The calculation of the input admittance before the FIR B_N when the extraction is carried out from source to load relates the FIRs B_N, the output element B_L, the non-unity inverter between them J_{N+1}, and the complex loaded termination Y_L as it is expressed in (5.6a). After a mathematical manipulation, the input admittance is decomposed into its real and imaginary parts. The circuital transformation performed in the right side of Fig. 5.3, assuming a unitary last inverter, must guarantee the initial calculated Y_{in}, so, the real and imaginary part of Y_{in} and Y'_{in} would be equal.

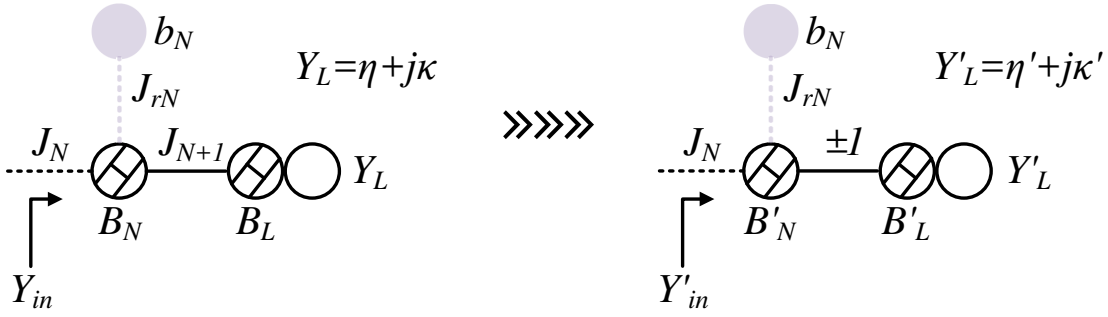

Figure 5.3: Last extraction step and the equivalent rearranged network with recalculated NRN's values to obtain a unitary last inverter.

$$Y_{in} = jB_N + \frac{J_{N+1}^2}{jB_L + Y_L} = jB_N + \frac{J_{N+1}^2}{jB_L + \eta + j\kappa} = jB_N + \frac{J_{N+1}^2(\eta - j(B_L + \kappa))}{\eta^2 + (B_L + \kappa)^2} \tag{5.6a}$$

$$\Re(Y_{in}) = \frac{\eta J_{N+1}^2}{\eta^2 + (B_L + \kappa)^2} \tag{5.6b}$$

$$\Im(Y_{in}) = B_N - \frac{(B_L + \kappa)J_{N+1}^2}{\eta^2 + (B_L + \kappa)^2} \tag{5.6c}$$

Imposing $|J_{N+1}| = 1$ in (5.6b) and considering $\Re(Y_{in}) = \Re(Y'_{in})$, the rearranged output element B'_L results in:

$$B'_L = -\kappa' \pm \sqrt{\frac{\eta'}{\Re(Y_{in})} - \eta'^2} \tag{5.7}$$

Imposing $|J_{N+1}| = 1$ in (5.6c) and considering $\Im(Y_{in}) = \Im(Y'_{in})$, the rearranged last FIR B'_N results in:

$$B'_N = \Im(Y_{in}) + \frac{B'_L + \kappa'}{\eta'^2 + (B'_L + \kappa')^2} = \Im(Y_{in}) + \frac{\Re(Y_{in})(B'_L + \kappa')}{\eta'} \tag{5.8}$$

Equation (5.7) offers two solutions for B'_L value, and therefore, two possible solutions for B'_N. Even though both are realizable solutions, we have to select the proper one according to the topology, i.e., negative B'_N are required to transform dangling resonators into series since AW resonators holds a static branch capacitor. In contrast, positive B'_N corresponds to shunt resonators. It should also be emphasized that there could be cases where the reachable values do not fit with the nature of the Nth resonator, so the filter can not be transformed into the acoustic domain.

In principle, the load Y_L and Y'_L must be equals, and therefore, its real and imaginary parts. To guarantee the feasibility of B'_L susceptance, according to (5.7), $\eta \leq 1/\Re(Y_{in})$. When this inequality

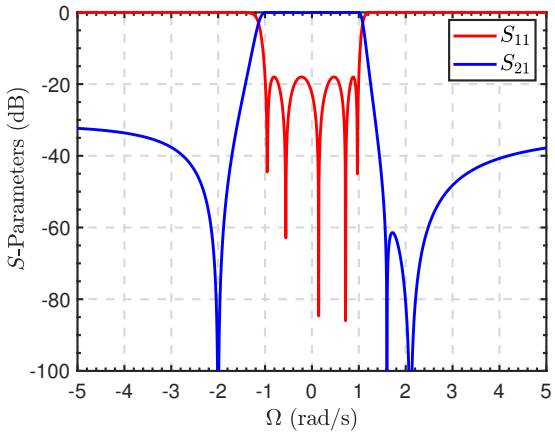

Figure 5.4: S-parameters filter A and B response.

is not fulfilled, η' would be force to its maximum possible value $\eta' = 1/\Re(Y_{in})$ in order to obtain a realizable $B'_L = -\kappa$. In this scenario, the real parts $\eta' \neq \eta$, and consequently, a mismatch will be produced in the output port in a similar way as occurs with real terminated impedances.

Let us consider three cases that illustrate the mathematical process and the effects on the filter response when the admittance redistribution is done:

- ◇ First example A is a symmetric filter with TZs at $\Omega_A = \{2.1, -2, 1.6, -2, 2.1\}$ rad/seg, RL_A=18 dB and normalized source and load $Z_{SA} = Z_{LA} = 0.8 + 0.65j\ \Omega$. This network presents a symmetric distribution around the central TZ $\rightarrow \Omega_{A3} = 1.6$, thus, the main-line inverter's modulus is unity $J_A = \{1, -1, 1, -1, 1, -1\}$. No redistribution would be required in this case.

- ◇ Second example B is an asymmetric filter with TZs at $\Omega_B = \{2.1, -2, 1.6, -2, 2.1\}$ rad/seg, RL_B=18 dB and normalized source and load $Z_{SB} = 1\Omega$ and $Z_{LB} = 0.8 + 0.65j\Omega$. The obtained admittance inverters $J_B = \{1, -1, 1, -1, 1, 1.9353\}$ are equal in magnitude except for the last one J_6. From (5.6b) and (5.6c) the input admittances is calculated:

$$\Re(Y_{inB}) = 0.7873 \longrightarrow 1/\Re(Y_{inB}) = 1.2702$$

$$\Im(Y_{inB}) = -1.2074$$

with $B_{5B} = -3.0230$ and $B_{LB} = -1.1245$. Since $\eta_B = 0.7529$ is lower than $1/\Re(Y_{inB})$, the redistribution is carried out successfully keeping $Y'_L = Y_L$. Applying (5.7) and (5.8) the new elements $B'_{LB} = -0.0123$ and $B'_{5B} = -1.8599$ are calculated. The filter response is shown in Fig. 5.4. As expected, both realization A and B have the same performance and a perfect match with the load port can be observed.

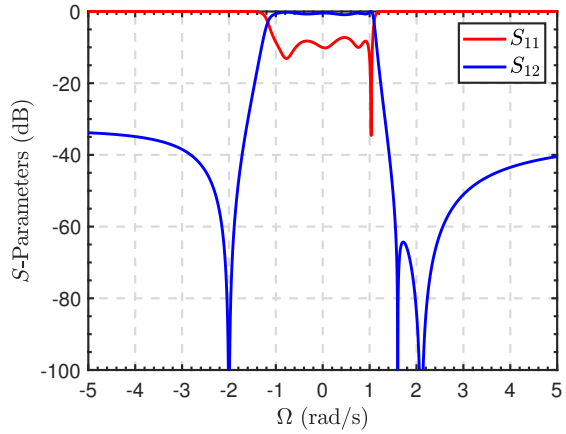

Figure 5.5: S-parameters filter C response.

◇ Third example C is an asymmetric filter with TZs at $\Omega_C = \{2.1, -2, 1.6, -2, 2.1\}$ rad/seg, RL_C=18 dB and normalized source and load $Z_{SC} = 0.5\ \Omega$ and $Z_{LC} = 0.2\ \Omega$. The obtained admittance inverters $J_C = \{1, -1, 1, -1, 1, 1.5811\}$ are equal in magnitude except for the last one J_6. From (5.6b) and (5.6c) the input admittances is calculated:

$$\Re(Y_{inC}) = 0.3937 \longrightarrow 1/\Re(Y_{inC}) = 2.5402$$

$$\Im(Y_{inC}) = -0.6037$$

with $B_{5C} = -0.8083$ and $B_{LC} = -2.5987$. Since $Y_L = \eta_C = 5$ is greater than $1/\Re(Y_{inC})$, we need to change the load termination to equalize the last inverter, thus, $Y'_L \neq Y_L$ and $Y'_L = 2.5402$. Applying (5.7) and (5.8) the new elements $B'_{LC} = -\kappa' = 0$ and $B'_{5C} = -0.6037$ are calculated. The filter response in the lowpass domain is shown in Fig. 5.5. As expected, a mismatch can be observed due to the variation of the load port from $Z_{LC} = 0.2\ \Omega$ to $Z'_{LC} = 0.3937\ \Omega$.

5.3 Synthesis Example

One design example is given to demonstrate the synthesis method in the AW domain. The example concerns the design of a seventh-order stand-alone filter with normalized complex terminations $Z_S = 0.8 + 0.65j\ \Omega$ and $Z_L = 0.9 - 0.80j\ \Omega$. The full-step process is illustrated, covering the definition of the characteristics polynomials, the extracted elements in the lowpass domain, and their transformation to bandpass.

The filter was designed for sub-band 41 with a passband from 2.585 to 2.66 GHz with a FBW= 2.8%. Having into account the filter specifications (spectrum mask) for this sub-band 41 and in order to fit with an effective electromechanical coupling constant k^2_{eff} = 6.83% (r-factor=17) in all resonators,

Table 5.3: Chebyshev characteristics polynomials of the complex terminated filter example.

Degree	$P(s)$	$F(s)$	$E(s)$
7	j	$0.7414 - 0.6710j$	1
6	3.12	$-0.1088 - 0.1202j$	$1.8714 - 0.1621j$
5	$14.73j$	$1.3559 - 1.2271j$	$3.5797 - 0.3082j$
4	46.38	$-0.1724 - 0.1905j$	$3.8509 - 0.5499j$
3	$72.39j$	$0.7235 - 0.6548j$	$3.4471 - 0.5623j$
2	229.00	$-0.0708 - 0.0782j$	$2.0651 - 0.4457j$
1	$118.55j$	$0.1007 - 0.0912j$	$0.8597 - 0.2224j$
0	375.27	$-0.0047 - 0.0052j$	$0.1835 - 0.0624j$
ϵ		1937.1	
ϵ_r		1	

Table 5.4: [ABCD] polynomials and calculated $P(s)$ for the complex terminated filter example.

Degree	$A(s)$	$B(s)$	$C(s)$	$D(s)$	$P(s)$
7	$-0.7049j$	2.2103	0.2586	$0.8108j$	-0.0004
6	1.3828	$-0.2554j$	$-0.0419j$	1.8157	$0.0014j$
5	$-2.6738j$	6.2302	2.2239	$2.6061j$	-0.0065
4	2.7091	$-0.7195j$	$-0.3594j$	3.9085	$0.0203j$
3	$-2.7441j$	5.2523	2.7236	$2.2622j$	-0.0317
2	1.3566	$-0.5414j$	$-0.3674j$	2.2163	$0.1003j$
1	$-0.7442j$	1.2101	0.7590	$0.4891j$	-0.0519
0	0.1059	$-0.0741j$	$-0.0572j$	0.2152	$0.1644j$

and also fulfill the technological bounds of the static capacitance of the filter (C_0) in each resonator, the synthesis procedure through an automatic search engine was performed. The following configuration was encountered as the filter specifications:

- ◇ TZs Ω_z (rad/s): {2.7114, -2.2744, 2.1056, -2.1126, 2.1066, -2.2742, 2.8555 }
- ◇ RL (dB): 18.8
- ◇ $\phi_{add\_11}(^\circ)$: -42.147

The obtained phase term ϕ_{add_11} was calculated to avoid external additional elements and guarantee the technological feasibility. The transfer and reflection polynomials for Chebyshev filtering characteristics, and the normalizing real constant ϵ and ϵ_r are summarized in Table 5.3. Polynomial $F(s)$ has been modified with the additional input phase according to (5.1). These polynomials are independent of source and load values.

To carry out the lowpass elements extraction following the steps described in Chapter 3, the ABCD matrix and the new $P(s)$ polynomial were calculated with (5.3). The resulting values are listed in Table

Table 5.5: Extracted nodal elements in the lowpass domain.

$Res.$	B_k	b_k	J_r
1	-2.5099	-2.7114	2.3305
2	3.5137	2.2744	2.7274
3	-3.0344	-2.1056	2.5258
4	3.6057	2.1126	2.7536
5	-3.0350	-2.1066	2.5260
6	3.5279	2.2742	2.7329
7	-1.9762	-2.7946	2.4695
B_S	0.006		
B_L	-1.1744		

Table 5.6: Bandpass elements of the filter obtained from the BVD model.

f_s [GHz]	k^2_{eff} [%]	C_0 [pF]	C_a [pF]	L_a [nH]
2.6424	6.83	0.4912	0.028	125.55
2.5428	6.83	4.0103	0.236	16.60
2.6224	6.83	0.4001	0.023	156.56
2.5481	6.83	4.1325	0.243	16.04
2.6224	6.83	0.4000	0.023	156.53
2.5428	6.83	4.0265	0.237	16.53
2.6470	6.83	0.4427	0.026	138.81
L_L	2.58 nH			

5.4. It is interesting to notice that in contrast with the example presented in Chapter 3, the matrix transfer polynomials equal N degree.

The extracted elements in the lowpass domain are shown in Table 5.5. It is worth to notice that as it is an asymmetric filter case, the last inverter has had to be recalculated to obtain even unitary values for the main-line admittances inverters J_i. Since $\eta = 0.6207$ is lower than $1/\Re(Y_{in}) = 1.2453$, the redistribution is carried out successfully keeping $Y'_L = Y_L$. Applying (5.7) and (5.8) the old elements $B_L = -0.5418$ and $B_7 = -1.9762$ were transformed to $B'_L = -1.1744$ and $B'_7 = -2.7946$. The original value of $J_8 = 0.7061$ was turned into -1.

The calculated lowpass elements are transformed in frequency with impedance denormalization to obtain the BVD equivalent circuit. Table 5.6 resumes the BVD element values extracted from the network. For this example, and related to the additional input phase ϕ_{add_11}, the external input element $C_S = 0.0073$ pF can be neglected due to its frequencial behaviour as an open circuit. The last resonator is series in the selected topology so that the external element would be in shunt position. S-parameters responses in lowpass domain of the filter calculated with (5.4) is shown in Fig. 5.6a considering a series and parallel quality factor Q_{AW}=1500. Finally, the filter's simulation using the values of the BVD model in the bandpass domain is depicted in Fig. 5.6b.

5.4 Extending the Capabilities of Complex Terminating AW Networks

The network synthesis with complex terminations can be carried out considering additional phase to the polynomial $F(s)$, as shown in the previous example. The input phase ϕ_{add_11} variation can be interpreted as a reference impedance renormalization, as the filter itself is unchanged [113]. It is expected that the additional phase, as a degree of freedom, can accommodate identical filter to different complex terminations, minimizing the change of the values in the coupling matrix M, and therefore, the Butterworth

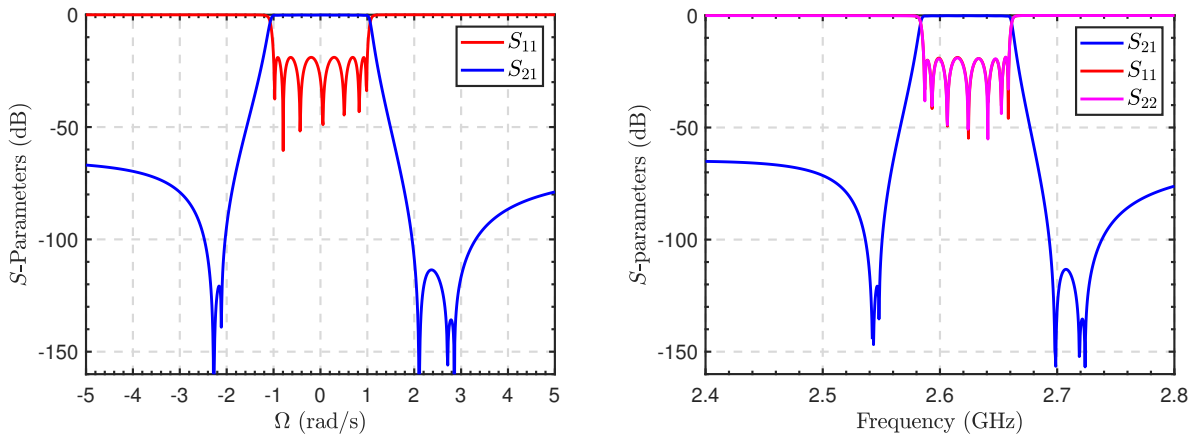

Figure 5.6: S-parameters of a seventh-order filter response with $Z_S = 0.8 + 0.65j\ \Omega$ and $Z_L = 0.9 - 0.80j\ \Omega$ (a) in the lowpass domain and (b) in the bandpass domain using the BVD model of the resonators.

Van-Dyke extracted elements in the bandpass domain. The theory presented in this section sustains, from the synthesis point of view, the usual practice of tuning the network first elements of a previously designed filter in order to match it with source impedances different from the original.

To demonstrate the impact of ϕ_{add_11}, a sweep of the normalized real and imaginary part of the source port was performed to complete circuital extractions in the bandpass domain, maintaining the normalized load port $Z_L = 1\Omega$. The normalized real part R_S has been swept in a range from 0.02 to 2 Ω and X_S in a range from -2 to 2 Ω, with a resolution of 200 points in each axis. The static capacitance C_{0k} and r_k-factor of each resonator have been calculated during the iterative procedure. This test was conducted over 3 fifth-order filters in sub-band 41 from 2.59 GHz to 2.65 GHz with the same TZs $\longrightarrow$ $\Omega = \{2.6877, -2.2682, 2.1093, -2.2666, 2.4422\}$ rad/seg and $RL = 16.3$ dB. The additional phase ϕ_{add_11} for each case were : 100°, 180° and -39.7°.

Figure 5.7 shows the static capacitance of each resonator varying the source port impedance for three different additional input phases ϕ_{add_11}. C_{0k} representation was limited to 10 pF. Values greater than 10 pF and lower than 0 pF are represented in white color. If we focus the attention on one column, e.g., the column corresponding to $\phi_{add\_11} = 100°$, it is clear that static capacitance of all resonators changed with the variation of Z_S. This behavior was also described in section 3.5 where a phase sweep with fixed Z_S was performed. In that case, all static capacitances changed too.

On the other side, Fig. 5.8 shows all resonators r-factor varying Z_S for three different additional input phases ϕ_{add_11}. r-factor representation was limited to 40. Values greater than 40 and lower than 0 were represented in white color. r-factor of resonators 2, 3, and 4 remain constant (r-factor=17) throughout the sweep of Z_S while r_1 and r_5 change their values in all cases.

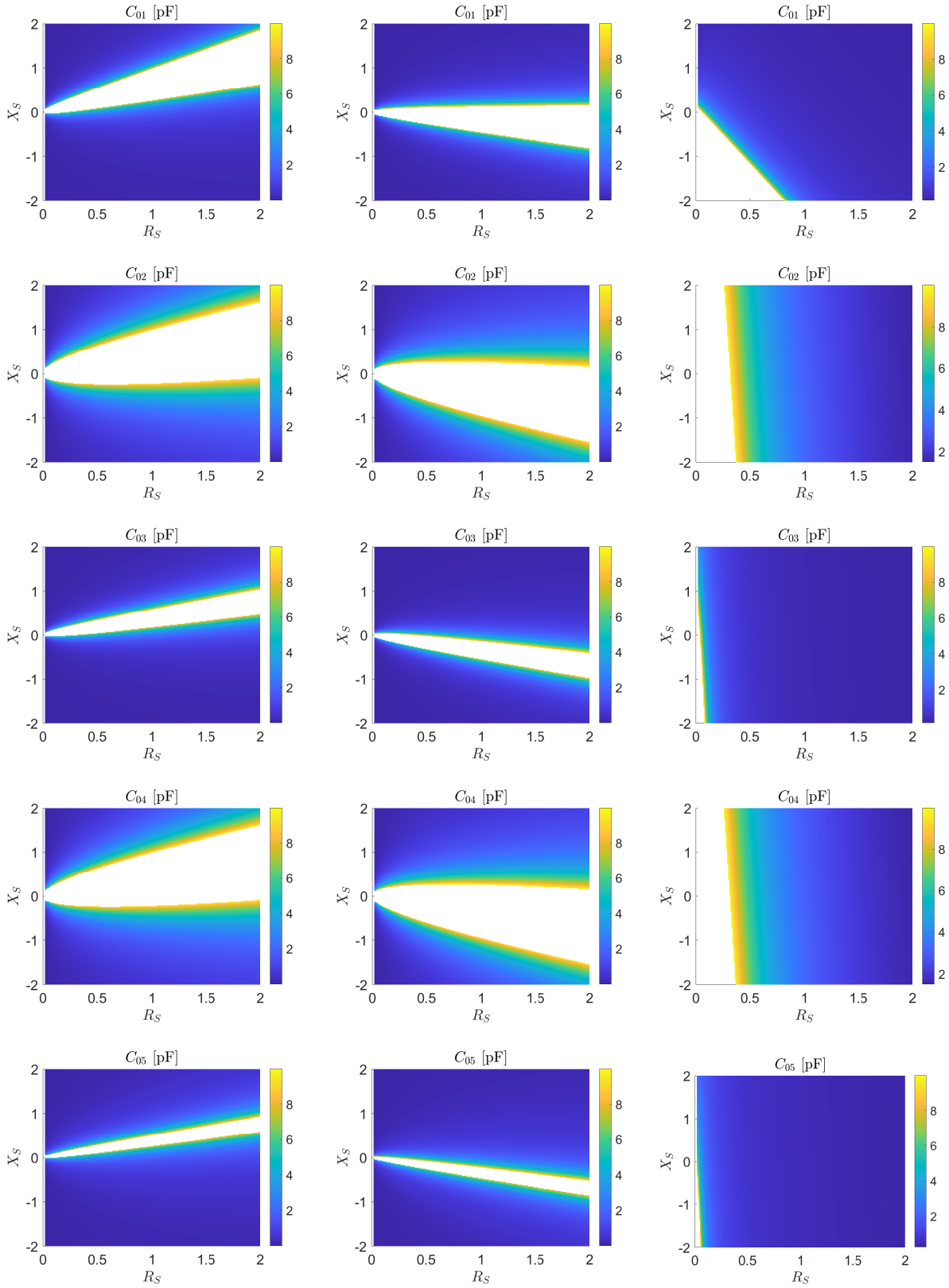

Figure 5.7: C_0 of all resonators varying the source port impedance for three different additional input phases ϕ_{add_11}.

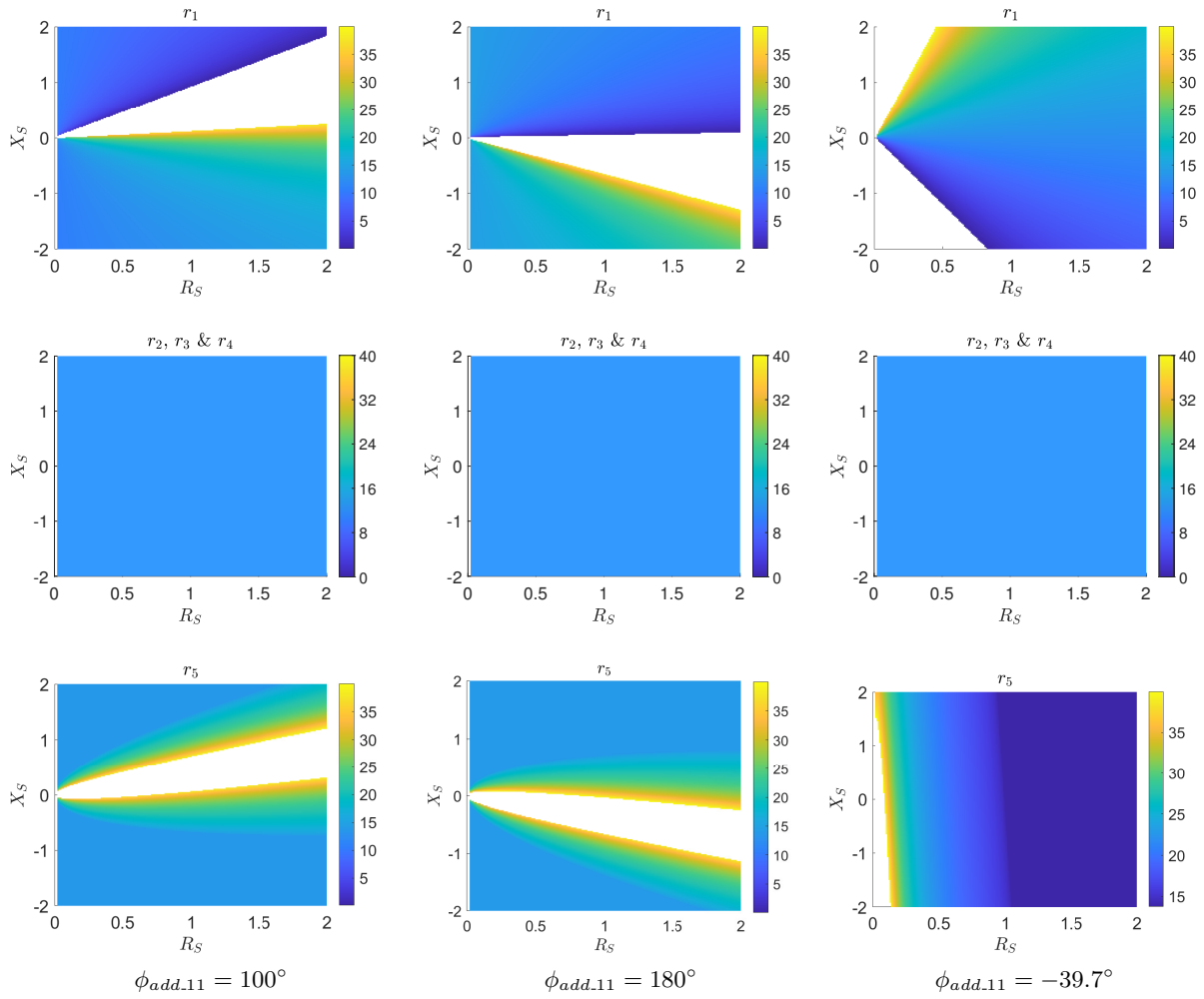

Figure 5.8: r-factor of the first and last resonators varying the source port impedance for three different additional input phases ϕ_{add_11}. Resonators 2, 3 and 4 remains constant its r-factor=17 throughout the sweep of Z_S.

C_{0k} and r_k-factor in section 3.5 and here behave in the same manner when a sweep of ϕ_{add_11} and Z_S are run respectively. Therefore, a direct link can be made between Z_S and ϕ_{add_11} values in order to find a family of pairs (Z_S ; ϕ_{add_11}) with the same filter response and element values for a set of TZs and RL.

5.4.1 Tuneability: One Element for Reduced Z_S Family

Analyzing one row in Fig. 5.7, e.g., the row corresponding to C_{05} and focusing on values around 9 pF (represented in yellow), a relation between the source impedance value and the additional phase can be observed.So, the same filtering response with equal resonators (meaning equal filters) can be obtained for three different source impedances. This is only possible changing the shunt input element B_S (series starting case) which is transformed to shunt inductor or capacitance component in the bandpass domain.

Table 5.7: Normalized $Z_S = R_S + jX_S$ with equal conductance and the corresponding additional input phase and extracted external input elements to obtain equal filter response.

R_S	X_S	$\phi_{add\_11}(^\circ)$	External input element
0.29	0.55	-86	1.00 pF
0.80	0.65	-39.72	0.016 pF
1.22	0.35	6.00	8.00 nH
1.27	-0.25	60.5	4.05 nH
0.95	-0.6	103.0	2.82 nH
0.34	-0.58	157.8	1.61 nH

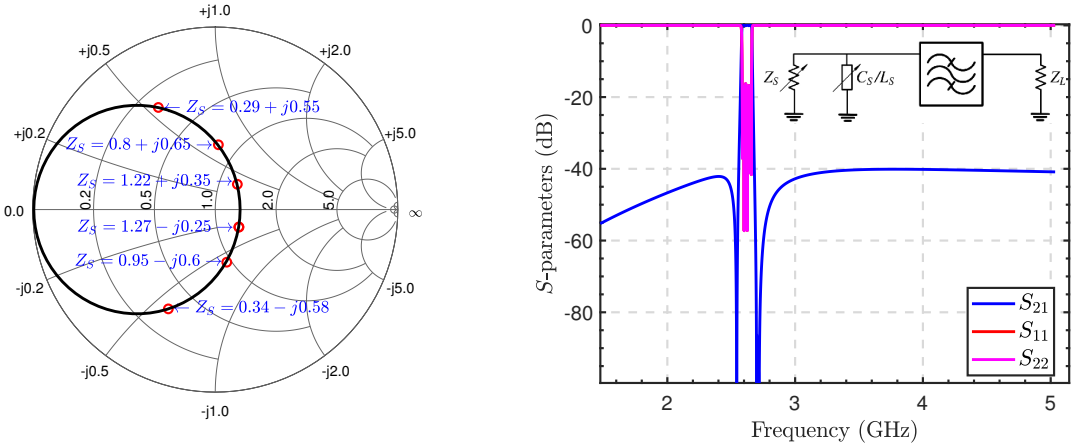

(a) (b)

Figure 5.9: (a) Position of source loads along the constant conductance circle G=0.753. (b) Bandpass filter response of synthesized networks with parameters shown in Table 5.7

It was found that exists a family of source impedances Z_S with constant conductance G that are matched with the complex input impedance of one filter varying only the value of the input shunt reactive element. Consequently, we can synthesize a filter for a given Z_{S1} with $\phi_{add\_11\_1}$ and the same filter will be matched to Z_{S2} with $\phi_{add\_11\_2}$ if Z_{S1} and Z_{S2} have the same conductance G.

Considering the TZs and RL mentioned before, if an homogeneous r-factor=17 for all resonators is required, an input impedance $Z_S = 0.8 + j0.65\ \Omega$ with $\phi_{add\_11} = -39.7^\circ$ will satisfy this technological constraint (see Fig. 5.8 last column). All source impedances that present a conductance $G = 0.753$ could be matched to the same filter obtaining equal responses varying only the input phase in the synthesis process, which means a change in the external element value. Table 5.7 shows different normalized Z_S values with its corresponding additional input phase and extracted external input elements. The reactive shunt element moves from capacitive to inductive. The locus of each impedance along de constant G circle is displayed in Fig. 5.9a. The filter bandpass response attained for this example, considering the input parameter combinations presented in Table 5.7 is shown in Fig. 5.9b.

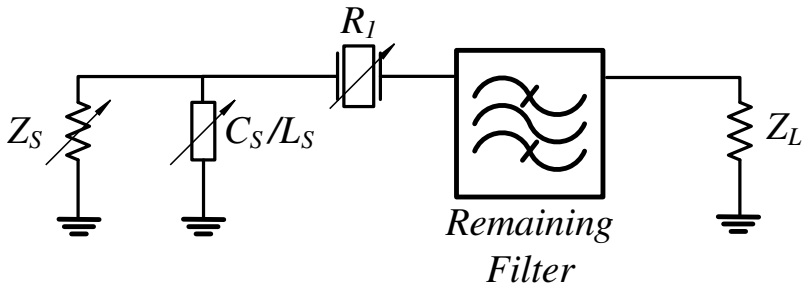

Figure 5.10: Network schematic to expand the reachable Z_S family.

5.4.2 Tuneability: Two Elements for an Expanded Z_S Family

Tuning only the first reactive element limits the reachable Z_S to a subset of defined families with the same G; therefore, some extra element should vary to expand the possible Z_S family. Fig. 5.10 illustrates the diagram of the proposed network. In addition to the external input element, the first resonator R_1 will change its technological values in order to preserve unalterable the rest of the network. Incorporating this tunable component allows the expansion of feasible source terminations to match with a predefined filtering network.

Under this premise, synthesizing an N degree filter with different additional input phases implies that r-factor from 2:N remains constant while only r_1 changes its value for Z_S variation in a defined region. Also, in this situation, static capacitance C_{0k} of resonators 2:N remains constant while C_{01} changes its value.

Let us established resonators R_2-R_5 from the filter obtained in the previous example with uniform r-factor as the model for the remaining filter in Fig. 5.10. To narrow down the mathematical space of possible source terminations, a practical region of interest was evaluated. This region is limited by a red line in Fig. 5.11. Five impedances in the edge of the region were selected as source impedances. External input element, r_1 and C_{01} extracted during the synthesis process are displayed in Table 5.8. Regarding the results of Table 5.8, it is worth to clarify that exist two possible ϕ_{add_11} values, so according to the

Table 5.8: Additional input phase and extracted elements corresponding to the selected normalized impedances $Z_S = R_S + jX_S$ to obtain equal filter response.

R_S	X_S	$\phi_{add\_11}(^\circ)$	External input element	r_1	C_{01} [pF]
0.80	0.65	-39.72	0.016 pF	17	0.45
1	1	130.85	1.34 pF	6.11	1.04
1	0	12.6	6.35 nH	15.17	0.50
0.2	1	30.8	1.7 pF	0.94	3.71
0.2	0.5	102.2	2.83 pF	7.84	0.86
0.2*	0	-35	20.19 nH	12.67	2.36

* There is no phase that achieve a uniform r for resonator 5; $r_5 = 28.55$ is the minimum reachable value.

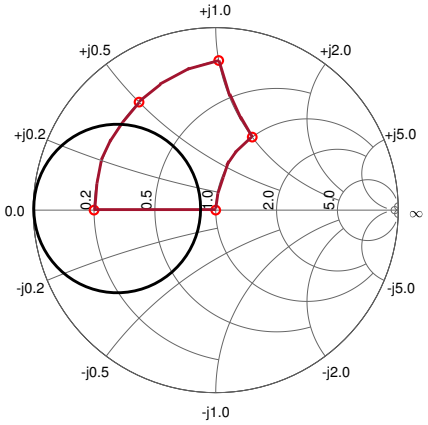

Figure 5.11: Impedance evaluation region: red. Black circle encloses the source impedances that do not comply with uniform r-factor in the Nth resonator.

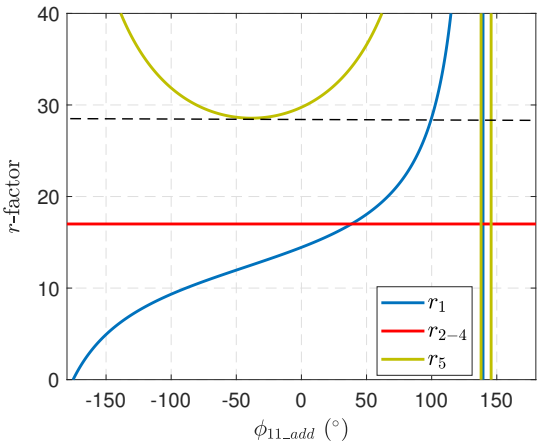

Figure 5.12: Capacitance ratio of all resonators vs ϕ_{add_11} when Z_S=0.2 Ω.

selected value, different sets of R_1 technological parameters can be obtained. This issue was explained in 3.5. To reach homogeneous capacitance ratio in all resonators, the obtained r_1-factor will require an external reactive element(series inductor to increase r in this case).

Even though tuning two elements expands the possible Z_S, it is understood that exists a forbidden impedance region where the uniform values of the N resonator's parameters are not accomplished. For $Zs = 0.2\ \Omega$ does not exist an input phase ϕ_{add_11} that fulfill the r-factor homogeneity required for resonator 5 because of the lower limit of $r_5 = 28.55$ as it is shown in Fig. 5.12. This region is limited by a conductance circle $G = 1.23$ for this example, and it is displayed in Fig.5.11.

5.5 Experimental Validation: Complex Terminated Bandpass Filter for a PA Co-Design

In the case of amplifiers, two technologies have been leading the RF applications: gallium nitride (GaN) and gallium arsenide (GaAs) for telecom infrastructure (PA) and handset (LNA and low-level PA), respectively. Adding the stringent requirements for linearity and power, make GaAs the material choice for PAs in the RF FEM. Even though GaN-on-SiC (silicon carbide) offers remarkable bandwidth, PAE, and power output, nowadays, exits some limitations for integration that may lead to drawback in the future.

The interest of integrating PA systems, including acoustic devices, is reflected in [13, 114] with a proposal of a multi-physical circuit consisting of a GaAs PA-BAW Tx filter co-design with Gain=13 dB for $P_{in} = 10$ dBm. Despite the lack of commercial high-power AW filters, one can find some reference examples in the market, like the recently discontinued BAW filter from Qorvo QPQ1300. The QPQ1300 was designed to withstand approximately 4W of input power while maintaining 2W output power and high rejection in massive MIMO and high power small cell applications. This commercial attempt shows the increasing interest in the integration of technologies and the concern to handle greater powers.

5.5.1 Introduction to the Co-design Approach

An energy-efficient PA design requires a transistor loaded by source- and load-port with matching networks transforming the optimum complex termination impedance into a real output termination impedance. These boundary conditions are generally determined by a load/pull analysis at fundamental and harmonic frequencies controlling harmonic content to reshape the waveforms within the transistor [115, 116]. Usually, the next stage is a filtering device that is generally defined with real input and output termination impedance. To connect PA and filter, an output matching network is placed, composed by reactive elements with lumped or distributed passive components to deliver power to a 50-Ω load [117, 118]. Those elements introduce losses and increase the complexity and device area.

Several authors have proposed using filtering devices with complex termination impedance to implement a co-designed inter-stage matching network. Fig. 5.13 shows the cascade topology with the conventional and the co-designed structure. In [108], it is introduced an elegant and straightforward solution for all-pole filters, based on a circuital approach, where modifying the coupling matrix entries of the first resonator source-coupling and self-coupling conveniently results in a network with the proper complex input impedance and the same original response. However, this solution is not valid for a fully canonical filter since other coupling matrix entries are involved.

To simplify the design and decrease the losses, several co-designs of PAs with filters have also been presented based on the same approach but employing different technologies [119–121]. In those designs, efficiencies are run by the optimum control of the impedance at harmonic frequencies and the resonator quality factor that affects the filter insertion loss. All cases employ an output matching network (OMN)

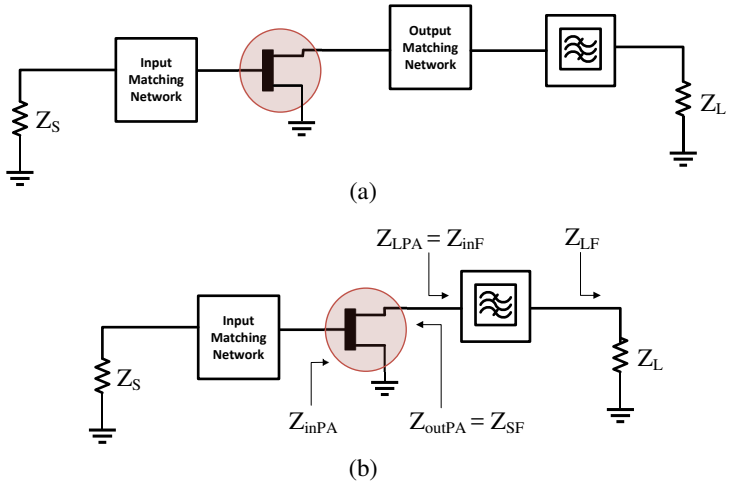

Figure 5.13: Power amplifier schematic circuit (a) Conventional topology with OMN and bandpass filter, and (b) Co-designed bandpass filter.

to deal with the harmonics content, while the filter is matched to the fundamental frequency f_0.

A trade-off between efficiency, output power, and filtering response is essential to obtain a good performance in a co-designed configuration. Thus, PA and filter behaviour must be properly characterized. In general terms, the filtering OMNs are designed considering the load-pull results to obtain the PA best performance, i.e., maximum power added efficiency (PAE) or gain, but unattending the intrinsic filter response as can be seen in [109, 122]. The selected PA load impedance (Z_{LPA}) does not match with the PA's output impedance (Z_{outPA}), entailing a filter mismatch that is reflected in the selective frequency response. A recurrent solution in these cases is a filter post-optimization process to ensure the desired frequency response of the entire PA-filter module [123].

This section tackles the PA-filter co-design technique from the filter synthesis point of view. The classical load-pull approach to evaluate the PA's performance and analyze PA output impedance's influence on the filter behaviour is faced. A closed formula based on X-parameters was employed to estimate the large-signal PA's output impedance. In a rigorous general formulation, including filter's input and output complex termination impedance filter, it is introduced a general control of the input reflection coefficient phase (ϕ_{add_11}) to set the second harmonic reflect for waveform shaping purposes accurately. This approach is valid for any filtering response and number of transmission zeros.

In Section 5.5.3 a PA-filter characterization is presented to state the boundary conditions for good PA's figures and also the calculation of the output impedance under-large signal operation. Later, in Section 5.5.4 a detailed synthesis filter and circuital extraction procedure are presented. Finally, in Section 5.5.5, a validation example that has been implemented and measured, is shown based on coaxial resonators technology.

5.5.2 Power Amplifier Characterization

A power amplifier is a circuit for converting DC-input power into a significant amount of RF/microwave output power. There is always some PA onboard for wireless communication equipment to boost the low-level analog signal to a certain level with a sufficient signal-to-noise ratio (SNR) over the communication link. High efficiency, output power, and gain are desirable in ideal cases, but a trade-off between them is expected in practice. Some of the parameters that participate in the performance evaluation of the PA are:

◇ **DC Power** (P_{DC})

It refers to the power used from the power supply in all DC terminals (drain and gate). DC power is calculated as follows:

$$P_{DC}(W) = V_{Drain}I_{Drain} + V_{Gate}I_{Gate} \tag{5.9}$$

Since I_{Gate} is intended to be too small around μA, the major contribution is obtained from I_{Drain}.

◇ **Gain** (G)

In lineal scale, Gain is the ratio between output and input power, whereas is their difference in dB scale:

$$G(dB) = 10log_{10}(\frac{P_{out}(W)}{P_{in}(W)}) = P_{out}(dBW) - P_{in}(dBW) \tag{5.10}$$

Gain is constant at low input power, and as the input power is increased, the amplifier starts compressing, reaching its 1dB compression point (P_{1dB}) in the nonlinear region, and gain starts decreasing. Large signal gain is obtained with the PA working at high input power (P_{in}), where nonlinear effects such as nonlinear capacitance and amplifier saturation occur.

◇ **Efficiency** (η) and **Power Added Efficiency** (PAE)

The amplifier efficiency is the ratio of RF output power and DC input power:

$$\eta = \frac{P_{out}}{P_{DC}} \tag{5.11}$$

This quantity is sometimes referred to as drain efficiency (or collector efficiency). This definition does not account for the RF power delivered at the amplifier's input. Since most power amplifiers have relatively low gains, the efficiency in (5.11) tends to overrate the actual efficiency. A better measure that includes the effect of input power is the power added efficiency (PAE), defined as:

$$PAE = \frac{P_{out} - P_{in}}{P_{DC}} = (1 - \frac{1}{G})\frac{P_{out}}{P_{DC}} \tag{5.12}$$

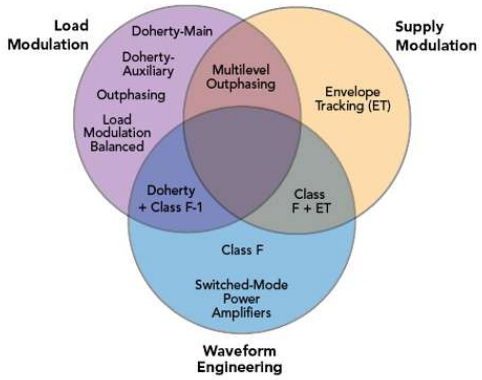

Figure 5.14: Efficiency enhancement mechanisms, their hybrids and possible areas for further improvement [124].

This PA figure of merit is typically presented in percentage, so the resulting value from (5.12) would be multiplied by 100.

To improve the RF power amplifier efficiency, one can take advantage of a wide variety of techniques that have shown to be effective in enhancing the average PA efficiency, providing longer battery life and a high integration level. Furthermore, some mechanism has been developed to enhance the efficiency and reduce the wasted power in an amplifier. Three base mechanisms can enhance a single-ended amplifier's efficiency: waveform engineering, supply modulation, and load modulation [124]. According to the mechanisms they use, popular enhancement methods are depicted in Fig. 5.14. The employed Venn diagram for classification helps identify where additional schemes are complementary and may further improve efficiency.

This thesis's PA design is based on the waveform engineering efficiency enhancement, particularly the harmonic-tuned operation in Class-F. The ideal Class-F requires multiple accurate harmonic terminations to exhibit a half-rectified sinusoidal current and rectangular voltage at the drain node where there is no power dissipation due to non-overlapping between the waves. When finite harmonics are considered (up to third harmonic), voltage and current waveforms transform to quasi-rectangular and quasi-half-sinusoidal respectively, decreasing the PA's efficiency from an ideal 100% to 80%.

Device Selection, Input Matching and Bias Networks

Over the past few years, Gallium Nitride (GaN) technology has been replacing GaAs because GaN is more efficient and has a higher power density resulting in higher power MMICs and FETs [125]. The higher power density of GaN devices have made it possible to manufacture single transistors or MMICs with higher output powers leading to the elimination of power-combining and thus reducing the overall device cost. GaN devices also have higher power efficiency than the GaAs devices, making them an unbeatable rival when the overall power consumption is essential. Moreover, GaN devices require higher

voltage and lower current for biasing, leading to narrower traces on the printed circuit boards, reducing the PCB size. Advantage has been taken from this fact when good isolation is required between RF path and bias network.

To validate the feasibility and effectiveness of the synthesis methodology discussed before in this chapter, a PA-filter co-design concept with a GaN HEMT transistor from Cree is presented. A CGH40006P transistor up to 6 GHz was selected as the RF power device [126]. The filter was designed to address sub-band 41 at 2.64 GHz with an FBW= 3.2%. According to the data provided by the manufacturer, the proper values for the transistor bias network are V_{GS}=-3 V and V_{DS}=28 V. It was also necessary to introduce an RC network to ensure the stability of the amplifier before the DC capacitor block in the gate: $R = 150\ \Omega$ and $C = 2.2\ pF$.

The manufacturer suggested bias networks for gate and drain were implemented as shown in detail in Fig. 5.15a. The drain-biasing network influences the overall efficiency and RF performance of the PA directly. Moreover, extra attention is required during its design to increase the PA's reliability due to the high voltage and current on the drain-biasing line. The DC, low-frequency, and high-frequency circumstances must be considered simultaneously to achieve desired PA performance and stable and reliable operation. The challenge in bias network design lies in having a good trade-off between these conditions [127]:

1. The current-handling capability and DC resistance of its DC characteristics.
2. The low frequency stability and biasing induced memory effects of its low frequency characteristics.
3. The isolation and RF leakage of its high-frequency characteristics.

On the other hand, the IMN was firstly designed as an LCC T-network with lumped components as it is observed in Fig. 5.15b. The final network was implemented, transforming the shunt capacitor C_2 and series inductor L_1 from lumped to distributed, obtaining the circuit in Fig. 5.15a. The combination of distributed microstrip lines and a lumped capacitor is less susceptible to parasitics, easy to tune, and provides an efficient PCB implementation with a small size for high frequency. The IMN was calculated at the fundamental frequency looking for the conjugate matching condition considering the outcome of the iterative source-pull process.

For the transistor characterization including the input matching and bias networks, a load-pull simulation was carried out with Agilent's Advanced Design System (ADS) setup. The load-pull reference plane is marked in Fig. 5.15a. The load–pull simulation provides the optimum load impedances at fundamental and harmonics, for maximum PAE and maximum output power which were used for designing the filter as power amplifier's OMN. Fig. 5.16 shows the contours obtained from the load-pull simulation of PAE (blue line, step 4%) and output power (red line, step 0.2 dBm) calculated at f_0=2.62 GHz, $2f_0$ and $3f_0$ with an input power $P_{in} = 25$ dBm under bias voltages V_{GS}=-3 V and V_{DS}=28

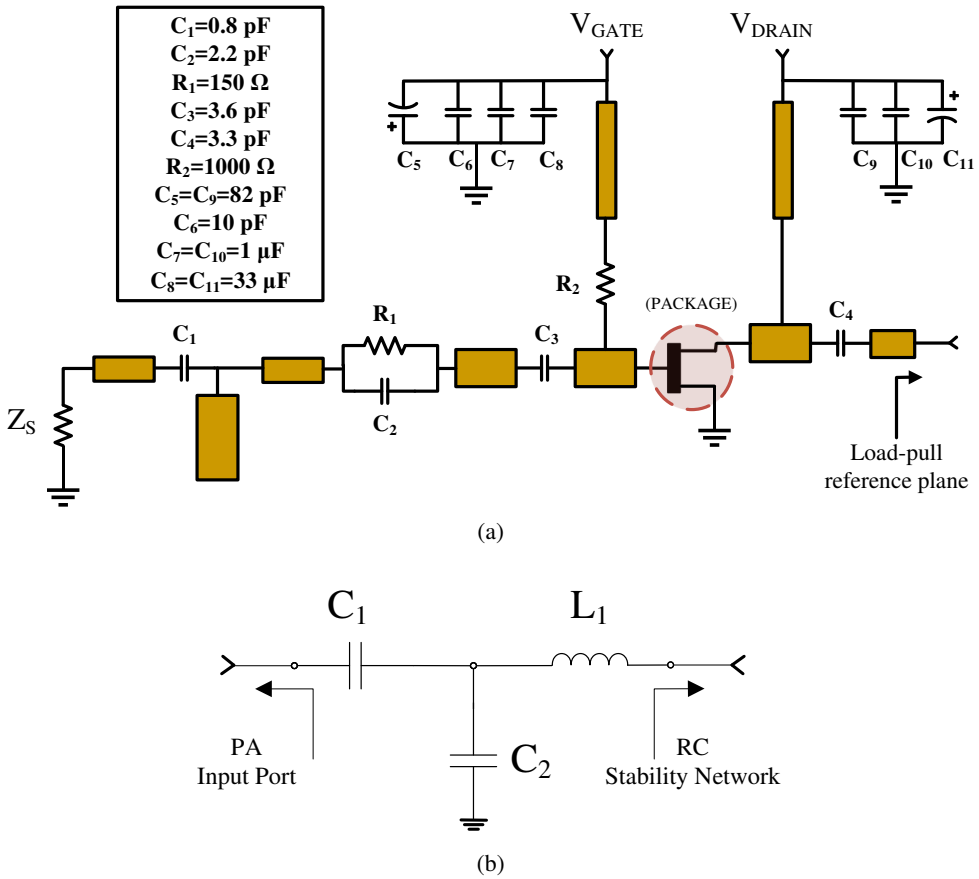

Figure 5.15: (a) Circuit schematic including IMN, RC stability , and Gate and Drain bias networks and (b) IMN with an LCC lumped elements T-network.

V. The optimum load transistor impedances obtained were $Z_{load-pullPA}(f_0) = 14 + 24.5j\ \Omega$ and $Z_{load-pullPA}(2f_0) = 0.01 - 30j\ \Omega$ for fundamental and second harmonic, while for the third one a large region is available. This situation allows a flexible impedance selection for this termination to ensure a high PA efficiency. This PA configuration achieves maximum PAE = 76 % and P_{out} = 39.4 dBm.

5.5.3 PA-Filter Module Integral Evaluation

In a PA design, the designer usually considers the contour condition obtained from load-pull simulation ($Z_{load-pullPA}$) to decide the boundary condition to attain the desired maximum figure for PAE or output power (see Fig. 5.16). This impedance needs to be synthesized by the filter so that it presents Z_{inF} = $Z_{load-pullPA}$ to the output terminal of the PA. This assumption leads to the desired PA figure's performance, but imposes a degradation of the filtering transmission response. In [108, 123] the authors realized that the regular efficiency-optimized or power-optimized impedance is not the optimal point for the co-design in terms of filter response shape, but they do not look out for the origin of this new optimal impedance neither identify it as Z_{outPA}. Because the PA large signal output impedance, Z_{outPA}, is different from the complex conjugate of Z_{inF}, the filter mismatch to its source impedance (Z_{SF}) will

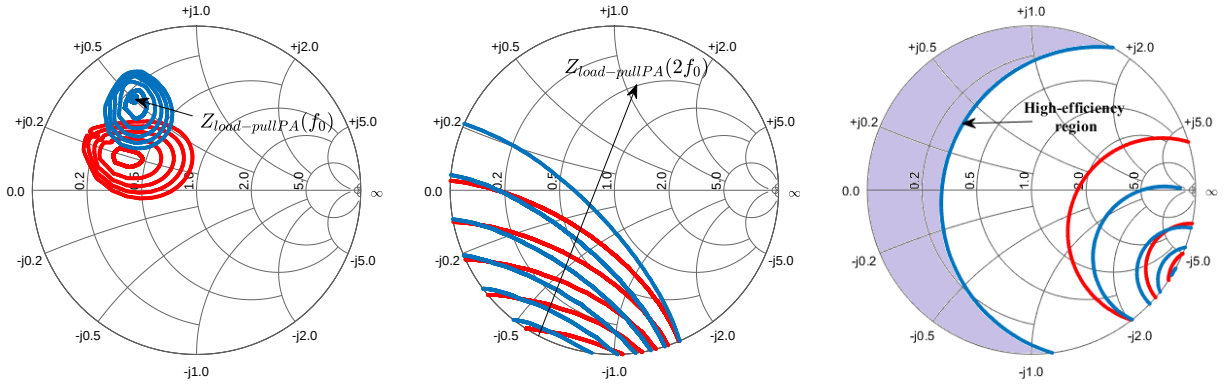

Figure 5.16: PAE (blue line, step 4%) and Output power (red line, step 0.2 dBm) contours from the load–pull simulation of the CGH40006 GaN transistor at (a) Fundamental frequency, (b) Second harmonic frequency (c)Third harmonic frequency.

result in a degraded transmission response and will affect PAE. Namely, maximum power transfer to a conjugate load is only meaningful in the small-signal case [128]. In fact, under large signal conditions,

$$Z_{outPA} \neq Z^*_{load-pullPA}. \tag{5.13}$$

Evidence of this degradation is shown in Fig. 5.17. An ideal filter response is synthesized with a fully canonical second-order filter and considering the complex input impedance of the contour condition found from the load-pull of circuit shown in Fig. 5.15a. Since $Z_{load-pullPA} = 14 + 24.5j\ \Omega$, the filter source impedance should be $Z_{SF} = Z^*_{inF} = 14 - 24.5j$. In Fig. 5.17, the ideal case when the filter is matched is shown in blue line. Since the output impedance of the PA is different from the synthesized filter's source impedance, when this filter is connected to the PA, the filter transmission response degrades as illustrated in the case of green and red lines in Fig. 5.17.

A post-optimization process is usually required to overcome the mismatch produced by the selection of $Z^*_{load-pullPA}$ as filter source impedance. Instead of later tuning the circuit to overcome the mismatch, a design approach leveraging filter synthesis is followed here. To extract the output impedance under large-signal conditions and therefore, gaining some control over the filter response impact and a better assessment of the device's PAE, a robust approach applying the X-Parameters technique is proposed.

X-parameters represent a linear approximation in the Fourier series coefficient domain of a nonlinear function as it varies small distances around a large-signal operating condition. These have been derived based on the polyharmonic distortion (PHD) model introduced by [129]. X-Parameters provide a complete description of the network's behavior, in both the nonlinear and linear regions of operation, being a super set of S-parameters. At low drive levels, all X-parameters become zero except for the ones that correspond to the S-parameters [130]. It is very interesting to observe that PA's output reflection coef-

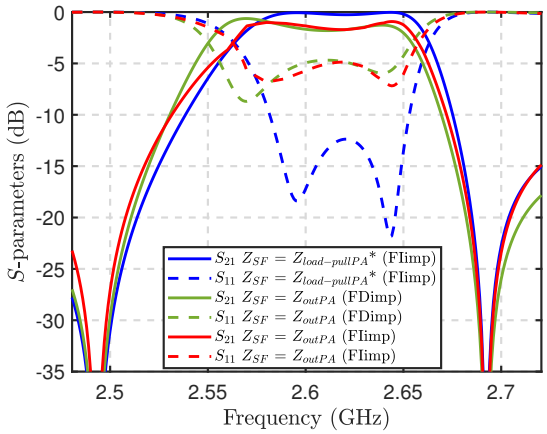

Figure 5.17: Filter transmission response $|S_{21}|$ for three source impedances: complex conjugate frequency-independent impedance (blue, FImp); PA output frequency-dependent impedance (green, FDimp); and PA output frequency-independent impedance (red, FImp). The corresponding $|S_{11}|$ is shown in dashed lines.

ficient, and therefore Z_{outPA}, is not an intrinsic property of the nonlinear amplifier under large-signal drive because it depends on variables outside the amplifier itself like input power, dc biasing, and source and load terminations [131]. This parameters provide essential guidelines regarding design process to follow when implementing output-matching networks in nonlinear systems.

The output impedance under large-signal drive based on the X-parameters can be obtained as follows [132]:

$$Z_{outPA} = X^Z_{2121} = Z_0 \frac{1 + P^2 + X^S_{2121} + X^T_{2121} P^4}{1 + P^2 - X^S_{2121} - X^T_{2121} P^4} \tag{5.14}$$

where $P = e^{j\angle A_{11}}$ and A_{11} is the input pseudowave at the fundamental frequency. $X^S_{21,21}$ and $X^T_{21,21}$ are large-signal reflection coefficients at the output port at the fundamental frequency and the superscripts S and T refer to the linear harmonic superposition and its conjugate, respectively. Regarding the subscript $_{21,21}$, the first and third indices stand for the considered port of the scattered wave and of the incident wave respectively, while the second and fourth allude to the harmonic index of the input fundamental frequency at the considered port for the scattered and for the incident waves, respectively. For computing Z_{outPA}, the terms of (5.14) were extracted using ADS software X-parameter generator for the PA circuit in Fig. 5.15. The parameters extraction was carried out for P_{in}=25 dBm, V_{GS}=-3 V and V_{DS}=28 V. To cover the filter passband, the fundamental frequency was swept from 2.55 to 2.68 GHz, creating a multi-dimension X-parameter data file. For the lumped-elements, ideal capacitors, inductors, and resistors were employed. The transistor nonlinear model was supplied by Cree Inc.

The PA's output impedance can be now estimated using (5.14) for all frequencies of interest under certain input conditions and loaded with 50 Ω and the second-order filter designed at the input and output port respectively. The filter response degradation simulated when this impedance value is con-

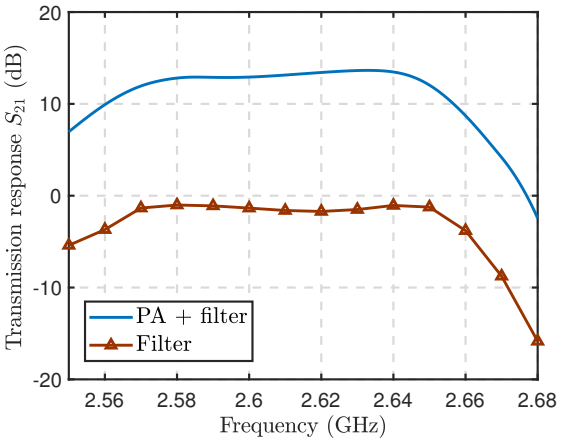

Figure 5.18: Comparison between filter response with the obtained X-parameters and the PA-filter performance.

sidered as Z_{SF} is shown in Fig. 5.17. Green trace displays the filter response as a consequence of the output impedance's frequency-dependent nature, while red trace highlights a frequency-independent performance. Indeed, the filter synthesis is usually carried out by deploying a frequency-independent source impedance, which is considered constant over the whole simulation frequency range, but this assumption leads to an erroneous filter response. When the filter is integrated into the circuit, Z_{SF} is no longer a frequency invariant impedance, so in the filter design process, a frequency-dependent impedance should be used to predict the final circuit performance better.

To prove the soundness of the calculation, Fig. 5.18 shows the comparison between the passive filter considering $Z_{SF} = Z_{outputPA}$ (green trace in Fig. 2) and the large-signal filter-PA transmission response in the passband. The agreement observed in the figure confirms (5.13) and endorses the X-parameters' role, ensuring the necessary accuracy in modeling the output reflection coefficient of nonlinear systems.

On the other hand, to evaluate the filter response and make the assessment and mapping of source impedance impact into the filter transmission response easier, a filter source-pull have been deployed. Source- and load-pull of transistors are widely used in power amplifier design, e.g. [128], but seldomly used with passive networks. Source-pull analysis can be used in a straightforward manner to find limits for the source impedance to bound the IL of the filter across the passband. Fig. 5.19 shows the insertion loss contours of the filter when the source port is not conjugately matched, where $IL = -20\log|S_{21}|$. Each contour encloses a range in the complex impedance plane where the IL in the passband is better than 0.3, 0.6 and 0.9 dB.

The contours were found by finding the IL contours at various frequencies in the band and intersecting them. The discontinuities in the contours are due to the contour intersection at different frequencies, usually defined by the corners and central frequency. The $Z_{outPA} = 11 - j8\,\Omega$ found from (5.14) is indicated in Fig. 5.19 with a cross marker, which corresponds to $IL = 1.7\,$dB. For this value, the PAE drops from 76 % (maximum) to 51.4 % due to the selection of $Z_{SF} = Z^*_{load-pullPA} = 14 - j24.5\,\Omega$.

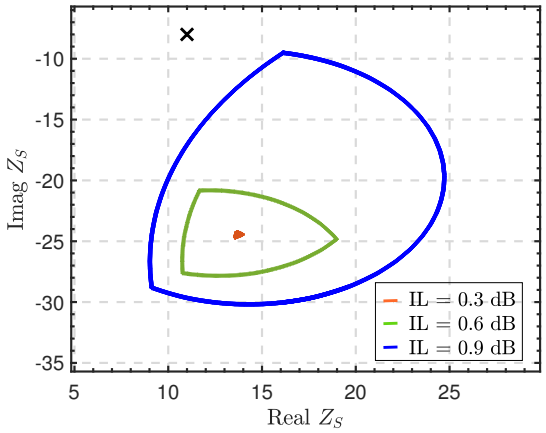

Figure 5.19: Contours of constant insertion loss for a passive filter design from Fig.5.17, obtained by source-pull simulations for a frequency range from 2.59 to 2.65 GHz. The contours discontinuities are defined by the corners and central frequencies. The position of the extracted Z_{outPA} from (5.14) corresponding to an IL=1.7 dB is also cross marked for comparison purpose.

The filter's reactive elements are ideal in this example. However, in real cases, the ohmic losses (≈0.3 dB) affects directly the efficiency, reducing it to 48 % [133]. At the end of Section 5.5.5 a numerical comparison is carried out to emphasize the advantages of the design approach.

Source-pulling a designed filter allows to obtain a bound for filter response degradation. This accurate and fast procedure enables the redesign of the filter to decide a filter configuration with a lower source-impedance sensitivity. The field experimentation shows that without a careful design, a severe degradation can be observed.

5.5.4 Applying the Complex Load Filter Synthesis Theory

An extracted pole topology was selected to synthesize the filtering network. In particular, the inline fully canonical topology represented in Fig. 5.20a was employed. This topology does not implement cross-coupling for a fully canonical realization. Additionally, if the transmission zeros are far enough, only the source and self-coupling matrix entries must be modified as occurs in all-pole networks. Moreover, this network is considered due to the modularity and flexibility provided. The transmission zeros can be placed arbitrarily and controlled directly with the natural series resonances.

As commented in the chapter's introduction, the proposed approach includes a tough control and sufficient accuracy of the out of band phase reflection coefficient. The additional phase value ϕ_{add_11} can be selected for placing the reflection coefficient at the second harmonic frequency just in the right place for increasing efficiency. Although the third harmonic filter termination can not be directly controlled with the synthesis method up to now, a good approximation can be obtained with a wise selection of the second harmonic termination to achieve good PA figures of merit. As the objective is to evaluate how to

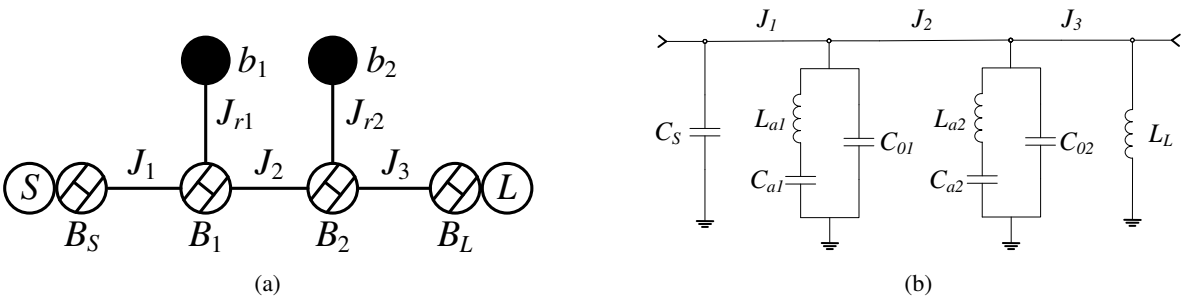

Figure 5.20: (a) Nodal diagram of an inline-topology filter with 2 dangling resonators (b) Circuital diagram of the fully canonical second-order filter.

control the impact of the filter source mismatch on efficiency, we will not take further consideration with the third harmonic.

In order to control the second-harmonic termination at filter input reference plane, the polynomial $F(s)$ have to be modified for controlling the input reflection coefficient phase as in (5.1). The additional phase of the reflection coefficient (ϕ_{add_11}) is introduced in the definition of the return loss as follows:

$$S_{11}(s) = e^{j\phi_{add\_11}} \frac{F(s)/\epsilon_r}{E(s)}. \tag{5.15}$$

To introduce the control of the second harmonic in the filter synthesis, ϕ_{add_11} must be related to the desired input impedance Z_{inF} evaluated at $2f_0$, obtained from a second harmonic load-pull analysis, and the source impedance Z_{SF}. The input impedance is then defined as

$$Z_{inF}(s) = \frac{{Z_{SF}}^* + S_{11}(s)Z_{SF}}{1 - S_{11}(s)}. \tag{5.16}$$

Substituting (5.15) in (5.16), ϕ_{add_11} is calculated as

$$e^{j\phi_{add\_11}} = \frac{E(s)\epsilon_r}{F(s)} \frac{Z_{inF}(s) - {Z_{SF}}^*}{Z_{inF}(s) + Z_{SF}} \tag{5.17}$$

Once the ϕ_{add_11} is defined, the $F(s)$ polynomial is recalculated with (5.1) to continue with the matrix development (5.3).

A second-order fully canonical filter is selected to drive the experimental validation. The synthesis follows the extraction procedure described before with the following configuration: normalized transmission zeros Ω_{TZ}= [-30.25, -17.90] rad/s, RL= 18 dB and $\phi_{add\_11}(^\circ)$= -34. The inline topology with dangling resonators of Fig. 5.20a allows the allocation of TZs in the upper and/or lower stop-band without any restriction, requiring positive NRN for the lower band and negative NRN for the upper band. The sign in the normalized domain determines the bandpass domain's nature, being a capacitor a positive

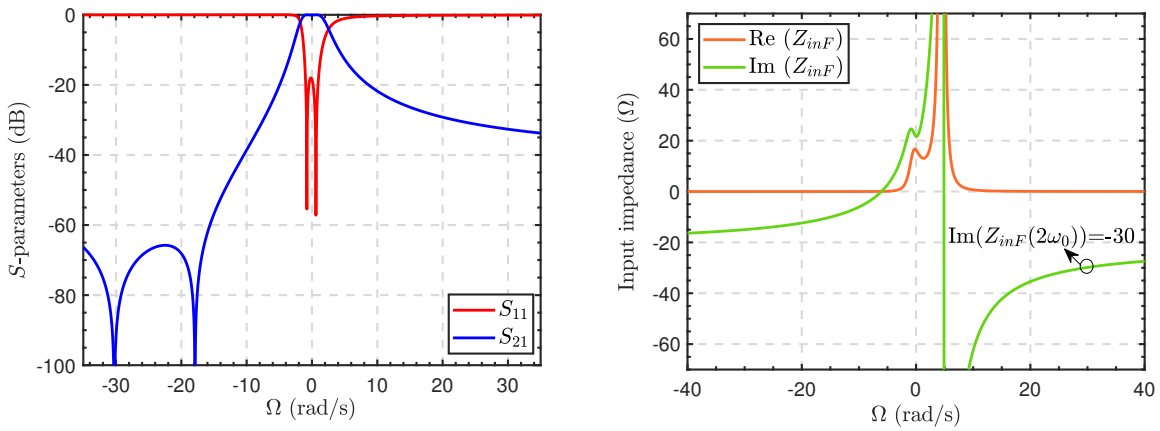

(a) (b)

Figure 5.21: (a) Filter response in the low-pass domain. (b) Filter input impedance in the low-pass domain.

NRN. To demonstrate the flexibility of the topology, both TZs were placed in the lower stop-band as is shown in Fig. 5.21a.

The filter source and load impedances were set to $Z_{SF} = 14 - 24.5j\ \Omega$ and Z_{LF} = 50 Ω, respectively. To obtain $Z_{inF}(2f_0) = Z_{load-pullPA}(2f_0) = -30j\ \Omega$, (5.17) was evaluated at $2f_0$, attaining $\phi_{add\_11} = -34°$. Fig. 5.21b shows the filter input impedance in the low-pass domain and the accuracy of the result. The elements of the low-pass nodal representation depicted in Fig. 5.20a were obtained as a result of the extraction procedure. Once all low-pass elements have been extracted, a narrow band frequency transformation and impedance denormalization were carried out.

5.5.5 PA-Filter Module Experimental Validation

To verify the proposed co-design approach and considering the points mentioned above in Section 5.5.3 and 5.5.4, a filtering PA (FPA) was designed. Fig. 5.22 displays an schematic of the FPA module. The electromagnetic simulation of the whole circuit was carried out with Ansys HFSS.

The PA load-pull simulation achieves a maximum efficiency of 76 % at $Z_{load-pullPA}(f_0) = 14.0 + 24.5j\ \Omega$, $Z_{load-pullPA}(2f_0) = -30j\ \Omega$ with a 3^{rd} harmonic termination of $Z_{load-pullPA} = Z_{inF}(3f_0) = 1 + 12.3j\ \Omega$. PAE contours at fundamental frequency are shown in Fig. 5.23 (green trace). On the other hand, the filter was designed as a second-order Chebyshev type centered at 2.63 GHz with RL= 18 dB, FBW = 3.2%, and 2 TZs at the lower stop-band. To overcome the efficiency reduction produced by the mismatch between Z_{outPA} and $Z^*_{load-pullPA}$ discussed in Section 5.5.3, and ensure a well-shaped filter, $Z_{SF} = 22 - 18j\ \Omega$ was selected. The filter's source impedance was estimated with (5.14). Additionally, a filter's source-pull was carried out to evaluate the source impedance impact in the transmission response (see Fig. 5.23, red trace). The minimum attained insertion loss is IL= 0.9 dB.

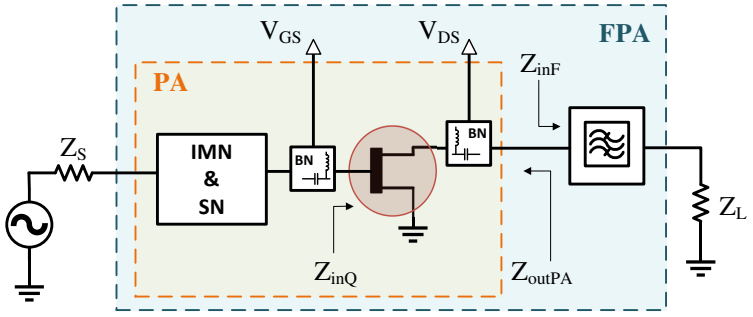

Figure 5.22: Single-stage power amplifier with a co-designed filter. The PA consists of an input matching (IMN), stability (SN) and input bias networks (BN) networks, and an output bias network (BN). For the filter power amplifier (FPA), an integrated bandpass filter is designed to present a complex impedance Z_{inF} to the transistor for high-power and/or high-efficiency operation.

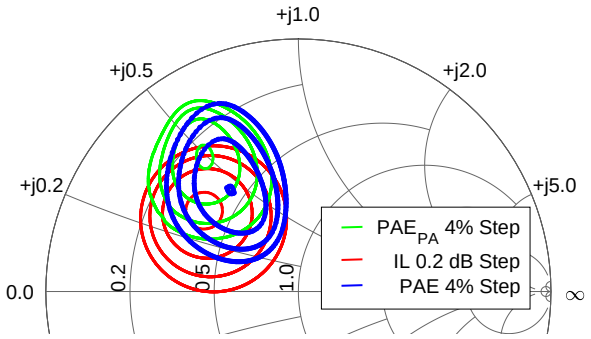

Figure 5.23: Contours of simulated PAE_{PA} from the load-pull at fundamental frequency, IL from the filter's source-pull and PAE calculated. The peak PAE_{PA} is 76 %, the minimum IL is 0.9 dB and the maximum PAE is 55.8 %.

The FPA module's effective efficiency is the resulting efficiency of the PA cascaded with a filter. Considering the PA's gain (G) and the loss produced by the cascaded passive network (L), the FPA's PAE is given by:

$$PAE = PAE_{PA}\left(\frac{GL-1}{G-1}\right) \tag{5.18}$$

where PAE_{PA} is the efficiency of the PA block. For high G values,(5.18) can be approximated to

$$PAE = PAE_{PA} * L = PAE_{PA} * 10^{-IL(dB)/10} \tag{5.19}$$

Contours line are generated with the resulting values (see Fig. 5.23, blue trace) and maximum PAE = 55.8 % is obtained at $Z_{LPA} = 22.6 + 21.6j\ \Omega$. As expected for well-matched networks, $Z^*_{LPA} \approx Z_{SF}$. Comparing this result with the obtained in Section 5.5.3, improved efficiency is accomplished. It proves that the proper selection of the filter's source generates the best efficiency and simultaneously takes care of filter transmission response.

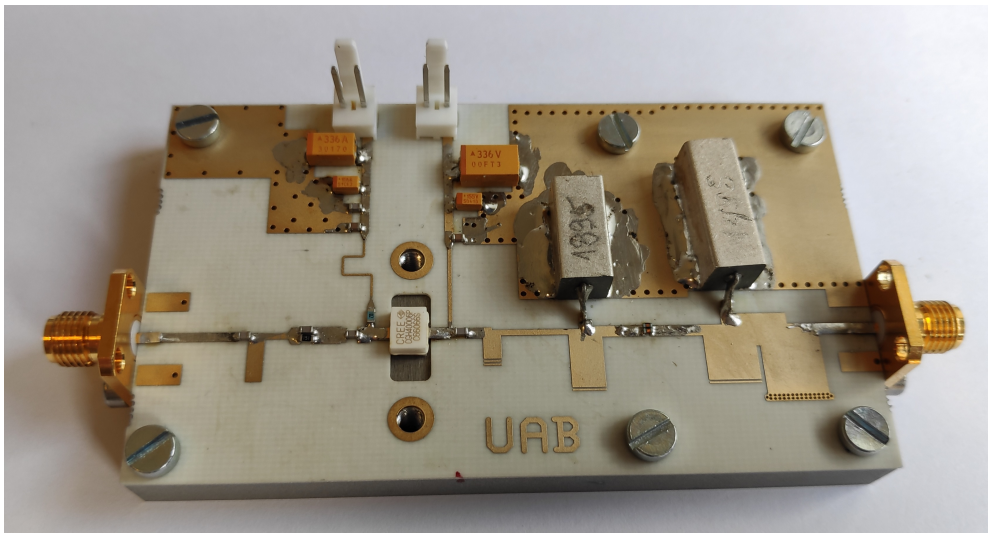

Figure 5.24: Photograph of the manufactured FPA module.

The fabricated filtering FPA device is shown in Fig. 5.24. The module with 74x48 mm dimensions was fabricated on 20 mil Rogers RO4003 substrate ($\epsilon_r = 3.55$).

For the filter realization,(see Fig. 5.20b), the inverters J_i were implemented using an equivalent π capacitor circuit, while the B_i were transformed as capacitances (C_0). A compact filter is accomplished by combining the π-networks and capacitive elements with source and load elements (C_S and L_L) and transforming them into a distributed one. The chosen technological solution for the dangling resonant nodes transformed to series LC resonators (L_a, C_a), has been based on square cross-section coaxial resonators from $T - Ceram$ with characteristic impedance $Z_0 = 10\ \Omega$ and dielectric constant $\epsilon_r = 36.5$. Bandpass filters made with coaxial resonators are a kind of filter technology that provides high-performance features like high selectivity, high power handling, excellent rejection, low passband insertion loss, etc. The resonators are made of high dielectric materials constant ϵ_r, reducing their size. Consequently, all the electrical characteristics are compacted in a small shielded structure, which makes these filters suitable for applications where small-sized devices are necessary. The selected resonator cross-section of 6 mm at f_0 provides a quality factor of $Q = 750$ as a typical value. To introduce TZs at 1.7 GHz and 2.15 GHz, two half-wave open circuited coaxial resonators with length $L = 17$ mm and $L = 13$ mm were implemented, respectively. Appendix A describes the circuital transformation procedure of the second-order filter from Fig. 5.20b to the implemented distributed filter with coaxial technology.

As mentioned in [109], accurate simulation of the coaxial resonator tab is fundamental to model the parasitics and propagation effects in this transition. Fig. 5.25a shows the 3-D simulated resonators in HFSS, including the tab transition and the reference plane. Moreover, checking Fig. 5.25b, the resonant frequencies that introduce the TZs can be observed. Due to the periodic frequency behavior of the coaxial resonator, a second series resonance falls in the upper stop-band, introducing an extra TZ and achieving a better skirt selectivity, as can be seen in Fig.5.25c.

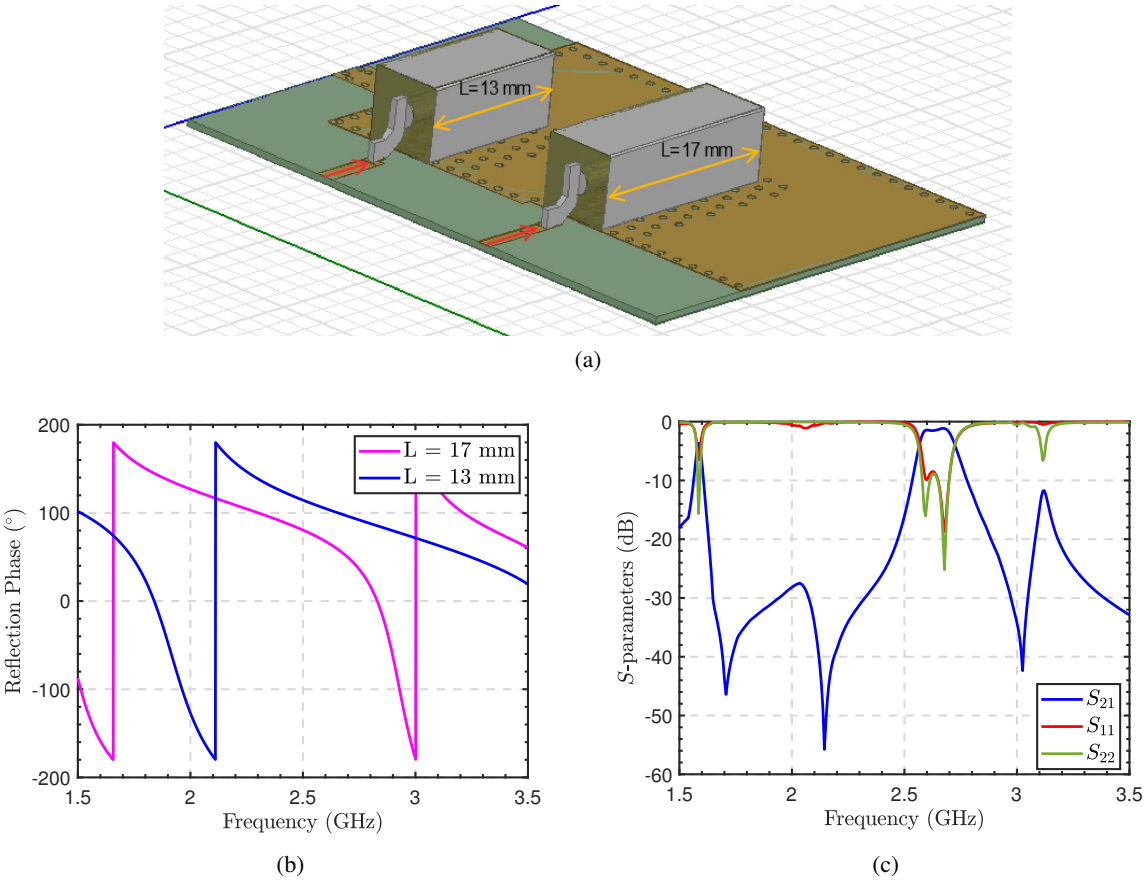

Figure 5.25: (a) Coaxial resonator model in HFSS where red arrows mark the reference simulation plane. (b) Reflection coefficient phase of the simulated resonators showing the position of the TZs. (c) Simulated filter response.

Continuous-Wave Measurements Setup and Results

For computing the FPA figure of merits, a harmonic-balance (HB) circuit simulation was conducted in ADS from Keysight. For the lumped-elements, models provided by Modelithics for Johanson Technologies capacitors and inductors, and resistors from KOA were employed. The fabricated circuit has been tested using an experimental setup with an Agilent network analyzer (PNA-X N5242A), which is shown in Fig. 5.26. The FPA was boosted by a driver amplifier (ZHL-2W-63-S+ from Mini-Circuits [134]) and attenuated before the data acquisition; the set-up includes a power sensor (U2002H from Keysight) for calibrated power measurements. Fig. 5.27 illustrates the diagram of the employed measurement setup and the relevant powers in-between. The transistor gate was biased at -3 V, resulting in a quiescent current of 67 mA at $V_{DS} = 28V$. The experiment was conducted over the band from 1.5 to 3.5 GHz.

The selected driver amplifier provides +33 dBm output power P_{driver} at saturation. The amplifier operates on a 28V DC supply and comes housed in compact aluminum alloy case with SMA connectors, a built-in bracket for mounting, and an optional heat sink for efficient cooling. This broadband amplifier does not have a flat gain over the band, as shown in Fig. 5.28. This behaviour forces to calibrate its output

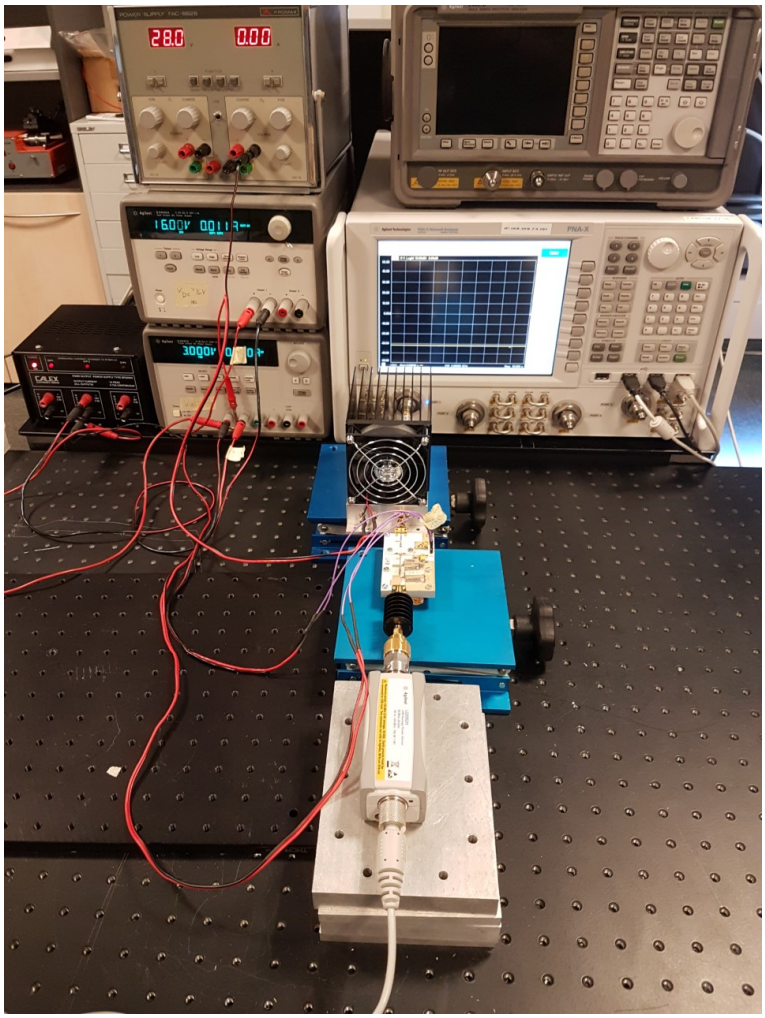

Figure 5.26: Experimental measurement setup with an Agilent network analyzer (PNA-X N5242A) followed by a 20 dB attenuator and a driver amplifier (ZHL-2W-63-S+) with 44 dB maximum gain at $f = 2.45$ GHz. For measuring the output power, a 30 dB attenuator was placed continued by the calibrated power sensor (U2002H)

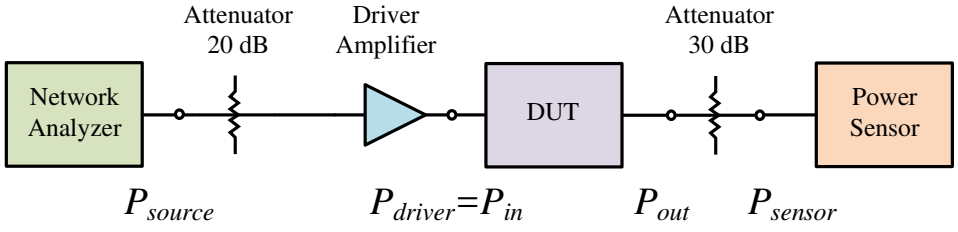

Figure 5.27: Diagram of the continuous-wave measurement setup and the main powers.

power (P_{driver}) in the setup at the first step before the measurement in order to obtain equal power at the input of the DUT P_{in} (in this case our PA-filter co-designed) for all frequencies evaluated.

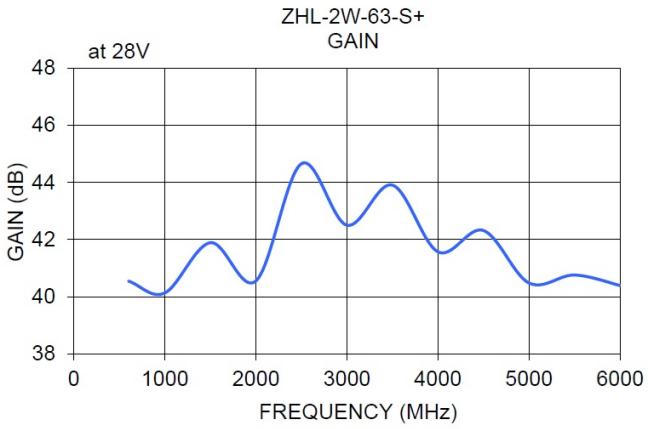

Figure 5.28: ZHL-2W-63-S+ Gain over the operation frequency range for a voltage supply of 28 V [134].

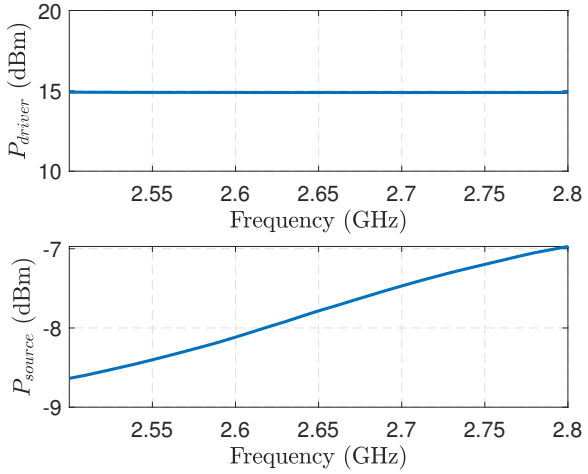

Figure 5.29: Calibration of the input power considering the chain PNA-X; Attenuator, Driver.

This calibration was carry out sweeping the PNA-X's frequency and the power P_{source} from -12.8 to 7.2 dBm. Considering the high gain of the driver with a maximum $G = 44.5$ dB at $f = 2.45$ GHz and the maximum leveled output power of the PNA-X 13 dBm [135], a 20 dB attenuator from Mini-Circuits (VAT 20+) was placed between them to ensure obtaining the necessary driver's output power range from 10 to 30 dBm to carry out the test. A 2-D matrix was constructed with the corresponding driver's output power P_{driver}. Having known the gain provided by the attenuator + driver array at each frequency, the required PNA-X's power to set a constant driver's output power can be calculated through a simple interpolation of the resulting matrix. Fig. 5.29 displays the calibrated $P_{driver} = P_{in} = 15$ dBm from 2.5 GHz to 2.8 GHz. The graph illustrates the correlation between the calculated P_{source}'s value and the measured P_{driver}. As the frequency increases, the required PNA's power increases too. This behaviour is due to the decreasing gain of the driver amplifier over the selected frequency's range and the natural compensation needed to equalize P_{driver}.

A second 30 dB medium power attenuator from Huber+Suhner [136] was employed to prevent any

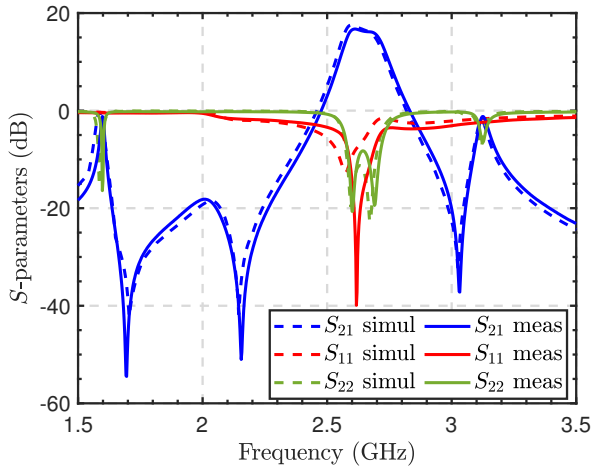

Figure 5.30: Comparison of simulated and measured small-signal S-parameters of the FPA circuit for P_{in}=0 dBm. The measure has a 20 MHz positive shift with a good agreement in a wideband range. High OoB rejection is achieved thanks to the TZs.

damage to the power sensor considering the internal sensor dynamic range from -50 to +30 dBm [137]. The last attenuator was also characterized over the frequency and the attenuation values were saved for a further calculation of $P_{out} = P_{sensor} - IL_{Atten30dB}$. FPA's PAE and gain were calculated with he leveled P_{in}, output power P_{out}, and DC current and voltages measured and stored.

The module's simulated and measured small-signal responses are displayed in Fig. 5.30. A 20 MHz frequency shift is observed in the passband, but an excellent agreement in the out-of-band (OoB) region. The implemented TZs provide a high OoB rejection of 35 dB from 1.63 GHz to 2.3 GHz. The graphic also shows the highly-selective bandpass response obtained with this design. The measured S_{11} denotes the excellent match at the central frequency f_0 produce by the IMN. On the other hand, the output return loss S_{22} describes distinctly the poles associated with the 2nd-order Chebyshev filter.

The measurement of Gain and PAE at the center frequency as a function of P_{out} are shown in Fig. 5.31. The measured 1-dB Gain compression occurs when the out power reaches 35 dBm, and the highest PAE of 50.4% is achieved when the output power is 37.5 dBm. Fig. 5.32 shows the measured output power, efficiency, and gain across the frequency under 27-dBm input stimulus (large-signal). The filtering shape in a wideband region is shown in the inset. As a result of the well-matched filter obtained in the design stage considering Z_{outPA}, a relatively constant Gain (in-band ripple $<$ 0.5 dB) and P_{out} can be appreciated in the passband.

The lower efficiency compared to previous works exhibited in Table 5.9 can be explained by the lack of higher harmonic terminations in our design, since only fundamental and second-harmonic were considered in the filter design as was discussed in Section 5.5.4. However, our objective of shapping the filter response was successfully achieved. Moreover, the resonator technologies from references [108, 120, 123] feature a higher unloaded Q values than our coaxial resonators, resulting in a lower in-band loss and consequently a higher PAE.

Table 5.9: Comparative Table

Ref	Order	Harmonic suppression	Resonator Technology	Amplifier Type	f_0 (GHz)	FBW (%)	G (dB)	P_{out} (dBm)	PAE (%)	Rejection $f_0 \pm 2*f_0*$FBW (dB)	In-band Gain ripple <0.5dB
[138]	2	2nd	Microstrip	Hybrid MOSFET	2.6	3.8	14.3	42.5	46	15	No
[122]	4	4th	Microstrip	Hybrid GaN PA	2	20	16.2	40.5	62	46.2	No
[108]	2	3rd	EVA Cavity	Hybrid GaN PA	3	3	10	40	68	20	Yes
[123]	3	3rd	EVA Cavity	Hybrid GaN PA	3.1	1.7	15.5	40	67	42	No
[120]	2	3rd	Cavity-Microstrip	Hybrid GaN PA	2.4	11	18.2	41	71	38	No
[109]	2	3rd	Ceramic Coaxial	Hybrid GaN PA	4.7	9	13.7	36	55	23	No
This thesis	2	2nd	Ceramic Coaxial	Hybrid GaN PA	2.64	3.2	10.7	37.5	50.4	35	Yes

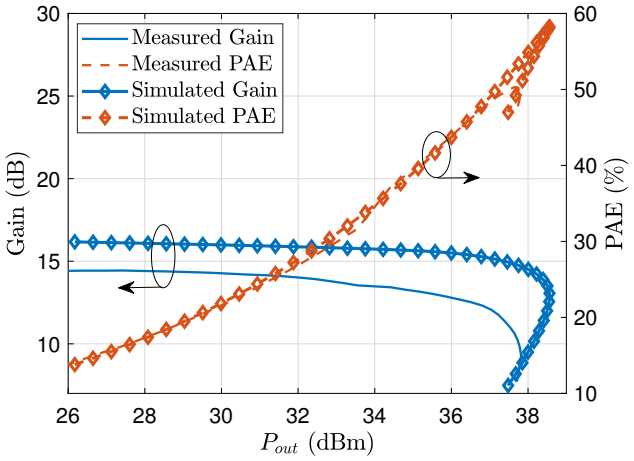

Figure 5.31: PAE and Gain vs P_{out} at the center frequency f_0=2.64 GHz.

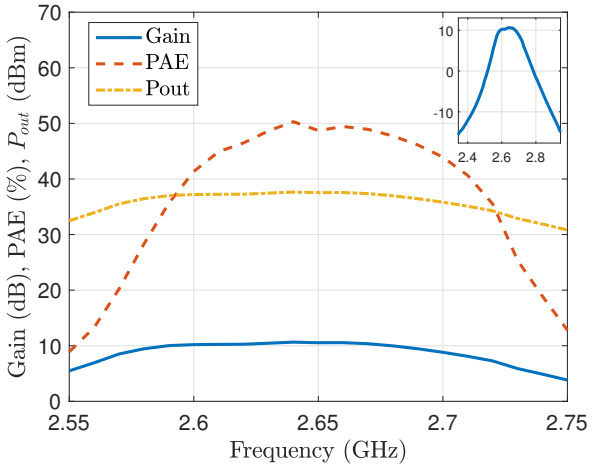

Figure 5.32: Measured PA-filter performance vs. frequency at P_{in}= 27 dBm. The inset with the measured gain evidences the filtering properties in a wider bandwidth.

In addition to the common figure of merits related with the amplifiers, the OoB rejection is added to convey the effect of introducing TZs in the filtering device, leading to steeper skirts according to the band specifications. Furthermore, the in-band gain ripple proofs the insertion loss stability in the

passband. These two features should be taken into account when we are evaluating a FPA since FPA design requires a trade-off between efficiency, output power and filter response to obtain the desired performance.

5.6 PA-Filters Co-design: Dual Band Case

Currently, carrier aggregation demands energy-efficient transmitters with high signal quality in a multi-frequency scenario; therefore the theory presented before should be extended to a multi-channel scheme. This section develops a high-efficiency dual-band dual-output PA for carrier aggregation. Several solutions have been exposed in the literature to design multi-frequency PAs for concurrent and nonconcurrent operation scenarios. In the concurrent scenario, a single PA amplifies multiple bands simultaneously instead of using separate amplifiers operating at broadly separated frequencies. The concurrent operation is particularly challenging as it often results in lower efficiency, degraded spectral emissions, and adjacent channel power ratio (ACPR) [139]. On the other hand, nonconcurrent performance comprises the alternation of stimuli at different frequencies using one transistor.

Some approaches are based on using multiple matching networks which provide the impedance transformation from complex to real at multiple frequencies [140], and also adding a dual-band filtering second stage that ensures the matching from real to 50 Ω impedance termination [141]. Alternately, in [142] it is used independent narrow bands PAs followed by an OMN at fundamental frequency connected to a wideband carrier combined network implemented as a diplexer. For dual-output scheme is also recurrent the use of optimized OMN designed to have frequency-selective characteristics [143, 144]

To overcome the drawbacks that previous works have presented for multifrequency PAs, and to simplify the design, multiplexer theory and co-design techniques are exploited together in this section to achieve a lower circuit complexity and higher efficiency. Fig. 5.33 shows the conventional multi-carrier cascade topology and the proposed co-designed structure. Following the guideline proposed previously, the exact synthesis technique is applied for controlling the complex input impedance at the fundamental frequency. In the single-channel case, the reflective termination at the second harmonic of a PA filtering matching network was controlled simultaneously, providing high efficiency. In contrast, the multi-frequency approach needs to accommodate the input phase employing the same foundations used for phase-matching filters in duplexers/multiplexers. Mixing both approaches turns out in an effective co-design strategy allowing lower complexity and size.

To demonstrate the feasibility of the aforementioned integration, a dual-output, dual-band RF PA-filter module (DO-DB) was designed and simulated following the procedure explained for the synthesis of filters with complex impedance terminations. To simplify the analysis and maintain the spotlight on the filtering network, a nonconcurrent operation was selected for the PA characterization. The merging of both approaches, multiplexer and complex impedance, apply for multiple frequencies, but a duplexer was selected for illustration purpose. The first filter was designed to address B7-Tx with f_1= 2.535 GHz

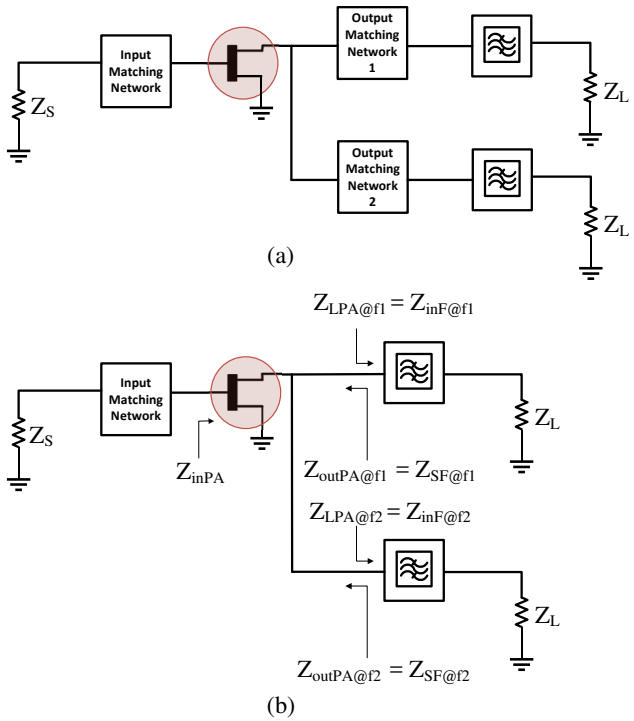

Figure 5.33: Dual band power amplifier schematic circuit (a) Conventional topology with OMNs and bandpass filters, and (b) Co-designed bandpass filters.

and the second was sub-band 41 at f_2=2.63 GHz with an FBW= 3.0% . Both bands have been used in previous examples through this dissertation.

The selected RF power device is the same GaN transistor from section 5.5, Cree CGH40006P. For transistor characterization, a load-pull simulation was carried out with Agilent's Advanced Design System (ADS) setup and employing the manufactured transistor model provided by Cree. In contrast with the previous validation example with a single-channel configuration, the load–pull simulations were performed at the two central frequencies f_1 and f_2 without optimizing the harmonic terminations. The load-pull reference plane displayed in Fig. 5.15 was used also for this example. As the input matching network was designed for the B41 sub-band, the same circuit fits this example thanks to the relative narrow duplex spacing between the channels. To improve the reflection at the input port for both bands ($S_{11} < -10$ dB), C_3 has been modified. For the sake of clarity, the updated figure is duplicated here in Fig. 5.34.

Because the additional phases $\phi_{add\_11,1}$ and $\phi_{add\_11,2}$ concerned with the filter's duplexer are focused on remove the duplexer loading effect instead of the harmonic impedances, at $2f_1$, $2f_2$, $3f_1$ and $3f_2$, the filters load the preceded PA. Harmonic terminations should be considered for each filter fundamental frequency load-pull simulation to obtain an accurate result. An iterative design procedure is required to compute the impedance resulting from the two filters' duplexer at the second and third harmonics looking from the reference plane ($Z_{LPA\_duplexer}$). Table 5.10 summarizes the values used for the fundamental

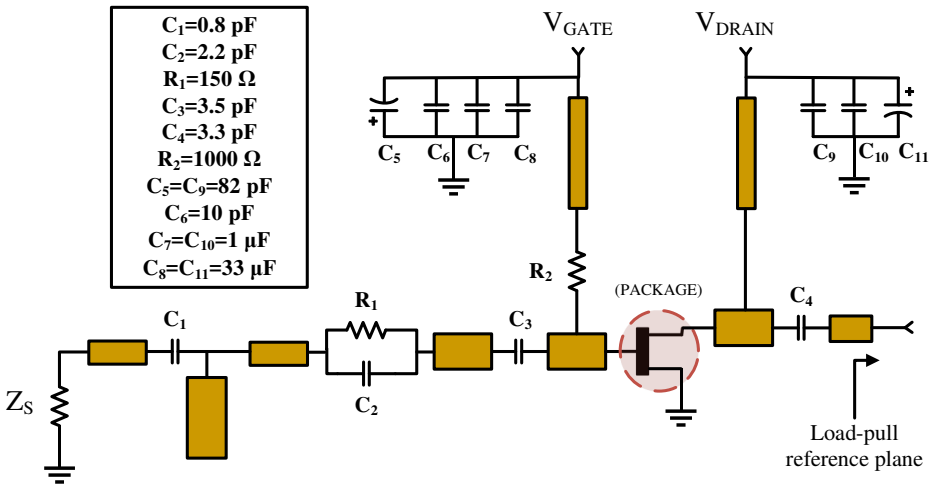

Figure 5.34: Circuit schematic including IMN, RC stability, and Gate and Drain bias networks

Table 5.10: Impedances presented after the junction due to the parallel combination of the filters

	$2f_1$ (5.07 GHz)	$2f_2$ (5.26 GHz)	$3f_1$ (7.605 GHz)	$3f_2$ (7.89 GHz)
$Z_{LPA\_duplexer}$ [Ω]	$11.673j$	$13.82j$	$6 - 175.58j$	$1.4 - 87.72j$

load-pull simulations. Fig. 5.35 illustrates the PAE and output power load-pull for the fundamental frequencies f_1 and f_2. The achievable maximum PAEs are 71.5 % at $Z_{load-pullPA@f_1} = 10.2+22.4j\ \Omega$ and 75.90 % at $Z_{load-pullPA@f_2} = 12.6 + 18j\ \Omega$. As expected, the maximum PAEs are obtained at similar impedance because of the channel's proximity.

In contrast to the simple duplexer network where the source load was contemplated as frequency independent, the PA-duplexer co-design case considers that the PA output impedance is frequency dependent. As was commented in the former chapter, the calculus of Z_{outPA} is based on X-parameters and relies on the reflection coefficients produced by the PA load (see equation (5.14)). Therefore, the estimation of $Z_{outPA@f_1}$ and $Z_{outPA@f_2}$ is a cumbersome and iterative process. For this example, $Z_{outPA@f_1} = 12 - 15j\ \Omega$ and $Z_{outPA@f_2} = 10 - 14j\ \Omega$ were computed. The theory related to the paramount importance of differentiating Z_{outPA} and $Z_{load-pullPA}$ was discussed in 5.5.3, and applies in the same manner to the duplexer case.

The filters were designed independently considering the source impedances $Z_{SF_1} = Z_{outPA@f_1} = 12 - 15j$ and $Z_{SF_2} = Z_{outPA@f_2} = 10 - 14j$, and the required open-circuit condition for the counter band. The modifying phase ϕ_{add_11} was computed by (3.39) to fix the duplexer condition in each case. Both filters start in series resonator configuration. Technological constraints like uniform coupling coefficient k^2_{eff} and performance specifications like high cross-isolation were taken into account. The input parameters for the synthesis process are listed below:

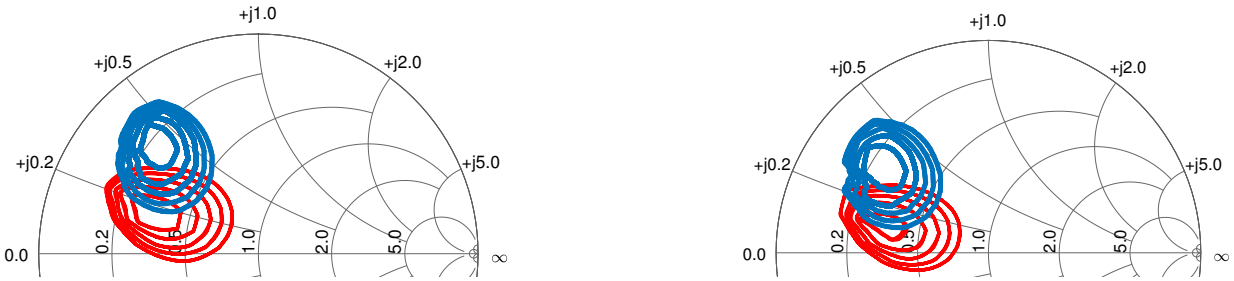

Figure 5.35: PAE and Output power contours from the load–pull simulation of the CGH40006 GaN transistor at fundamental frequency: (a) B7-Tx (b) B41-Tx. PAE: blue line (step 2%) and output power: red line (step 0.2 dBm).

B7-Tx

- Ω_{Tx} (rad/s): { 1.3625, -2.4533, 1.8162, -1.9938, 2.6404 }
- RL (dB): 15
- $\phi_{add\_11}(^{\circ})$: -45.1

B41-Tx

- Ω_{Rx} (rad/s): {1.8421, -2.3342, 2.1095, -2.3224, 2.7867 }
- RL (dB): 20
- $\phi_{add\_11}(^{\circ})$: 40.73

The duplexer schematic is represented in Fig. 5.36 being the extension of Fig. 5.34 for the complete DO-DB power amplifier. The input external elements L_S were merged in one element at the input of the common port. Table 5.11 summarizes the extracted values of the BVD model for the duplexer to obtain $k^2_{eff} = 6.76$ %. Comparing the additional phase ϕ_{add_11} for B7-Tx in the duplexer example of Chapter 3, similar values can be appreciated since B7-Rx and the selected sub-band B41-Tx have comparable center frequencies. The current example addresses low input complex source impedance in the synthesis process (vs 50-Ω), therefore, to fulfill the technological acoustic constraints, high C_0 values in parallel resonators and external inductive elements appear in the outcome. In B7-Tx case, L_{ext} are placed in series with the first and second resonator to assure technological feasibility. The presented example has not been optimized, so a post-processing procedure could tune the value of the BVD elements.

For the simulation, acoustic resonator quality factors $Q_{AW} = 1500$ were selected, while for the input/output and external inductive elements $Q_L = 50$. The smaller static capacitors yield for both filters in resonators 3 and 5 contribute to the total area reduction but imply several resonators cascading to deal with the power density. Transmitter filters have to tackle high power levels guaranteeing a device's

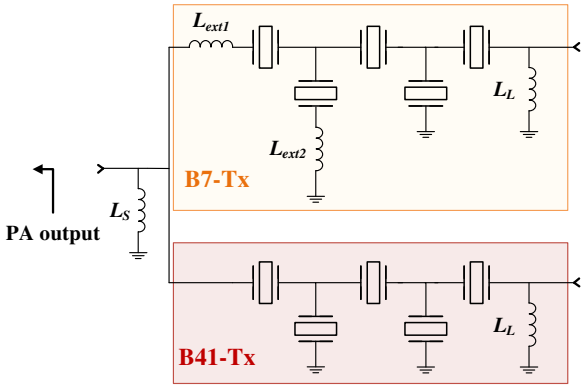

Figure 5.36: Duplexer's schematic representation of the DO-DB PA-filter module.

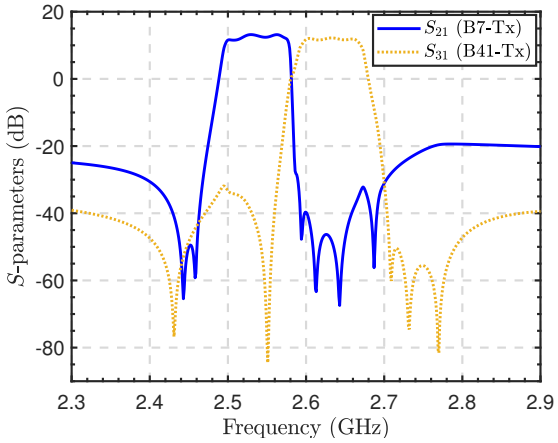

Figure 5.37: S-parameters under non-concurrent CW stimulus P_{in} = 25 dBm.

minimum lifetime. To evaluate the power density most critical points, the upper skirt passband is selected [9].

The simulated scattering parameters under non-concurrent large-signal stimulus P_{in}=25 dBm is observed in Fig. 5.37. The frequency highly-selective shape corresponds with the expected filter response. The in-band ripple is about 1.3 dB and 0.6 dB due to the intrinsic Chebyshev response and the inaccuracy of the estimated Z_{outPA} for B7 and B41 band respectively. Furthermore, the equivalent duplexer input impedance seen from the load-pull reference plane ($Z_{LPA\_duplexer}$) presents a short circuit at specific frequencies, introducing additional transmission zeros in the lower band at 2.43 GHz in B41-Tx, and in the upper band at 2.68 GHz in B7-Tx. These zeros contribute then to the OoB rejection in each case.

An input power swept was performed to evaluate the effective efficiency and gain of the DO-DB module for an input power range between 10 and 30 dBm. The simulation results at central frequency for each band are depicted in Fig. 5.38. The simulated 1-dB Gain compression for B7-Tx occurs when

Table 5.11: PA-Duplexer example's BVD elements

Resonator	L_a (nH)	C_a (pF)	C_0 (pF)	k^2_{eff}	L_{ext} (nH)
B7-Tx					
1	14.77	0.27	4.6	6.76	0.57
2	11.77	0.35	6.03	6.76	0.15
3	67.4	0.06	0.99	6.76	
4	10.09	0.41	7.07	6.76	
5	75.07	0.05	0.86	6.76	
L_S(nH)			2.91		
L_L(nH)			2.44		
B41-Tx					
1	33.6	0.11	1.86	6.76	
2	12.72	0.30	5.2	6.76	
3	102.03	0.03	0.6	6.76	
4	12.01	0.32	5.47	6.76	
5	85.6	0.04	0.71	6.76	
L_S(nH)			1.25		
L_L(nH)			3.45		

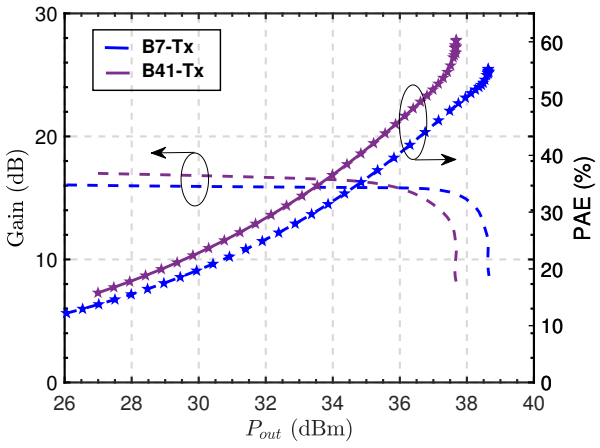

Figure 5.38: PAE and Gain vs P_{out} at the center frequencies f_1=2.53 GHz and f_2=2.63 GHz .

the out power reaches 37.9 dBm, and the highest PAE of 55.17% is achieved when the output power is 38.6 dBm. For B41-Tx, the simulated 1-dB Gain compression occurs when the out power reaches 35.7 dBm, and the highest PAE of 60.3% is achieved when the output power is 37.6 dBm.

To evaluate the obtained PA figure of merit, namely, output power, efficiency, and gain; a simulation of a single-band excitation across frequency under CW was carried out. Fig. 5.39 shows the outcome of this simulation. For the designed value P_{in}=25 dBm, the module attained: P_{out}=38.43 dBm, Gain=13.43 dB and PAE=52.4 % for f_1, and P_{out}=37.6 dBm, Gain=12.6 dB and PAE=57.2 % for f_2. As a result of the well-matched filter obtained in the design stage considering Z_{outPA}, a relatively constant Gain

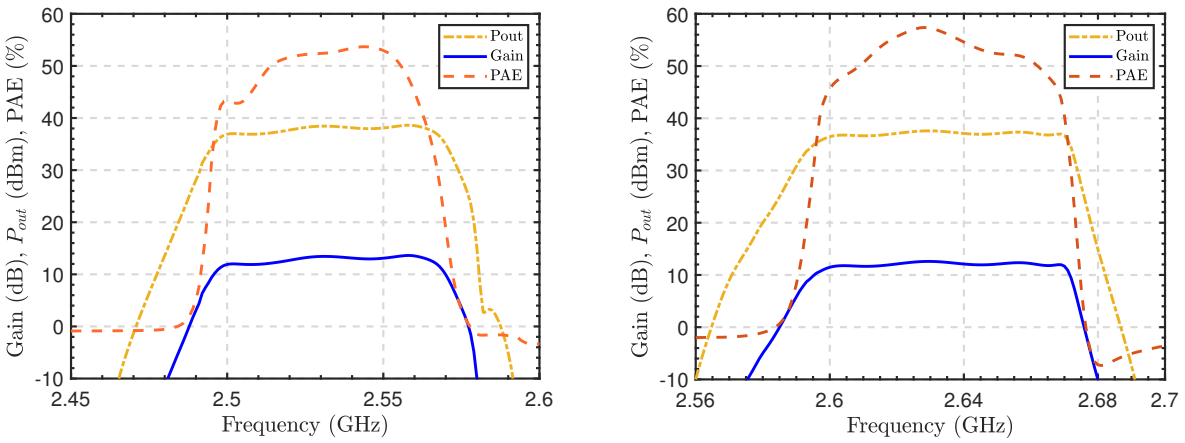

Figure 5.39: Simulated PA-filter performance vs. frequency at P_{in}= 25 dBm: (a) B7-Tx and (b) B41-Tx

.

(in-band ripple $<$ 0.8 dB) and P_{out} can be appreciated in the passband. Despite the lack of optimized harmonic terminations, high efficiency is obtained over the passband frequencies better than 40% and 45% for B7-Tx and B41-Tx respectively. When comparing with other published works like [144], it is important to consider that the filter losses and mismatch are included in the obtained result due to the PA-duplexer integration, while in [144] and other works, only the non-filtering OMNs were included.

5.7 Chapter Summary

In this chapter, a synthesis methodology for acoustic ladder filters with complex impedance terminations has been presented. The spectrum fulfillment and the technological accommodation constraints of micro-acoustics technologies have been taken into account to obtain a complete solution. Moreover, it addressed the tuneability of the reactive input element to match the same filter to different complex source impedances, giving the designer a degree of freedom for filter adjustment.

A co-designed approach was implemented, achieving a good performance in the design of the PA and filter building blocks. The regular efficiency-optimized or power-optimized impedance obtained with a PA load-pull is not the optimal point for the PA-filter co-design in terms of filter shape. Therefore, in this chapter, is highlighted the importance of Z_{outPA} calculation as the Z_{SF} needed for an accurate filter matching. A closed formula for Z_{outPA} estimation based on X-parameters is also presented. A source-pull technique was applied to a passive network to analyze the filter in-band insertion loss variation. Moreover, a general method based on a filter synthesis technique to control the complex input impedance at the fundamental frequency and second harmonic concurrently for a PA-filter co-design was developed. The approach introduces an input reflection coefficient phase control (ϕ_{add_11}) to accurately set the second harmonic reflect for waveform shaping purposes, achieving a less complicated,

efficient, and compact design.

Without loss of generality, an example with coaxial resonators has been implemented. A fully canonical second-order filter was designed, yielding the desired Chebyshev filter response. Using the proposed control method, the second harmonic impedance termination was included in the synthesized filter, avoiding external elements for that purpose. The fabricated PA module presents a maximum PAE= 50.4% and P_{out}= 37.5 dBm under 27-dBm input stimulus at 2.64 GHz. An excellent balance between PA performance and filter shape was accomplished.

At the end of the chapter was presented a dual-band dual-output PA-filter, co-designed from the filter synthesis point of view. In a rigorous general formulation including input complex termination impedance, was used the control of the input reflection coefficient phase through ϕ_{add_11} to avoid loading effects in the duplexer. First of all, the PA was characterized to state the boundary conditions of the duplexer network. Later, a detailed synthesis of each filter and the circuital extraction procedure was shown. The amplifier was designed with a duplexer-like filtering network that presents an impedance match or a near-open circuit condition at each frequency on each branch to separate the bands into two channels. Using a commercial GaN transistor, a co-designed DO-DB module was implemented, providing the expected Chebyshev filter behavior with high selectivity response. A high maximum power-added efficiency of 52% and 57% for P_{in}=25 dBm at duplexer central frequencies were reached in a simulated environment.

CHAPTER 6

Conclusions and Future Work

6.1 Conclusions

The mobile communication market has grown explosively in the last years. Handset users and businesses are expecting and asking for an increase in data capacity and data link speeds. Therefore, to satisfy the demand, it is necessary more instantaneous bandwidth, higher transmit powers, more antennas and more efficient modulation schemes. All these requirements are intended to be cover by the upcoming 5G standard leveraging the carrier aggregation technology. One of the key 5G enabling components, RF filters, is being asked to be smaller, cheaper, reliable, with low insertion loss, high selectivity and out of band rejection, and with integration capabilities. Under this stringent environment, only the RF filters based on acoustic wave technologies can offer a competitive performance.

In this work is developed a theoretical and practical approach for designing AW modules where the integration of ladder-type filters into a multiplexer or the co-design with passive/active elements were addressed relying on the technological limitations. This proposal aims to provide a systematic methodology that prevents the common practice of modifying a previous design and optimize the variables to fulfill the new requirements. With the proposed methodologies is possible to connect synthesis techniques with the stringent constraints required by micro-acoustic technologies, providing an initial solution closer to a real one and ready for a following faster optimization process.

At the beginning of this dissertation, in Chapter 2, were faced the principal physical foundations, piezoelectric substrates, and implemented grounded and emerging technologies for acoustic resonators, being SAW and BAW the dominated resonator technologies for filtering devices. Despite the technological breakthroughs, this trend is expected to continue for future mobile communication systems due to the maturity and excellent performance. Additionally, critical resonator properties like effective coupling coefficient k^2_{eff} and quality factor Q were analyzed.

With the main physical characteristics and fundamental properties described, a resonator model was necessary for modeling and estimating the performance of the filtering network. To analyze the resonator electrical behaviour, the widely accepted Butterworth Van Dyke (BVD) electrical model composed by a series LC tank in parallel to a capacitance was characterized. Because the synthesis of ladder-type filtering networks is performed from a lowpass function, it was exposed an equivalent network in the lowpass domain. Furthermore, a nodal representation with dangling resonators equivalent to the lowpass BVD circuit was expounded. The nodal approach presents some advantages like modularity and the lack of a direct source-load path to ensure the fully canonical behavior.

The ladder-type filter interpretation as dangling resonators sandwiched between admittance inverters allows the acquisition of the lowpass elements by means of the extracted pole technique. Therefore, in Chapter 3, the lowpass synthesis procedure for the design of AW filters was faced using generalized Chebyshev filtering function. This function permits to synthesize symmetric and asymmetric filters of even or odd degrees for doubly terminated networks with any set of prescribed finite transmission zeros, return losses and band specifications. The associated characteristics polynomials and normalization constant were turned into an electrical circuit prototype using a synthesis approach based in the [ABCD] transfer matrix. The lowpass extracted elements can be also accommodated in a coupling matrix configuration as it is a useful representation tool for the simulation and network analysis.

The above proposed synthesis technique enables the management of the input reflection coefficient phase ϕ_{add_11} linked to the characteristic polynomials. In the this chapter was summarized the role-playing by this term in diverse practical cases and the paramount importance of the appropriate interpretation. Common cases like the implementation of stand-alone filters without external input or/and output elements and the phase matching conditions for duplexers were addressed. On the other hand, was proven the relation between phase and filter technological parameters. The analysis of ϕ_{add_11} shown that the phase value will affect the static capacitance of all filter resonators C_0, but also the first and last resonator capacitance ratios. It was observed that the phase can also be used to improve the performance of the designed filter significantly reducing the total area without affecting the amplitude response of the filter.

Having phase control is essential for duplexers and multiplexers design. Consequently, Chapter 4 tackled the design of star-junction AW multiplexers based on minimum susceptance networks (MSN). An exhaustive theoretical characterization of MSN regardless of the filtering function doubly or singly-terminated was deployed with the introduction of ϕ_{add_11} as a classification key. A new methodology to synthesize singly filters allowing phase adjustment was also presented in this chapter. Having doubly and singly filters the same capabilities for changing the input coefficient phase, a comparative studio was carried out concluding that STFs fulfill MSN conditions betters than DTFs

To avoid the filter's mutual loading in the multiplexer, and looking for the proper phase matching, some approaches mixing MSNs and non-MSNs were discussed considering contiguous and non-contiguous band contexts. Simultaneously, two scenarios were considered with fixed or flexible frequency plan. The proposed guidelines yield an excellent seed for further optimization process. Even

though each filter was synthesized individually, the multiplexer total response was computed through a numerical solution based on a matrix approach developed in this chapter. A closed scattering matrix formula was found for an ideal star-junction multiplexer dependent on the port number of the junction. Two triplexer examples were simulated and manufactured: 1) with lumped elements for a fixed frequency plan, and 2) with three BAW filters acquired from Qorvo and a switch from Menlo for a flexible frequency plan. The obtained results validate the theory proposed along the chapter.

As part of the AW filter integration strategy, the synthesis of filters terminating in complex impedances was addressed in Chapter 5. Hence, the synthesis methodology presented in Chapter 3 was extended to complex source and/or load terminations. A detailed synthesis and circuital extraction procedure was presented taking into consideration the technological acoustic limitations. This approach enables the co-design of passive and active networks with the filter to decrease complexity, losses, and device area simultaneously.

An illustrative example was presented to validate the complex filter termination theory and exploit the in-line fully canonical topology. A co-designed power amplifier bandpass filter module where the PA's output impedance influence is considered on the filter performance, was discussed at the end of the chapter. A two-pole filter was designed, providing a complex input-impedance to obtain the best efficiency but simultaneously taking care of filter transmission response that will appear affected by a non-complex conjugate transistor output impedance. Although the manufactured module is based on coaxial resonators technology, previous filter examples demonstrate the soundness of this approach for AW technology.

Additionally, a dual-band dual-output power amplifier co-designed with filters was presented in this chapter. To simplify the design for multifrequency PAs, multiplexer theory and co-design techniques were exploited together in this chapter to achieve a competitive solution. The exact synthesis technique was applied for controlling the complex input impedance at the fundamental frequency of each channel. In the single-channel case, the reflective termination at the 2^{nd} harmonic can be controlled simultaneously, providing high efficiency. In contrast, the multifrequency approach accommodates the input phase ϕ_{add_11} employing the same foundations used for phase matching filters in duplexers/multiplexers.

Few only-simulation examples and experimental validations were shown in this dissertation to demonstrate the proposed theoretical approaches. All of them were summarized in tables with numerical results and sometimes compared with external works. During the Ph.D. program, several simulation tools based on numerical calculation like MATLAB were developed integrating the synthesis methodologies and the different approaches for each situation.

6.2 Future Work

The acoustic wave filters synthesis is the core of all the content addressed in this thesis and has been investigated over the last years due to its paramount role in the first tier design. Our research group have tackled several issues related to network analysis, power management, technological feasibility and new topologies seeking an accurate understanding from a mathematical and physical point of view [9–11]. With the leap to complex modules that combine several filters, the methodology has evolved to innovative procedures that has to face more challenging requirements but considering the acoustic resonator (and filters) as the main cell. Thanks to the evolution and the acquired knowledge, some research topics could be explored in the near future:

1. **Lossy lowpass coupling matrix implementation:** The coupling matrix approach is a useful tool that contains most of the relevant information about the network. Modeling the circuit in matrix form is particularly useful because matrix operations can then be applied. Moreover, the coupling matrix can include some of the real-world properties of the filter's elements. The mBVD model with its associated resistances R_s, R_a and R_0 can be updated by a new model. To achieve a more reliable and flexible admittance matrix response in the lowpass domain, is needed a new nodal diagram that includes the losses produced by the circuital elements of this new model. Nodes of different nature: resonant and non-resonant should be taken into account for a generalized solution. The new lossy model will require the expansion of M, W and Y matrices in (3.34), adding the lossy elements in the Y matrix and reorganizing the M and W matrices.

   Adding the losses to the coupling matrix elements will provide a more realistic S-parameters response of ladder networks, which is itself closer to the final bandpass performance.

2. **Synthesis methodology of AW filters based on matrix rotations:** Up to now, the developed AW filter synthesis tools were based on iterative extraction procedures for inline extracted-pole lowpass prototype filters. Depending on the filter mask requirement specifications, by using standard double-precision arithmetic the maximum reachable order is limited by round-off errors, while for combined topologies with RN and NRN-RN nodes the order decreases. To overcome the errors accumulated in such cases, a new synthesis method by means of a set of iteratively similarity coupling matrix (CM) transformations from the canonical transversal coupling matrix representation should be considered. This algorithm will provide, under some conditions, higher robustness in front of high-order filters. This contribution will become a step forward in consolidating AW-oriented EDA tools.

3. **Synthesis of AW star-junction multiplexers:** The multiplexer synthesis in this work was addressed considering the filter individual performances as MSNs or non-MSNs to avoid the loading effect when are connected to a common junction. The assessment of an iterative solution which evaluates the characteristic polynomials of both, the overall multiplexer and the composing filters,

could improve the methodology and the obtained results. The objective is an equirriple CPRL resulting from non-Chebyshev filtering functions. New filtering functions that accommodates AW technology will be explored.

4. **Asymmetric polynomials for AW filters terminating in complex impedance:** In this thesis the symmetric polynomial definition has been used for the synthesis of filter with complex port impedances. This implementation forces an admittance redistribution at the last extraction step to guarantee even unity main-line inverters. The asymmetrical polynomial definition approached in [11] for unitary load impedances can be investigated and extended to general situations to avoid mismatched networks due to the impedance redistribution.

5. **Filters manufacturing based on PAW resonators with $LiNbO_3$ substrate:** The methodologies presented in this thesis for modules design have been experimentally validated with non-acoustic technologies. Even though some years ago previous results obtained by the research group were validated by one of the most relevant manufacturers of acoustic devices, measures were not included in public publications because of intellectual property limitations. Considering the relevance of having an accessible fabrication process, the design of a PAW resonator have been studied with $LiNbO_3$ piezoelectric substrate. The acknowledgment of an established design-manufactured non-industrial-level procedure is essential for further research on synthesis techniques of acoustic devices. Thus, intensify the efforts towards the technological independence will accelerate the validation process and add reliability to the current and upcoming methodologies.

APPENDIX A

Circuital Transformation from Dangling to Coaxial Resonator

In order to introduce TZs in the in-line filter bandpass response, the dangling resonator is considered in Section 5.5.5. The circuital transformation leads to a series resonator (L_a-C_a) in parallel to a capacitor (C_0). The series resonator behaves as an open circuit stub with $\beta l = 90°$ (quarter-wave) and the shunt capacitor C_0 behaves as an open circuit stub with $\beta l < 90°$ as its is shown in Fig. A.1.

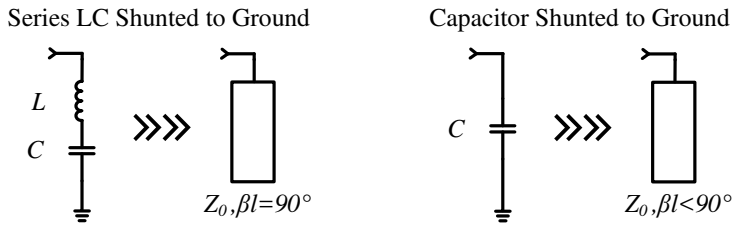

Figure A.1: Lumped element equivalents for shunted series resonator and capacitor.

Looking for small size and high performance, coaxial technology was selected to implement the open-stub resonator. Coaxial resonators are manufactured as quarter-wave (short-circuited) or half-wave (open-circuited) resonators. This condition enforces us to employ $\lambda/2$ open circuited resonators at $2f_0$ that behave as $\lambda/4$ open-circuited resonators at f_0. The length of an square cross-section $\lambda/2$ coaxial resonator is calculated as:

$$l = \frac{300}{2f\sqrt{\epsilon_r}} \quad [mm] \tag{A.1}$$

where $f = \omega/2\pi$ (GHz) and ϵ_r represents the dielectric permittivity.

The filter synthesis process is carry out as usually introducing the Ω_{TZ}, RL , Z_S and ϕ_{add_11} as the

input parameters. The coupling matrix M is obtained, but some values must be scaled to fit the parameters with the existing technology, especially the resonator's characteristic impedance Z_{0_cr} provided by the manufacturer. Taking into consideration the transmission zeros positions and Z_{0_cr} of the chosen coaxial resonator, series resonator can be calculated as:

$$L_{ai\_cr} = \frac{\pi Z_{0\_cr}}{4\omega_{TZi}} \tag{A.2a}$$

$$C_{ai\_cr} = \frac{1}{L_{ai\_cr}\omega_{TZi}^2} \tag{A.2b}$$

where ω_{TZi} are the transmission zero frequencies in the bandpass domain, and $i = 1 : N$ being N de number of dangling resonators.

With the fixed values of L_{ai_cr} and C_{ai_cr}, the corresponding lowpass element L_{m_cr} for each resonator is calculated using

$$L_{mi\_cr} = \frac{1}{2\alpha Z_0}\left(L_{ai\_cr}\omega_{TZi} + \frac{1}{C_{ai\_cr}\omega_{TZi}}\right) \tag{A.3}$$

Since the circuital filter diagram showed in Fig. 5.20b illustrates the representation of two BvD shunt resonators, the admittance inverter J_{ri} and X_{mi_cr} would be recalculated as

$$J_{ri\_cr} = \frac{1}{\sqrt{L_{m\_cr}}} \tag{A.4}$$

$$X_{mi\_cr} = \frac{-\Omega_{TZ}}{J_{ri\_cr}^2} \tag{A.5}$$

The original M matrix has changed its values. In order to find the proper values in the matrix representation linked to the coaxial resonator technology, a numerical factor γ is founded to scale the M matrix. This factor affects linearly and in a quadratic proportion the main-line inverters J_k ($k = i + 1$) and NRNs B_i respectively.

$$\gamma_i = \frac{J_{ri\_cr}}{J_{ri}} \tag{A.6}$$

$$J_{k\_cr} = J_k(\gamma_i)(\gamma_{i-1}) \tag{A.7}$$

$$B_{i\_cr} = \gamma_i^2 B_i \tag{A.8}$$

Having the values of B_{i_cr}, the lowpass element X_{0_cr} is computed as

$$X_{0i\_cr} = \frac{-1}{B_{i\_cr}} \tag{A.9}$$

Finally, the last bandpass element of the static branch C_{0i_cr} is calculated. The sign of Ω_{TZ} , i.e. the position in the lower/upper band, defines the nature of the element: capacitive or inductive

$$C_{0i\_cr} = \frac{-1}{Z_0 \Omega_{TZ} X_{0i\_cr}} \Longrightarrow \Omega_{TZ} < 0 \tag{A.10}$$

$$L_{0i\_cr} = \frac{X_{0i\_cr} Z_0}{\Omega_{TZ}} \qquad \Longrightarrow \Omega_{TZ} > 0 \tag{A.11}$$

The validation example of Section 5.5.5 was designed with two zeros at the lower band , so (A.10) was applied. The main-line inverters are transformed to bandpass domain as usually to complete the procedure and transformed to pi-networks capacitors/inductor inverters. Since the bandpass transformation is narrow-band, a post-optimization stage was needed in the filter design.

$$J_{k\_cr} = \frac{J_{k\_cr}}{Z_0} \tag{A.12}$$

Bibliography

[1] 3GPP, "Technical specification group services and system aspects: Release 16. tr 21.916," Tech. Rep., July 2020.

[2] G. G. Fattinger, A. Volatier, M. Al-Joumayly, Y. Yusuf, R. Aigner, N. Khlat, and M. Granger-Jones, "Carrier aggregation and its challenges - or: The golden age for acoustic filters," in *2016 IEEE MTT-S International Microwave Symposium (IMS)*, May 2016, pp. 1–4.

[3] R. Aigner, S. Marksteiner, L. Elbrecht, and W. Nessler, "RF-filters in mobile phone applications," in *TRANSDUCERS '03. 12th International Conference on Solid-State Sensors, Actuators and Microsystems. Digest of Technical Papers (Cat. No.03TH8664)*, 2003, vol. 1, pp. 891–894 vol.1.

[4] W. Hong, Z. H. Jiang, C. Yu, D. Hou, H. Wang, C. Guo, Y. Hu, L. Kuai, Y. Yu, Z. Jiang, Z. Chen, J. Chen, Z. Yu, J. Zhai, N. Zhang, L. Tian, F. Wu, G. Yang, Z. C. Hao, and J. Y. Zhou, "The role of millimeter-wave technologies in 5G/6G wireless communications," *IEEE Journal of Microwaves*, vol. 1, no. 1, pp. 101–122, 2021.

[5] Qorvo, "Evolution of carrier aggregation (CA) for 5G: What's new in mobile CA," Brochure, 2019.

[6] Cédric Malaquin and Antoine Bonnabel, "How the RF front-end world is being ruled in the 5G era," *Microwave Journal*, Dec. 2020.

[7] 3GPP TS 38.101-1, "NR; user equipment (UE) radio transmission and recep-tion; part 1: Range 1 standalone," Tech. Rep., 3GPP, Jan. 2019.

[8] 3GPP TS 38.101-2, "NR; user equipment (UE) radio transmission and recep-tion; part 2: Range 2 standalone," Tech. Rep., 3GPP, Jan. 2019.

[9] Alfred Giménez Bonastre, *RF Filters and Multiplexers Based on Acoustic Wave Technologies with Ladder-Type and Cross-Coupled Topologies*, Ph.D. thesis, Universitat Autònoma de Barcelona, 2016.

[10] Iuliia Evdokimova, *Direct Bandpass Methodology for Synthesis and Design of Satnd-Alone Filters and Duplexers Based on Acoustic Wave Technologies*, Ph.D. thesis, Universitat Autònoma de Barcelona, 2018.

[11] Ángel Triano Notario, *Advanced Synthesis Techniques for Parallel-Connected and Cross-Coupled Filters Based on Acoustic Wave Technologies*, Ph.D. thesis, Universitat Autònoma de Barcelona, 2020.

[12] V. S. Cortes, L. Liu, U. Stehr, M. Fischer, A. Frank, V. Chauhan, M. Hein, J. Müller, R. Weigel, G. Fischer, and A. Hagelauer, "Design of a power amplifier module in a novel silicon-ceramic substrate for an lte transmitter," in *2017 IEEE Asia Pacific Microwave Conference (APMC)*, 2017, pp. 448–451.

[13] V. Chauhan, L. W. Wandji, X. Peng, V. Silva Cortes, A. Frank, M. Fischer, U. Stehr, R. Weigel, and A. Hagelauer, "Design and performance of power amplifier integration with BAW filter on a silicon-ceramic composite and standard epoxy/glass substrate," in *2018 IEEE MTT-S International Microwave Workshop Series on Advanced Materials and Processes for RF and THz Applications (IMWS-AMP)*, 2018, pp. 1–3.

[14] V. Silva Cortes, J. Nowak, V. Chauhan, U. Stehr, M. A. Hein, G. Fischer, and A. Hagelauer, "RF MEMS modules: A multiphysical design methodology based on system performance requirements," *IEEE Microwave Magazine*, vol. 20, no. 10, pp. 44–55, 2019.

[15] D. C. Malocha, "SAW/BAW acoustoelectronic technology for filters and communication systems," in *2010 IEEE 11th Annual Wireless and Microwave Technology Conference (WAMICON)*, 2010, pp. 1–7.

[16] S. Mahon, "The 5G effect on RF filter technologies," *IEEE Transactions on Semiconductor Manufacturing*, vol. 30, no. 4, pp. 494–499, 2017.

[17] C. C. W. Ruppel, "Acoustic wave filter technology–a review," *IEEE Transactions on Ultrasonics, Ferroelectrics, and Frequency Control*, vol. 64, no. 9, pp. 1390–1400, 2017.

[18] T. Bauer, C. Eggs, K. Wagner, and P. Hagn, "A bright outlook for acoustic filtering: A new generation of very low-profile SAW, TC-SAW, and BAW devices for module integration," *IEEE Microwave Magazine*, vol. 16, no. 7, pp. 73–81, 2015.

[19] J.G. Smits, *Eigenstates of Coupling Factor and Loss Factor of Piezoelectric Ceramics*, Technische Hogeschool Twente, 1978.

[20] Songbin Gong, *Quality Factor and Coupling in Piezoelectric MEMS Resonators*, Springer International Publishing, 2017.

[21] G. G. Fattinger, "BAW resonator design considerations - an overview," in *2008 IEEE International Frequency Control Symposium*, 2008, pp. 762–767.

[22] Ken-Ya Hashimoto, *RF Bulk Acoustic Wave Filters for Communications*, Artech House, 2009.

[23] C.S. Lam, Anming Gao, Chih-Ming Lin, and Jie Zou1, "A review of lamé and lamb mode crystal resonators for timing applications and prospects of lamé and lamb mode piezomems resonators for filtering applications," in *Sixth International Symposium on Acoustic Wave Devices for Future Mobile Communication Systems*, 2018.

[24] Ken-Ya Hashimoto, *Surface Acoustic Wave Devices in Telecommunications: Modelling and Simulation*, Springer-Verlag Berlin Heidelberg, 2000.

[25] K. M. Lakin, "Equivalent circuit modeling of stacked crystal filters," in *Thirty Fifth Annual Frequency Control Symposium*, 1981, pp. 257–262.

[26] J. D. Larson, P. D. Bradley, S. Wartenberg, and R. C. Ruby, "Modified Butterworth-Van Dyke circuit for FBAR resonators and automated measurement system," in *2000 IEEE Ultrasonics Symposium. Proceedings. An International Symposium (Cat. No.00CH37121)*, 2000, vol. 1, pp. 863–868 vol.1.

[27] D. A. Feld, R. Parker, R. Ruby, P. Bradley, and S. Dong, "After 60 years: A new formula for computing quality factor is warranted," in *2008 IEEE Ultrasonics Symposium*, 2008, pp. 431–436.

[28] R. Ruby, R. Parker, and D. Feld, "Method of extracting unloaded q applied across different resonator technologies," in *2008 IEEE Ultrasonics Symposium*, 2008, pp. 1815–1818.

[29] Jordi Verdú Tirado, *Bulk AcousticWave Resonatorsand their Applicationto Microwave Devices*, Ph.D. thesis, Universitat Autònoma de Barcelona, 2010.

[30] R. Aigner and G. Fattinger, "3G – 4G – 5G: How BAW filter technology enables a connected world," in *2019 20th International Conference on Solid-State Sensors, Actuators and Microsystems Eurosensors XXXIII (TRANSDUCERS EUROSENSORS XXXIII)*, 2019, pp. 523–526.

[31] K. Hashimoto, M. Yamaguchi, S. Mineyoshi, O. Kawachi, M. Ueda, and G. Endoh, "Optimum leaky-SAW cut of litao/sub 3/ for minimised insertion loss devices," *1997 IEEE Ultrasonics Symposium Proceedings. An International Symposium (Cat. No.97CH36118)*, vol. 1, pp. 245–254 vol.1, 1997.

[32] M. Ueda, T. Nishihara, J. Tsutsumi, S. Taniguchi, T. Yokoyama, S. Inoue, T. Miyashita, and Y. Satoh, "High-Q resonators using FBAR/SAW technology and their applications," in *2005 IEEE/MTT-S International Microwave Symposium - IMS*, June 2005.

[33] P. Warder and A. Link, "Golden age for filter design: Innovative and proven approaches for acoustic filter, duplexer, and multiplexer design," *IEEE Microwave Magazine*, vol. 16, no. 7, pp. 60–72, 2015.

[34] Jie Zou, *High-Performance Aluminum Nitride Lamb Wave Resonators for RF Front-End Technology*, Ph.D. thesis, University of California, 2015.

[35] A. Teshigahara, K. Hashimoto, and M. Akiyama, "Scandium aluminum nitride: Highly piezoelectric thin film for RF SAW devices in multi GHz range," in *2012 IEEE International Ultrasonics Symposium*, 2012, pp. 1–5.

[36] Ken ya Hashimoto, *Piezoelectric MEMS Resonators*, Springer International Publishing, 2017.

[37] R. Nakagawa, T. Suzuki, H. Shimizu, H. Kyoya, and K. Hashimoto, "Influence of electrode materials and structural design on third-order nonlinear signals of SAW devices," in *2016 IEEE International Ultrasonics Symposium (IUS)*, 2016, pp. 1–4.

[38] J. Zou and C. S. Lam, "Electrode design of AlN lamb wave resonators," in *2016 IEEE International Frequency Control Symposium (IFCS)*, 2016, pp. 1–5.

[39] R. Aigner, "Tunable filters? reality check foreseeable trends in system architecture for tunable RF filters," *IEEE Microwave Magazine*, vol. 16, no. 7, pp. 82–88, 2015.

[40] J. Costa, S. McHugh, N. Rice, P. J. Turner, B. A. Willemsen, N. O. Fenzi, R. B. Hammond, J. D. Ha, C. H. Lee, and Takahiro Sato, "Design and characterization of SAW filters for high power performance," in *2017 IEEE International Ultrasonics Symposium (IUS)*. sep 2017, IEEE.

[41] J. D. Larson, J. D. Ruby, R. C. Bradley, J. Wen, Shong-Lam Kok, and A. Chien, "Power handling and temperature coefficient studies in FBAR duplexers for the 1900 MHz PCS band," in *2000 IEEE Ultrasonics Symposium. Proceedings. An International Symposium (Cat. No.00CH37121)*, 2000, vol. 1, pp. 869–874 vol.1.

[42] R. Ruby, "Review and comparison of bulk acoustic wave FBAR, SMR technology," in *2007 IEEE Ultrasonics Symposium Proceedings*, 2007, pp. 1029–1040.

[43] R. M. White and F. W. Voltmer, "Direct piezoelectric coupling to surface elastic waves," *Applied Physics Letters*, vol. 7, no. 12, pp. 314–316, 1965.

[44] Robert Aigner, *Piezoelectric MEMS Resonators*, Springer International Publishing, 2017.

[45] J. Zou and A. P. Pisano, "Temperature compensation of the AlN Lamb wave resonators utilizing the S1 mode," in *2015 IEEE International Ultrasonics Symposium (IUS)*, 2015, pp. 1–4.

[46] T. Takai, H. Iwamoto, Y. Takamine, H. Yamazaki, T. Fuyutsume, H. Kyoya, T. Nakao, H. Kando, M. Hiramoto, T. Toi, M. Koshino, and N. Nakajima, "Incredible high performance SAW resonator

on novel multi-layerd substrate," in *2016 IEEE International Ultrasonics Symposium (IUS)*, 2016, pp. 1–4.

[47] T. Takai, H. Iwamoto, Y. Takamine, T. Fuyutsume, T. Nakao, M. Hiramoto, T. Toi, and M. Koshino, "I.H.P. SAW technology and its application to microacoustic components (invited)," in *2017 IEEE International Ultrasonics Symposium (IUS)*, 2017, pp. 1–8.

[48] H. Iwamoto, T. Takai, Y. Takamine, M. Hiramoto, and M. Koshino, "A novel SAW resonator with incredible high-performances," in *2017 IEEE International Meeting for Future of Electron Devices, Kansai (IMFEDK)*, 2017, pp. 102–103.

[49] Yan Liu, Yao Cai, Yi Zhang, Alexander Tovstopyat, Sheng Liu, and Chengliang Sun, "Materials, design, and characteristics of bulk acoustic wave resonator: A review," *Micromachines*, vol. 11, no. 7, 2020.

[50] K. M. Lakin, G. R. Kline, and K. T. McCarron, "Development of miniature filters for wireless applications," *IEEE Transactions on Microwave Theory and Techniques*, vol. 43, no. 12, pp. 2933–2939, 1995.

[51] K. M. Lakin and J. S. Wang, "Acoustic bulk wave composite resonators," *Applied Physics Letters*, vol. 38, no. 3, pp. 125–127, 1981.

[52] R. C. Ruby, P. Bradley, Y. Oshmyansky, A. Chien, and J. D. Larson, "Thin film bulk wave acoustic resonators (FBAR) for wireless applications," in *2001 IEEE Ultrasonics Symposium. Proceedings. An International Symposium (Cat. No.01CH37263)*, 2001, vol. 1, pp. 813–821 vol.1.

[53] Johan Bjurström, Ilia Katardjiev, and Ventsislav Yantchev, "Lateral-field-excited thin-film lamb wave resonator," *Applied Physics Letters*, vol. 86, no. 15, pp. 154103, 2005.

[54] Michio Kadota and Shuji Tanaka, "Simulation of solidly mounted plate wave resonator with wide bandwidth using 0-th Shear Horizontal mode in $LiNbO_3$ plate," *Japanese Journal of Applied Physics*, vol. 54, no. 7S1, pp. 07HD09, jun 2015.

[55] Songbin Gong, *Piezoelectric MEMS Resonators*, Springer International Publishing, 2017.

[56] Ventsislav Yantchev and Ilia Katardjiev, "Thin film lamb wave resonators in frequency control and sensing applications: a review," *Journal of Micromechanics and Microengineering*, vol. 23, no. 4, pp. 043001, mar 2013.

[57] Y. Yang, A. Gao, R. Lu, and S. Gong, "5 GHz lithium niobate MEMS resonators with high fom of 153," in *2017 IEEE 30th International Conference on Micro Electro Mechanical Systems (MEMS)*, 2017, pp. 942–945.

[58] Y. Yang, L. Gao, and S. Gong, "An X-band lithium niobate acoustic RFFE filter with FBW of 3.45and IL of 2.7 dB," in *2020 IEEE/MTT-S International Microwave Symposium (IMS)*, 2020, pp. 249–252.

[59] J. B. Shealy, J. B. Shealy, P. Patel, M. D. Hodge, R. Vetury, and J. R. Shealy, "Single crystal aluminum nitride film bulk acoustic resonators," in *2016 IEEE Radio and Wireless Symposium (RWS)*, 2016, pp. 16–19.

[60] Akoustis, "https://akoustis.com/products/filters/applications/all-products/," 2021, Accessed: 2021-02-03.

[61] V. Plessky, S. Yandrapalli, P.J. Turner, L.G. Villanueva, J. Koskela, and R.B. Hammond, "5 GHz laterally-excited bulk-wave resonators (XBARs) based on thin platelets of lithium niobate," *Electronics Letters*, vol. 55, no. 2, pp. 98–100, 2019.

[62] P.J. Turner, B. Garcia, V. Yantchev, G. Dyer, S. Yandrapalli, L.G. Villanueva, R.B. Hammond, and V. Plessky, "5 GHz band n79 wideband microacoustic filter using thin lithium niobate membrane," *Electronics Letters*, vol. 55, no. 17, pp. 942–944, 2019.

[63] J.F. Nye, *Physical Properties of Crystals: Their Representation by Tensors and Matrices*, Clarendon Press, 1972.

[64] David Morgan, *Surface acoustic wave filters: With applications to electronic communications and signal processing*, Academic Press, 2010.

[65] R. Weigel, D. P. Morgan, J. M. Owens, A. Ballato, K. M. Lakin, K. Hashimoto, and C. C. W. Ruppel, "Microwave acoustic materials, devices, and applications," *IEEE Transactions on Microwave Theory and Techniques*, vol. 50, no. 3, pp. 738–749, 2002.

[66] Horace Lamb, "On waves in an elastic plate," *Proceedings of the Royal Society of London. Series A, Containing Papers of a Mathematical and Physical Character*, vol. 93, no. 648, pp. 114–128, 1917.

[67] Igor. A. Viktorov, *Rayleigh and Lamb Waves: Physical Theory and Applications*, Springer US, 1967.

[68] Claudia Steinem and Andreas Janshoff, "Piezoelectric resonators," *Sensors*, 2005.

[69] Zhongqing Su, Lin Ye, and Ye Lu, "Guided lamb waves for identification of damage in composite structures: A review," *Journal of Sound and Vibration*, vol. 295, no. 3, pp. 753 – 780, 2006.

[70] Augustus E. H. Love, *Some Problems of Geodynamics*, Cambridge University Press, 2015.

[71] W.P. Mason, *Piezoelectric Crystals and Their Application to Ultrasonics*, Bell Telephone Laboratories series. Van Nostrand, 1950.

[72] W.P. Mason, *Electromechanical Transducers and Wave Filters*, Bell Telephone Laboratories series. D. Van Nostrand Company, 1948.

[73] M. Solal, V. Laude, and S. Ballandras, "A P-matrix based model for SAW grating waveguides taking into account modes conversion at the reflection," in *IEEE Symposium on Ultrasonics, 2003*, 2003, vol. 2, pp. 1708–1713 Vol.2.

[74] V. Chauhan, C. Huck, A. Frank, W. Akstaller, R. Weigel, and A. Hagelauer, "Enhancing RF bulk acoustic wave devices: Multiphysical modeling and performance," *IEEE Microwave Magazine*, vol. 20, no. 10, pp. 56–70, 2019.

[75] R. Baum, "Design of unsymmetrical band-pass filters," *IRE Transactions on Circuit Theory*, vol. 4, no. 2, pp. 33–40, 1957.

[76] J. D. Rhodes and R. J. Cameron, "General extracted pole synthesis technique with applications to low-loss te/sub011/ mode filters," *IEEE Transactions on Microwave Theory and Techniques*, vol. 28, no. 9, pp. 1018–1028, 1980.

[77] S. Amari and G. Macchiarella, "Synthesis of inline filters with arbitrarily placed attenuation poles by using nonresonating nodes," *IEEE Trans. Microw. Theory Techn.*, vol. 53, no. 10, pp. 3075–3081, Oct 2005.

[78] S. Amari and U. Rosenberg, "New building blocks for modular design of elliptic and self-equalized filters," *IEEE Transactions on Microwave Theory and Techniques*, vol. 52, no. 2, pp. 721–736, 2004.

[79] E. Guerrero, P. Silveira, J. Verdú, Y. Yang, S. Gong, and P. de Paco, "A synthesis approach to acoustic wave ladder filters and duplexers starting with shunt resonator," *IEEE Transactions on Microwave Theory and Techniques*, vol. 69, no. 1, pp. 629–638, 2021.

[80] H. Bode, *Network analysis and feedback amplifier design*, van Nostrand New York, 1945.

[81] GL Matthaei and EG Cristal, "Theory and design of diplexers and multiplexers," *Advances in microwaves*, vol. 2, pp. 237–324, 1967.

[82] I. Evdokimova, A. Gimenez, J. Verdú, and P. de Paco, "Synthesis of ladder-type acoustic filters in the band-pass domain," in *2017 47th European Microwave Conference (EuMC)*, 2017, pp. 640–643.

[83] I. Evdokimova, J. Verdú, and P. de Paco, "Bandpass phase correction methodology for ladder-type acoustic filters," in *2018 48th European Microwave Conference (EuMC)*, 2018, pp. 683–686.

[84] Richard J. Cameron, Chandra M. Kudsia, and Raafatr R. Mansour, *Microwave filters for communications systems: fundamentals, design, and applications*, Wiley, 2018.

[85] R.J. Cameron, "General coupling matrix synthesis methods for chebyshev filtering functions," *IEEE Transactions on Microwave Theory and Techniques*, vol. 47, no. 4, pp. 433–442, apr 1999.

[86] S. Tamiazzo and G. Macchiarella, "Synthesis of cross-coupled prototype filters including resonant and non-resonant nodes," *IEEE Trans. Microw. Theory Techn.*, vol. 63, no. 10, pp. 3408–3415, Oct 2015.

[87] A. Gimenez and P. de Paco, "Involving source-load leakage effects to improve isolation in ladder acoustic wave filters," in *2016 IEEE MTT-S International Microwave Symposium (IMS)*, 2016, pp. 1–4.

[88] Á. Triano, J. Verdú, P. de Paco, T. Bauer, and K. Wagner, "Relation between electromagnetic coupling effects and network synthesis for aw ladder type filters," in *2017 IEEE International Ultrasonics Symposium (IUS)*, 2017, pp. 1–4.

[89] Á. Triano, P. Silveira, J. Verdú, and P. de Paco, "Phase correction of asymmetrical chebyshev polynomials for extracted-pole fully canonical filters," in *2019 IEEE MTT-S International Microwave Symposium (IMS)*, 2019, pp. 838–841.

[90] R.J. Cameron, "Advanced coupling matrix synthesis techniques for microwave filters," *IEEE Transactions on Microwave Theory and Techniques*, vol. 51, no. 1, pp. 1–10, 2003.

[91] A. E. Atia and A. E. Williams, "New types of bandpass filters for satellite transponders," *COMSAT Technical Review*, vol. 1, no. 1, 1971.

[92] A. Giménez, J. Verdú, and P. de Paco Sánchez, "General synthesis methodology for the design of acoustic wave ladder filters and duplexers," *IEEE Access*, vol. 6, pp. 47969–47979, 2018.

[93] P. Silveira, J. Verdú, and P. de Paco, "Star-junction multiplexer design under minimum susceptance networks approach," in *2019 IEEE/MTT-S International Microwave Symposium - IMS*, June 2019.

[94] R. I. Cameron and M. Yu, "Design of manifold-coupled multiplexers," *IEEE Microwave Magazine*, vol. 8, no. 5, pp. 46–59, 2007.

[95] R. Levy, "Synthesis of general asymmetric singly- and doubly-terminated cross-coupled filters," *IEEE Transactions on Microwave Theory and Techniques*, vol. 42, no. 12, pp. 2468–2471, Dec 1994.

[96] A. Garcia-Lamperez, M. Salazar-Palma, and T. K. Sarkar, "Analytical synthesis of microwave multiport networks," in *2004 IEEE MTT-S International Microwave Symposium Digest*, June 2004, vol. 2, pp. 455–458 Vol.2.

[97] G. Macchiarella and S. Tamiazzo, "Novel approach to the synthesis of microwave diplexers," *IEEE Transactions on Microwave Theory and Techniques*, vol. 54, no. 12, pp. 4281–4290, Dec 2006.

[98] G. Macchiarella and S. Tamiazzo, "Synthesis of star-junction multiplexers," *IEEE Transactions on Microwave Theory and Techniques*, vol. 58, no. 12, pp. 3732–3741, Dec 2010.

[99] Ke-Li Wu and Wei Meng, "A direct synthesis approach for microwave filters with a complex load and its application to direct diplexer design," *IEEE Transactions on Microwave Theory and Techniques*, vol. 55, no. 5, pp. 1010–1017, may 2007.

[100] Y. Yang, M. Yu, X. Yin, and Q. Wu, "On the singly terminated and complementary networks," *IEEE Transactions on Microwave Theory and Techniques*, vol. 67, no. 3, pp. 988–996, March 2019.

[101] H. Orchard, "Loss sensitivities in singly and doubly terminated filters," *IEEE Transactions on Circuits and Systems*, vol. 26, no. 5, pp. 293–297, May 1979.

[102] J. Tow, "Comments on "lower bounds on the summed absolute and squared voltage transfer sensitivities in RLC networks," *IEEE Transactions on Circuits and Systems*, vol. 26, no. 3, pp. 209–211, March 1979.

[103] G.I. Atabekov, *Linear network theory*, International Series of Monographs in the Science of the Solid State. Pergamon Press, 1965.

[104] J. Verdú, I. Evdokimova, P. de Paco, T. Bauer, and K. Wagner, "Systematic synthesis methodology for the design of acoustic wave stand-alone ladder filters, duplexers and multiplexers," in *2017 IEEE Int. Ultrason. Symp. (IUS)*, Sep. 2017.

[105] Y. Yang, Q. Wu, X. Yin, and M. Yu, "Singly terminated network and contiguous multiplexer design," in *2018 IEEE/MTT-S International Microwave Symposium - IMS*, June 2018, pp. 1234–1237.

[106] P. Silveira, J. Verdú, and P. de Paco, "Scattering matrix solution for an ideal star-junction multiplexer based on ladder-type filters," *International Journal of Microwave and Wireless Technologies*, vol. 12, no. 10, pp. 954–959, 2020.

[107] X. Y. Zhang and J. Xu, "Multifunctional filtering circuits: 3D multifunctional filtering circuits based on high-Q dielectric resonators and coaxial resonators," *IEEE Microwave Magazine*, vol. 21, no. 3, pp. 50–68, 2020.

[108] K. Chen, J. Lee, W. J. Chappell, and D. Peroulis, "Co-design of highly efficient power amplifier and high-q output bandpass filter," *IEEE Trans. Microw. Theory Techn.*, vol. 61, no. 11, pp. 3940–3950, Nov 2013.

[109] Jose Antonio Estrada, Jose R. Montejo-Garai, Pedro de Paco, Dimitra Psychogiou, and Zoya Popovic, "Power amplifiers with frequency-selective matching networks," *IEEE Transactions on Microwave Theory and Techniques*, pp. 1–1, 2020.

[110] D. A. Frickey, "Conversions between S, Z, y, H, ABCD, and T parameters which are valid for complex source and load impedances," *IEEE Trans. Microw. Theory Techn.*, vol. 42, no. 2, pp. 205–211, Feb 1994.

[111] Huan Meng and Ke-Li Wu, "Direct optimal synthesis of a microwave bandpass filter with general loading effect," *IEEE Transactions on Microwave Theory and Techniques*, vol. 61, no. 7, pp. 2566–2573, jul 2013.

[112] Chuan Ge, Xiao-Wei Zhu, Xin Jiang, and Xiao-Jie Xu, "A general synthesis approach of coupling matrix with arbitrary reference impedances," *IEEE Microwave and Wireless Components Letters*, vol. 25, no. 6, pp. 349–351, jun 2015.

[113] Meng Meng and Ke-Li Wu, "Direct synthesis of general Chebyshev bandpass filters with a frequency variant complex load," in *2010 IEEE MTT-S International Microwave Symposium*. may 2010, IEEE.

[114] Kyle Holzer and Jeffrey S. Walling, "One Watt gallium arsenide class-E power amplifier with a thin-film bulk acoustic resonator filter embedded in the output network," *The Journal of Engineering*, vol. 2015, no. 5, pp. 174–176, 2015.

[115] Steve C. Cripps, *RF Power Amplifiers for Wireless Communications*, ARTECH HOUSE INC, 2006.

[116] Bahl, *Fundamentals of RF and Microwave Transistor Amplifiers*, John Wiley & Sons, 2009.

[117] N. Kumar, C. Prakash, A. Grebennikov, and A. Mediano, "High-efficiency broadband parallel-circuit class E RF power amplifier with reactance-compensation technique," *IEEE Transactions on Microwave Theory and Techniques*, vol. 56, no. 3, pp. 604–612, mar 2008.

[118] S. Y. Zheng, Z. W. Liu, X. Y. Zhang, X. Y. Zhou, and W. S. Chan, "Design of ultrawideband high-efficiency extended continuous class-F power amplifier," *IEEE Transactions on Industrial Electronics*, vol. 65, no. 6, pp. 4661–4669, 2018.

[119] Li Gao, Xiu Yin Zhang, Shichang Chen, and Quan Xue, "Compact power amplifier with bandpass response and high efficiency," *IEEE Microwave and Wireless Components Letters*, vol. 24, no. 10, pp. 707–709, oct 2014.

[120] Qing-Yi Guo, Xiu Yin Zhang, Jin-Xu Xu, Yuan Chun Li, and Quan Xue, "Bandpass class-F power amplifier based on multifunction hybrid cavity–microstrip filter," *IEEE Transactions on Circuits and Systems II: Express Briefs*, vol. 64, no. 7, pp. 742–746, jul 2017.

[121] Yang Gao, Fan Zhang, Xin Lv, Cheng Guo, Xiaobang Shang, Lei Li, Jiashan Liu, Yuhuai Liu, Yi Wang, and Michael J. Lancaster, "Substrate integrated waveguide filter–amplifier design using

active coupling matrix technique," *IEEE Transactions on Microwave Theory and Techniques*, vol. 68, no. 5, pp. 1706–1716, may 2020.

[122] X. Qi and F. Xiao, "Filtering power amplifier with up to 4th harmonic suppression," *IEEE Access*, vol. 8, pp. 29021–29026, 2020.

[123] Kenle Chen, Tsung-Chieh Lee, and Dimitrios Peroulis, "Co-design of multi-band high-efficiency power amplifier and three-pole high-Q tunable filter," *IEEE Microwave and Wireless Components Letters*, vol. 23, no. 12, pp. 647–649, dec 2013.

[124] Gareth LLoyd, "The maximally efficient amplifier," *Microwave Journal*, vol. 63, Apr. 2020.

[125] Michael Schefter and Mehdi Ardavan, "A comparison of GaN vs GaAs system performance," *AEROSPACE CHINA*, vol. 19, no. 3, pp. 17, 2018.

[126] CREE Wolfspeed, "CGH40006P 6W, RF power GaN HEMT," https://www.wolfspeed.com/downloads/dl/file/id/306/product/511/cgh40006p.pdf.

[127] Osman Ceylan, Lazaro Marco, and Sergio Pires, "Refine biasing networks for high PA low-frequency stability," *Microwaves and RF*, vol. 57, pp. 52–56, 2018.

[128] John F. Sevic, *The Load-Pull Method of RF and Microwave Power Amplifier Design*, WILEY, 2020.

[129] Verspecht and D.E. Root, "Polyharmonic distortion modeling," *IEEE Microwave Magazine*, vol. 7, no. 3, pp. 44–57, jun 2006.

[130] Charles Baylis, Robert Marks, Josh Martin, Hunter Miller, and Matthew Moldovan, "Going nonlinear," *IEEE Microwave Magazine*, vol. 12, no. 2, pp. 55–64, apr 2011.

[131] David Root, Jason Horn, Jan Verspecht, and Mihai Marcu, *X-Parameters: Characterization, Modeling, and Design of Nonlinear RF and Microwave Components*, Cambridge University Press, 2013.

[132] Chie-In Lee, Wei-Cheng Lin, and Yan-Ting Lin, "Large-signal output characteristic investigation of the mosfets in the breakdown region based on X-parameters," *Journal of Electromagnetic Waves and Applications*, vol. 29, no. 14, pp. 1867–1874, 2015.

[133] P. Bell, Z. Popovic, and C.W. Dyck, "MEMS-switched class-A-to-E reconfigurable power amplifier," in *2006 IEEE Radio and Wireless Symposium*. 2006.

[134] Mini-Circuits, "ZHL-2W-63X-S+ high power amplifier, 600 - 6000 MHz, 50 Ω," https://www.minicircuits.com/WebStore/dashboard.html?model=ZHL-2W-63-S

[135] Keysight Technologies, "Keysight 2-port and 4-port PNA-X network analyzer," https://literature.cdn.keysight.com/litweb/pdf/N5242-90007.pdf?id=1118335.

[136] Huber+Suhner, "RF Attenuator 5930-SMA-50-010/19-N," https://ecatalog.hubersuhner.com/media/documents/datasheet/en/pdf/84066962 .

[137] Keysight Technologies, "U2002H 50 MHz-24 GHz USB power sensor," https://www.keysight.com/en/pd-1444406-pn-U2002H/50-mhz-24-ghz-usb-power-sensor?cc=US&lc=eng.

[138] Yuan Chun Li, King Cheung Wu, and Quan Xue, "Power amplifier integrated with bandpass filter for long term evolution application," *IEEE Microwave and Wireless Components Letters*, vol. 23, no. 8, pp. 424–426, aug 2013.

[139] K. Rawat and F. M. Ghannouchi, "Design methodology for dual-band doherty power amplifier with performance enhancement using dual-band offset lines," *IEEE Transactions on Industrial Electronics*, vol. 59, no. 12, pp. 4831–4842, 2012.

[140] K. Rawat and F. M. Ghannouchi, "Dual-band matching technique based on dual-characteristic impedance transformers for dual-band power amplifiers design," *IET Microwaves, Antennas Propagation*, vol. 5, no. 14, pp. 1720–1729, 2011.

[141] X. Fu, D. T. Bespalko, and S. Boumaiza, "Novel dual-band matching network for effective design of concurrent dual-band power amplifiers," *IEEE Transactions on Circuits and Systems I: Regular Papers*, vol. 61, no. 1, pp. 293–301, 2014.

[142] K. Chen, E. J. Naglich, Y. Wu, and D. Peroulis, "Highly linear and highly efficient dual-carrier power amplifier based on low-loss RF carrier combiner," *IEEE Transactions on Microwave Theory and Techniques*, vol. 62, no. 3, pp. 590–599, 2014.

[143] A. Duh, S. Rahimizadeh, T. Barton, and Z. Popović, "A 3.5/5.9-GHz dual-band output matching network for an efficiency-optimized multiband power amplifier," in *2018 IEEE Topical Conference on RF/Microwave Power Amplifiers for Radio and Wireless Applications (PAWR)*, 2018, pp. 75–78.

[144] T. Cappello, A. Duh, T. W. Barton, and Z. Popović, "A dual-band dual-output power amplifier for carrier aggregation," *IEEE Transactions on Microwave Theory and Techniques*, vol. 67, no. 7, pp. 3134–3146, 2019.

[145] David A. Feld, Reed Parker, Richard Ruby, Paul Bradley, and Shim Dong, "After 60 years: A new formula for computing quality factor is warranted," in *2008 IEEE Ultrasonics Symposium*, 2008, pp. 431–436.